Dpto. de Física Teórica y del Cosmos & CAFPE
Universidad de Granada

Search for Ultra-High Energy Neutrinos at the Pierre Auger Observatory

Author:

Jose Luis Navarro Quirante

Advisor:

Dr. **Sergio Navas Concha**

Doctoral program:

Programa Oficial de Postgrado en Física (P16.56.1)

- December 2012 -

Editor: Editorial de la Universidad de Granada
Autor: José Luis Navarro Quirante
D.L.: GR 1075-2013
ISBN: 978-84-9028-476-6

D. Sergio Navas Concha, Profesor Titular de Universidad,

CERTIFICA: que la presente memoria, Search for Ultra High Energy Neutrinos at the Pierre Auger Observatory, ha sido realizada por D. Jose Luis Navarro Quirante bajo su dirección en el Dpto. de Física Teórica y del Cosmos de la Universidad de Granada, así como que éste ha disfrutado de estancias en el extranjero por un periodo superior a tres meses en el Labaratoire de Physique Nucleaire et Hautes Energies (LPNHE) en París (Francia).

Granada, 31 de Octubre de 2012

Fdo: Sergio Navas Concha

El doctorando D. Jose Luis Navarro Quirante y el director de la tesis Dr. Sergio Navas Concha,

Garantizamos, al firmar esta tesis doctoral, que el trabajo ha sido realizado por el doctorando bajo la dirección del director de la tesis y hasta donde nuestro conocimiento alcanza, en la realización del trabajo, se han respetado los derechos de otros autores al ser citados, cuando se han utilizado sus resultados o publicaciones.

Granada, 31 de Octubre de 2012

Director de la Tesis

Fdo: Sergio Navas Concha

Doctorando

Fdo: Jose Luis Navarro Quirante

A Luis Adrián y Jakelyne.
A mis padres y hermana.
A mis abuelos.

Contents

"Cuando advierta que para producir usted necesita obtener autorización de quienes no producen nada; cuando compruebe que el dinero fluye hacia quienes trafican no bienes, sino favores; cuando perciba que muchos se hacen ricos por el soborno y por influencias más que por el trabajo, y que las leyes no lo protegen contra ellos, sino, por el contrario son ellos los que están protegidos contra usted; cuando repare que la corrupción es recompensada y la honradez se convierte en un autosacrificio, entonces usted podrá afirmar, sin temor a equivocarse, que su sociedad esta condenada."

Ayn Rand (1981)

Agradecimientos

Este es sin duda el capítulo más difícil de escribir. Resumir en un par de páginas tantas cosas por agradecer y a tanta gente es imposible. Todos los que han compartido algún momento conmigo en los últimos años son culpables de un modo o de otro de la escritura de esta tesis. Por adelantado pido disculpas a los que se me hayan podido olvidar.

Tengo que agradecer en primer lugar a mi tutor, Sergio Navas Concha, ya que su labor, su paciencia y su mano izquierda han sido fundamentales para que esta tesis haya llegado a término. Durante estos años me ha enseñado la importancia de ser sistemático en la investigación, me he impregnado de su fabulosa capacidad para transmitir resultados y ser didáctico y he intentado aprender de su metodología y su orden. Aunque me queda mucho por mejorar en todos estos aspectos, su influencia me ha ayudado a ser mejor científico. Agradezco su apoyo, consejos y ayuda tanto en temas profesiones como extraprofesionales y los buenos momentos pasados en todos los viajes que hemos compartido.

A Antonio Bueno Villar, quien merece una mención especial. Desde el primer momento y hasta el final ha proporcionado todos los medios necesarios que estaban a su alcance, no solo para que esta tesis se hiciera realidad, sino para asegurarnos a todos y cada uno de los estudiantes del grupo el mejor futuro y currículum posible y en mi caso, de forma totalmente desinteresada. Su filosofía "los méritos tienen que ser de los estudiantes" es un ejemplo a seguir. Su influencia tanto en esta tesis, como en mi formación como científico y también como persona tienen un valor incalculable. Espero poder devolver algún día, de una forma u otra, todo lo que me ha proporcionado, pero por el momento lo único que puedo hacer es decir: Gracias Antonio.

Al Dpto. de Física Teórica y del Cosmos y todos sus miembros, por acogerme entre sus filas. Gracias también a todos los miembros del grupo experimental: A Julio Lozano Bahilo, hombre de bien y tranquilo, y más que compañero, un amigo, siempre mezclado con los estudiantes como uno más y siempre predispuesto, con él he compartido muy buenos momentos y conversaciones. A Alberto Gascón, por aportar la seriedad necesaria para mantener la decencia en el despacho. A Bruno Zamorano, por aportar su refinado estilo con la lengua inglesa. A Laura Molina, por su interminable paciencia. A Patricia Sánchez, la más joven, por recordarnos los beneficios de la filosofía "every weekend". A Rafa y Mariano, por alegrar el despacho con su refinado humor. Y a la parte técnica del grupo, María Dolores, Ginés y Angel Ruiz, cuyo trabajo en GRID ha sido clave para la realización de esta tesis.

A mis compañeros de despacho anteriores, Adrián, Roberto, Jorge, Mari Carmen y Nacho por su apoyo y todos los momentos buenos que hemos compartido. Una mención especial para Diego García que además de un excelente compañero ha sido un gran amigo con el que he compartido buenos y malos momentos que hemos superado juntos. Y por supuesto a Antonio Jesús Melgarejo,

el principal responsable de mi entrada en el grupo experimental y su incondicional apoyo. A todos vosotros, gracias, os deseo lo mejor.

A parte del ámbito laboral y profesional, esta tesis no se hubiera escrito de no ser por el apoyo de toda mi familia. En especial de mi hijo Luis Adrián, que sin saberlo, me ha proporcionado la fuerza suficiente para no rendirme en los momentos difíciles y continuar hasta el final. A mi esposa Jakelyne, por toda su comprensión y su inigualable paciencia ante meses de trabajo sin descanso, sin vacaciones y sin fines de semana. Gracias por ser la mejor esposa del mundo. A mis padres, que con su esfuerzo me proporcionaron una carrera universitaria, y gracias a su ayuda y apoyo he podido escribir esta tesis. A mi hermana, cuñado y sobrinas por su apoyo. A mis abuelos, que jamás han tenido dudas de que escribiría esta tesis y al resto de mi familia por estar siempre ahí. Tampoco quiero olvidarme de mis suegros Gilmar y Joana, por cuidar a Luis Adrián y Jakelyne durante mis frecuentes viajes.

A todos mis amigos, especialmente a Fran, a quien considero mi hermano, por la cantidad de momentos irrepetibles que hemos pasado juntos y mantenerse siempre cerca y a Lia por "meterlo en vereda". Y por supuesto, Ana y Fernando, que siempre me han animado. No quiero olvidarme de mis compañeros de Física, en especial, Raúl Rica y Octavio Jiménez, quienes a pesar de las distancias, siempre se han preocupado por seguir en contacto. Finalmente a dos personas que me enseñaron el apasionante mundo de la montaña y que desafortunadamente se quedaron para siempre en ella: Gerardo y "Primi", Gracias por tan magníficos momentos juntos.

Finalmente agradecer a todas las personas que sin animo de lucro ponen medios y software libre a nuestro alcance como Wikipedia, wordreference, youtube, mejorenvo, Duncan in China, Ubuntu, y un largo etc y a todos los científicos del mundo, ya que gracias a su trabajo, y a pesar de ser ingratamente reconocido por la sociedad, han hecho posible la tecnología y la calidad de vida que disfrutamos. Sin Ciencia, no hay Futuro.

A todos vosotros y a muchos otros: Gracias.

Acknowledgements

Just a few words for the foreign people. First, I would like to thank the group of Antoine Letessier-Selvon in Paris for their hospitality during my three months there. Especially, I would like to thanks Pierre Billoir for his superb ideas. He is one of the best physicists I have ever met and he transmitted me the passion for science, for the sake of science itself. Thanks to Piera Luisa Ghia for her patience and careful reviews of my publications. To the people of Orsay, especially Oliver Deligny and Isabelle Lhenry-Yvon for their invaluable help. To Jim Matthews and Karl Heinz Kampert for their support.

Of course, this thesis is the result of a global collaboration, thanks to all the people involved in the Pierre Auger Observatory for making it possible. Especially to Jaime Alvarez, who I always considered a college rather than a physic coordinator due to his kindness. And finally to Javier Gonzalez for a lot of useful explanations on the $\overline{\text{Off}}\underline{\text{line}}$.

Introducción

En la década de 1910, la comunidad científica descubrió que la tierra estaba continuamente bombardeada por radiación de origen cósmico. Desde entonces esta radiación, hoy conocida con el nombre de rayos cósmicos, ha sido profundamente estudiada con el fin de comprender su composición y su origen. Actualmente se sabe que la energía de esta radiación cubre un amplio rango, extendiéndose hasta energías del orden de cientos de EeV, por lo tanto, estas partículas tienen energías imposibles de alcanzar en aceleradores artificiales. El proceso que estas partículas sufren para alcanzar energías tan extremas es aun desconocido. El flujo de estas partículas decrece rápidamente con la energía. Los rayos cósmicos de baja energía se pueden estudiar directamente con detectores instalados en satélites y están compuestos principalmente por fotones y núcleos atómicos ligeros.

En la parte alta del espectro energético se concentran los llamados Rayos Cósmicos Ultra-Energéticos (Ultra-High Energy Cosmic Rays; UHECRs) cuyo flujo aproximado es de una partícula por siglo y por kilómetro cuadrado. Esta cantidad no es suficiente para ser detectada directamente, por lo tanto conocemos relativamente poco de ellos y propiedades tan importantes como su origen, su composición química o los mecanismos de aceleración que sufren para alcanzar energías tan extremas siguen siendo un misterio actualmente, después de 100 años de su descubrimiento. Por supuesto, cualquier nuevo conocimiento en el campo de los Rayos Cósmicos se traduce en nuevo conocimiento en el área de la física de partículas, contribuyendo a la comprensión de sus mecanismos de interacción. Cuando estas partículas alcanzan la tierra, colisionan con los núcleos atómicos de la atmósfera, que actúa como amplificador de la partícula incidente, produciendo millones de partículas que "llueven" sobre la superficie terrestre. Este proceso es llamado Lluvias Aéreas Extensas (Extensive Air Showers; EAS) [1]. Actualmente los estudios sobre UHECRs se centran en extraer información de las partículas primarias a través de las propiedades de las EAS que provocan.

La búsqueda de Neutrinos Ultra-Energéticos (Ultra-High Energy Neutrinos; UHEνs) emitidos en objetos astrofísicos es uno de los campos más desafiantes de la física de astropartículas. Los UHEνs juegan un papel fundamental en la comprensión del origen de los rayos cósmicos. Su detección abriría una nueva ventana al universo, permitiendo observar regiones hasta ahora ocultas a los observatorios debido a la gran cantidad de materia interestelar interpuesta en su campo de visión. Además, los neutrinos no son desviados por los campos magnéticos, por lo tanto apuntan directamente a su fuente. Aunque los UHEνs no han sido observados hasta el momento, varios modelos astrofísicos y cosmológicos predicen su existencia, por lo tanto, su detección puede ayudar a confirmar o rechazar modelos de producción y propagación de rayos cósmicos. Esta tesis está enfocada a la búsqueda de UHEνs usando los datos obtenidos por el Observatorio Pierre Auger [2].

El Observatorio Pierre Auger ha sido diseñado para estudiar las propiedades de los rayos cósmicos de energías mayores de 10^{18} eV. Es el único observatorio híbrido del mundo, combinando técnicas de detección mediante fluorescencia y superficie simultáneamente. Aunque el detector de superficie (surface detector; SD) del Observatorio Pierre Auger ha sido diseñado para la detección de UHECRs, se ha demostrado que tiene la capacidad de detectar tanto UHEνs interaccionando

en la atmósfera a ángulos casi horizontales (downward-going [3]) como neutrinos interaccionando en la corteza terrestre (Earth- skimming [4]). La discriminación de EAS inducidas por neutrinos aprovecha la posibilidad de estos de interaccionar profundamente en la atmósfera, allí donde los rayos cósmicos no pueden penetrar.

La principal limitación a la observación de neutrinos viene de la gran cantidad de señal de fondo comparada con la señal esperada de neutrinos. La búsqueda de neutrinos, hasta el momento, se ha centrado en lluvias casi horizontales ($\theta > 75°$), donde la cantidad de atmósfera es suficiente para absorber la contribución de origen hadrónico y la probabilidad de interacción del neutrino es mayor. Sin embargo, la detección e identificación de neutrinos usando lluvias menos inclinadas no está descartada y ha sido estudiada como parte de esta tesis doctoral. La nueva búsqueda de neutrinos se centras en el rango de ángulo cenital comprendido entre 60° - 75°. Además se han actualizado los resultados del análisis de neutrinos "Earth-skimming".

También se ha evaluado la sensitividad del Observatorio Pierre Auger a fuentes puntuales de neutrinos. Como se muestra en este documento, se han calculado límites muy restrictivos al flujo esperado de neutrinos en función de la declinación para un rango angular de más de 100°. Esta región angular se ha visto incrementada por la contribución del análisis a bajo ángulo.

La primera parte de esta tesis (capítulos 1 al 3) se dedica a la introducción de los conceptos principales en el campo de los rayos cósmicos y las lluvias extensas inducidas por estos, así como a la introducción del Observatorio Pierre Auger, poniendo especial atención en los conceptos más relevantes para la búsqueda de neutrinos.

La segunda parte del documento (capítulos 4 al 7) está centrada en la descripción del análisis llevado a cabo para la búsqueda de UHEνs a bajo ángulo cenital. Las simulaciones necesarias para el estudio se describen en el capítulo 4 mientras que el método usado para su identificación se describe en el capítulo 5. La exposición del Observatorio a neutrinos a bajo ángulo usando el método descrito se presenta en el capítulo 6 y los resultados obtenidos para el flujo difuso se presentan en el capítulo 7.

En la tercera parte de la tesis (capítulos 8 y 9) se presentan los resultados de la búsqueda de neutrinos provenientes de fuentes puntuales. En primer lugar, en el capítulo 8 se presenta un límite mejorado para el canal Earth-skimming, dejando los resultados para fuentes puntuales al capítulo 9. El documento finaliza con dos apéndices donde se exponen los detalles técnicos relevantes del análisis así como las contribuciones realizadas, dentro del marco de esta tesis, al paquéte de simulación y análisis $\overline{\text{Off}}\underline{\text{line}}$.

Introduction

In the 1910s, the scientific community discovered that the Earth was continuously bombarded by radiation of extraterrestrial origin. Since then, this radiation, now know as Cosmic Rays (CRs), has been deeply studied in order to understand its nature and origin. Nowadays, we know that the energy of this radiation expands over a wide energy range, extending up to energies of the order of hundreds of EeV. Thus, these particles carry energies impossible to reach by human-made accelerators. The processes that particles suffer to achieve those extreme energies are still unknown. The flux of these particles drops rapidly with energy. Cosmic rays of relativity low energies can be directly measured with satellite detectors and they are mainly composed of photons and light nuclei. The highest limit of the energy spectrum is represented by the so called Ultra High Energy Cosmic Rays (UHECRs) which have a flux of about 1 particle per century per square kilometre. The amount of these energetic particles is not enough to be detected directly. Consequently, we know relatively little about them. Very important properties as their origin, chemical composition and acceleration mechanisms to reach that extremely high energies are a mystery even today, 100 years after their discovery. Of course, any increase in the knowledge of cosmic rays translates directly in an increase of knowledge in particle physics, contributing to improve the understanding of their mechanisms of interaction. When cosmic rays reach the Earth, they collide with atomic nuclei of the atmosphere which acts as amplifier of the incoming particle, producing millions of particles falling over the Earth surface. This process is the so called Extensive Air Shower (EAS) [1]. Current studies of UHECRs aim to extract information of the primary particles by means of the properties of the EASs they induce.

Searching for Ultra High Energy Neutrinos (UHEν_s) emitted from astrophysical objects is one of the most challenging fields of astroparticle physics. The motivations for such studies are very strong. UHEν_s play a key role in the understanding of the origin of UHECRs. Their observation would open a new window to the universe since they can give information on regions that are otherwise hidden by large amounts of matter in the field of view of the observatories. Moreover, neutrinos are not deviated by magnetic fields and would point back to their sources. Even though no direct observation of UHEν_s has been occurred yet, their existence is predicted by different astrophysical and cosmological scenarios so the search for neutrinos can confirm or discard production and propagation models of cosmic rays. This Ph.D. thesis is focused on the experimental search for UHE neutrinos using the data collected by the Pierre Auger Observatory [2].

The Pierre Auger Observatory has been conceived to study the properties of cosmic rays from 10^{18} eV to the highest energies. It is currently the largest cosmic ray observatory in the world using a hybrid technique that combines both surface and fluorescence detectors at the same site. Although the primary goal of the surface detector array (SD) is to detect UHECRs, it has been shown that it can also identify very inclined downward-going [3] and Earth-skimming [4] neutrinos. The discrimination of EASs induced by neutrinos takes advantage of the possibility of neutrinos to interact deep in the atmosphere (or in the Earth crust), while cosmic rays of hadronic origin interact soon after entering the upper part of the atmosphere.

The main limitation to the observation of clear signatures of UHE neutrinos comes from the

associated background which is extremely huge compared to the expectation rates for neutrinos. Up to now, the search for neutrinos in Auger has been reduced to the study of nearly horizontal showers ($\theta > 75°$), where the amount of atmosphere is large enough to absorb background of hadronic origin and to increase the interaction probability of neutrinos. Nevertheless, the detection and discrimination of neutrinos using less inclined showers is not discarded and has been studied as part of this Ph.D. thesis. The new analysis presented in this document is focused on the zenith angular region [60° - 75°], extending the exposure of the Pierre Auger Observatory to the detection of UHE neutrinos. Moreover, an update of the analysis searching for Earth-skimming τ neutrinos is also reported.

The sensitivity of the Pierre Auger Observatory to point-like sources of neutrinos with UHE has been also evaluated. As shown in this work, stringent limits to neutrino fluxes as function of the source declination are established in a large fraction of the sky spanning more than 100° in declination. The contribution of the neutrino search analysis at low zenith angles extends the sensitivity of the Observatory to regions of the sky otherwise hidden to the high zenith angle analyses.

The first part of the thesis (chapters 1 to 3) gives an introductory theoretical background on cosmic rays, extensive air showers and the Pierre Auger Observatory. In chapter 1, a short review on the basic features of cosmic rays and multi-messengers is given, including a summary of the most recent discoveries in these fields. Chapter 2 is devoted to the description of EASs induced either by cosmic rays or by neutrinos and the experimental tools used for their detection. The Pierre Auger Observatory is described in chapter 3 with special emphasis on the characteristics of the surface array, necessary to understand the techniques developed to analyse the data. A special section is dedicated to describe the neutrino signatures and the way of detecting them.

The second part of the document (chapters 4 to 7) is focused on the description of the analysis carried out to search for UHE neutrinos in the low zenith angular region. Simulations are needed to define the most suitable observables which allow the ν identification. Chapter 4 is devoted to the simulation and reconstruction of neutrino induced EASs while their identification using the SD is presented in chapter 5. The method follows a *blind search* procedure based on a Fisher discriminant algorithm. The exposure of the Observatory to neutrinos using this new analysis is presented in chapter 6. The search for neutrino candidates in the data collected by Auger, including the obtained limits to the diffuse flux of UHE neutrinos, is described in chapter 7.

The third part of the thesis (chapters 8 and 9) reports on the results for the search of point-like sources of UHE neutrinos. First, in chapter 8 we present an improved limit to the diffuse flux of Earth-skimming τ neutrinos. Then, the sensitivity of the Observatory to point-like sources of neutrinos as function of the source declination is derived in chapter 9. This study includes the search for Earth-skimming neutrinos as well as for downward-going neutrinos at low angle. The document ends with two technical appendices where the results on the Fisher polynomial and the contributions made in the framework of this Ph.D. thesis to the Auger $\overline{\text{Off}}\underline{\text{line}}$ package are reported.

Part I

Theoretical background

1 Ultra High Energy Cosmic Rays

After the discovery of radioactivity by Henry Becquerel in 1896 it was generally believed that atmospheric ionization was caused only by Earth radioactivity. It implied that air ionization should decrease with height. Different studies were made to confirm this assumption with controversial results. Finally in 1914 Victor Hess, helped with electrometers and free balloons flights, proved that the ionization rates increase when increasing height. These results were better explained assuming incoming radiation to the Earth. He also ruled out the Sun as the unique origin of this ionization source making measurements during a near total eclipse. His results were awarded with the Novel Prize in Physics in the year 1936. The term Cosmic Rays (CRs) was coined by Robert Millikan in 1925 and in those days the cosmic rays were supposed to be gamma rays. However, during the 1930's it was found that cosmic rays must be electrically charged particles because of the East-West asymmetry observed in their arrival directions. Nowadays, the term "Cosmic Rays" is used to design exclusively *charged particles or nuclei* incoming to Earth. Almost 30 years after their discovery it was realized that particles reaching ground are correlated in time [5] which lead to the detection of Extensive Air Showers (EASs). Since then, their properties have been deeply analysed. Now we know that cosmic particles are continuously bombarding the Earth. They arrive at our atmosphere and collide with one of its atoms generating millions of secondary particles that reach ground (figure 1.1). The composition of the cosmic rays is dominated by nuclei of atoms, from hydrogen to iron and even beyond [6], accelerated in places not yet identified. Protons represent approximately 90% of the primaries at the lower energies (10^{11} eV) but as we go to energies above $\sim 10^{18}$ eV and study Ultra High Energy Cosmic Rays (UHECRs), heavier nuclei become more abundant. On the other hand, the experimental determination of their properties becomes more difficult since the flux drops below one particle per km^2 and year. Suitable detectors need huge apertures which is achieved by exploiting EASs induced by the cosmic rays in Earth's atmosphere, which effectively acts as a calorimeter.

1.1 Origin and propagation of Cosmic Rays

It is known that most of the low energy cosmic rays, up to some GeV, come from the Sun. However, CRs of higher energies must have another origin. There are two main scenarios trying

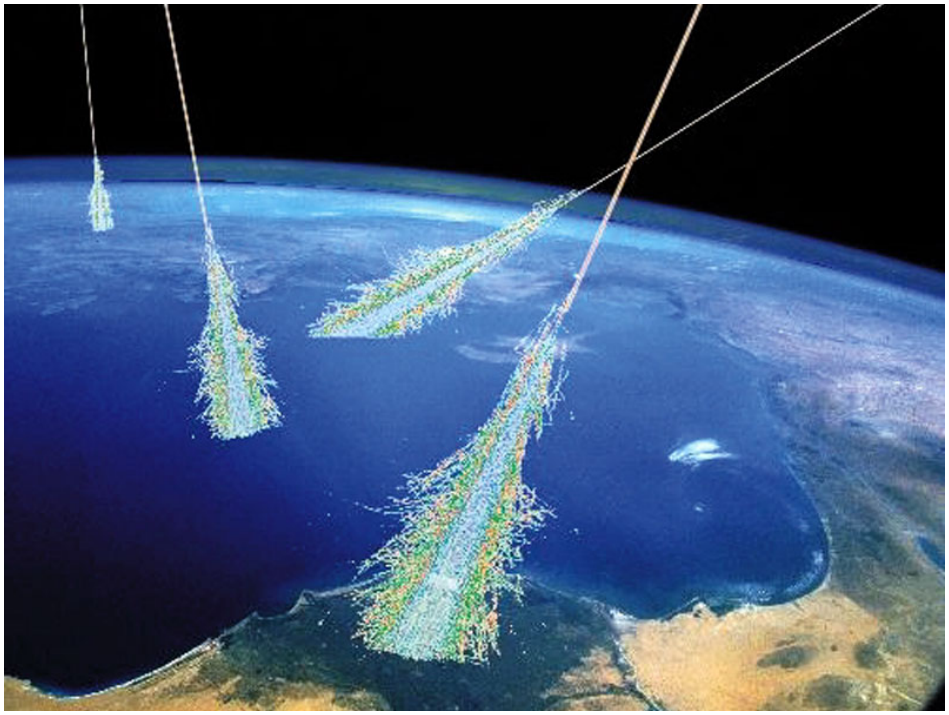

Figure 1.1: An illustration of cosmic rays inducing extensive air showers in Earth's atmosphere.

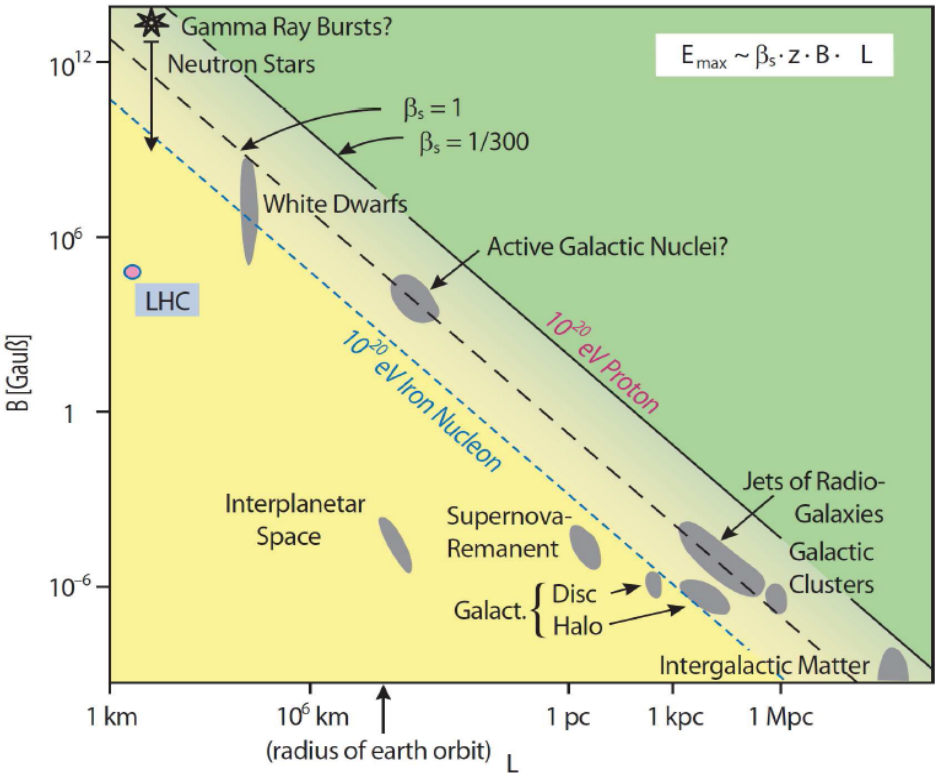

Figure 1.2: The Hillas plot: magnetic field strength and size of possible astrophysical objects that are candidate sites of UHE particle acceleration. Objects below the diagonal line can not be sources of ultra high energy cosmic rays.

to find a solution to the basic problem of how to transfer efficiently a macroscopic amount of energy, of the order of 20 Jules, to a microscopic particle. The first scenario, so-called *bottom-up*, supports accelerating mechanisms at the sources or in their vicinity. In the second, so-called *top-down* scenario, the accelerator itself is suppressed and particles are produced directly at such energies via the decay of super-massive relics of the Big Bang or via the decay of topological defects.

With the observational facts collected in the last decade by experiments like HiRes [7] and the Pierre Auger Observatory [2], the situation has been greatly clarified. A cut-off at the end of the energy spectrum is clearly visible at about 10^{20} eV [8] and the limits to the fraction of ultra high energy photons and Ultra High Energy Neutrinos (UHEν_s) [9, 4, 3] have disfavoured the top-down models. On the other hand the possibility of a dominant iron component of cosmic rays at the highest energies decreases in a factor $\sim$30 the hard conditions placed by bottom-up accelerators to reach the 100 EeV barrier. Nevertheless, after many decades of investigation, the nature of the highest cosmic rays has not been still solved.

1.1.1 Bottom-up scenarios

There are two main and distinctive mechanisms capable to accelerate particles at astrophysical site: diffusive shock acceleration, based on the Fermi mechanism [10], and one shot acceleration in very high electric field generated by rapidly rotation of compact magnetized objects [11, 12] such us young neutron stars.

Diffusive acceleration takes place near shock waves and rely on the repeated scattering of charged particles on magnetic irregularities back an forth across the shock. This mechanism naturally provides a power low spectrum whose predicted spectral index is within the range of the experimental measurements. Figure 1.2 shows the Hillas plot, summarizing the conditions on potential acceleration sites using a relation between the maximum energy ($E_{\max}$) of a particle of charge Z_e and the size (R) and strength of the magnetic field (B) of the site in the region of the shock:

$$E_{\max} = k\beta Z_e \left(\frac{B}{\mu\mathrm{G}}\right)\left(\frac{R}{\mathrm{kpc}}\right) \ \mathrm{EeV} \tag{1.1}$$

where β represents the velocity of accelerating shock wave (in units of c) and $k < 1$.

Looking at the Hillas diagram one sees that only a few astrophysical sources satisfy this necessary but not sufficient condition. Among the possible candidates we can find neutron stars, Active Galactic Nuclei (AGNs), radio galaxies and Gamma Ray Bursts (GRBs). All the objects above the iron line are capable to accelerate cosmic rays up to the required energies. However, these scenarios present some difficulties. The first one is related with the probability of losing energy in the surrounding of the sources, where the energy density is not negligible, via synchrotron radiation, Compton processes or photo-disintegration in the case of nuclei. An additional difficulty is the probability of losing energy by interactions with the Cosmic Microwave Background (CMB) [13] during their propagation from the source to the Earth as explained in section 1.1.2.

1.1.2 Propagation of Cosmic Rays

One fundamental problem which must be examined concerns the cosmic ray propagation from their sources to the vicinity of the Earth where they are observed [14] in the case of bottom-up scenarios. It is believed that when cosmic rays leave their sources, they are diffused through the interstellar space by the magnetic fields which control and randomize their motion. Along this propagation through the interstellar space, cosmic ray composition and spectra are affected by at

least two mechanisms. One is fragmentation produced in nuclear reactions with the interstellar material, and the other is Coulomb interactions including ionization energy loss. Galactic and extra-galactic magnetic fields affect cosmic ray trajectories. As we have an enormous ignorance about the strength of magnetic fields as well as about the charge and the sources of cosmic rays, it is not possible to correct the deflections they suffer during propagation [15].

The GZK mechanism

In the highest-energy region, not only deflection by the intergalactic field, but also the energy losses of cosmic rays in the intergalactic radiations fields, such as microwave, infra-red (IR), and radio backgrounds, become important. Soon after the discovery of cosmic background radiation by Pencias and Wilson [13], the three physicists Greisen [16], Zatsepin and Kuzmin [17] predicted that there would be a cut-off in the spectrum of protons around 6×10^{19} eV due to photo-production on the microwave background. This has become know as the Greisen-Zatsepin-Kuzmin (GZK) cut-off.

The dominant reactions of **protons** p with background photons ($\gamma_{2.7K}$) are the following:

$$\begin{aligned} p + \gamma_{2.7K} \quad & \rightarrow \Delta^+(1232) \quad \rightarrow n + \pi^+ \\ & \rightarrow \Delta^+(1232) \quad \rightarrow p + \pi^0 \\ & \rightarrow p + e^+ + e^- \end{aligned} \tag{1.2}$$

The two first processes ("photo-pion production") are the dominant ones, with a threshold energy and mean free path of about $10^{19.6}$eV and ∼6 Mpc, respectively. In the case of the third process ("pair production") the corresponding thresholds are about 10^{18} eV and ∼1 Mpc. If the sources are sufficiently distant, photo-pion production processes should lead to a cut-off in the energy spectrum of protons around 4×10^{19} eV (the GZK cut-off). As a consequence, the universe becomes opaque to protons with energies above 10^{20} eV on distance scales above ∼100 Mpc, and ultra high energy cosmic ray sources must be relatively close to Earth to be detected. The attenuation lengths of protons in the microwave background is show in figure 1.3 for two different models. Both are in reasonably agreement.

In the case of **heavy nuclei** of mass A, the situation slightly changes since the dominant loss processes are photo-disintegration [18] and pair production [19]:

$$\begin{aligned} A + \gamma_{2.7K} \quad & \rightarrow (A-1) + N \\ & \rightarrow (A-2) + 2N \\ & \rightarrow A + e^+ + e^- \end{aligned} \tag{1.3}$$

where N is a nucleon (proton or neutron). The energy loss due to IR photons is only effective below 5×10^{19}eV, while energy loss in interactions with microwave background photons is most significant for energies above 2×10^{20}eV [20, 21].

In the case of **gamma rays**, pair creation through interaction with the cosmic background radiation is most important [22] in a wide energy range above the threshold of 4×10^{14},

$$\gamma + \gamma_{2.7K} \rightarrow e^+ + e^- \tag{1.4}$$

It should be noted that attenuation due to pair creation on diffuse background of radio photons becomes dominant over microwave effects above 2×10^{19}eV. Taking into account the contributions

of normal galaxies, radio galaxies, and the microwave background to the extragalactic radio background intensity [23], the attenuation length of gamma rays in the total photon background spectrum [24] is shown by a dot-dashed line in figure 1.3 [25].

Finally, UHEν_s interact manly with the theoretically expected relic neutrino background (RNB), the dominant interaction modes being the exchange of a W or a Z boson. RNB interactions dominate over neutrino-nucleon interactions because the RNB particle density is about 10 orders of magnitude larger than the baryon density. An extensive description on the origin and expected fluxes of UHEν_s is given in chapter 1.3.

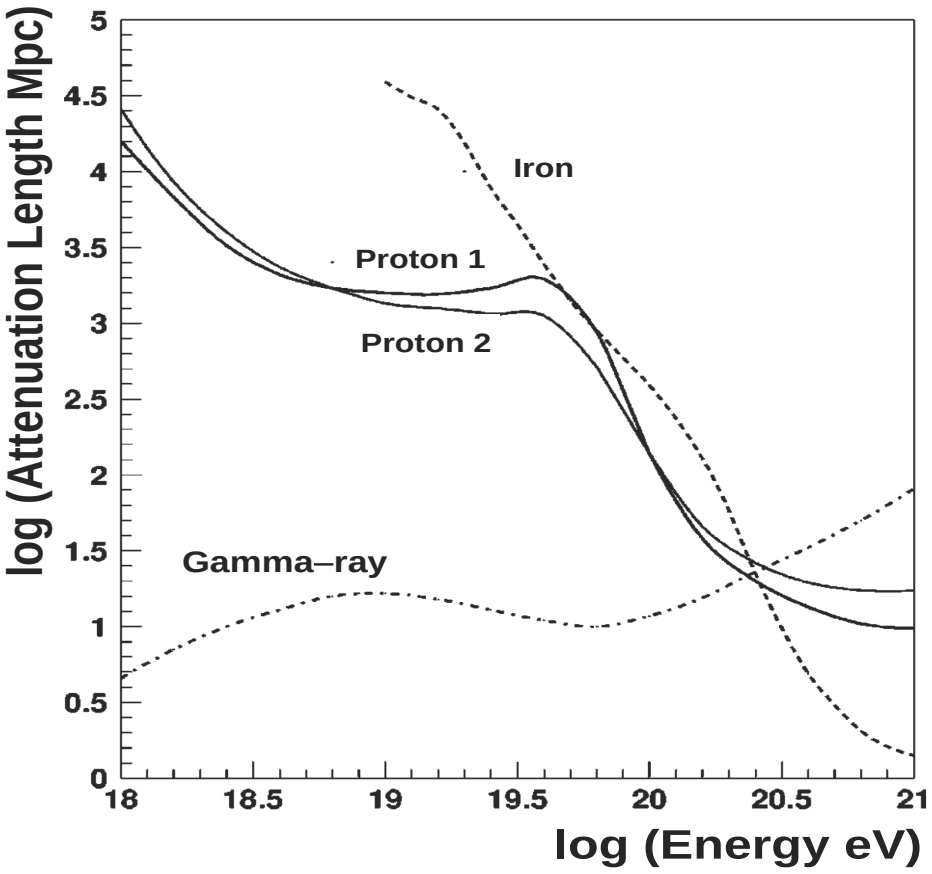

Figure 1.3: Attenuation length of proton (Proton 1 from [26] and Proton 2 from [27]), iron [20] and gamma-ray [25] in the microwave, infra-red, and radio background radiations as a function of energy.

1.1.3 Top-down scenarios

The belief that the highest-energy cosmic rays cannot be explained within the current canon of knowledge has led to a plethora of alternative exotic suggestions. One approach has been to invent mechanisms to avoid energy losses in the 2.7 K radiation field. For example, the suggestion

that a stable supersymmetric hadron may be responsible for creating the largest showers [28] and the speculation that Lorentz invariance might break down at the Lorentz factors of interest so that the GZK effect is heavily suppressed [29, 30, 31, 32]. Exotic entities from the early universe have been invoked with the decay of topological defects, such as monopoles or strings, or the possibility of superheavy relic particles from the post-inflation era, all having their advocates. Some of these processes predict distinctive signatures in the form of copious fluxes of neutrinos and gamma rays, in addiction to a hadronic channel.

1.2 UHCRs: recent results

The resolution of the long standing mystery of UHECRs requires a coordinate approach on different complementary fronts: the energy spectrum, the studies on their apparent arrival directions, their chemical composition and the so-called multi-messenger interface with high energy photons, neutrinos and neutrons. In the following sections we briefly describe the most recent results on these fields except for neutrinos that will be discussed in section 1.3.

1.2.1 Energy spectrum

The energy spectrum of cosmic rays (primary particle flux as a function of energy, $J(E)$) is almost featureless. Extending from 10^9 eV (solar cosmic rays) up to 10^{20} eV, it follows a power law with an exponent (*spectral index*) almost constant and close to 3 ($\mathrm{J} = \mathrm{dN/dE} \propto \mathrm{E}^{-3}$). The flux decreases more than 20 orders of magnitude along this energy range as expected in the case of stochastic acceleration of charged particles at astrophysical shocks [10]. Figure 1.4 shows the highest part of the spectrum as measured by several experiments (multiplied by $\mathrm{E}^{2.7}$). At lower energies the flux is proportional to $\mathrm{E}^{-2.7}$ (appearing flat), whereas at higher energies, two changes in the spectral index are evident, one at $\sim 10^{15}$ eV [33, 34] and other at 10^{18} eV [35] referred to as the *knee* and the *ankle*, respectively. All the spectral features might be interpreted either as a change of the acceleration mechanism at sources, either as a propagation effect or as a change of the hadronic interaction cross section with increasing energy.

Recent observations of UHECRs reveal a spectrum whose shape supports the long-held notion that sources of UHECRs are extragalactic. As show in figure 1.4, the crucial spectral feature recently established at the highest energies is a steeper decline in flux above about 30 EeV [36]. This feature was first established by the HiRes Observatory [7, 37] (but not by AGASA [38]), and confirmed with higher statistics by the Pierre Auger Observatory [8, 36]. The preliminary data from Telescope Array [39, 40] is in good agreement given an overall energy re-scaling of 0.8 which is within the systematic errors in the absolute energy scale of 22%.

The confirmed presence of a spectral feature similar to the predicted GZK cut-off, settles the question of whether acceleration in extragalactic sources can explain the high-energy spectrum, ending the need for exotic alternatives designed to avoid the GZK feature. However, the possibility that the observed softening of the spectrum is mainly due to the maximum energy of acceleration at the source, E_{max}, is not easily dismissed. A confirmation that the observed softening is the GZK feature, awaits supporting evidence from spectral shape (at energies above 100 EeV), anisotropies (which are expected above GZK energies), composition, and the observation of produced secondaries such as neutrinos and photons.

1.2.2 Anisotropies

One of the keys to understand the nature of UHECRs is their distribution over the sky, which depends on the location of the UHECR sources, as well as on the UHECR mass composition

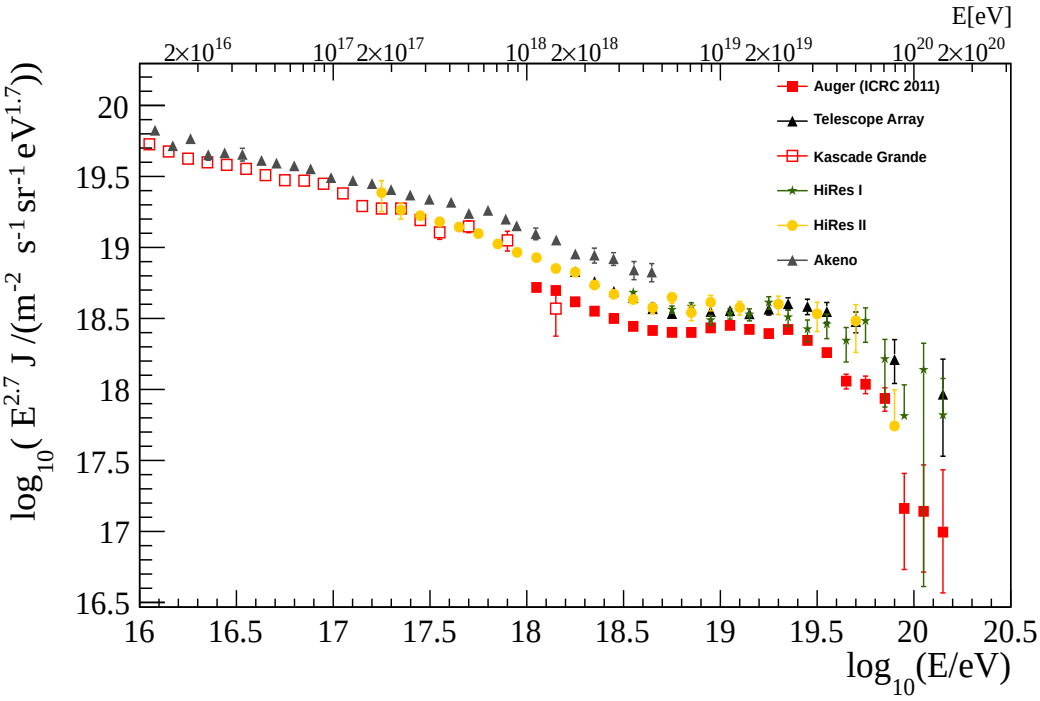

Figure 1.4: Upper end of the cosmic ray spectrum (multiplied by $E^{2.7}$) as measured by several experiments.

and large-scale magnetic fields. The GZK effect limits the horizon from which UHECRs can be observed below 100 Mpc. At these scales the matter is distributed very anisotropically, dominated by the Centaurus-Hydra-Virgo-Pavo supercluster, and so must be the distribution of UHECR sources.

Thanks to its excellent pointing accuracy ($\sim 1°$), the Pierre Auger Observatory can search for point-like sources of UHECRs, the main obstacle being the presence of magnetic fields on the way from extragalactic sources to the Earth. Such searches have given evidence for a positive correlation [41, 42, 43] within an angle of 3.1° between the arrival directions of showers having energies in excess of 55 EeV and the positions of nearby (<75 Mpc) AGNs from the VCV catalogue [44]. The most recent update of the results (figure 1.5, data up to June 2011) yields a total of 28 of 84 events showing a correlation with a nearby AGN, which amounts to a (33±5)% correlation –much smaller than the (62±10)% measured with the first period of data– versus 21% expected from isotropy. The chance probability of observing such a correlation from a random distribution remains below 1%. The Telescope Array has recently showed that 11 out of 25 events correlate [45], finding a signal strength of 44% while 24% is expected from isotropy. The two observations are consistent and show that an anisotropy signal is weak at these energies probably due to a large isotropic background.

Finally, searches for directionally-aligned events have been also performed showing no significant evidence for the existence of correlated multiplets in the present data set [46].

1.2.3 Mass Composition

The third key that can help to resolve the mystery behind the origin of UHECRs is their composition as a function of energy observed on Earth. Direct composition measurement of the

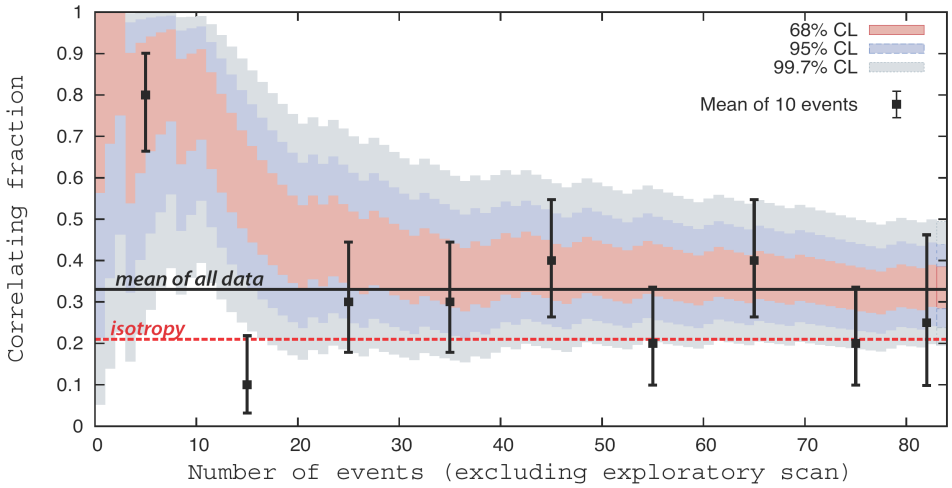

Figure 1.5: Pierre Auger correlation studies: the most likely value of the degree of correlation p_{data} is plotted as function of the total number of time-ordered events (see [41, 42, 43] for details). The 68%, 95% and 99.7% confidence level intervals around the most likely value are shaded. The horizontal dashed line shows the isotropic value $p_{\text{iso}} = 0.21$ and the full line the current estimate of the signal $p_{\text{iso}} = 0.33 \pm 0.05$. The black symbols show the correlation fractions bins of independent 10 consecutive events.

primaries can not be achieved for energies above ≈ 100 TeV with space-based experiments. For higher energies, composition is derived from the extracted information of the EAS created by the primary cosmic ray when it interacts with the atmosphere (see chapter 2).

The main difference between showers induced by a proton and an iron nucleus of the same energy is that the latter interact higher in the upper atmosphere than the former do. In the UHECR region the average depth $< X_{\text{max}} >$ at which shower development reaches maximum is smaller by about 100 g cm^{-2} for iron than for proton, and the fluctuation of X_{max} around the mean, RMS(X_{max}), is lower by about 40 g cm^{-2}. These estimates, obtained from models of the shower development, are quite robust. The dependence on energy of these quantities is predicted to be linear in the logarithm of the energy.

The Auger measurements of these quantities obtained with the Fluorescence Detector data [47, 48] are presented in figures 1.6a and 1.6b. Both quantities show a characteristic change at $E \simeq 5 \cdot 10^{18}$ eV suggesting an evolution from lighter to more massive nuclei when compared to EAS simulations. However, the issue is not yet settled. Data from other observatories [49, 50, 51] do not show such a trend as clearly as the Auger data do.

Since the Fluorescence Detector has a limited duty cycle of about 10%, Surface Detector array observables sensitive to the longitudinal shower development are also being investigated. The Pierre Auger Collaboration has presented measurements of the mean depth $< X^{\mu}_{\text{max}} >$ of muon production [52, 53], determined by tracking the space-time coordinates of muon signals back from the ground along their light-like paths to their production point on the shower axis (see figure 1.6c). Additionally, the asymmetry Θ_{max} in the rise time of signals [48] between the earliest and the latest triggered tanks for non vertical events is sensitive to mass composition (see figure 1.6d). These analyses also indicate an increasing faster shower development as the energy rises, compatible with Fluorescence measurements. The challenge for hadronic interaction models is to describe all these observations consistently for a given mass composition assumption.

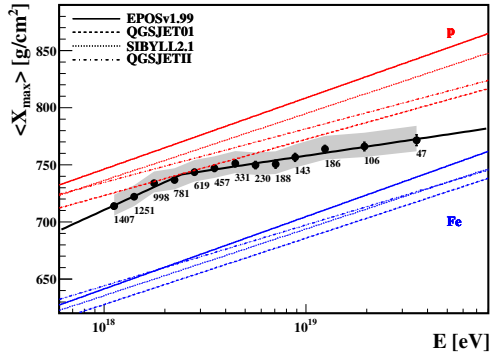

(a) $< X_{\max} >$ vs Energy

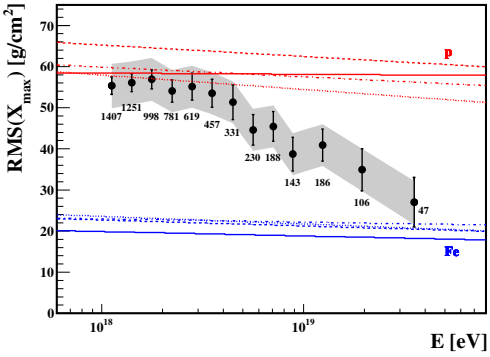

(b) $RMS(X_{\max})$ vs Energy

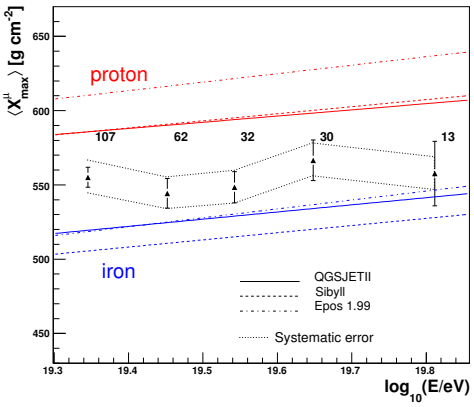

(c) $< X^{\mu}_{\max} >$ vs Energy

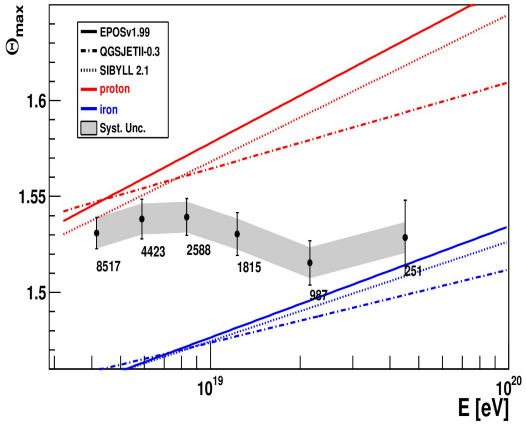

(d) $\Theta_{\max}$ vs Energy

Figure 1.6: Pierre Auger Mass composition sensitive variables as function of energy [47, 48]. Data (points) are shown with the predictions for proton and iron for several hadronic interaction models. The error bars correspond to the statistical uncertainty. The number of events in each bin is indicated. Systematic uncertainties are indicated as a band. 1.6a $< X_{\max} >$ as a function of the energy. 1.6b $RMS(X_{\max})$ as a function of the energy. 1.6c Average $< X^{\mu}_{\max} >$ as a function of the energy. 1.6d $\Theta_{\max}$ as a function of the energy.

1.2.4 The Multi-messenger information

The detailed composition of UHECRs is still to be understood, but it is clear that primaries are not dominated by photons or neutrinos [54]. The search for Ultra High Energy (UHE) photons and neutrinos is part of the research program of CR Observatories for several reasons. All the scenarios invoked to explain the origin of UHECRs predict fractions of primary photons and neutrinos, along with a nuclear component. They are produced as a result of the decay of charged pions generated in interactions of cosmic rays within the sources themselves ("astrophysical" origin), and/or in their propagation through background radiation fields ("cosmogenic" origin) [55]. In fact, charged pions, which are photo-produced by UHECR protons interacting with the CMB radiation, decay into UHEν_s. However, the predicted flux has large uncertainties, since it depends on the chemical composition of primaries and on the nature, cosmological evolution and spatial distribution of astrophysical sources [56, 57]. If UHECRs are heavy nuclei, the UHEν yield is strongly suppressed [58]. Top-down models of UHECR origin [24] including topological defects

of super-heavy dark matter models predict a significant fraction of photons and neutrinos at the highest energies. Whatever the production, their detection or their absence can throw valuable information about the origin of cosmic rays. Finally, both photons and neutrinos point back to the sites of production, revealing details of sources and of their acceleration mechanisms and opening a new window to the most extreme universe.

UHEν_s are very useful because they are not absorbed by the cosmic backgrounds while propagating through the universe. However, their small interaction cross-section makes it difficult to detect them on the Earth. They will be discussed in detail in section 1.3.

Current upper limits on the photon flux from Auger, AGASA and Yakutsk experiments [54] are shown in figure 1.7 together with predictions for the GZK photon flux and for top-down models [59]. The derived limits by the Auger Collaboration on the photon fraction of 0.4%, 0.5%, 1.0%, 2.6% and 8.9% above 1, 2, 3, 5 and 10 EeV demonstrate that particle physics motivated top-down models are strongly disfavoured giving support to an astrophysical origin of UHECRs. The bounds also help to reduce the systematic uncertainties on primary mass composition, energy spectrum and proton-air cross section measurements in the EeV range.

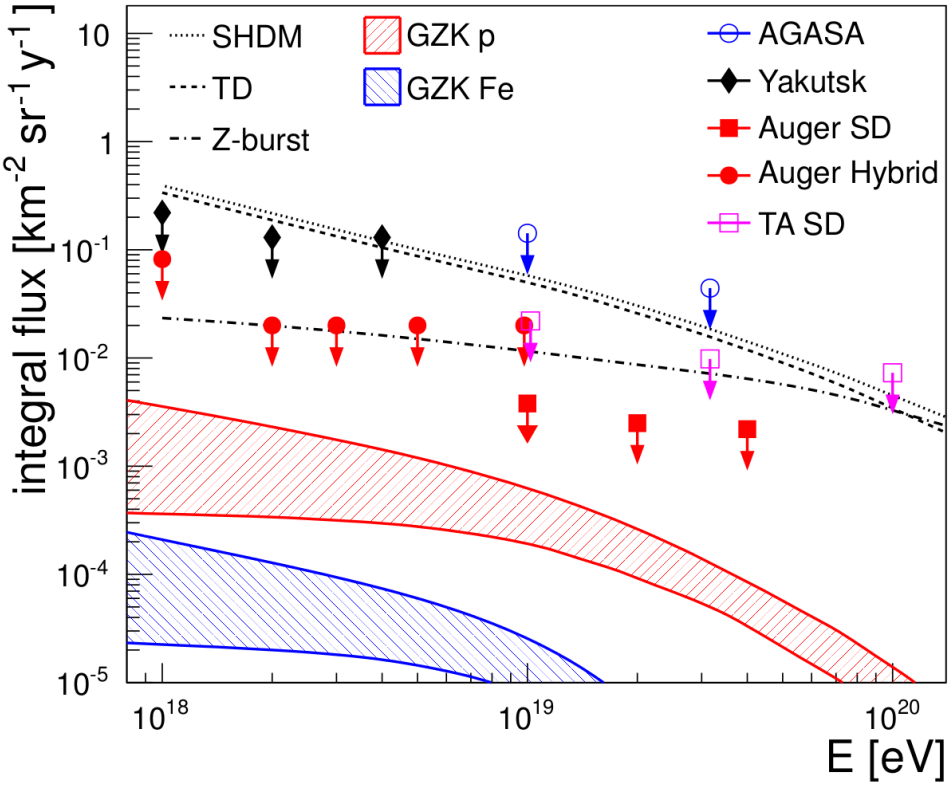

Figure 1.7: Integral photon flux limits at 95% C.L. from Auger, AGASA and Yakutsk [54]. The shaded region and the lines give the predictions for the GZK photon flux [59] and for top-down scenarios (SHDM, TD and Z-burst) [59].

1.3 Ultra High Energy Neutrinos

The neutrino [60, 61] is a neutral elementary particle, carrying spin 1/2, that scatters only through the weak interaction, and consequently rarely interacts in matter. Neutrinos come in three flavours labelled according to the charged lepton that accompany neutrino production

in charge-changing weak interactions, namely, electron, muon or tau. Neutrinos play a very special role in astrophysics [62, 63]. They are predicted in a large kind of astrophysical processes such us the Big Bang, supernovae core-collapse, cooling of neutron starts or nuclear reactions inside the stars. Each one of this processes generate a different and characteristic neutrino spectrum. Figure 1.8 shows the diffuse "grand unified" neutrino spectrum from the lowest energies corresponding to the cosmological relic blackbody spectrum of temperature $\simeq 1.9$ K to the highest energy neutrinos. This section is focused on the study of the so-called UHEν, with energies above 10^{17} eV. As explained in section 1.1, the puzzle of cosmic rays above this energy is still not solved. The detection (or the absence) of UHEν can shed some light to the question about the origin and propagation of UHECR.

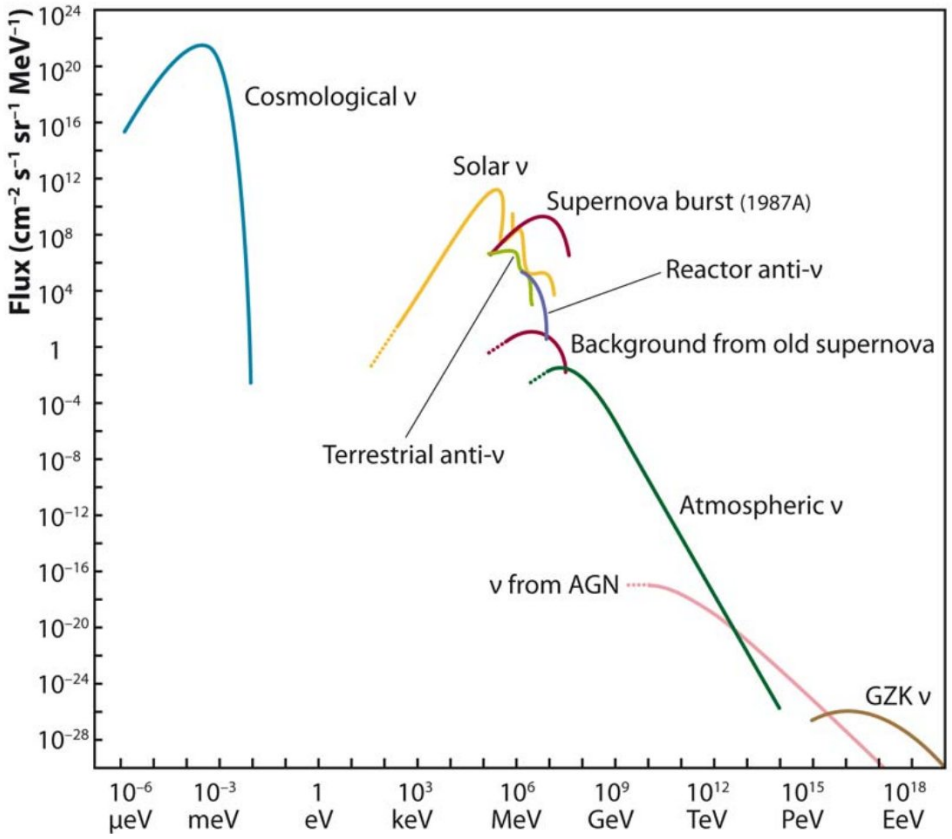

Figure 1.8: The "grand unified" neutrino spectrum (taken from http://www.aspera-eu.org/images/stories/files/Roadmap.pdf). Solar neutrinos, burst neutrinos from SN1987A, reactor neutrinos, terrestrial neutrinos and atmospheric neutrinos have been already detected. Another guaranteed although not yet detected flux is that of neutrinos generated in collisions of ultra-energetic protons with the 3 K CMB, the so-called GZK neutrinos.

1.3.1 Origin of Ultra High Energy Neutrinos

UHEν_s are predicted by different models. Depending on the production mechanism they can be classified in three categories: astrophysical, cosmological and exotic neutrinos. The later are produced in top-down models of cosmic ray generators as discussed in section 1.1.3. This models predict large fluxes of neutrinos and photons and, as explained in section 1.2.4, are seriously disfavoured by the current limits to photon and neutrino fluxes. Consequently, only astrophysical

and cosmological neutrinos will be discussed in the following sections. Neutrinos from bottom-up scenarios can be produced by the interaction of primaries in their sources or in their vicinity as well as during their propagation to the Earth. Depending on the interaction point, they can be classified as astrophysical or as cosmological neutrinos.

Astrophysical Neutrinos

Neutrinos produced inside an astrophysical source of cosmic rays or in its vicinity are embraced together as astrophysical neutrinos. Their main importance is that due to their low interaction cross-section, they carry almost unaltered information from the source. Astrophysical neutrinos are generated when accelerated protons interact with matter ($p+\bar{p} \rightarrow \pi^+ + \pi^- + \pi^0$) or radiation fields ($p + \gamma \rightarrow \Delta^+(1232) \rightarrow p + \pi^0$ or $n + \pi^+$) of the source or in his surroundings.

While the resulting neutrons are likely to interact before decaying, charged pions decay and produce neutrinos:

$$\pi^+ \rightarrow \mu^+ + \nu_\mu \rightarrow e^+ + \nu_e + \bar{\nu_\mu} + \nu_\mu \tag{1.5a}$$

$$\pi^- \rightarrow \mu^- + \bar{\nu_\mu} \rightarrow e^- + \bar{\nu_e} + \nu_\mu + \bar{\nu_\mu} \tag{1.5b}$$

Assuming that pions of negative and positive charge occur equally, the production flavour ratio of neutrinos at the source is

$$(\nu_e : \nu_\mu : \nu_\tau) = (\bar{\nu}_e : \bar{\nu}_\mu : \bar{\nu}_\tau) = (1 : 2 : 0) \tag{1.6}$$

This implies that tau neutrinos are not produced in astrophysical sources. However, since neutrinos have non-vanishing mass eigenvalues, they oscillate [64] on their way to Earth. Neutrino flavors-eigenstates $\mid \nu_\alpha \rangle$ and mass-eigenstates $\mid \nu_j \rangle$ are connected via

$$\mid \nu_\alpha(t) \rangle = \sum_{j=1}^{3} U_{\alpha j} e^{-iE_j t} \mid \nu_j \rangle \tag{1.7}$$

where the mixing matrix ($U_{\alpha j}$) depends on three angles (θ_{12}, θ_{13}, θ_{23}) and a phase δ. Assuming values for the mixing angles ($\frac{\pi}{6}$,$\frac{\pi}{4}$,0) as described in [65, 66], and applying the equation for a neutrino flavour changing from the source to the Earth, the ratio would be [67]:

$$(\nu_e : \nu_\mu : \nu_\tau) = (\bar{\nu}_e : \bar{\nu}_\mu : \bar{\nu}_\tau) = (1 : 1 : 1) \tag{1.8}$$

for path lengths exceeding the size of solar system. Since tau neutrinos are essentially absent above 100 GeV in the atmospheric neutrino background, identification of a ν_τ would be a strong evidence for astrophysical origin.

Depending on the source, astrophysical neutrinos can be classified as galactic and extragalactic neutrinos. The striking difference is their maximum energy. Since galactic sources can not accelerate protons above 3×10^{18} eV, and the neutrino carries only a fraction of the proton energy, galactic neutrinos are out of be classified as UHEν_s.

Potential UHEν sources are almost the same types of objects that may accelerate extragalactic cosmic rays, an upper limit to the flux can be extracted from the measured spectra of cosmic rays. Waxman & Bahcall [68] compute an upper limit for neutrinos produced in GRBs assuming a cosmic ray injection flux of E^{-2} power law spectrum in the range from 10^{19} to 10^{21} eV. Accounting for a proper normalization of luminosity, the maximum diffuse neutrino flux is:

$$E_\nu^2 \ \Phi_{\nu_\mu + \bar{\nu}_\mu} = 1.5 \times 10^{-8} \, \xi_z \qquad \text{GeV cm}^{-2} \text{ s}^{-1} \text{ sr}^{-1} \tag{1.9}$$

which only depends on ξ_z, a constant summarizing the product of the cosmological evolution of the UHECR sources. For an evolution proportional to $(1-z)^3$, ξ_z has a value of about 3. The upper limit of Waxman & Bahcall is not universally accepted. Another, more detailed, model for the upper limit of the neutrino flux was derived by Mannheim, Protheroe & Rachen [69].

Cosmological Neutrinos

They were suggest by Berensinsky and Zatsepin in 1969 [55]. Cosmological neutrinos are the by-product of the GZK mechanism as discussed in 1.1.2. They are the result of the decay of pions and neutrons produced in the GZK interaction. The production chain is similar to the astrophysical neutrinos, but the interaction of the primary particle (proton, neutron or nuclei) occurs with thermal photons of the CMB instead of photons from the radiation field of the astrophysical source. This source of neutrinos is independent of whether the UHECRs are produced inside jets or at the termination shocks of AGNs or GRBs, or indeed from some other source altogether. The exact flux of these cosmogenic neutrinos depends on many factors of UHECRs, such as the total emissivity of the universe, the acceleration spectrum, the maximum acceleration energy in the sources, the cosmological evolution or the chemical composition. Multiple calculations on the flux of cosmogenic neutrinos combining different production models and composition [57, 56, 58] can be found in the literature. As an example, the neutrino flux at production from model [58] is shown in figure 1.9. The peak around 10^{15}eV is due to the $\bar{\nu}_e$ from neutron decay whereas one at 10^{18}eV corresponds to the ν_μ and $\bar{\nu}_\mu$ from pion and muon decays.

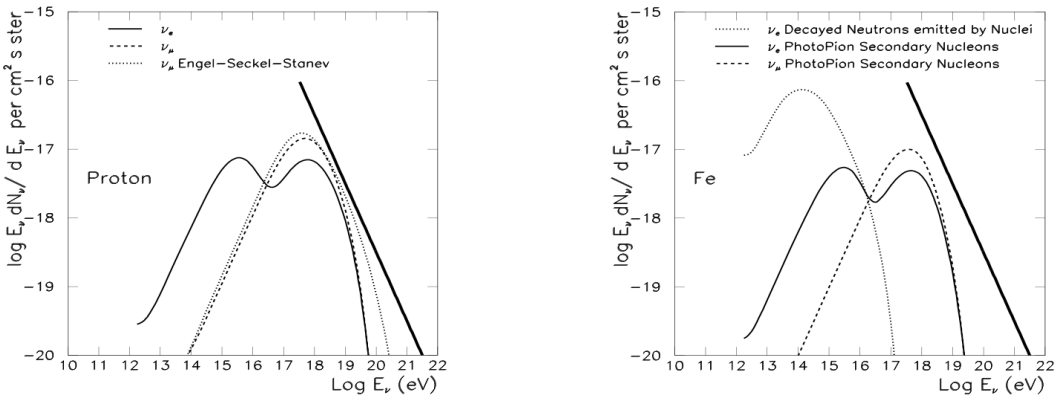

Figure 1.9: Electron and muon neutrino fluxes for primaries with a maximum energy at acceleration of $4Z \times 10^{20}$ [58]. Left: results for proton primaries including the results from [70]. Right: result for iron primaries. The thick solid line in both plots shows the Waxman-Bahcall limit [68, 71].

A measurement of neutrino fluxes would be of great help in addressing the question of the origin of the UHECRs. For example, if the composition is dominated by heavy nuclei, the individual nucleons will cut off at a relatively low energy which will decrease the fluxes of the $\geq 10^{18}$ eV neutrinos. The flux of neutrinos corresponding to the decay of neutrons will increase, as show in figure 1.9. A question that remains open is whether the observed steepening at the highest energies corresponds to the GZK effect or whether it is simply the source reaching his maximum energy as shown by the Hillas diagram (Fig. 1.2). As an illustration of the relevance of this point for neutrino astronomy, figure 1.10 shows the dependence of the predicted flux of cosmogenic $\nu_\mu + \bar{\nu}_\mu$ on the maximum energy assumed at the sources. The peak and the maximum flux are energy dependent, consequently a measurement (or an upper bound) of the flux at these energies could help on the understanding of the question about the GZK cut-off.

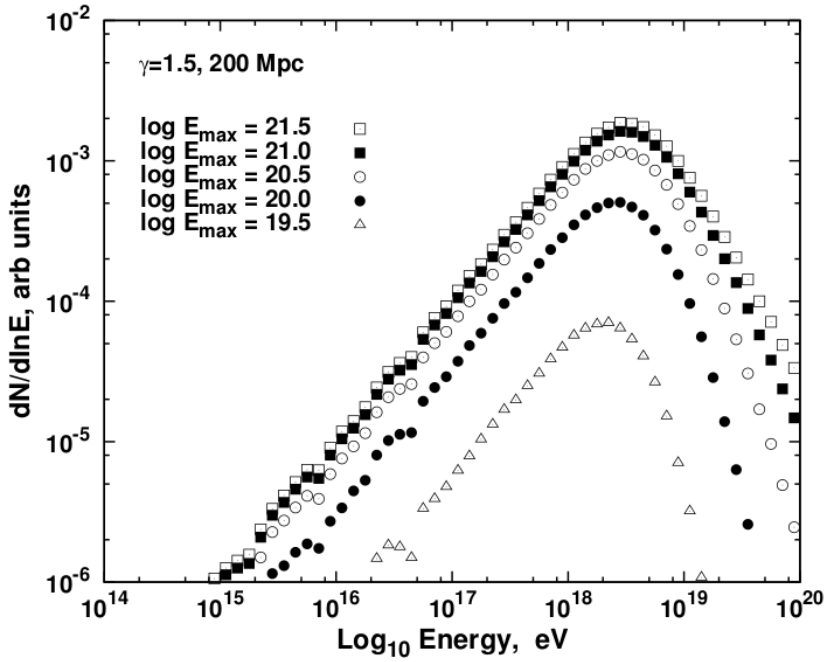

Figure 1.10: Muon neutrinos and antineutrinos generated in the propagation of protons on 200 Mpc for different values of the maximum proton energy at acceleration [72].

1.3.2 Neutrino detection techniques and recent results

As mentioned before, the only extraterrestrial neutrinos observed up to now are low energy neutrinos (in the MeV range) from the Sun [73] and Supernova SN1987A [74]. The challenge for current neutrino telescopes is the detection of higher energy neutrinos.

Neutrinos can interact with nucleons of matter via charged current (CC) or neutral current (NC) interactions:

$$\nu_l\,(\bar{\nu}_l) + N \xrightarrow{\text{CC}} l^-\,(l^+) + X \tag{1.10a}$$

$$\nu_l\,(\bar{\nu}_l) + N \xrightarrow{\text{NC}} \nu_l\,(\bar{\nu}_l) + X \tag{1.10b}$$

Here, X denotes the hadronic product of the interaction, leading to a hadronic cascade, and l is a charged lepton. The NC interaction of the three flavours results in purely hadronic showers which arise from nuclear recoil. In CC interactions, around 20% of the total energy goes into the hadronic cascade and the remaining 80% is carried by the lepton. Electrons produce electromagnetic cascades in the propagation medium. Taus have very distinct signatures. In the first $\nu_\tau N$ interaction an hadronic cascade is produced, the resulting τ propagates and eventually decays producing a second cascade in which a further ν_τ is generated. In contrast, muons only undergo radiation losses and leave track-like signatures. The track and the energy of the muon can be reconstructed if the lepton leaves Cherenkov radiation [75]. Underwater and ice telescopes are able to detect such neutrinos and, at the same time, are able to keep the background from atmospheric muons negligible, since they are placed several kilometers below the Earth's surface and detect up-going neutrinos. This has, nevertheless, a limitation. Above 10^{15} eV, the Earth starts becoming opaque to neutrinos and only downward-going or Earth-skimming neutrinos can be observed. The background is due to a plethora of downward-going cosmic rays and high-energy atmospheric muons.

The interaction of neutrinos with atomic electrons is also possible, although suppressed except for the resonance $\bar{\nu_e} + e^- \rightarrow W^-$, which dominates over all processes but in a very narrow energy range around $E_{\bar{\nu_e}} = 6.4 \times 10^{15}$ eV [76].

A crucial ingredient in the study of UHEν is the high energy neutrino-nucleon cross section, which provides a probe of quantum chromodynamics (QCD) in the kinematic region of very small values of Bjorken x –fraction of the momentum of the incoming nucleon taken by the struck quark– and large values of Q^2 –invariant mass of the exchanged vector boson–. Through their interactions in the Earth or the atmosphere, neutrinos above 10^{17} eV probe higher center-of-mass energies than those accessible by human-made accelerators. According to the equation:

$$\sqrt{S_{\nu N}} \equiv \sqrt{2ME_\nu} \simeq 14 \left(\frac{E_\nu}{10^8 \text{ GeV}} \right)^{\frac{1}{2}} \text{TeV} \tag{1.11}$$

for neutrino incoming energies bigger than 10^{17} eV, the energy at center-of-mass is above 14 TeV, a factor two bigger than the 7 TeV provided currently by the LHC accelerator. At this energies one has $x \lesssim 10^{-4}$ at $Q^2 \approx 10^4$ GeV^2. The description of QCD dynamics in this high energy range is still a subject of intense debate and there are several calculations in the literature taking into account different effects and parameter values [77, 78], including predictions with physics beyond the Standard Model [79].

Figure 1.11 shows predictions from [80] for the neutrino cross-sections including associated uncertainties, which derive essentially from the uncertainties on the parton distribution functions (PDFs) of the nucleon. Reference [80] uses the conventional next-to-leading-order DGLAP formalism [81] of QCD considering modern PDF sets which include the latest HERA data [82] in order to provide the best benchmark cross-sections and uncertainty estimates. We anticipate here that predictions from [80] will be used in section 6.1 to compute the neutrino exposure at the Pierre Auger Observatory.

Typically, the neutrino-nucleon interaction cross-sections $\sigma_{\nu N}^{\text{CC,NC}}$ increases as $E_\nu^{1/3}$, which translates in a reduction of the free mean path of neutrinos with energy. Interactions lengths are given by:

$$L = \frac{1}{N_A \times \sigma_{\nu N}^{\text{CC,NC}}} = 1.7 \times 10^7 \left(\frac{1}{\sigma_{\nu N}^{\text{CC,NC}}[\text{pb}]} \right) \text{ km of water equivalent} \tag{1.12}$$

where 1 km in water $\approx 10^3$ km in air.

Both, the increase of cross-section and the decrease of interaction length give the chance of detecting neutrinos in the Earth with large volume detectors. Current detection techniques for UHEν are based on very different techniques like the study of the extensive air showers produced in the atmosphere by the neutrino interactions, the observation of the Cherenkov radiation (light or MHz-GHz waves) produced by the resulting interaction products or the search with radio telescopes. Depending on the detection medium and technique, neutrino detectors can be classified as follows:

Ice Detectors: The largest neutrino detector, called IceCube [84] and built based on the AMANDA [85] technique, is located in the Antarctic ice, at a depth between 1500 m and 2500 m below the surface covering a geometric volume of 1 km^3 with 80 strings carrying 60 photomultiplier (PMT) each. IceCube can identify the three neutrino flavours through the detection of the Cherenkov light emitted by the charged debris of their collisions in ice. The muonic channel is favoured since muons can travel in straight line paths for several kilometers, enhancing the interaction volume and making easier the angular reconstruction. The detector is optimized for the detection of upward-going neutrinos in the PeV energy

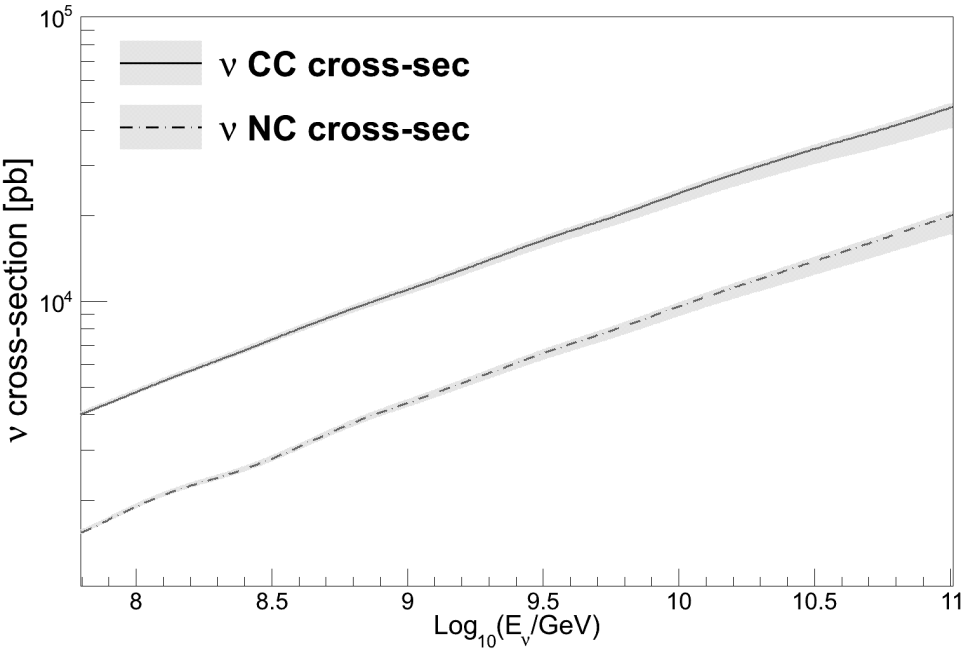

Figure 1.11: Neutrino cross-sections on isoscalar target for CC and NC scattering according to HERAPDF1.5 [83]. Data taken from [80].

range. It is also equipped with an array of surface detectors able to identify EASs (see chapter 2).

Water Detectors: The optical detection of Cherenkov light in water has already been probed for low energy neutrinos from the Sun, reactors and accelerators. Increasing the neutrino energy requires an increase of the detector volume. For this reason natural reservoirs of water are used. Examples of this kind of detectors are BAIKAL [86, 87] in the Lake Baikal, and some experiments in the Mediterranean sea, such as ANTARES [88], NEMO [89] or NESTOR [90], the goal in the next years is being to build a 1 km^3 large-scale detector [91].

Radio Detectors: They are based in the Askaryan effect [92]. The Cherenkov effect is not only present at optical and UV wavelengths, but has a strong component at radio wavelengths. The power of the effect is proportional to the number of ionizated particles in the medium. While cascade signals produce a significant radio signal, single mouns do not radiate enough to be observed. The Askaryan effect was observed for cascade-like events in sand [93], salt [94] and ice [95]. It is used for neutrino detection in experiments like RICE [96], and ANITA [97] in the Antarctic ice. SALSA [98] detects the Askaryan effect in salt domes and LUNASKA [99] tries to observe the Askaryan effect produced by neutrinos interacting in the Moon.

Acoustic Detectors: Neutrino induced cascades are compact and have high energies densities, which produce acoustic detectable signals. On contrary muons do not have enough energy density to produce a detectable acoustic pulse. The SAUND [100] was the first array build for acoustic neutrino detection. AMADEUS [101] is deployed along with ANTARES for acoustic detection in sea water. In the same way SPATS [102] is deployed within IceCube in order to test acoustic properties in Antarctic Ice.

Air Shower Detectors: This is the case of the Pierre Auger Observatory. The Earth atmosphere has a maximum depth of about 0.36 km of water equivalent when traversed horizontally ($\theta = 90°$) at sea level, far smaller than typical UHEν_s interaction lengths. Therefore, neutrinos can induce extensive air showers developing deep in the atmosphere –in contrast to cosmic ray hadrons which interact on top of the atmosphere– that can be used as distinctive signature. With this kind of techniques, neutrino energies in the EeV range and above can be explored. A detailed review of the EAS properties and the application to neutrino detection is given in chapter 2.

The most basic approach on astronomy is to look for an excess of neutrinos from a particular direction in the sky. AMANDA, BAIKAL, ANTARES, and IceCube make systematic sky maps and no significant excess has been seen in any of them. A related approach is to look for an excess of events from a list of objects selected because they are likely neutrino sources. IceCube is by far the most sensitive detector in this category. Other interesting analysis is to look for events correlated in time, either with each other or with a gamma-ray event [103]. The strongest limit from IceCube in terms of constrain models that relate cosmic ray origin with production of neutrinos is the absence of neutrinos in coincidence with GRBs. Recently data sets from two years of IceCube have been combined to obtain a significant limit [104] on models [105] in which GRBs are the main source of extragalactic cosmic rays. No neutrino was found during the intervals of observed gamma-ray emission.

It is also important to search for neutrinos from the whole sky instead of only from specific sources. This search has to be focused at extremely high energies, where the atmospheric background contamination is negligible. The most stringent limits to this flux comes from the Pierre Auger Observatory [3, 106] at energies above 10^{17} eV and from IceCube [107] for energies in the range $5 \times 10^{14} - 10^{17}$ eV as shown in figure 1.12. Even though a preliminary result, the IceCube Collaboration has recently claimed the observation of two neutrino candidates in the 1–10 PeV energy range and of unknown origin [107]. The detection of these two events, for an expected background of 0.14 events in 672.7 days of analysed data, encourages the search of these elusive particles.

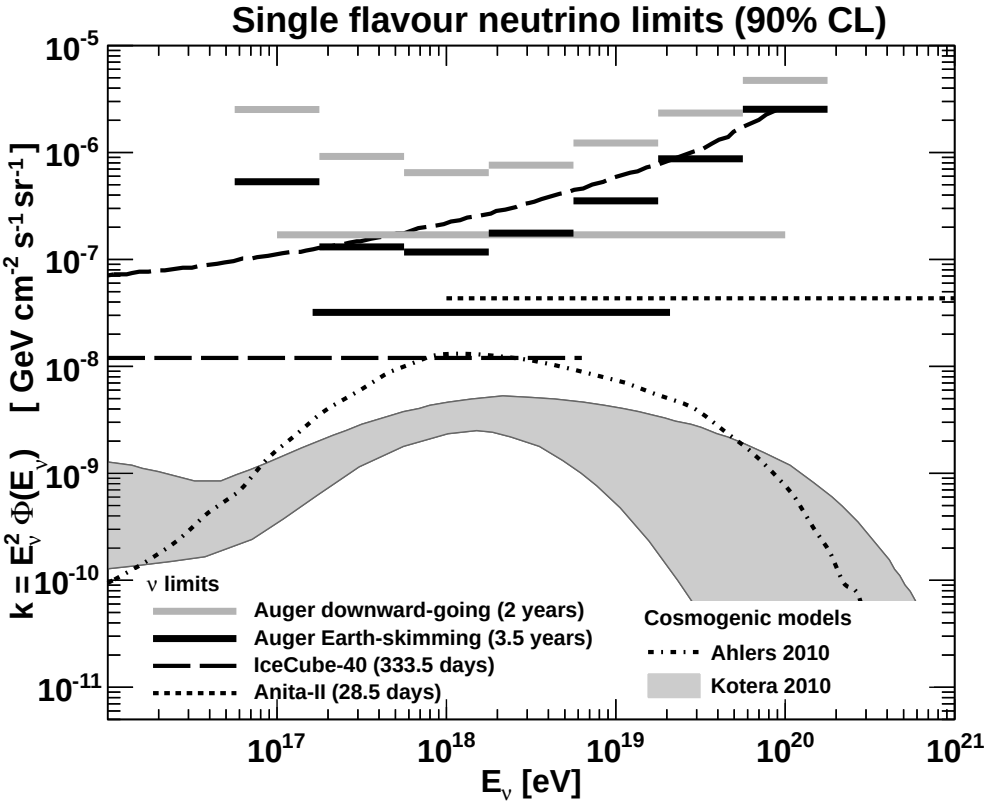

Figure 1.12: Differential and integrated upper limits at 90% C.L. to the diffuse flux of UHEνs (single flavour assuming equipartition) from the Pierre Auger Observatory [3], the IceCube collaboration [108] and the Anita-II experiment [109]. The IceCube differential limit has been scaled by a factor 1/2 due to the different binning in energy. Thin lines are the expected fluxes for three theoretical models of cosmogenic neutrinos (scaled to a single flavour when necesary). "p, Fermi-LAT" [56] corresponds to the best fit to UHECR spectrum incorporating Fermi-LAT bound with dip transit at 10^{19} eV. "p, evol-FRII" [57] assumes the FRII strong source evolution with a pure proton composition, dip transition model and maximum energy of UHECRs at the sources $E_{p,\max} = 10^{21.5}$ eV. "Fe. uniform" [57] represents the iron rich composition, low $E_{p,\max}$, uniform evolution of the UHECR sources case.

2
Extensive Air Showers

Extensive Air Showers (EASs) are the result of the collision of cosmic rays arriving to the Earth with air atoms in the top layers of the atmosphere. This interaction produces a cascade of new particles carrying a portion of the energy of the primary incoming particle. These secondary particles fall over the Earth surface like a shower, covering an extension of hundred or thousand of meters which qualify them as extensive. The atmosphere acts as a calorimeter of variable density with a vertical depth of more than 11 interaction lengths and 26 radiation lengths.

In this chapter we discuss on the basic properties of the extensive air showers induced by nuclei (section 2.1) and neutrinos (section 2.3) and review on the current experimental techniques used for their detection at ground (section 2.2).

2.1 Proton/Nucleus Induced Extensive Air Showers

For an incoming proton of 10^{19} eV hitting vertically the top of the atmosphere, the amount of cascade particles at sea level is about 3×10^{10} with a mean kinematic energy of 200 keV and it extends over a surface of a few km^2. The 99% of these particles are photons and electrons/positrons (electrons in the following) in a ratio of about 6 to 1, carrying the 85% of the energy. The remaining particles are either muons, with an average energy of 1GeV (10% of the total energy), pions with few GeV (4% of the energy), and neutrinos and baryons. The different nature of the constituent particles allow to separate the shower in three components as show in figure 2.1: electromagnetic, muonic and hadronic component. The exact development of the shower is a complicated process and there is a plethora of models in the literature trying to explain the cascade behaviour. Nevertheless the basic properties of the cascade can be extracted from a simplified model of the electromagnetic cascade evolution [110] together with an extension to hadronic cascades [111].

2.1.1 Electromagnetic Showers: the Heitler‘s model

The evolution of an extensive air shower in his first epoch is dominated by electromagnetic processes [112]. When a baryonic cosmic ray interacts with an air nucleus high in the atmosphere, it leads to a cascade of secondary mesons and nucleons that stay close to the shower axis. The earliest generations of charged pions interact again and produce a hadronic core that continues

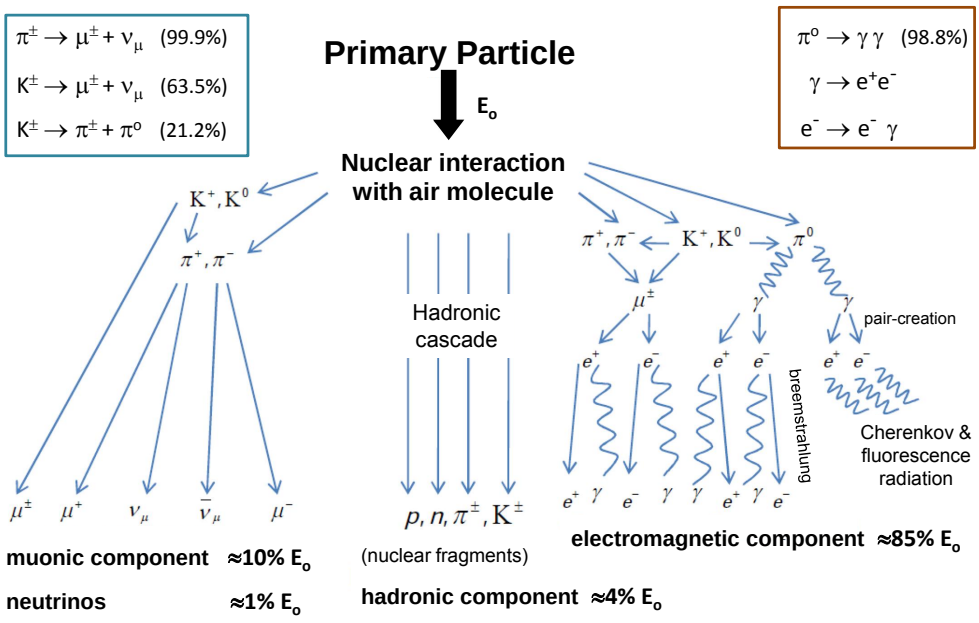

Figure 2.1: Main components of an extensive air shower.

to feed the muonic and electromagnetic components of the cascade. Electromagnetic particles are essentially produced by the photons produced via the decay of neutral pions and η particles. The evolution of the electromagnetic component is driven by electron bremsstrahlung and pair production [113].

Heitler presented a simplified model to describe the evolution of electromagnetic cascades as a perfect binary tree. At each step all particles interact and produce two secondaries of equal energy. This description assumes that electrons split their energy in half via bremssstrahlung emission of a single photon ($e^- \rightarrow e^-\gamma$) that eventually produces an electron-positron pair ($\gamma \rightarrow e^-e^+$) of equal energy. In this simplified approach, energy losses by collision are ignored and cross sections are taken as independent of energy. The interaction step length d in the cascade is therefore given by the radiation length of the medium λ_r ($\lambda_r = 37$ g/cm^2 in air) as $d = \lambda_r \ln 2$. After n steps the particle number is $N_n = 2^n$ (see figure 2.2 (a)) and their individual energy is E_0/N_n, where E_0 is the initial energy of the primary particle. This development continues until the individual energy drops below a critical value where the rate of energy loss of electrons via bremsstrahlung is equal to the rate of energy loss by ionization. This energy is about $E_c^{\gamma} = 80$ MeV in air. At this point, the electromagnetic cascade has reached his maximum development and the number of particles ($N_{\max} = 2^{N_c}$) is given by the ratio of the original energy to the critical one. What follows is the gradual extinction of the electromagnetic cascade. Despite their simplicity, the Heitler model reproduces correctly three properties of electromagnetic cascades:

1. The number of particles at the maximum of the cascade is proportional to the energy of the particle that induces the air shower: $N_{\max} = E_0/E_c^{\gamma}$.

2. The evolution of the depth of maximum development of the shower has a logarithmic dependence with energy: $X_{\max} = X_0 + \lambda_r \ln(E_0/E_c^{\gamma})$, where X_0 is the position of the primary interaction, usually expressed in units of atmospheric depth (g/cm^2).

3. The elongation rate (rate of evolution of $X_{\max}$ with energy) defined as:

$$D_{10} \equiv \frac{dX_{\max}}{d\log E_0} = 2.3\lambda_r \tag{2.1}$$

is given by the radiation length of the medium. The elongation rate in air is about 85 g/cm^2.

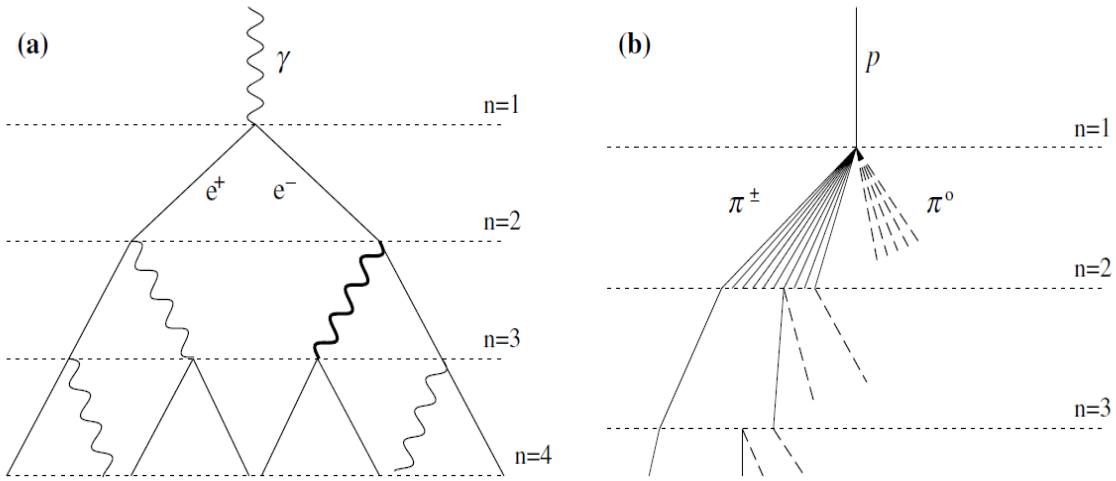

Figure 2.2: Schematic representation of the Heitler model for electromagnetic (a) and hadronic (b) cascade development.

Simulations of electromagnetic cascades confirm these properties although the particle number at maximum is overestimated in a factor 2 to 3 and the predicted ratio of electrons to photons is 2 while measurements show a value of 1/6. This is because electrons lose energy much faster than photons and multiple photons are emitted during bremsstrahlung processes.

For an accurate description of the shower, more ingredients have to be taken into account. The relevant quantities participating in the development of the electromagnetic cascade are the probability for an electron to radiate a photon and the probability for a photon to produce a pair e^+e^-. These probabilities are determined by the properties of air and the cross sections of the two processes. Moreover, at a given energy the change from radiation losses to ionization losses depopulates the shower. One can thus categorize the shower development in three phases: the growth phase, in which all the particles have energy bigger than E_c^{γ}; the shower maximum, X_{max}; and the shower tail, where the particles only lose energy, get absorbed or decay (see Figure 2.3).

An additional difficult problem is the lateral spread of the shower particles, the so called Lateral Distribution Function (LDF). In bremsstrahlung and pair production the secondary particles are not emitted exactly in the direction of the primary one. The average transverse momentum in these processes is of the order of the electron mass m_e. In addition, electrons change their direction by Coulomb scattering. The theory of the lateral spread of the shower particles was developed by Greisen [114] and by Kamata & Nishimura [115]. The approximate solution for the lateral distribution of electrons is called the Nishimura-Kamata-Greisen (NKG) formula, that gives the density of shower electrons as:

$$\rho(r) = k\left(\frac{r}{r_M}\right)^{-\beta}\left(1+\frac{r}{r_M}\right)^{-(\beta-\gamma)} \tag{2.2}$$

where ρ(r) is the charged particle density at a distance r from the core, r_M is the Molière radius[1], β and γ are determined experimentally and k is a normalization constant proportional to the shower size.

All the formulae above give the average shower behaviour, which may be different from the shower profile of an individual shower. Each shower starts at different depth which creates significant fluctuations in the shower development. In addition, one should add intrinsic fluctuations which depend on the interaction lengths of each particle. Given the difficulty to compute analytically such fluctuations in the shower development, the best estimation is obtained using Monte-Carlo techniques. There are different maintained codes, of which the best known is EGS4 [116] that will be used in this work (see section 4.1.2).

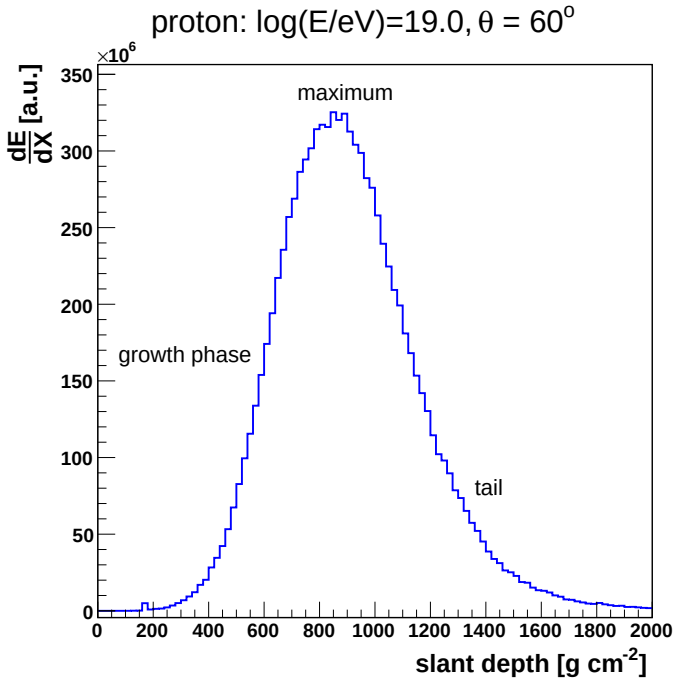

Figure 2.3: Example of a longitudinal development of an EAS, generated with CORSIKA [117], for a proton of 10 EeV entering the atmosphere with an incident zenith angle of 60°.

2.1.2 Extension to hadronic showers

Heitler's model can be adapted to describe hadronic showers [111, 118]. In this case the relevant parameter is the hadronic interaction length λ_I. At each step of thickness $\lambda_I \ln 2$ it is assumed that hadronic interactions produce $2N_\pi$ charged pions and N_π neutral ones. While π^0 decay immediately to two photons and feed the electromagnetic part of the shower, π^+ and π^- interact further. The hadronic cascade continues to grow, feeding the electromagnetic part at each step, until charged pions reach an energy where decay is more likely than a new interaction. A schematic of an hadronic cascade is shown in figure 2.2 (b).

The interaction length and the pion multiplicity ($3N_\pi$) are energy independent in the model. The energy is equally shared by the secondary pions. For pion energy between 1 GeV and 10 TeV a charged multiplicity of 10 ($N_\pi = 5$) is an appropriate number. One third of the available

[1]The Molière radius varies inversely with the density in the medium and it is of the order of 100 m at the Pierre Auger Observatory altitude (1400 m $\equiv$ 875 g/cm^2).

energy goes into the electromagnetic component while the remaining 2/3rd continues as hadrons. Therefore the longer it takes for pion to reach the critical energy E_c^π (20 GeV in air) the larger will be the electromagnetic component. Pions only decay to muons below the critical energy, consequently, in long developing showers the energy and the number of muons will be smaller. Moreover, because of the density profile of the atmosphere, E_c^π is larger high above ground than at sea level and deep showers will produce fewer muons. According to those principles, primaries with larger cross sections will have a larger muon to electron ratio at ground.

To obtain the number of muons in the shower one simply assumes that all charged pions decay into muons when reach the critical energy. $N_\mu = (2N_\pi)^{n_c}$ where $n_c = \ln(E_0/E_c^\pi)/\ln 3N_\pi$ is the number of steps needed for the pions to reach E_c^π. Introducing $\beta = \ln 2N_\pi/\ln 3N_\pi$ we have:

$$N_\mu = (E_0/E_c^\pi)^\beta \tag{2.3}$$

Detailed simulations give values of β in the range 0.9 to 0.95 [119]. On contrast to electrons, the muonic component does not scale linearly with the primary energy but at lower rate.

The determination of the position of the shower maximum depends not only of the energy, but also on the cross section, the inelasticity of each interaction and the energy transfer from hadronic to electromagnetic component. A good approximation of the elongation rate can be obtained when introducing the cross section and multiplicity energy dependence. For a proton air cross section of 550 mb at 10^{18} eV and a rate of change of about 50 mb per decade of energy [120] one obtains:

$$\lambda_I \simeq 90 - 9\log(E_0/\mathrm{EeV}) \ \ \mathrm{g/cm^2} \tag{2.4}$$

With the assumptions of [111], the elongation rate can be calculated:

$$D_{10}^p = \frac{4}{5}D_{10}^\gamma - 9\ln 2 \simeq 62 \ \ \mathrm{g/cm^2} \tag{2.5}$$

This result that only depends on the cross section and multiplicity evolution with energy is quite robust and it is in good agreement with simulation codes [119]. Long time ago, Lindsley introduced the *elongation rate theorem* that stipulates that the elongation rate for electromagnetic showers (D_{10}^γ) is an upper limit to the elongation rate for hadronic showers (D_{10}^p) as show in equation 2.5.

The extension of this description to nuclear primaries can be done by the superposition model, which assumes that the nuclear interaction of a nucleus with atomic number A is equivalent to the superposition of A nucleons of individual energy E_0/A. Consequently, showers from nuclei will develop higher, faster and with less shower to shower fluctuations than showers initiated by lighter nuclei. Moreover, pions will reach the critical energy faster and the relative number of muons increase with the atomic number. From this simple assumptions one can directly see that:

1. Shower induced by nuclei with atomic number A will develop higher in the atmosphere. The offset with respect to proton showers is simply: $X_{\max}^A = X_{\max}^p - \lambda_r \ln A$.

2. Showers initiated by nuclei with atomic number A will have a larger muon number: $N_\mu^A = N_\mu^p A^{1-\beta}$

3. The evolution of the primary cross section and multiplicity with energy for nuclei is the same as for protons. Different nuclei will have identical elongation rates and will show up as parallel lines in an $X_{\max}$ vs. energy plot.

4. The fluctuation of the position of $X_{\max}$ from one shower to another is smaller for heavy nuclei than for light ones.

Simulations confirm qualitatively all the above properties. Nevertheless, as interaction cross sections and particle production at these high energies are not known, they have to be extrapolated from measurements at lower energies leading to big systematics uncertainties. This makes difficult the design of efficient algorithms, so models of showers are continuously evolving.

The NKG formula (eq. 2.2) may also be extended to describe showers initiated by baryons [121]. The modified NKG formula provides a good description of the e^+e^- lateral distribution at all stages of shower development at shower core distances, r, sufficiently far from the hadronic core. One of the earliest parameterizations of the muon LDF in vertical showers was empirically derived by Greisen [114],

$$\rho_\mu(r) \approx k' \left(\frac{r}{r_G}\right)^{-0.75} \left(1 + \frac{r}{r_G}\right)^{-2.5} \tag{2.6}$$

where $r_G = 320$ m is analogous to the Molière radius.

2.2 Detection of Extensive Air Shower

The main experimental difficulty to measure the properties of cosmic rays at the highest energies is the extremely low flux expected at these energies (about 1 particle per km^2 per year at 10^{18} eV). Only detectors covering vast areas of thousands of km^2 can collect a significant number of events to perform statistical analyses. The observation of cosmic rays is indirect, through the detection of their induced showers. The atmosphere acts in both ways, as a calorimeter and as amplifier of the particle multiplicity.

Nowadays, the most commonly used detection techniques exploit Cherenkov, fluorescence and radio emission by the EAS during the propagation into the atmosphere, as well as the direct detection of particles in the shower reaching ground. The election of the method strongly depends on the energy range of interest and on the magnitude under study.

2.2.1 Cherenkov Detection

The first effect is the emission of Cherenkov light [75] by the charged particles moving along the propagation in the atmosphere. The Cherenkov intensity is proportional to the primary energy, while the slope of the lateral distribution is related to the depth of maximum shower development. Nevertheless, the Cherenkov cone is collimated around the shower axis, consequently one needs small spacing between detectors to allow a measurement of the lateral distribution. In addition, the duty cycle is low because it can only operate in clear dark nights. These two restrictions make inappropriate this technique to study EASs beyond 10^{17} eV where a detector of large extension is needed to measure a flux. The most active current array is Tunka [122], located in the Tunka valley (Siberia).

2.2.2 Fluorescence Detection

Nitrogen molecules of air are excited by the passage of charged particles of EASs. The result of this process is an isotropic emission of ultraviolet light (UV). The fluorescence yield is 4 photons per electron per meter at ground level pressure. Under clear moonless night conditions, using square meters telescopes of sensitive photo-detectors, the UV emission of the most energetic EASs can be observed at distances up to 20 km. This large aperture compensates the low duty cycle compared to ground arrays. The technique is specially suitable for energies above 10^{18} eV where the number of excited molecules is enough to produce a detectable signal over the background. Fluorescence telescopes directly measure the longitudinal profile of electrons along the shower axis, consequently it is sensitive to composition of the primary cosmic ray through the $X_{\max}$

variable. In addition a calorimetric estimate of the primary energy can be extracted. Nevertheless a constant monitoring of atmosphere conditions is necessary to account for corrections of the scattering and the absorption of fluorescence light from the production point to its detection by the telescopes. The first fruitful detection of fluorescence light from UHECRs was made by Tanahashi and his collaborators [123]. As explained in chapter 3, the Pierre Auger Observatory combines this technology with surface array detectors.

2.2.3 Surface Detector Arrays

Depending on the primary energy of the incoming cosmic ray, the induced EAS can spread over hundreds or thousands of m^2 at ground level. The direct detection of individual particles belonging to the shower is possible with an array of surface detectors deployed over large surfaces and spaced by hundreds of meters. These detectors have to be able to measure the energy and arrival time of the shower secondaries to allow the reconstruction of the direction of the primary cosmic ray. Angular resolutions of $\sim 1^\circ$–3° are reached with current operating arrays, much smaller than the deflections suffered by cosmic rays in the magnetic fields of the universe. The primary energy can be estimated from the lateral distribution of the signal in the perpendicular plane to the shower axis. The two most popular types of surface detectors are plastic scintillators and water Cherenkov tanks.

Plastic scintillators are equally sensitive to all charged particles. They can be deployed either at the surface where they detect all charged particles traversing them, or underground at different depths where they detect muons at different threshold energies. Their main disadvantage is the drop of efficiency when the zenith angle of the shower increases due to their small thickness. The KASCADE [124] experiment uses this kind of array [125] in combination with a hadronic calorimeter.

Water Cherenkov tanks are sensitive to the Cherenkov light of charged particles traversing the water. In principle the amount of signal coming from electrons and from muons is different and can be distinguished. In addition, their dimensions allow the detection of horizontal showers ($\theta \sim 90^\circ$). On the other hand, they are harder to deploy. As discussed in chapter 3, this technology is used by the Pierre Auger Observatory.

2.2.4 Radio Detection

Radio signals induced by EASs are of geosynchronous origin. When shower electrons and positrons propagate through the geomagnetic field they are bent in the opposite direction. This creates an electric dipole that propagates with the velocity of light and generates radio waves through synchrotron radiation [126]. At the characteristic emission frequencies (less than 100 MHz) the atmospheric absorption is very low. The threshold energy for detectable EAS by radio emission is around 10^{17} eV. The signal depends on the angle between the shower axis and the direction of the geomagnetic field, as well as the atmospheric conditions. Radio signals are very efficient for highly inclined air showers. In addition, the deploy of antennas over wide surfaces is cheap. In most of the detections, the radio antennas are triggered by an air shower array, this is the case of LOPES [127] which works together with KASCADE. Current research on radio signals focuses on the improvement of shower reconstruction and the possibility of self-triggering. The last has been achieved by the AERA project [128], as part of the Pierre Auger Observatory.

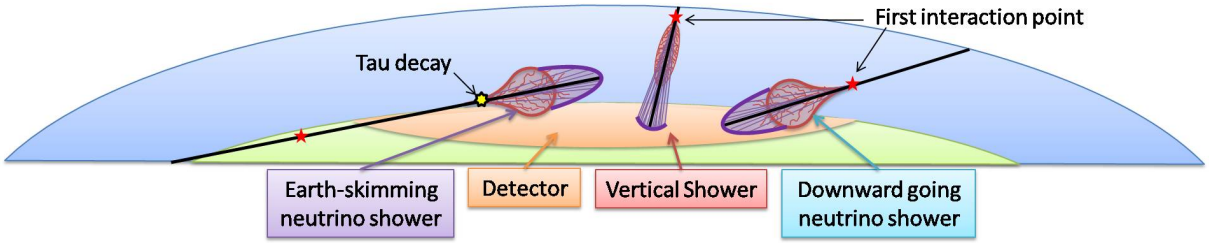

Figure 2.4: Representation of the different interactions produced by cosmic rays and neutrinos of different channel.

2.3 Neutrino Induced Extensive Air Showers

UHEν_s induce EASs which develop different in the atmosphere than those induced by cosmic rays mainly by two reasons. First, the neutrino-nucleon cross section at 10^{18} eV ($\sim$10 nb) is smaller than the proton-nucleon cross section (550 mb) in more than 7 orders of magnitude. This small value of the cross section makes the atmosphere quasi-transparent for neutrinos and they can interact at any depth while protons and nuclei only interact in the top layers of the atmosphere (see figure 2.4). Second, neutrinos interact via weak interaction while protons interact mainly via the strong force. In addition, in the weak interaction the interchanged boson can be either a $W^{\pm}$ (resulting in the so called CC channel of interaction), or a Z^0 (which mediates in the NC channel of interaction). The different nature of the first interaction translates in a different shower development. Attending to the flavour of the primary neutrino and to the interaction channel (CC or NC) the products of the first interaction can be very different. This is summarized in the figure 2.5.

Electron neutrinos interacting through CC channel produce two overlapped showers: a hadronic shower which carries a variable fraction of the primary neutrino energy and a pure electromagnetic shower induced by the resulting high energy electron/positron of the first interaction that carries the rest of the energy. Depending on the fraction of energy carried by the resulting electron, the electromagnetic to hadronic ratio of the mixed shower can be very different.

The CC interaction of muon neutrinos produces a hadronic shower carrying a fraction of the primary energy and an energetic muon. The resulting muon is hardly detectable by current air showers detectors and the probability to decay before reaching the detector is quite small, consequently the energy carried by the muon is lost and only the hadronic shower can be identified.

Neutrinos of any flavour can induce air showers through NC interactions that are indistinguishable from CC muon induced cascades. Again the resulting neutrino of the first interaction escapes carrying in average the 80% of the primary energy. The discrimination between EASs induced by the two processes is impossible with the current detectors.

Finally, CC interactions of tau neutrinos are particularly interesting. After the first collision, a hadronic shower plus a tau lepton are generated. While the hadronic shower develops in the atmosphere and can be detected at ground, the resulting tau lepton has a decay length of about 10 km. If the amount of atmosphere is large enough, the decay of the tau will produce a secondary shower that will be unsynchronized with the primary hadronic shower. This is the so called double-bang effect, which might be identified by EAS detectors. In addition, quasi-horizontal ("Earth-skimming") tau neutrinos can interact in the Earth crust or even in the mountains surrounding the detector producing a hadronic shower –that will be absorbed by the

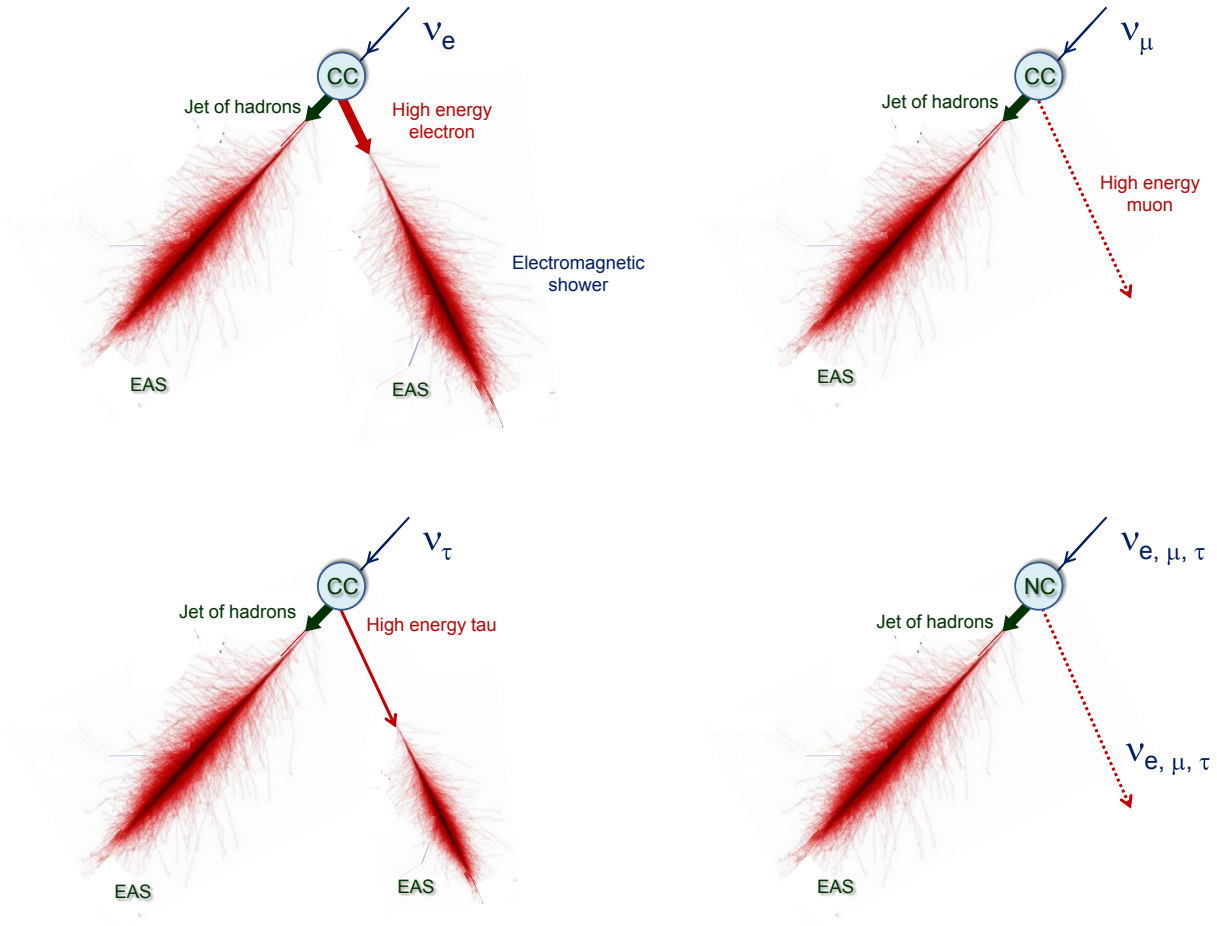

Figure 2.5: Sketch of the different kind of interactions and induced showers by UHE neutrinos.

rock– plus a tau lepton which can scape and decay giving again a detectable shower close to ground. Even though this process is not restrictive only to tau neutrinos, the contribution to the total Earth-skimming channel from ν_e and ν_μ processes is very small since the electron is easily absorbed by the rock and the muon escapes with no detectable signal produced.

2.3.1 Detection of Neutrino Induced Extensive Air Showers

Detection of neutrino induced showers lies mainly in the identification of EASs initiated very deep in the atmosphere, which have a characteristic signature, over a large repertory of backgrounds. As explained above, hadronic primaries interact in the top of the atmosphere while neutrinos can interact deeper. This translates in a different muonic to electromagnetic ratio between hadronic and neutrino induced showers. The bigger the difference between both points of first interaction, the stronger the difference in the ratio. Moreover, protons interact deeper in the atmosphere than nucleus do, and have a bigger fluctuation of the first interaction point (section 2.1.2). Consequently proton primaries are the main source of background for neutrino searches.

Therefore, the neutrino detection is focused in the identification of inclined showers, where the amount of atmosphere is enough to allow a big volume of atmosphere where neutrino can interact and the probability of a proton to penetrate is strongly suppressed. For proton showers at zenith angles above $\approx 60^\circ$ the electromagnetic component of the induced shower is almost extinguished before they reach ground. This kind of showers are commonly called "old showers". On contrary, deep neutrino showers ("young showers") can reach ground with a large amount of electromagnetic component if their first interaction point is deep enough.

For all these reasons, *the typical (distinguishable) neutrino EAS signature is a inclined young shower*. This concept is also valid for ν_τ interacting in the mountains or Earth-skimming neutrinos since the EAS induced by the resulting tau lepton is also a "young shower". Muons, which travel in straight lines, reach the detector mainly at the same time producing a narrow time signal characteristic of an old shower. On contrary, the electromagnetic component is delayed due to its multiple interactions, leaving the typical wide signal of a young shower. The capability of a detector in distinguishing this two kind of signals is strongly related with the capability of identify neutrino induced EASs.

Nevertheless a carefully treatment of the background should be considered. Deep interacting protons or a delayed shower development can exhibit some electromagnetic component even for inclined showers and could be misidentified as neutrino candidates. Another source of background comes from high energetic muons propagating into the atmosphere which can induce an electromagnetic shower by the emission of bremsstrahlung photons. The probability of muon bremsstrahlung is larger when increasing the zenith angle. An additional process that could contribute to the background is the production, propagation and interaction of B mesons as described in [129]. Finally signals of atmospheric muons or low energy showers in coincidence with an EAS that could not be properly resolved by the detector can contribute to the background. An special treatment of this *accidental* signals was the object of the dedicated study reported in section B.1.

3

The Pierre Auger Observatory

The Pierre Auger Observatory [2] aims at measuring the properties of the highest-energy cosmic rays (above 10^{18} eV) using a large array of surface detectors (SD) combined with air fluorescence detectors (FD). From its original inception, the Pierre Auger Observatory was meant to achieve full sky coverage through the operation of two sites, one in each Earth hemisphere. The southern site of the Observatory, officially completed in November 2008, consists of an array of over 1660 surface detectors and 27 telescopes deployed at 4 sites and overlooking the ground array. It is located outside the city of Malargüe (Argentina), and covers an extension of around 3000 km^2 of the "pampa amarilla". The site is relatively flat, near the base of the Andes and the mean altitude is 1400 m above sea level, which correspond to a vertical atmosphere depth of ∼875 g cm^{-2}. The detector layout is shown in the figure 3.1. In the following we will refer only to the southern site.

The Pierre Auger Observatory is the unique hybrid cosmic ray detector in the world. The fluorescence cameras detect scintillation light of excited nitrogen molecules when an EAS traverses the atmosphere. It allows a calorimetric estimation of the shower and inter-calibration of the surface detector. Nevertheless, the FD only works on clear moonless nights, which translates in a low duty cycle of around ∼12%. On contrary, the SD provides data near the 100% of lifetime.

Although the detector was mainly designed for detection of cosmic rays, it has the capability of detecting neutral particles through their induced EASs and particularly neutrinos as described in section 2.3. The low duty cycle of the FD combined with the low probability of neutrino interaction derives in a negligible exposure to neutrinos of the fluorescence technique compared to the SD. Consequently the work presented in this Ph.D. thesis will concentrate in the search of EASs induced by neutrinos using only the information collected by the SD of the Pierre Auger Observatory. In the next sections the main features of the experiment are described, with more attention given to the properties and performances of the SD in order to better understand the typical neutrino signatures which are searched for.

3.1 Fluorescence detector (FD)

Detection of UHECRs using nitrogen fluorescence emission induced by EASs is a well established technique, used previously by the Fly's Eye [130] and HiRes [131] experiments. It is also used by

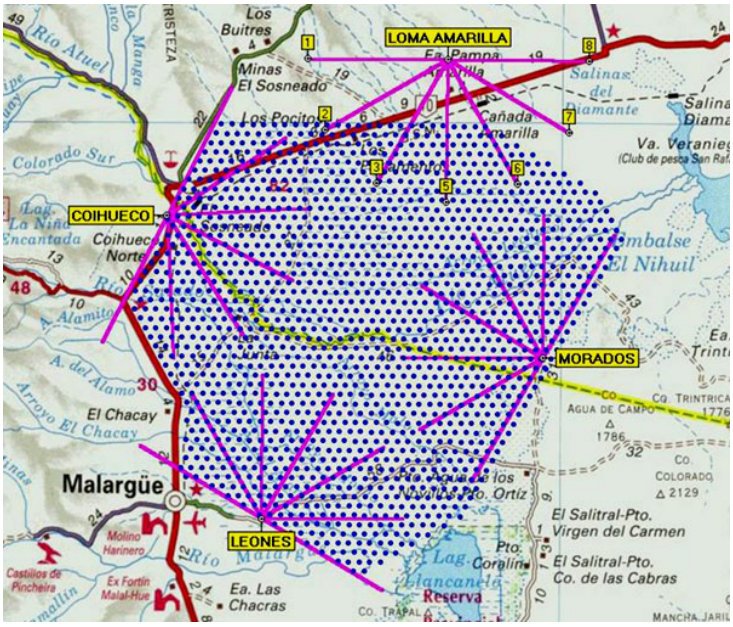

Figure 3.1: Layout of the Pierre Auger Observatory near Malargüe, Argentina. The dots represent the SD stations. The lines show the field of view of the fluorescence telescopes.

the Telescope Array [132] that was recently constructed.

Charged particles generated during the development of EASs excite atmospheric nitrogen molecules, and these molecules emit fluorescence light in the $\sim 300 - 430$ nm range. The number of emitted fluorescence photons is proportional to the energy deposited in the atmosphere due to electromagnetic energy losses by the charged particles. By measuring the rate of fluorescence emission as function of atmospheric slant depth X, an air fluorescence detector measures the longitudinal development profile dE/dX of the air shower. The integral of this profile gives the total energy dissipated electromagnetically, which is approximately 90% of the total energy of the primary cosmic ray.

For any waveband, the fluorescence yield is defined as the number of photons emitted in that band per unit of energy loss by charged particles. The absolute fluorescence yield in air at 293 K and 1013 hPa for the 337 nm fluorescence band is 5.05 ± 0.71 photons/MeV of energy deposited, as measured in [133]. For reconstruction of cosmic ray showers at the Pierre Auger Observatory, this absolute measurement is combined with the relative yields at other fluorescence bands [134]. Since a typical EAS develops along 10 km in altitude, it is also important to stress that the fluorescence yield is also dependent on pressure, temperature and humidity of the air [134, 135]. Consequently, a detailed atmospheric monitoring program including light detection and ranging (LIDAR) stations [136] (small receiver telescope and pulsed laser beam emitter) mounted at each FD building makes routine surveys of the vertical profile of aerosols and atmosphere inhomogeneities to reduce as much as possible the uncertainties in the energy estimation. In addition, systems which monitor clouds, the horizontal attenuation length, the scattering phase function and the meteorological situation are deployed on site [137].

The fluorescence detector [138] comprises four observation sites: Los Leones (figure 3.3a), Los Morados, Loma Amarilla and Coihueco. They are located at small elevations on the perimeter of the SD array. Six independent telescopes, each with a field of view of $30° \times 30°$ in azimuth and elevation, are located in each FD site. The telescopes face towards the interior of the array so that the combination of the six telescopes provides 180° coverage in azimuth (figure 3.3b). This

arrangement of four FD sites ensures 100% FD triggering efficiency above 10^{19} eV over the entire area of the surface detector. In addition to these 24 peripheral telescopes, the Observatory includes three "high elevation telescopes" located inside the SD array, near Coihueco (see section 3.3 for more details).

Figure 3.3c depicts an individual FD telescope, housed in a clean climate-controlled building. Nitrogen fluorescence light enters through a large UV-passing filter window and a Schmidt optics corrector ring. The light is focused by 10 square meter spherical mirror onto a camera of 20×22 pixels with PMT light sensors. Light pulses in the pixels are digitized every 100 ns, and a hierarchy of trigger levels culminates in the detection and recording of cosmic ray air showers. Each camera is calibrated individually by and end to end procedure once per year. It accounts for cumulative effects in the data taking process. Also, before and after each night of data taking, a relative calibration of the PMT is performed. This relative calibration tracks both short and long term changes in detector response.

For a reliable reconstruction of the geometry and the energy of an EAS the information of one fluorescence telescope is not enough. It needs information of the surface detector in order to fix the impact point of the shower core with ground, which breaks the ambiguity over all the possible contained axis in the same shower detector plane (see figure 3.2). These are the so called "hybrid events". Other possibility is the simultaneous detection of the shower by two or more telescopes ("stereo events"). The intersection of the shower detection plane of each telescope defines the axis of the EAS.

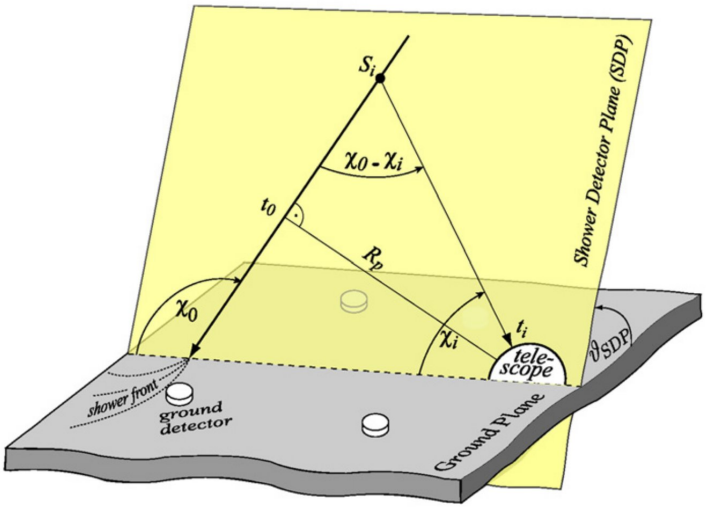

Figure 3.2: Illustration of the geometrical shower reconstruction from the observables of the fluorescence detector.

3.2 Surface detector (SD)

The SD array of the Pierre Auger Observatory consists on 1660 water Cherenkov detectors arranged on a triangular grid of 1.5 km spacing and covering an area of about 3000 km^2. These surface stations detect at ground level the secondary particles of the EAS and thus samples their lateral density distribution.

Each water Cherenkov detector of the surface array has a 10 m^2 surface circular area and 1.2 m height, with three 9 inch PMTs looking through optical coupling material into the 12

tonnes of water volume, which is contained in a Tyvek® reflective liner [2, 139]. Each detector operates autonomously, with its own electronics and communications systems powered by solar energy as show in figure 3.4. Each PMT provides two signals, which are digitized by a 40 MHz 10 bit Flash Analog to Digital Converter (FADC) (25 ns time bin) [139]. One signal is directly taken from the anode of the PMT, and the other signal is provided by the last dynode, amplified and inverted within the base of the PMT electronics to a total signal nominally 32 times the anode signal. The two signals provide sufficient dynamic range to cover with good precision both, the signals produced near the shower core ($\sim$ 1000 particles/μs) and those produced far from it ($\sim$ 1 particle/μs). The signals from the three PMT are sent to a Central Data Acquisition System (CDAS) once a candidate shower event triggers the surface array. Previously, the signals are calibrated locally as discussed in section 3.2.1 and selected by an hierarchical trigger system (section 3.2.2).

3.2.1 SD calibration

The calibration of each detector is performed locally and automatically because the total bandwidth available for data transmission from the detectors to the CDAS is 1200 bits per second, which precludes the possibility of any remote calibration. Calibration relies on the measurement of the average charge collected by a PMT from the Cherenkov light produced by a vertical and central through-going muon, named vertical-equivalent muon (VEM or Q_{VEM}) [140]. The SD station in its usual configuration has no way of distinguish vertical muons. However the distribution of the light of atmospheric muons gives a peak on both the charge distribution Q^{peak}_{VEM} and the pulse height I^{peak}_{VEM} (figure 3.5) which are proportional to those produced by a vertical muon. The peak Q^{peak}_{VEM} is at approximately 1.09 VEM for the sum of the 3 PMTs and (1.03 ± 0.02) VEM for each PMT, both measured with a muon telescope providing the trigger for vertical and central muons in a reference tank [141]. The difference between these two values is due to the fact that the three PMTs measure the total signal, whereas the individual PMT primarily measure the portion of the signal deposited closest to them. In figure 3.5, the second peak produced by the response of atmospheric muons is clearly visible, while the first peak is caused by the convolution of the trigger on a steeply falling distribution from low energy particles. The dashed histogram is produced by an external muon telescope providing the trigger to select only vertical and central muons. The shift observed is caused by the convolution of photo-electron statistics on an asymmetric peak in the track length distribution and local light collection effects.

The SD calibration procedure can be summarized in three main steps:

1. Set up the end-to-end gains of each of the 3 PMTs to have I^{peak}_{VEM} at channel 50.

2. Continually perform a local calibration to determine I^{peak}_{VEM} in channels to adjust the electronics-level trigger. This compensates for drifts which occur in the previous step.

3. Determine the value of Q^{peak}_{VEM} to high accuracy using charge histograms, and use the known conversion from Q^{peak}_{VEM} to 1 VEM to obtain a conversion from the integrated signal in VEM units.

The calibration parameters are determined with a 2% accuracy every 60 s and transmitted to the CDAS with each event.

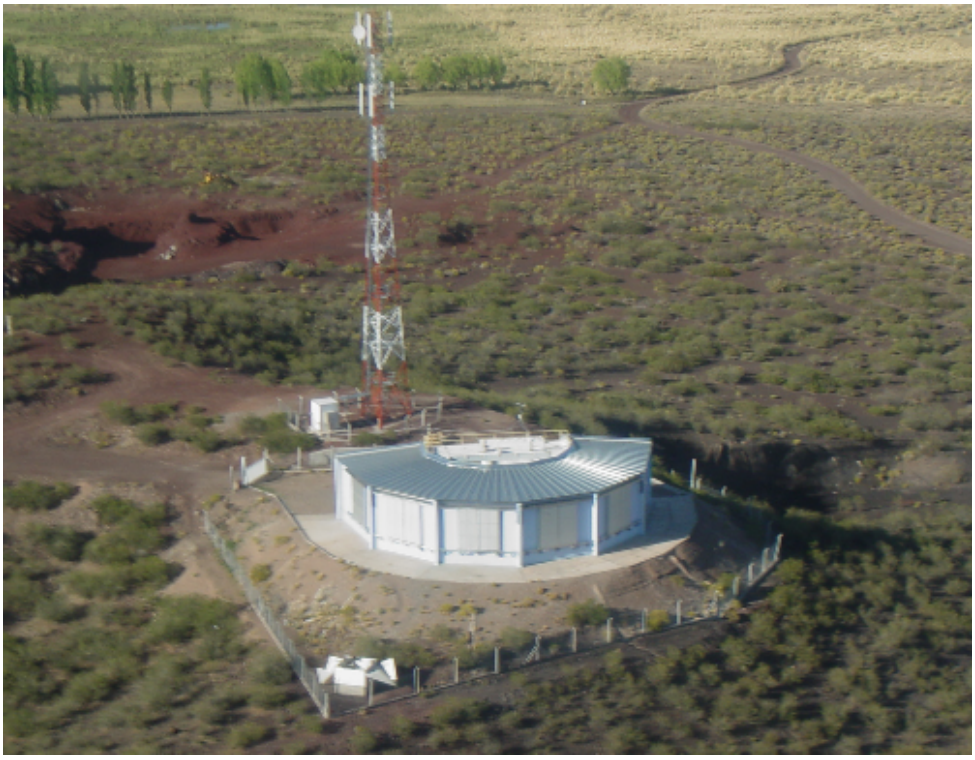

(a) FD site at *Los Leones*.

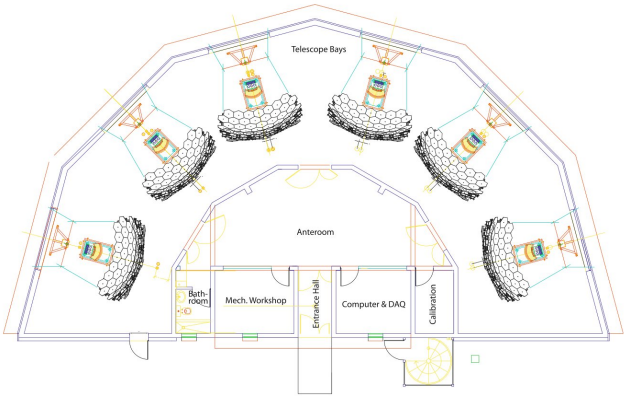

(b) Schematic top view of a fluorescence eye.

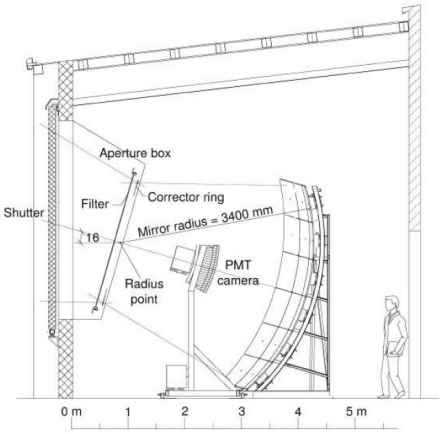

(c) Scheme of a fluorescence detector.

Figure 3.3: The fluorescence detector FD of the Pierre Auger Observatory. 3.3a *Los Leones* fluorescence telescope. 3.3b Top view of the 6 bays enclosing the PMT cameras. The angular range of 180° in azimuth is clearly visible. 3.3c Scheme of the components of a fluorescence camera.

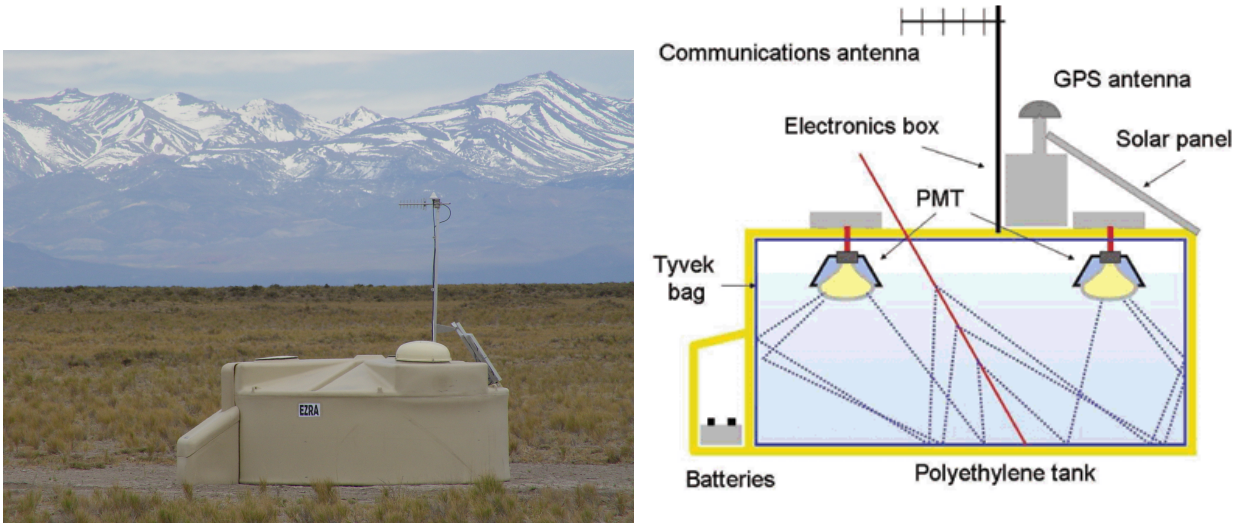

(a) Photo of a station of the surface array deployed in the field with the Andes in the background.

(b) Schematic view of the station components.

Figure 3.4: View of a SD station of the Pierre Auger Observatory with its components.

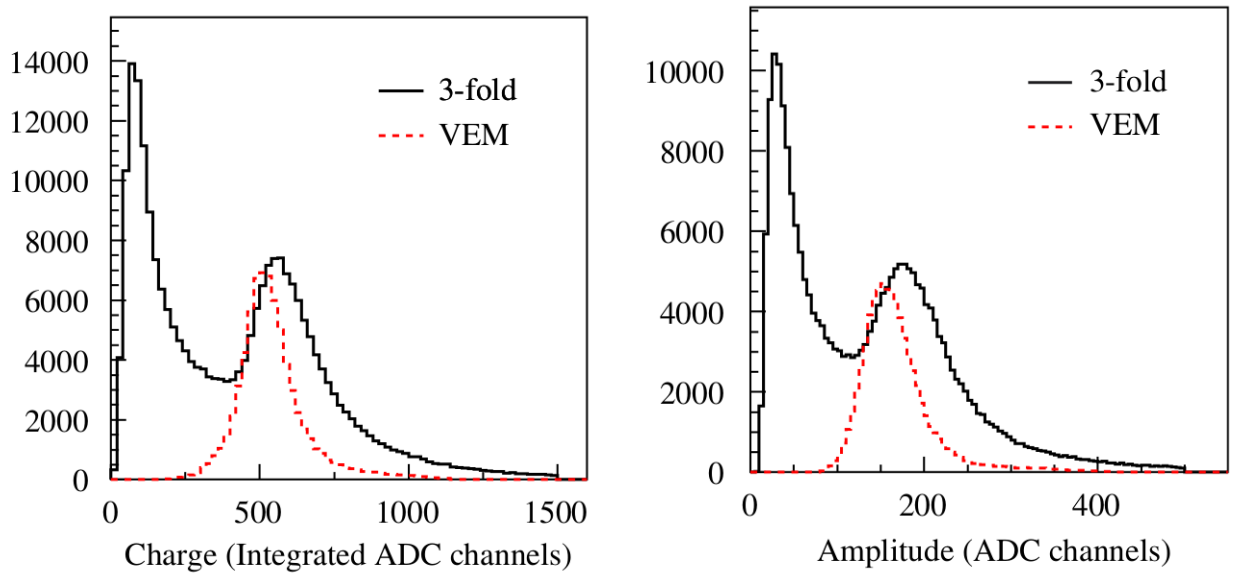

(a) (b)

Figure 3.5: Charge and pulse height histograms from a SD station triggered with a 3-fold coincidence between the three PMTs at trigger level of five channels above the baseline. The signal is summed for the three PMTs. In the solid histogram the second peak is due to the vertical through-going atmospheric muons (VEMs), while the first peak is a trigger artifact (see text). The dashed histogram is produced by vertical and central muons selected with an external muon telescope.

3.2.2 SD Trigger

The SD Data Acquisition (DAQ) trigger must fulfil both physical and technical requirements. The main limitation to the rate of recordable events comes from the wireless communication system which must serve continuously 1660 stations spread over 3000 km^2, each using an emitter consuming < 1 W power to transmit to collectors as far as 40 km away. The maximum sustainable rate of events per detector is < 1 per hour, to be compared to the 3 kHz counting rate per station due to the atmospheric muon flux. The trigger thus must reduce the single station rate, without inducing loss of physics events. To deal with all these requirements, the design of the SD DAQ trigger has been realized in a hierarchical form, where at each level the single station rate becomes less and less, by means of discrimination against background stricter and stricter. At the same time it is designed to allow the storage of the largest possible number of EASs candidates. Two levels of trigger (called T1 and T2) are formed at each detector. T2 triggers are combined with those from other detectors and examined for spatial and temporal correlations, leading to an array trigger T3, which is performed by the CDAS. The T3 trigger initiates data acquisition and storage. The logic of this trigger is summarized in figure 3.6.

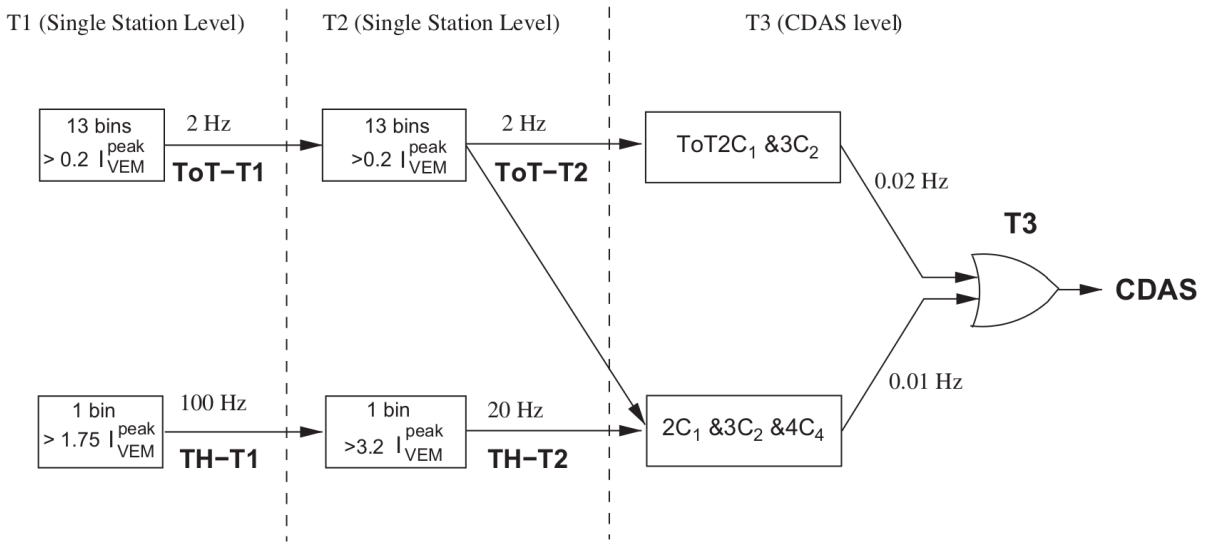

Figure 3.6: Schematics of the hierarchy of the trigger system of the Auger surface detector.

The T1 triggers data acquisition in each surface detector: data are stored on the local disk for 10 s waiting for a possible T3. Two independent modes are implemented as T1, having been conceived to detect, in a complementary way, the electromagnetic and muonic components of an EAS. The first mode is a Threshold trigger (TH) which requires the coincidence of the three PMTs each above 1.75 I_{VEM}^{peak}. If the station only has active two (one) PMTs, the threshold becomes 2 (2.8) I_{VEM}^{peak}. This trigger is used to select large signals that are not necessarily spread in time. It is particularly effective for the detection of showers with a dominant muonic component. This trigger reduces the rate due to atmospheric muons from ~ 3 kHz to ~ 100 Hz. The second T1 mode of trigger focus in the selection of broad signals, produced usually far from the shower core where the particles are more dispersed in time. This mode is called Time-over-Threshold trigger (ToT) and at least 13 bins (>325 ns) in 120 FADCs bins of a sliding window of 3 μs are required to be above a threshold of 0.2 I_{VEM}^{peak} in coincidence in 2 out of 3 PMTs. This trigger is optimized for the selection of near-by, low energy showers, dominated by the electromagnetic component, or for high energy showers where the core is distant. The time spread of the signals

arises from a combination of scattering (electromagnetic component) and geometrical effects (muons) [142, 143]. Since the average signal duration of a muon is only about 150 ns, the time spread of the ToT (325 ns) is very efficient eliminating the random muon background. The ToT rate at each detector is <2 Hz and comes mainly from the coincidence of two muons arriving within the 3 μs sliding window.

The T2 trigger is applied in the station controller to reduce to about 20 Hz the rate of events per detector. This reduction is needed to cope with the bandwidth of the communication system between the detectors and the central campus. Only T2 triggers are sent to the CDAS for the formation of the next level trigger. All ToT-T1 triggers are promoted to the T2 level, whereas TH-T1 triggers are requested to pass a further higher threshold of 3.2 I_{VEM}^{peak} in coincidence among the three PMTs. For detectors with only two (one) PMTs the threshold becomes 3.8 (4.5) I_{VEM}^{peak}.

The T3 trigger is not a local station trigger but a central trigger processed by the CDAS. It is based in spatial and temporal combination of T2 triggers over the whole array. This array trigger has two modes. For easier explanation it is convenient to define the concept of crown for a given detector. The first crown corresponds to the six nearest stations forming an hexagon around the given station. The extension to a crown of order n is trivial as show the figure 3.7.

The first T3 trigger mode requires for at least three stations that have passed the ToT condition and fulfil a minimum requirement of compactness, namely, one of the detectors must have at least one T2 station in the first crown and another T2 station in the second crown (see figure 3.7a). It is called "$ToT2C_1\&3C_2$", where C_n denotes nth crown. Once the spatial coincidence is imposed, timing criteria is required: each T2 must be within $(6 + 5C_n)$ μs of the first one. Since ToT as a local trigger has a very low background, this trigger selects 90% of physical events and it is mostly efficient for showers below 60°.

The second T3 mode is more permissive. It requires a four-fold coincidence of any T2 with a moderate compactness. Among the four fired stations within appropriate time windows, at least one must be in the first crown, another must be in the second crown and the last one can be as far as the four crown. This trigger is called "$2C_1\&3C_2\&4C_4$". The time criteria is the same as for the "$ToT2C_1\&3C_2$". An example of such T3 configuration is show in figure 3.7b. This trigger is efficient for the detection of horizontal showers that, being rich in muons, generate in the detectors signals that have narrow time spread, with triggered detectors having wide-spread patterns on the ground. Nevertheless, only the 10% of the selected events are real showers.

Once a T3 is formed, all FADC signals from detectors passing the T2 are sent to the CDAS, as well as those from detectors passing T1 but not the T2, provided that they are within 30 μs of the T3. With the full array configuration this trigger selects about 2800 events per day of which the 56% are real showers.

Next level of trigger is performed offline and requires for a space and time configuration of triggered stations compatible with a plane shower front moving at the speed of the light. Thus it is a physics trigger. Two criteria are defined, with different aims. The first, so-called 3ToT, requires three nearby stations, passing the T2-ToT, in a triangular pattern (figure 3.8b). Due to their compactness, events with zenith angles below 60° are selected with an efficiency above the 98%. The second criterion, so-called 4C1, requires four nearby stations, with no condition on the kind of T2 (figure 3.8a). This 4C1 trigger brings to $\sim 100\%$ the efficiency for showers below 60% and favour the selection of events with larger zenith angles.

The last trigger condition is a fiducial trigger called T5. This trigger deals with events falling close the border of the array, where important information can be missing. Such events could have wrong core position, and consequently incorrect energies. The main goal of this trigger is thus to select only events well contained in the array, ensuring that the core is properly reconstructed.

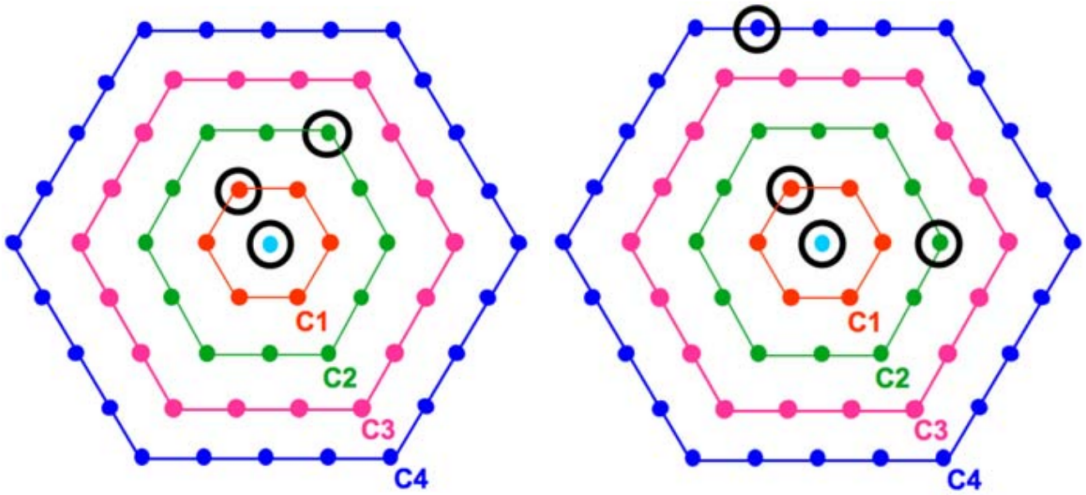

(a) $ToT2C_1\&3C_2$ trigger. (b) $2C_1\&3C_2\&4C_4$ trigger.

Figure 3.7: The two possible minimal T3 configurations.

T5 requires that the station with highest signal has all the stations of the first crown working at the time of the event. This is the so-called 6T5 trigger. A less restrictive criteria requires only 5 stations working in the first crown an it is called 5T5 trigger (figure 3.8c). It is important to stress that due to the large number of stations in the surface array, a 1% of the detectors are expected to be not functioning at any moment, even with constant maintenance, consequently the T5 trigger protects also against showers falling at any hole of the detector. We advance here that the shower selection criteria designed in this work to search for neutrinos will require a 6T5 trigger in order to ensure that the core and the signal in the surrounding stations are properly reconstructed (section 5.2).

3.3 Enhancements

The Pierre Auger Observatory was designed to be fully efficient detecting the most energetic EASs above $\sim 10^{18.5}$ eV. However, for a better discrimination between astrophysical models, a knowledge of the evolution of the cosmic ray composition in the expected transition region between galactic to extragalactic cosmic rays (10^{17} to 10^{19} eV) is required. To achieve this objective two improvements to the original conception have been developed.

The Auger Muons and Infill for the Ground Array (AMIGA) project aims at the construction of both, a dense surface of water Cherenkov detectors set out on an hexagonal spacing with sides of 750 m and 433 m, named "infill array", together with an associated set of muon detectors, each of 30 m^2 buried at a depth of 2.3 m which corresponds to a vertical depth of 540 g cm^{-2}. The 750 m infill facility extends over 23.5 km^2 while the 433 m infill covers only 5.9 km^2. The spacing between detectors enables detection of cosmic rays down to an energy of 3×10^{17} eV and 10^{17} eV respectively. The muon extension is composed by 64 scintillator counters situated near the water Cherenkov detectors. They will allow a direct estimation of the number of muons above 1 GeV of energy. Thus a muonic to electromagnetic ratio can be extracted aiding primary particle identification.

Regarding the fluorescence technique improvements, three High Elevation Auger Telescopes (HEAT) have been installed overlooking the AMIGA facility. The design of the HEAT is very

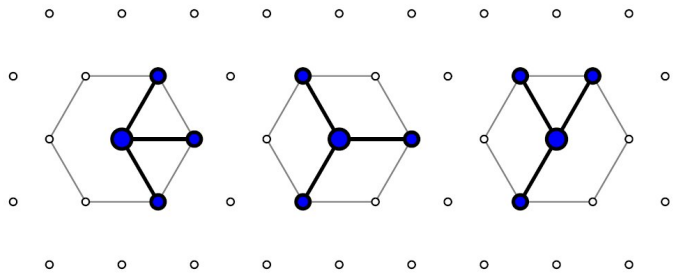

(a) Three minimal $4C1$ configurations.

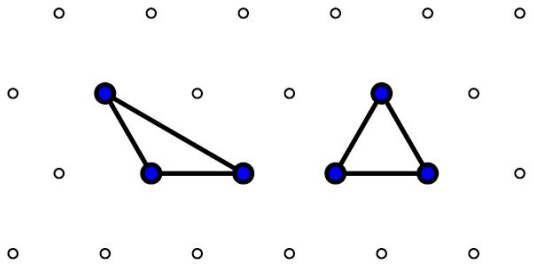

(b) Two minimal $3ToT$ configurations.

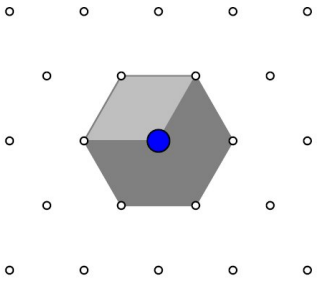

(c) 6T5 and 5T5 trigger quality configuration.

Figure 3.8: T4 (minimal) and T5 configurations. 3.8a The three minimal compact configurations for the 4C1-T4 trigger. 3.8b The two minimal compact configurations for the 3ToT-T4 trigger. 3.8c The 6T5 hexagon (shadow area) and the 5T5 hexagon (dark shadow area).

similar to the original FD system, except for the ability to tilt the telescopes upwards by 29°. It brings a field of view of $30° \times 40°$ when tilted. It enables the observation of the shower maximum for cosmic rays of energy down to 10^{17} eV.

As discussed in section 2.2, UHE EASs can be detected by the radio emission they induced. For this purpose, the Pierre Auger Collaboration has develop the Auger Engineering Radio Array (AERA) project, which aims to the detection of the 10 – 100 MHz radio band emitted by EASs in a self-triggered way. AERA consist in three stages. Stage 1 has 21 radio-detection stations arranged in a triangular grid with 150 m spacing. Stages 2 and 3, with larger detector spacings of 250 m and 375 m, increase the total area covered to nearly 20 km^2. AERA has an energy threshold of approximately 10^{17} eV.

The Pierre Auger Observatory is also developing various projects to demonstrate whether or not the detection of microwave radiation from EASs [144] is feasible. Three of these projects are prototypes for a large imaging antenna, namely, the Air-shower Microwave Bremsstrahlung Experimental Radiometer (AMBER), Microwave Detection of Air Showers (MIDAS) and FDWave. A different project aims to the detection of microwave emission through antenna horns located on each surface detector of the Observatory, this is called the Extensive Air Shower Identification using Electron Radiometer (EASIER) project. MIDAS is a self-triggering system while AMBER, FDWave and EASIER use the trigger from the Auger detectors to record the emission.

A review on all the enhancements of the Pierre Auger Observatory was recently published in [128].

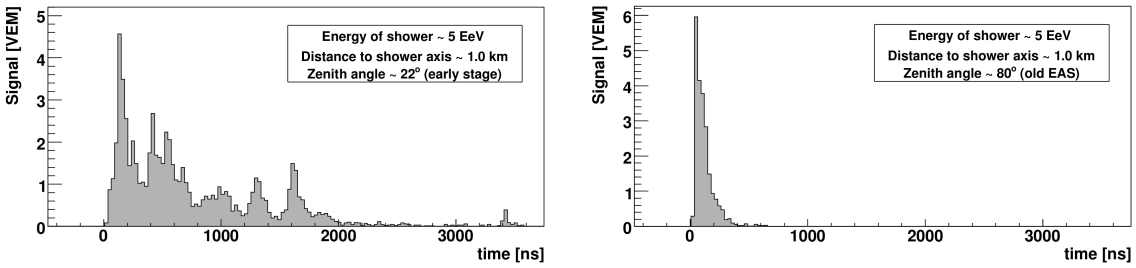

(a) Typical broad signal from a "young" EAS.

(b) Typical narrow signal from an "old" EAS.

Figure 3.9: FADC traces of SD stations at 1 km from the shower core for two showers of 5 EeV collected by the Pierre Auger Observatory. 3.9a Shower arriving in the early stages of development ("young" shower). 3.9b Shower arriving in the late stage of development ("old" shower).

3.4 Neutrino signatures in the surface detector

The surface detector of the Pierre Auger Observatory has the capability of detecting and identifying neutrinos in the EeV range and above through their specific signatures in the surface detector. Up to now, the zenith angular range between 75° to 95° has been explored and the searches have produced negative results [3, 106]. The main goal of this Ph.D. thesis is the study of the possibility of detecting UHEν_s with the surface array of the Pierre Auger Observatory in a lower zenith angular region, between 60° to 75°.

The concept for UHEν identification is relatively simple (section 2.3): while protons, heavier nuclei and even photons interact shortly after entering the atmosphere, neutrinos can generate showers initiated deeply into the atmosphere. When considering vertical showers ($\theta < 60°$), even the ones initiated by protons or heavy nuclei have a considerable amount of electromagnetic component at the ground ("young" shower front). However, when looking at higher zenith angles the atmosphere is thick enough (thicker than about three vertical atmospheres) so that the cosmic rays interacting high in the atmosphere have shower fronts dominated by muons at ground ("old" shower front). A neutrino with $\theta > 60°$ interacting deep will present a young shower front and, consequently, can be distinguished.

At the SD level, young showers induce signals spread in time over hundreds of nano-seconds in a fraction of the stations triggered by the shower, while old showers induce narrow signals spreading over typically tens of nano-seconds in practically all the stations of the event. With the 25 ns time resolution of the FADC of the water Cherenkov stations, the distinction between traces induced by young and old shower fronts can be easily accomplished. Figure 3.9 shows examples of those two types of traces. In summary, the search for UHEν_s relies in the identification of inclined "young" showers, i.e. with a large electromagnetic component.

Two magnitudes are particularly effective on the discrimination between old and young showers: the number of ToT triggered stations and the signal Area over Peak (AoP). As discussed in section 3.2.2, ToT-T2 triggers are especially suitable for the selection of broad signals, a high number of ToT-T2 triggered stations in an inclined event being an evidence of a young shower. The AoP is defined as the ratio of the integrated signal of the station over the biggest value of the signal. Narrow signals exhibit an AoP~ 1 while wide signals have values of AoP$\gg 1$. The

combination of these variables together with a good inclined shower selection is the key for an efficient neutrino discrimination.

Exploring the sky looking for UHEν_s down to $\theta \sim 60^\circ$ implies a sizeable improvement on the exposure and hence on the limit in case no candidates are found. The extension of the angular window below 60° has, however, some drawbacks. Decreasing the zenith angle also reduces the amount of atmosphere, i.e. the effective target volume for the neutrino to interact. For instance, at $\theta = 80^\circ$ the maximum slant depth is about 5030 g cm^{-2} while at 65° becomes 2070 g cm^{-2}. As a consequence, the nucleonic-induced showers look "younger" when arriving at ground –they exhibit a higher electromagnetic component, especially in the first triggered stations– making their separation from ν-induced showers more difficult. Finally, "accidental signals" (sections B.1 and B.2) become especially dangerous at this angular range since they can bias the angular reconstruction in more than one decade. All the previous issues make the UHEν search in the low angular region more challenging than in the already explored 75° to 95° window.

Part II

Neutrino analysis in the 60° to 75° of zenith angle

4

Simulation and Reconstruction of ν-induced Showers at the Surface Array

The identification of EASs induced by UHEν_s is based on their characterization by means of Monte-Carlo simulations. These simulations should reproduce the first interaction of the neutrino with an air nucleus as well as the propagation of the secondary particles through the atmosphere and the response of the surface detector array at ground. The Monte-Carlo simulation is a key ingredient on the challenge of detecting UHEν_s since the selection criteria, the detector sensitivity to neutrino-induced showers and the expected event rates strongly rely on them.

In this work, a complete end-to-end Monte-Carlo chain was developed involving a sequence of three steps. As described in section 4.1.1, the first step consists on the generation of the ν-nucleon primary interaction and the bulk of secondary particles which initiate the shower. Then, the shower evolution in the atmosphere is simulated and the particles propagated to ground as explained in section 4.1.2. In a later step the detector response to particles hitting the surface stations is simulated (section 4.1.3).

The shower properties are reconstructed with the official simulation and reconstruction package $\overline{\text{Off}}\underline{\text{line}}$ [145] of the Pierre Auger Collaboration. As explained in section 4.2, some improvements to the standard $\overline{\text{Off}}\underline{\text{line}}$ code have been developed in the frame of this Ph.D. thesis to increase the neutrino detection efficiency. The outcome of the full simulation chain for the generated neutrino-induced showers is reported in section 4.3 in terms of reconstruction efficiencies.

4.1 The Shower Simulation

The six possible neutrino interaction channels (depicted in figure 2.5) have been characterized by the generation of only two sets of simulations. Since the resulting neutrino of a NC interaction is undetectable, EASs induced by the three neutrino flavours ν_e, ν_μ and ν_τ interacting trough the NC channel are indistinguishable. Therefore, only one set of hadronic showers (ν_e NC was chosen in our case) was simulated to calculate the NC contribution to the exposure.

The same principle applies to ν_μ CC interactions since the produced μ is very penetrating, escaping detection. Also, since the inelasticity distributions for the NC and CC interactions are very similar [76, 77], it is a good approximation to use the same set of NC showers to simulate

the ν_μ CC channel, accounting of course for their difference in cross-section. On average, the secondary neutrino produced in a NC interaction carries about 80% of the primary energy. Given that the probability that this neutrino escapes detection is very high, only a small fraction of the primary particle energy is transferred to the shower.

The ν_τ CC channel requires a special treatment since at EeV energies the decay length of the τ is comparable to the length of the atmosphere and the τ can initiate a second shower that might trigger the SD increasing the exposure of the Observatory to ν_τ events. In this work, this "double-bang" showers were not included in the simulation and the ν_τ CC channel will be treated as the ν_μ CC channel, an approximation that underestimates the detection efficiency for ν_τ events.

Finally, the electron produced in a ν_e CC process interacts on average one radiation length after production, initiating an electromagnetic shower aligned with the hadronic shower from the nuclear debris which can be fully detected.

Consequently the ν_e channel was taken as reference for the simulations and events in the CC and NC generated and used to estimate the contribution from the other channels.

4.1.1 Primary neutrino interaction

UHEν_s interact with atmospheric atoms through a deep inelastic process. This process is simulated with the HERWIG code [146, 147] which is integrated into the COsmic Ray SImulations for KAscade (CORSIKA) package (see section 4.1.2. It is worth mentioning that a small modification had to be made in HERWIG to force the interaction channel (CC or NC) of the primary collision. The parton momentum fraction distributions of the beam particles are used in the generation of initial-state parton showers and also in the non-perturbative process of linking the shower with the beam hadron and its remnant. Since the parton showering is done in leading-logarithmic order, and the differences between leading order and next-to-leading order are not expected to be distinguishable at ground level after the propagation of the secondaries through the atmosphere, there is no strong motivation to use next-to-leading order parton distribution functions. The structure function used for this analysis is the average of two of the published fits in [148], the so-called MRST98 distribution. Systematic uncertainties related with the parton distribution function and with the primary interaction generator will be discussed in section 6.2.

For the CC channel, fixed energies were simulated in the range 10^{17} to $10^{20.5}$ eV in logarithmic energy steps of 0.5. For NC events the hadronic shower is expected to carry in average the 20% of the incoming ν_e energy. Consequently the simulated energy range was shortened to $10^{18} - 10^{20.5}$ eV since lower energies show a negligible trigger probability. For both interaction channels fixed zenith angles between 60° to 75° in steps of 3° have been simulated using random azimuth angles between 0° to 360° (see table 4.1). To maximize the simulation efficiency all injected neutrinos are forced to interact at fixed injection points D, uniformly distributed along the shower axis in steps of 100 g cm^{-2} (atmospheric depth units). Injection points too close to ground having a trigger efficiency below 10% are omitted, as well as points very close to the top of the atmosphere where the neutrino induced showers are expected to be indistinguishable from proton showers. Figure 4.1 shows all the injection depths simulated for each Monte-Carlo zenith angle.

For each bin of energy, zenith and injection depth (E, $\theta_{\rm MC}$, D) a total of 50 primary neutrinos of each channel were injected and the induced EAS tracked down to the detector surface. Then, each shower was injected ("replicated") 5 times in the detector simulator with random core positions to account for signal fluctuations due to differences in the impact point of the shower core. The whole simulation was produced using the GRID technology [149, 150].

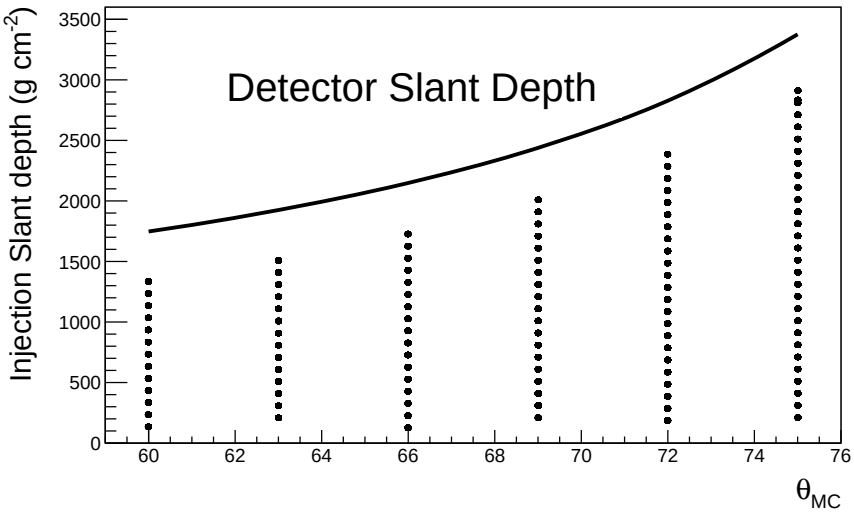

Figure 4.1: Atmospheric slant depth at the altitude of the Pierre Auger Observatory, located at 1400 m above the sea level, as function of the zenith angle (solid line). The dots indicate the depths at which primary Monte-Carlo neutrinos have been injected. The top of the atmosphere is at 0 g cm^{-2}.

$log_{10}(E/eV)$	17.0	17.5	18.0	18.5	19.0	19.5	20.0	20.5
$\theta_{\rm MC}$	60°		63°		66°	69°	72°	75°
# interaction depths (D)	13		14		17	19	23	29
Max. interaction depth (g cm^{-2})	1640		1820		2040	2330	2720	3270
Min. interaction depth (g cm^{-2})	140		220		140	230	120	170

Table 4.1: Summary of the simulated neutrino energies, zenith angles and injection depths. For each angle, a different number of interaction depths ranging from a Max. to a Min. value in steps of 100 g cm^{-2} is simulated. Each (E, $\theta_{\rm MC}$, D) bin contains 50 simulated primary neutrinos and 250 showers at ground. The two first energy bins were not considered in the NC interaction channel.

4.1.2 Atmospheric Shower Simulation

In a second step, the secondaries produced by the first collision are injected in the EAS simulation CORSIKA package [117]. This code tracks the particles across the atmosphere up to their arrival at ground level. The program allows one to simulate interactions and decays of nuclei, hadrons, muons, electrons, photons and the corresponding antiparticles into the atmosphere up to energies of some 10^{20} eV. It allows to combine different high and low energy hadronic interaction models, use either explicit (EGS4) or analytic (NKG) electromagnetic development as well as explicit generation of Cherenkov light if required. In combination with PYTHIA [151], it allows the simulation of the tau lepton decay. For the Monte-Carlo set of this analysis we used QGSJET01c [152] as high energy hadronic model. When the particle energy drops below 200 GeV, the QGSJET01c model is replaced by the FLUKA [153] low hadronic model. Differences between hadronic models are not expected to be very significant for neutrino analysis because the neutrino discrimination mainly depends on the electromagnetic component. An estimation of the systematic uncertainties contribution from high energy hadronic models is given in section 6.2.

The development of the electromagnetic component of the shower is fully simulated with the EGS4 [116] Monte-Carlo method. The analytic NKG [114, 115] method is not recommended since it does not account for Earth curvature, which is important at angles above 60°. For example, in a 10^{19} eV γ-induced shower, $\theta = 60°$ and assuming no pre-conversion with the Earth magnetic field, the maximum of the electromagnetic component simulated by EGS4 is reached deeper in the atmosphere by ~ 100 g cm^{-2} slant depth than predicted by NKG.

For primary energies above 10^{16} eV the computing times become excessively long even for the GRID technology. To reduce the times to tolerable duration the so called "thin sampling" mechanism is introduced [154]. With the thinning algorithm all particles below an adjustable fraction of the primary energy (thinning level $\epsilon_{th} = E/E_0$) which emerge from an interaction are exposed to the thinning algorithm. Only one of these particles is followed and an appropriate weight is given to it while the other particles below the thinning level are dropped. For further details see references [116, 154, 155]. An additional improvement which uses a limitation of the particle weights [156], is included to reduce undesired statistical fluctuations on particle densities far from the shower core. For our simulations a thinning value of 10^{-6} has been assumed.

Realistic values of magnetic field and Earth curvature at the detector position are used. We include an steering CORSIKA input file as example of the parameters used for one of the simulated showers.

```
RUNNR 556954
PRMPAR 66
ERANGE 3.162e+10 3.162e+10
THETAP 7.500e+01 7.500e+01
FIXHEI 1.321e+06 1
NSHOW 1
THIN 1.000000e-06 3.162278e+04 1.000000E+04
PHIP -180. 180.
ATMOD 1
SEED 1670860 0 0
SEED 1670861 0 0
SEED 1670862 0 0
SEED 1670863 0 0
SEED 1670864 0 0
OBSLEV 1452.E2
```

```
MAGNET 19.812 -14.3187 Malargue at 06/2009
ECUTS 0.05  0.05 0.00025  0.00025
MUADDI T
MUMULT T
ELMFLG F T
STEPFC 1.
LONGI T 5. T T
ECTMAP 2.5E5
MAXPRT 1
DIRECT ./
DATBAS T
USER juliolb
PAROUT T T
QGSJET T 0
QGSSIG T
HILOW 200
HADFLG 0 0 0 0 0 2
FLATOUT F
THINH 1 100
EXIT
```

Once the CORSIKA simulation is completed, the program provides a file with all the surviving particles at ground level containing all the relevant information for posterior analysis. It includes among others, timing, energy, momentum, weight (if thinned) and Particle Data Group code [157] of each particle. If required, the same information can be extracted at different observation levels. It also provides a table with the energy deposit and the number of particles along the atmosphere, which is particularly interesting for fluorescence telescope simulations.

4.1.3 Surface Detector Response

The last step on the production of the ν-induced showers corresponds to the simulation of the surface detector response, which is achieved using the $\overline{\text{Off}}\underline{\text{line}}$ package. This code is a framework which provides the mechanisms for encapsulating the steps involved in the simulation and reconstruction into well defined *modules*. They can be configured and sequenced by external files. As an example, the simulation sequence module used on this analysis is shown below:

```
<sequenceFile>
  <enableTiming/>
  <moduleControl>
  <loop numTimes="1" pushEventToStack="yes">
    <module> EventFileReaderOG </module>
    <loop numTimes="5" pushEventToStack="yes">
      <module> EventGeneratorOG </module>
      <loop numTimes="unbounded" pushEventToStack="no">
        <module> CachedShowerRegeneratorOG </module>
        <module> G4TankSimulatorOG  </module>
      </loop>
      <module> SdSimulationCalibrationFillerOG </module>
      <module> SdPMTSimulatorOG                </module>
```

```
      <module> SdFilterFADCSimulatorMTU        </module>
      <module> SdBaselineSimulatorOG           </module>
      <module> TankTriggerSimulatorOG          </module>
      <module> TankGPSSimulatorOG              </module>
      <module> CentralTriggerSimulatorXb       </module>
      <module> CentralTriggerEventBuilderOG    </module>
      <module> EventBuilderOG                  </module>
      <module> EventFileExporterOG             </module>
    </loop>
  </loop>
  </moduleControl>
</sequenceFile>
```

The simulation of the detector response starts by reading the files containing the shower particles at detector level (*EventFileReader* module). Then, the *EventGeneratorOG* module chooses the position where the shower axis impacts over the detector. This module allows the user to choose a fixed position over the surface array or randomize the impact point of the shower. In our analysis the core position is randomized in a square area of 5×5 km^2 around a fixed station at the center of the surface array, ensuring that fluctuations of the station signals due to different relative positions of the core with respect to each station are taken into account.

In the next step the module *CachedShowerRegeneratorOG* iterates over all the particles at detector level undoing the thinning applied by the CORSIKA shower simulator. For each thinned particle, a set of new particles is generated with a Gaussian distribution of timing and the corresponding momentum, and energy. Then, particles hitting a surface station are piled up and tracked with the *G4TankSimulatorOG* module, which simulates the Cherenkov light produced by the particles crossing the tank and all the absorption and reflections processes of light up to its arrival to the PMT. The calibration constants described in section 3.2.1 are simulated in the module *SdSimulationCalibrationFillerOG* while the output signal of the photo-multiplier tubes (FADC traces for all stations) as well as the filter response and the baseline of the signal are simulated by the modules *SdPMTSimulatorOG*, *SdFilterFADCSimulatorMTU* and *SdBaselineSimulatorOG* respectively.

The decision of whether or not a signal from a certain station fulfils the local trigger criteria (defined in section 3.2.2) is taken in module *TankTriggerSimulatorOG*, and once all local trigger stations are computed, the event trigger (performed by the CDAS) is simulated by the *CentralTriggerSimulatorXb*. If the event fulfils the T3 trigger condition, the remaining modules of the sequence copy the information from the simulation container class to the event class and store the data in a file for the posterior reconstruction. For this simulation process an "ideal" SD array, *i.e.* with fully efficient stations, all working continuously in time and placed at 1400 m above the sea level on a perfect triangular distribution of 1.5 km spaced grid, is used. As anticipated previously, each EAS generated by the simulated primary neutrinos is injected 5 times with random core positions in the $\overline{\text{Off}}\underline{\text{line}}$ detector simulation chain in order to increase the statistics to 250 events for each (E, θ, D) bin.

4.2 Shower Reconstruction

The event reconstruction is another crucial step of the analysis. It is also performed within the $\overline{\text{Off}}\underline{\text{line}}$ package where the modular approach allows one to adapt effortlessly the generic reconstruction procedure to a specific reconstruction developed and tuned in the framework of this Ph.D. thesis to increase the neutrino identification efficiency. In the following sections the

role of each module involved in the Offline shower reconstruction (listed below) is described with detail.

```
<sequenceFile>
  <enableTiming/>
  <moduleControl>
    <loop numTimes="1" pushEventToStack="yes">
      <module> EventFileReaderOG           </module>
      <module> EventCheckerOG              </module>

      <!-- Sd Event pre-selection Chain -->
      <module> SdCalibratorOG              </module>
      <module> SdEventSelectorOG           </module>
      <module> SdMonteCarloEventSelectorOG </module>
      <module> SdTopDownSignalSelectorUGR  </module>

      <!-- Sd Event Reconstruction Chain -->
      <module> SdPlaneFitOG                </module>
      <module> LDFFinderKG                 </module>

      <!-- Sd Event post-selection and exporting -->
      <module> SdEventPosteriorSelectorOG  </module>
      <module> RecDataWriterNG             </module>
    </loop>
  </moduleControl>
</sequenceFile>
```

The first six modules concern the event reading and pre-selection, the next two have to do with the angular reconstruction of the shower and the two last modules are related to the event trigger and relevant information storage for posterior analysis. It is important to stress that the reconstruction sequence and procedure followed with simulated and real data events is exactly the same, with the exception of the *SdMonteCarloEventSelectorOG* module which is obviously not called in the later.

4.2.1 Event pre-Selection Chain

The reconstruction procedure starts opening and checking the integrity of the file containing the event data to be reconstructed. It is performed by the *EventFileReaderOG* and the *EventCheckerOG* modules respectively. The event data contains the FADC traces of all the stations participating in the event (*candidate stations* in the following). Applying the calibration constants of each station at the time of the event, the FADC traces are converted to calibrated VEM traces and the arrival time of the signal to each station (*start time* hereafter) is computed. Both, calibration of the traces and start time computation are performed by the *SdCalibratorOG* module.

The module *SdEventSelectorOG* carries out different actions, all of them related to the candidate station selection and the T4 and T5 trigger level (see section 3.2.2). The summary of these actions is the following:

Lightning event removal: Lightning event is detected as a series of oscillations in the FADC traces of all tree PMTs. If the signal does not exceed 1000 FADC counts and makes more

than 3 baseline crossings, the signal is considered as originating from a lightning event. The whole event, or only the affected station can be rejected. In our analysis we reject the whole event if lightning signal is detected at any station.

Engineering Array stations: These stations were used to test the viability of a hybrid detector at the beginning of the experiment. Their construction and electronic implementation differs from the final stations used. Consequently they are discarded for standard event reconstruction.

Doublet and infill stations: Doublets of stations are used for timing studies. The station with the highest identification number (ID) is always rejected even if the partner station is not present in the event. All the infill stations (see section 3.3) are also discarded.

Bottom Up selection: This step pretends the rejection of triggered stations non participating in the event. It selects a seed of three stations that maximize the sum of the signals. It requires for compatibility with a planar shower front propagating at speed of light with relative large tolerance. In addition it checks for geometrical compactness removing isolated stations. This selection is especially suitable for events below 60°, consequently we use an alternative approach (Top Down selection) described in the following module.

T4 trigger calculation: This module computes the T4 trigger criteria (see section 3.2.2). In addition it allows to discard events that do not pass the T4 trigger. In our analysis the T4 trigger is not used.

T5 trigger calculation: Finally the module computes the T5 trigger criteria. For our analysis we discard events not fulfilling the 6T5 trigger (see section 3.2.2).

For specific Monte-Carlo studies, a dense ring of virtual stations at a certain distance of the core can be placed. These stations that do not represent the real array are rejected by the module *SdMonteCarloEventSelectorOG*.

The last module of the event selection, *SdTopDownSignalSelectorUGR*, was specifically designed and developed in the frame of this work to improve the neutrino selection efficiency [158] carrying out two basic and inter-related functions: the top down selection of stations and the rejection of accidental signals. We concentrate here on the description of the top down procedure which concerns both Monte-Carlo and real data events, leaving for the next section the discussion on the treatment of the accidental signals (absent in simulated events).

The method, inspired from [159], identifies and piles up signal elementary segments of the VEM traces of all the stations. Then a top down procedure [160] is applied over the elementary segments to select the physical ones, fitting a shower front plane over the segments. If the fit does not converge, segments are recursively rejected until the convergence is achieved. After this procedure, stations with no segments are rejected, while the others are selected as candidate stations. If one station has two selected segments, the one with the biggest fit residual time is rejected. Finally the trace is scanned to search for possible sub-segments after the selected one following the same criteria defined in [159]. This procedure is also very efficient rejecting accidental signals and selecting inclined shower events. For high multiplicity events (with more than 20 stations) the computing time required by the module becomes excessive due to the large number of signals to be analyzed and the standard $\overline{\text{Off}}\underline{\text{line}}$ treatment of accidentals and top down selection is applied [159, 160]. A detailed explanation of the *SdTopDownSignalSelectorUGR* module functionality is given in appendix B.

At the end of the station selection process, only events with three or more candidate stations are kept for the angular reconstruction.

4.2.2 Treatment of Accidental Signals

Along with the secondary particles belonging to the main shower, the surface detector stations are continuously hit by a continuous flux of atmospheric muons and, in a lesser extent, by little showers developing close to the detector. Indeed, muons are the most numerous charged particles at sea level (mean energy of $\simeq$4 GeV), mostly produced from pion decays in the upper part of the atmosphere ($\sim$15 km). Local showers are initiated by secondary particles interacting with the atmosphere close to ground. Signals produced by atmospheric muons consist typically of narrow peaks in the FADC traces which, when occurring in a station already hit by shower particles, appear most of the times to be isolated (either before or after the main shower signal) due to their random time occurrence. On the other hand, low energy showers hitting a single station produce either broader signals or larger and narrow signals similar to the ones produced by atmospheric muons.

We recall here that the search for neutrino induced showers is based on the selection of inclined and young showers (section 2.3.1). Both, atmospheric muons and local showers are specially dangerous in neutrino searches for two reasons. First, they are able to trigger locally the detector array on isolated stations distorting the zenith reconstructed angle or, in the worst case, making the reconstruction fail. This effect is specially dangerous for nucleonic showers coming at zenith angles close to the edge of the criteria to select *inclined* neutrinos. A bias of few degrees on the reconstructed angle produced by an accidental signal might allow those vertical background showers to pass the inclined selection cuts, being accepted as fake neutrino candidates. Second, they modify the FADC trace of the stations hit by the main shower which can strongly bias both the reconstructed angle and the discriminating analysis variables. An increase on the total signal makes the shower looking younger than it is, increasing the probability to pass the neutrino selection criteria.

The pernicious effect of the accidental signals on the event reconstruction is nicely depicted in figure 4.2, where a real data event is reconstructed with a zenith angle of 58.6 ± 0.4 degrees using seven stations. A look to the distribution of time residuals and the high value of the resulting fit χ^2 already indicate strong inconsistencies between the start times of the selected stations. A careful inspection of the FADC traces recorded by the photo-multipliers of station n^o 641 (the one with the biggest signal in this case) reveals the presence of a small signal arriving about 65$\times$25 ns before the main signal, a clear candidate for being an accidental signal. The standard reconstruction algorithm considers this early prompt signal as the start time for the shower reconstruction (vertical dashed lines in the plot) which causes a miss-reconstruction of the zenith angle, spoiling the residual time fit.

In order to improve the accidental signal rejection in an automated way, a dedicated code was developed in the framework of this Ph.D. thesis as a part of the *SdTopDownSignalSelectorUGR* module already introduced in section 4.2.1. The algorithm identifies all the elementary signals of all the stations in the event and applies a top down selection procedure over them, rejecting signals recursively until a pattern compatible with a quasi planar front shower moving at the speed of light is found. Signals which have large residual times with respect to the front shower fit are rejected, which automatically selects the physical EAS signals rejecting the accidental ones. In addition to the top down procedure, an extra safety cut on the minimum signal of the stations is imposed by the module. Since accidental signals exhibit typically a charge of few VEMs, the stations with total signal below 3 VEMs are considered as accidental and discarded from the analysis, starting by the one with the smallest signal and stopping if the remaining

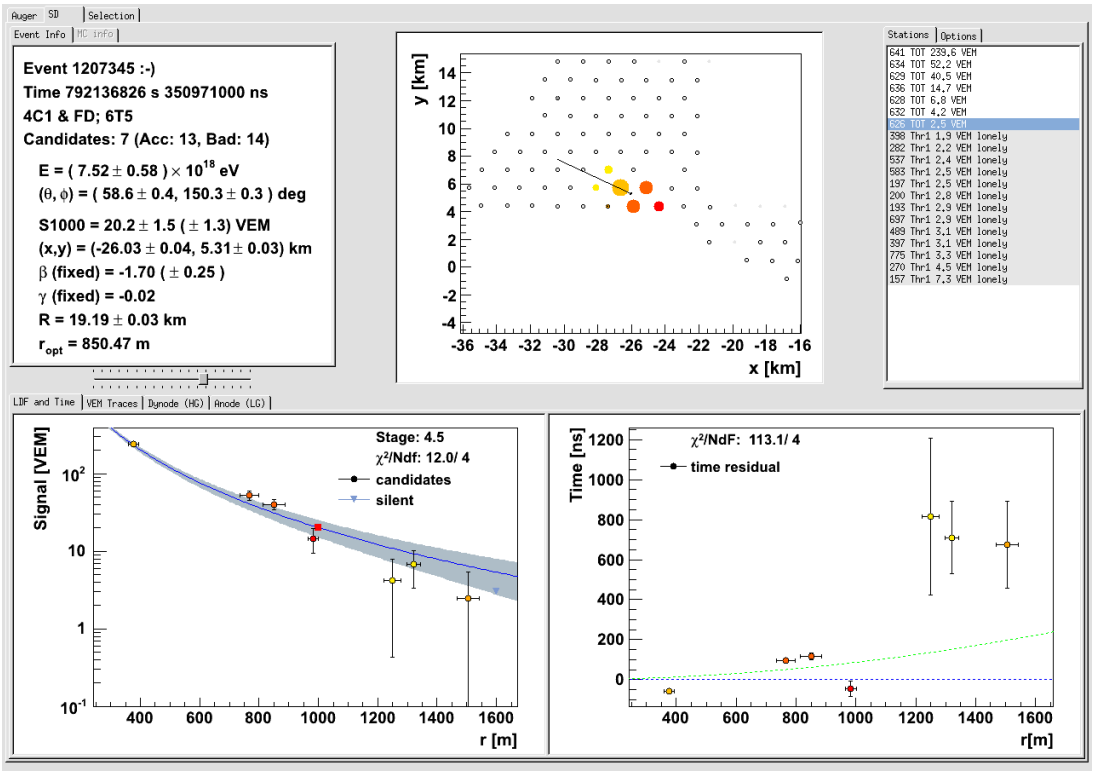

(a) SD Event 1207345 affected by the presence of an accidental signal.

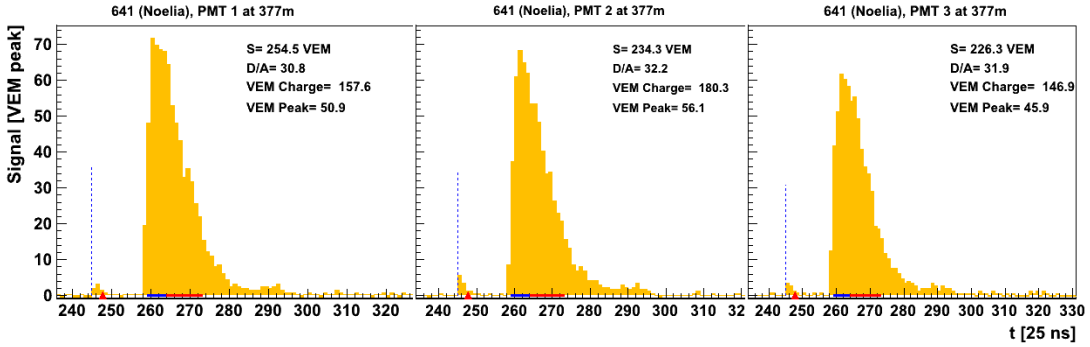

(b) FADC traces of the three photo-multipliers placed at the station affected by the accidental signal.

Figure 4.2: Example of real data event (SD ID 1207345) recorded with the surface detector array affected by an accidental signal. Figure 4.2a shows the results of the standard event reconstruction using the seven selected stations. Figure 4.2b shows the FADC traces of the three PMTs of the station affected by the accidental signal (station ID 641). The signal start time (indicated by the dashed lines) is given by the accidental signal.

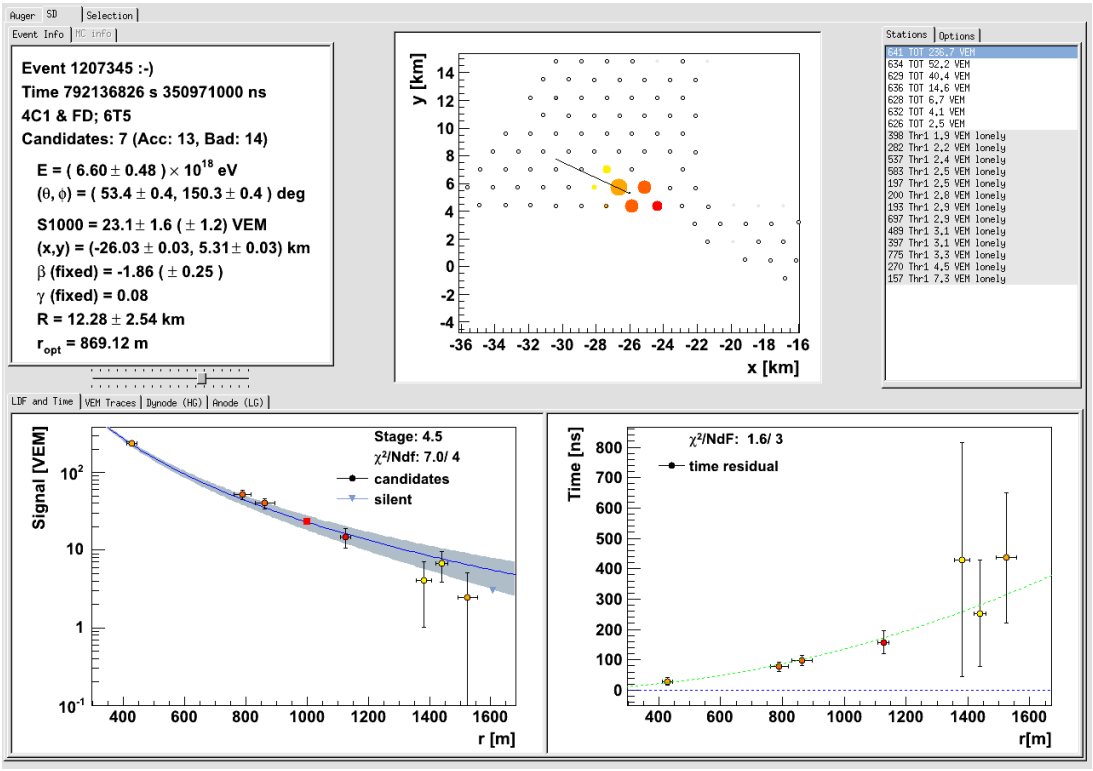

(a) SD Event 1207345 after accidental signal correction.

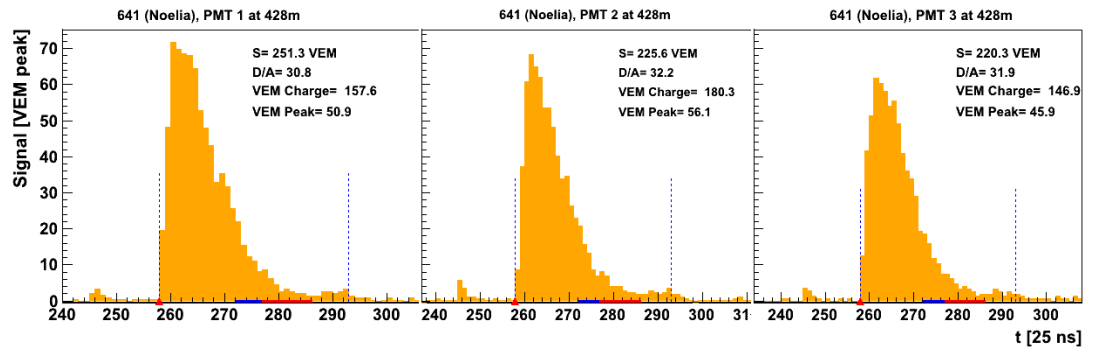

(b) FADC traces and start times of station 641 after accidental signal correction.

Figure 4.3: Same event as shown in figure 4.2 after the accidental signal correction made by the *SdTopDownSignalSelectorUGR* module. The start times of PMTs in station ID 641 (dashed vertical lines in bottom plot) are fixed and the angular reconstruction improved.

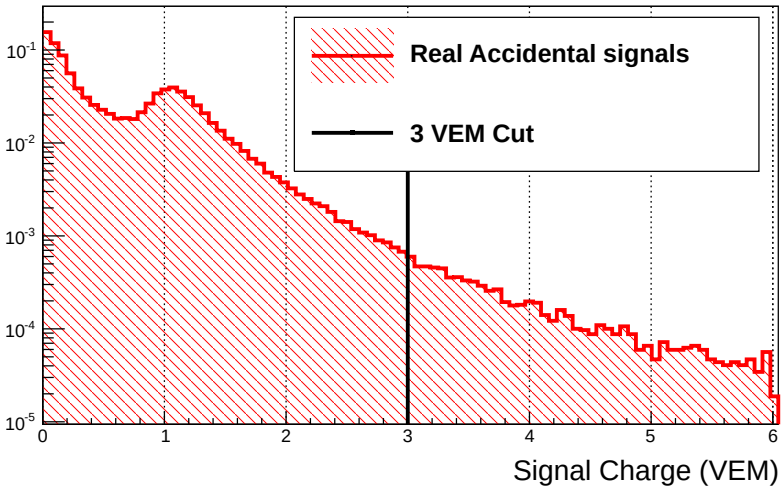

Figure 4.4: Charge distribution of true accidental signals recorded in SD stations and extracted from real data events [161]. The muon bump appears clearly above a background and peaking at ∼1 VEM. Stations with a total charge smaller than 3 VEM are excluded from the analysis (see text for details).

number of stations is below 6. As shown in figure 4.4 this selection rejects most of the stations affected by accidental signals, the impact on the angular resolution being smaller than 0.1°.

Figure 4.3 shows the result of applying the accidental signal rejection algorithm on the event depicted in figure 4.2. In this example, the correction of the signal start times in station 641 shifts the reconstructed angle by −5° improving the residual fit. The use and technical details of the module are reported in section B.2.

4.2.3 Angular Reconstruction Chain

The angular reconstruction is one of the pillars of this analysis. It is performed in various stages by the modules *SdPlaneFitOG* and *LDFFinderKG*. Additionally, the *LDFFinderKG* module allows the energy reconstruction of the shower from the lateral distribution of signal as mentioned in section 2.2. Nevertheless, the energy reconstruction of the incoming neutrino can not be performed and the energy of the shower is not used in the current analysis due to different reasons. First, depending on the nature of the first interaction, the fraction of energy carried by the induced EAS can be very different. Moreover, the possibility of the neutrino to interact at different deeps in the atmosphere introduces an extra parameter of dependence that is not taken into account in the current energy reconstruction algorithms. In addition, the *LDFFinderKG* module uses a lateral distribution function based on an approximation of the NKG formula. The NKG treatment is not accurate for inclined showers above 60° of zenith angle. An alternative energy reconstruction can be performed for inclined showers. It relies on the number of muons at ground, but the large amount of electromagnetic component of neutrino induced shower makes this treatment unusable.

Regarding the angular reconstruction, it is performed as follows. A shower track (see figure 4.5) can be visualized as a point $\vec{x}(t)$ moving with the speed of light c along the straight line with axis $\hat{a}$ (normalized), and hitting the origin at time t_0,

$$-\hat{a}(\vec{x}(t) - \vec{b}) = c(t - t_0). \tag{4.1}$$

The signal-weighted barycenter of the stations involved in the fit is set as the *origin* $\vec{b}$ from where all the distances are measured. Similarly, the weighted bary-time is set as time origin. The initial

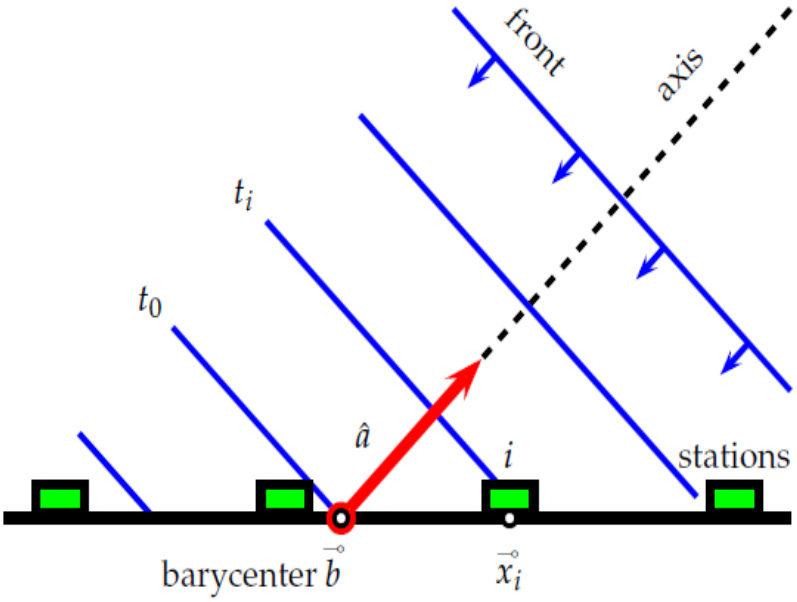

Figure 4.5: Schematic of the plane front arrival.

shower *impact point* on the ground is equal to the weighted barycenter (origin). But subsequently is replaced by more accurate estimations.

The *shower plane* is a plane perpendicular to the shower axis (first rough approximation to the shower front), moving along with the same speed and containing the shower forehead. To infer on the time $t(\vec{x})$ when the shower plane is passing through some chosen point $\vec{x}$ (on the ground), the point is projected to the shower axis,

$$ct(\vec{x}) = ct_0 - (\vec{x} - \vec{b})\hat{a} \tag{4.2}$$

Let us assume that the positions of the stations are given with absolute precision and the only deviations can be due to the time uncertainty σ_t of the signal start. The function to minimize is thus the squares of the time differences between the measured signal start and the model (4.2) time prediction

$$\chi^2 = \sum_i \frac{[t_i - t(\vec{x}_i)]^2}{\sigma_{t_i}^2} = \sum_i \frac{[ct_i - ct_0 + \vec{x}_i\,\hat{a}]^2}{c^2\sigma_{t_i}^2} \tag{4.3}$$

with $\vec{x}_i = \vec{x}_i - \vec{b}$ the position and t_i the signal timing of the station i with variance $\sigma_{t_i}^2$.

Writing the axis with $\hat{a} = (u, v, w)$, the station coordinates with $\vec{x}_i = (x_i, y_i, z_i)$, and $c\sigma_{t_i} = \sigma_i$, we are left with

$$\chi^2 = \sum_i \frac{[ct_i - ct_0 + x_i u + y_i v + z_i w]^2}{\sigma_i^2} \tag{4.4}$$

Note that with the functional χ^2 also a constraint

$$u^2 + v^2 + w^2 - 1 = 0 \tag{4.5}$$

is inherited. Due to this constraint, the problem is obviously not linear (easily seen when $w = \sqrt{1-u^2-v^2}$ is inserted into the χ^2 expression).

Nevertheless, an approximate solution can be obtained from the simplified linear model. If all stations lay close to some plane, then $z_i \ll x_i, y_i$. So, the z-component is neglected and the linear χ^2 is obtained.

The approximate solution can serve as a starting point to more elaborate fitting attempts. It can fail only in one case, when a linear dependence of the (z-projected) station positions is found (as when having three stations in a line). For higher station multiplicity the occurrence of such a situation is highly improbable.

A more realistic shower front model is based on a curved front fit. It extends the plane fit method with a parabolic term that describes the curvature of the shower front near the impact point $\vec{c}$, i.e. $\rho \ll R_c$. Using $\vec{x} = \vec{x}^{\circ} - \vec{c}$, we extend Equation 4.2 to

$$ct(\vec{x}) = ct_0 - \hat{a}\,\vec{x} + \frac{\rho(\vec{x})^2}{2R_c} \tag{4.6}$$

with perpendicular distance $\rho(\vec{x})^2 = (\hat{a} \times \vec{x})^2 = x^2 - (\hat{a}\,\vec{x})^2$. But, in order to obtain the first approximation to the radius of curvature let us first consider a slightly different model.

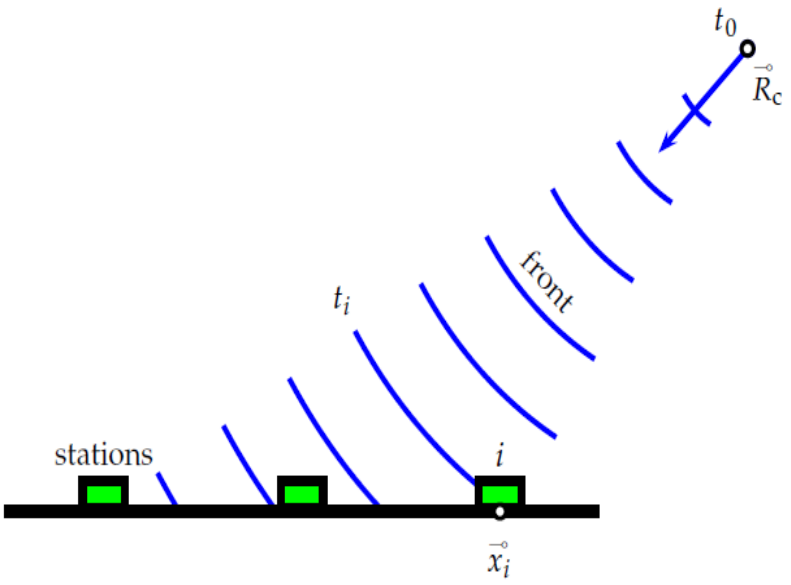

Figure 4.6: Schematic of the spherical shower front development.

The shower development is approximated as starting at time t_0 from one single point (see figure 4.6) and propagating towards the stations, so the timing t_i at the station i is

$$c(t_i - t_0) = |\vec{R}_c - \vec{x}_i| \tag{4.7}$$

with $\vec{R}_c$ the apparent origin of the shower. Time propagation of the shower front is thus described as an expanding sphere. In this form the timing information is clearly decoupled from any information on the impact point. The only relevant geometrical parameter of the spherical model is the apparent origin of the shower $\vec{R}_c$. The shower axis is a derived quantity obtained only after the position of the impact point is known. The spherical model thus effectively separates the timing and LDF fit.

The expected solid angle differences between the plane-fit and curvature-fit axis $\hat{a}$ are of the order of a half degree.

The exact curvature fit involves a 3D minimization of a function

$$\chi^2 = \sum_i \frac{[c(t_i - t_0) - |R_c\hat{a} - \vec{x}_i|]^2}{c^2\sigma_{t_i}^2} \tag{4.8}$$

with accurate $z_i \neq 0$ treatment.

The differences to the approximate estimation of R_c and this one are about 10 m, while the solid angle difference between the axes is of the order of a few 0.1°.

In all start-time related issues the intrinsic time variance model [162] is used by default. In this model the number of particles (muons) n in the signal is estimated from VEM station signal S, corrected for the zenith angle dependence of the average track length $\bar{\ell}$,

$$\bar{\ell}(\theta) = \frac{V}{A(\theta)} = \frac{\pi r^2 h}{\pi r^2 \cos\theta + 2rh\sin\theta} \tag{4.9}$$

and the number of particles is

$$n = S\,\frac{\bar{\ell}(0^\circ)}{\bar{\ell}(\theta)} = S\,[\cos\theta + (2h/\pi r)\sin\theta] \tag{4.10}$$

where h and r are tank height and radius, respectively.

Posterior Trigger Selection

The shower reconstruction ends with the *SdEventPosteriorSelectorOG* module, which computes the 6T5 *posterior* trigger requiring the 6 stations of the first crown around the nearest station to the reconstructed axis to be active at the time event. Note that this trigger condition differs from the previous 6T5 criteria since now the station of reference is the one closest to the reconstructed axis. Events not passing this 6T5 *posterior* trigger criteria are rejected.

Finally, all the relevant information of the simulation and the reconstruction process is stored in light files by the *RecDataWriterNG* module.

4.3 Results on the Reconstruction of ν-induced Showers

In this section we report on the performances of the reconstruction of ν induced showers in terms of efficiency and angular resolution. Figure 4.7 shows the reconstruction efficiency as function of the first neutrino interaction depth and simulated zenith angle. The region of maximum efficiency is well contained inside the range of simulated depths for all angles. On the other hand, figure 4.8 shows the distribution of the reconstructed impact points (shower cores) of the simulated events passing the reconstruction selection criteria. Even though the showers were randomly generated in a square surface using a uniform distribution function, the distribution of reconstructed events is clearly non-uniform: smaller efficiencies are obtained for events with the simulated core very close to a station. This effect has two origins. First, in these cases, the mean distance of the three closest stations to the core is maximized, decreasing the event trigger probability, especially for low energy showers. In addition, the FADC traces of the photo-multipliers in the station closest to the core are often saturated and the station is removed from the analysis, decreasing the performance of the reconstruction algorithm.

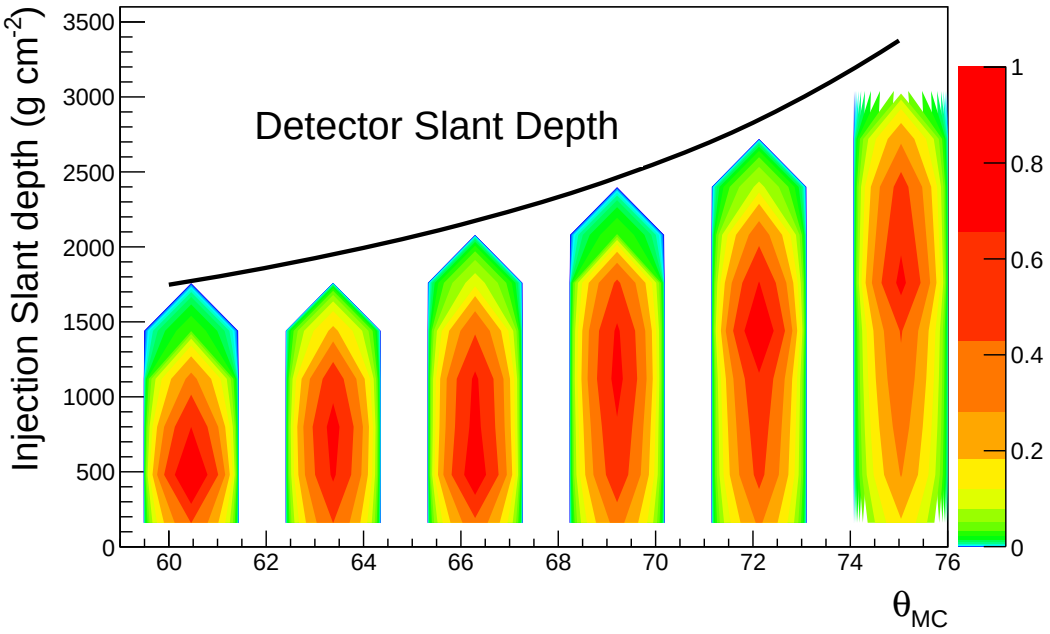

Figure 4.7: Efficiency of reconstructed showers at each injection depth as function of θ_{MC}. Since the values of injection depths and θ_{MC} are discrete, the size of the bins has been increased for a better visualization. The black line shows the detector slant depth. The top of the atmosphere is at 0 g cm^{-2}.

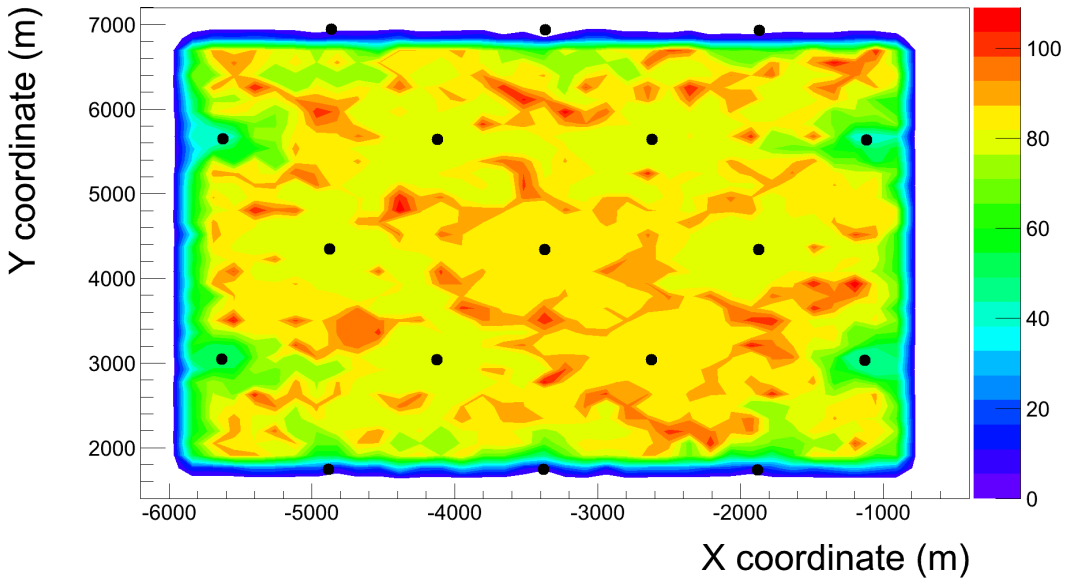

Figure 4.8: Distribution of simulated core positions for all simulated Monte-Carlo events fulfilling the reconstruction criteria. Black dots indicate the locations of the SD stations.

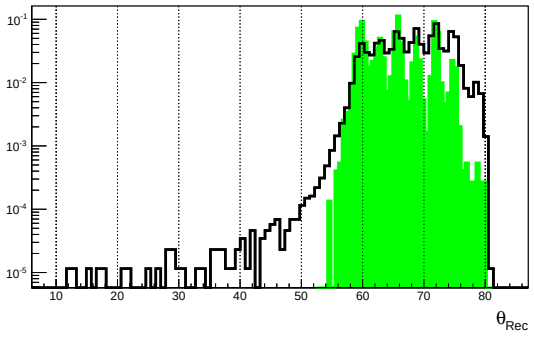

(a) Reconstructed angle for ν_e CC simulated events.

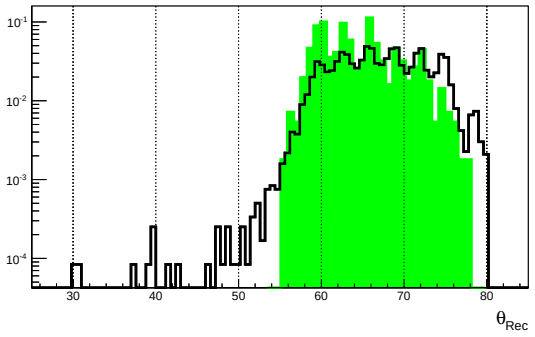

(b) Reconstructed angle for ν_e NC simulated events.

Figure 4.9: Reconstructed zenith angles for the data sets ν_e CC (4.9a) and ν_e NC (4.9b). The open histogram includes all events while the full histogram includes only events interacting high in the atmosphere (interaction slant depth < 300 g cm^{-2}).

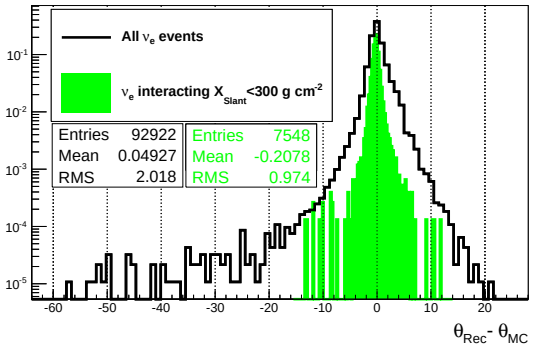

(a) Angular resolution for simulated ν_e CC events.

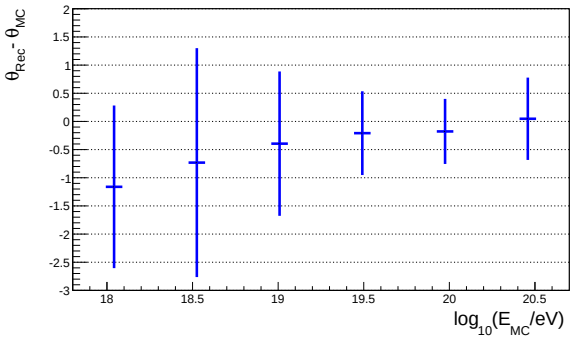

(b) Angular Resolution vs Energy.

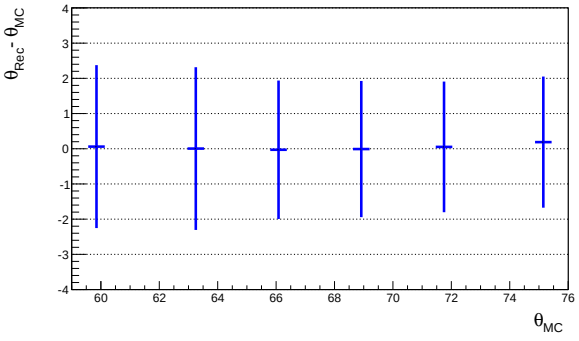

(c) Angular Resolution vs θ_{MC}.

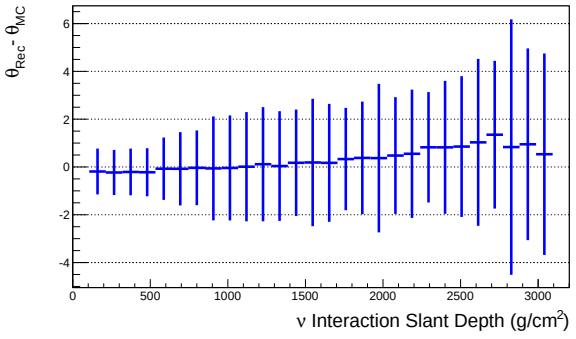

(d) Angular Resolution vs Slant Depth.

Figure 4.10: Results on the angular resolution ($\theta_{\mathrm{MC}} - \theta_{\mathrm{Rec}}$) for simulated ν_e CC showers. 4.10a: Angular resolution distribution. The open histogram includes all events while the full histogram includes only events interacting high in the atmosphere (interaction slant depth < 300 g cm^{-2}). 4.10b, 4.10c, 4.10d: Angular resolution dependence with energy, zenith angle and interaction depth. Top of the atmosphere at 0 g cm^{-2}. Error bars are not on the mean but account for the spread of the distribution.

Figure 4.9 shows the distribution of reconstructed angles for the simulated data set of neutrinos. Six peaks corresponding to the simulated Monte-Carlo angles (table 4.1) are clearly visible. The open histogram containing the full Monte-Carlo data set shows a long tail extending to small values of the zenith angle and produced by neutrinos interacting deep in the atmosphere. These particular neutrinos exhibit a larger curvature of the shower front than verticals ones ($\theta < 60^\circ$), being poorly reconstructed by the standard reconstruction algorithms which are optimized for nucleonic showers initiated in the top of the atmosphere. The tail disappears when only neutrinos interacting at slant depths smaller than 300 g cm^{-2} are represented (full histogram). A worsening of the resolution is observed for neutrinos interacting through the NC channel (figure 4.9b) compared to the ν_e CC events (figure 4.9a), mainly due to the severe reduction of the detectable energy carried by the shower. The impact on the efficiency due to this effect is discussed later in section 5.4.

The angular resolution, defined as the standard deviation of the distribution of differences between the reconstructed and Monte-Carlo simulated zenith angle ($\theta_{\rm Rec} - \theta_{\rm MC}$), is shown in figure 4.10. In the case of the CC channel, the angular resolution is of about 2° when all events are considered (open histogram), whereas for neutrinos injected at a high altitude (full histogram) it improves to $\sim 1^\circ$ (i.e. of the order of the resolution quoted by Auger for standard vertical nucleonic showers). Moreover, the quoted angular bias between the measured and simulated zenith angles is very small (below $\sim 2^\circ$ in all cases).

The evolution of the angular resolution with the energy, zenith angle and interaction depth is shown in figures 4.10b, 4.10c and 4.10d. As expected, the angular resolution improves with the neutrino energy whereas no sizeable dependence on the resolution with $\theta_{\rm MC}$ is observed. On the other hand, both the mean and the spread of the distribution (shown by the error bars) of the angular resolution increase with the slant deep of the first neutrino interaction.

5

Identification of ν-induced Showers

This chapter is devoted to the description of the criteria defined to identify neutrino induced showers. The analysis is based on a *blind search* approach to avoid any artificial bias on the choice of the discriminating variables and on the final values of the cuts.

Therefore, to tune the algorithms needed to separate neutrino induced showers from the much larger background of hadronic showers and optimize the numerical values of the cuts, the data sample of real events collected by Auger was divided in two groups (excluding periods of array instability). A fraction of the data, the so called *background training sample*, was dedicated to define the selection algorithms. This is done together with the generated Monte-Carlo neutrino samples detailed in chapter 4, in order to minimize the background contribution by keeping the highest possible signal detection efficiency. The training data, described in section 5.1, are assumed to be overwhelmingly constituted of background showers. Moreover it intrinsically contains, by construction, any kind of physical and detector effects that could be absent in the even most sophisticated Monte-Carlo simulation. The remaining fraction of data events, called *signal search sample*, is not used until the selection procedure is established, and then it is *unblinded* to search for neutrino candidates.

The procedure to select potential neutrino induced showers, based on the inclined and young criteria, is described in section 5.2. The ultimate decision of whether or not a shower becomes a neutrino candidate relies on a Fisher multivariate discriminant method [163], which is fed with several experimental observables obtained from the properties of the shower signals at ground, as reported in section 5.3. The data training sample and the neutrino Monte-Carlo events are injected to the Fisher algorithm as background and signal training samples, respectively. The stability of the analysis against temporal evolutions of the surface detector array is studied in section 5.3.3. Finally, the performances of the whole procedure in terms of neutrino detection efficiencies is discussed in section 5.4.

5.1 The "training" and "search" Event Samples

As mentioned before, the Fisher discriminant method used in this work requires the input of two different samples of events (signal-like and background-like events) that are used to train the algorithm. Signal-like induced showers are obtained from Monte-Carlo simulations as described

in section 4.1.

At the UHEs, the uncertainties on hadronic models, the ignorance of unknown physical processes and the unpredictable detector effects make very difficult a reliable estimation of the background using Monte-Carlo simulations. In addition, the minimum number of simulated showers that would be required to properly populate the tails of the distributions with a statistically significant number of entries is currently unaffordable with the current resources given the high CPU time required for the full simulation of a shower and the huge parameter space present in the neutrino search.

In the absence of a reliable and complete Monte-Carlo simulation of the background processes, the alternative approach consists on the use of a portion of real data events as background estimator. Given the low neutrino fluxes predicted by current theoretical models this sample is assumed to be overwhelmingly, if not completely, made of standard nucleonic background showers. This training data sample should be large enough to ensure that it represents also the search data sample where neutrinos will be searched for and, in particular, that it contains all possible physical and detector effects present in the search data sample. In other words, even though smaller in size the training sample should be like a "twin" of the search sample. On the other hand, a compromise has to be taken on the size of the samples since the larger the training sample the smaller the remaining data sample to search for neutrinos.

In the case of the analysis presented in this work, the background training sample is made by the 20% of the full data sample of events collected by the surface detector array in the period from 01 January 2004 to 31 December 2011, which is equivalent to a full surface detector array composed of 1420 6T5 hexagons recording data continuously during (0.81±0.01) years (see table 5.1). Periods of surface detector instabilities are rejected. The selection of the 20% fraction of events in the mentioned period of time is based on the Auger SD event ID, which must be divisible by 5 to be selected, ensuring a fully randomized sample uniformly distributed in time in which all time dependent detector effects are taken into account.

Concerning the data search sample, only events dated before 31 May 2010 are considered. This date was established by the Collaboration as the end of the blind search period for all published analyses searching for UHEν_s in Auger, namely the downward-going ν channel at high angle, the Earth-skimming ν_τ search and the search for point-like sources of UHEν_s [3, 106] (see also chapters 8 and 9). Given that there is a work in progress within the Pierre Auger Collaboration aiming at combining the three neutrino searches currently in use, and in order to avoid any possible influence on the final criteria of such a combination (that still remains to be defined), the same date for the end of the search sample was fixed.

Therefore, the data search sample is made by showers with Auger identification number non-divisible by 5 in the period from 01 January 2004 to 31 May 2010, which corresponds to an equivalent exposure of (2.21±0.03) years of data recorded with a full surface detector array working continuously. These events are kept unprocessed until the full analysis procedure and selection cuts are defined. Only at this moment the sample is "unblinded" and neutrino candidates searched for (see section 7.1).

5.2 Pre-Selection of Neutrino-like Showers

While hadrons and even photons interact soon after entering the atmosphere, neutrinos can penetrate large amounts of matter and generate a "young" shower close to the SD array. Examining inclined showers enhances the differences between young showers and those produced early in the atmosphere. Young showers are expected to have a significant electromagnetic component at the ground, while the electromagnetic component of nucleonic inclined showers

	Downward-going neutrino search
MC ν training sample	Monte-Carlo simulated events $\theta_{\rm MC} \in [60°, 75°]$ (table 4.1)
	Analysed data period from 01 January 2004 to 31 December 2011
Background training data sample	20% of analysed data $\equiv (0.81 \pm 0.01)$ yr of full Auger equivalent exposure (surface events with ID divisible by 5)
Signal search data sample (*blind*)	80% of analysed data (only up to 31 May 2010) $\equiv (2.21 \pm 0.03)$ yr of full Auger equivalent exposure (surface events with ID non-divisible by 5)

Table 5.1: Training and blind search periods for the search for downward-going neutrino candidates. The equivalent period of time of a full surface detector array is also indicated.

is largely suppressed due to attenuation in the atmosphere. The first step on the analysis is therefore the pre-selection of young and inclined showers, which is done together with a fiducial cut to guarantee a good shower containment inside the SD array. We recall here that exactly the same reconstruction procedure is applied to the background and to the Monte-Carlo ν training samples.

Inclined Shower Selection: Showers are only pre-selected if their reconstructed zenith angle is in the range $58.5° < \theta_{\rm Rec} \leq 76.5°$. This angular window exceeds by $\pm 1.5°$ the minimum and maximum simulated values of $\theta_{\rm MC}$ in order to account for the angular resolution quoted in section 4.3. A further cut on the quality of the angular reconstruction is applied: the absolute error on the reconstructed angle $\Delta\theta_{\rm Rec}$ is required to be smaller than 3°. The efficiency of this cut is 92.0% (80.0%) for ν_e CC (NC) neutrinos. Figure 5.1 shows the distribution of reconstructed angles for the events in the background training sample after these first pre-selection cuts.

Fiducial quality Cut: The aim of this cut is to ensure that the relevant stations that will be further used in the analysis (the ones close to the shower core) are operational and fully contained into the surface array when the shower triggers the detector. This is achieved by imposing the 6T5 trigger condition so that only the events conforming the 6T5 trigger (T5 stations hereafter) are pre-selected. Even in the case that a shower falls at the edge of the SD array and the total footprint is not fully contained, the choice of the 6T5 trigger ensures that the stations carrying the relevant information for the analysis are kept. The impact of the 6T5 cut is a reduction on the number of background events of $\sim$23% almost uniform for all zenith angles (light gray histogram in figure 5.1).

Young Shower Selection: Among the selected showers fulfilling the previous requirements we select those with FADC traces that spread in time, a feature of young showers in the early stage of development. As already described in section 3.2.2, the ToT trigger is indicative of the presence of a high electromagnetic component in the FADC trace and hence of a young shower. The cut requires that at least 75% of the triggered T5 stations have a ToT local trigger. This criteria has a high background rejection efficiency (64.5% in total), specially

at high angles as shown in figure 5.1, while rejecting only 2.5% of the neutrino events.

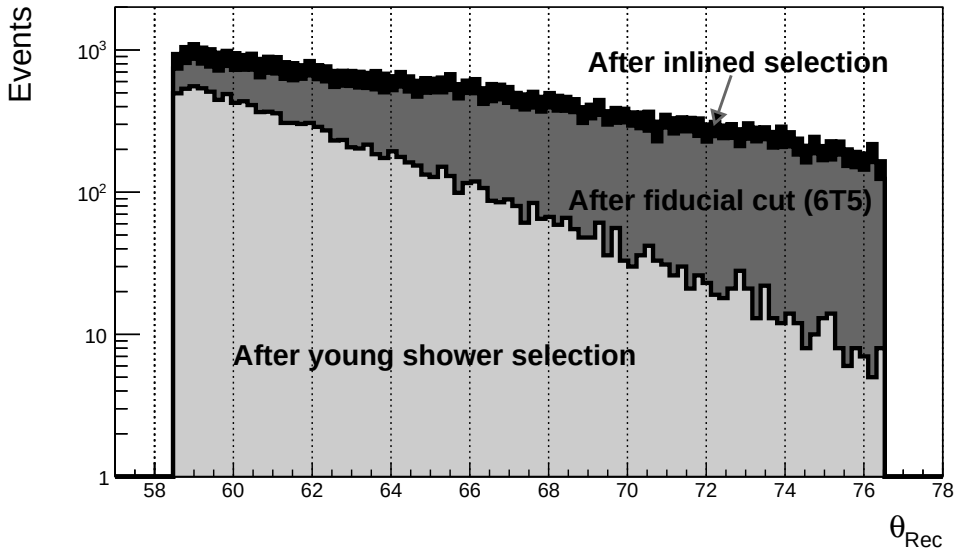

Figure 5.1: Distributions of the reconstructed angle for events in the background training sample passing the pre-selection criteria. Cuts (1) on the reconstructed angle value and error, (2) on the shower containment and (3) on the shower age are applied sequentially.

5.3 Identification of Neutrino Events

The final neutrino identification criteria follow the pre-selection cuts. The discrimination power is optimized with the aid of a multi-variate technique known as Fisher discriminant [163]. In this method the event selection is performed in a transformed variable space with zero linear correlation, by distinguishing the mean values of the signal and background distributions. The linear discriminant analysis determines an axis in the correlated hyperspace of the input variables such that, when projecting the output classes (signal and background) upon this axis, they are pushed as far as possible away from each other, while events of a same class are confined in a close vicinity. The linearity property of this classifier is reflected in the covariance matrix of the discriminating variable space C, which can be decomposed into the sum of a within-class matrix W and a between-class matrix B. They respectively describe the dispersion of events relative to the means of their own class and relative to the overall sample means. The elements of the covariance matrix are given by $C_{kl} = B_{kl} + W_{kl}$ where:

$$W_{kl} = \sum_{U=S,B} \langle x_{U,k} - \bar{x}_{U,k} \rangle \langle x_{U,l} - \bar{x}_{U,l} \rangle = C_{S,kl} + C_{B,kl} \tag{5.1}$$

where S and B denote the signal and background samples, respectively, and $\bar{x}_{U,k}$ is the average of a variable $x_{U,k}$ for the sample,

$$B_{kl} = \frac{1}{2} \sum_{U=S,B} (\bar{x}_{U,k} - \bar{x_k})(\bar{x}_{U,l} - \bar{x_l}) \tag{5.2}$$

where $\bar{x}_k$ denotes the average for the entire sample.

Thus the Fisher coefficients F_k are given by:

$$F_k = \frac{\sqrt{N_S N_B}}{N_S + N_B} \sum_{l=1}^{n_{var}} C_{kl}^{-1}(\bar{x}_{S,l} - \bar{x}_{B,l}) \tag{5.3}$$

The Fisher discriminant value $\mathcal{F}$ for an event i is given by:

$$\mathcal{F}_{(i)} = F_0 + \sum_{k=0}^{n_{var}} F_k x_{k(i)} \tag{5.4}$$

where the offset F_0 centres the sample mean $\bar{y}_{Fi}$ of all events (background + signal) at zero, k runs over the variables x_k used to construct the lineal discriminant and F_k is the Fisher coefficient defined in equation 5.3.

By construction of the method, no discrimination at all is achieved when a variable has the same sample mean for signal and background, even if the shapes of the distributions are very different. The method is implemented within the package *Toolkit for Multivariate Data Analysis with ROOT* (TMVA) [164] which has been used in this analysis.

5.3.1 Building the Fisher: discriminating variables and training

The Fisher method maximises the discrimination power between events of two samples, but the efficiency of the method strongly depends on training the algorithm with the proper variables. A careful and systematic work was carried out looking for the optimal set of discriminating variables, the ones providing the better signal to background (S/B) separation together with a convenient behaviour of the Fisher distribution tail.

The AoP of a station is defined as the total signal of the station trace divided by the peak value. The station trace is defined as the average of the FADC signals of each working PMT belonging to this station. The AoP is very sensitive to the spread on time of the FADC signal trace. It typically peaks at the value of one for pure muonic signals, increasing the value as the electromagnetic component of the trace increases. The power of this variable on discriminating between signal and background events is very strong as shown in figure 5.2.

Out of all triggered stations of an event, the ones closed to the shower core exhibit the highest S/B discrimination power in terms of AoP. The first triggered stations ("early stations") can still contain some electromagnetic component for background events, specially for those arriving at the smaller zenith angles. On the other hand, the electromagnetic component on the last triggered stations ("late stations") can be reduced also for ν-induced showers, in particular at the larger zenith angles (see figure 5.3).

This effect can be visualized in figure 5.4 where the AoP of the stations is represented as function of their distance to the core. Negative (positive) values of the distance to core correspond to early (late) stations. The maximum separation between both samples is reached for distances smaller than 1500 m. T5 triggered stations are typically placed at distances below this value so they are pre-selected as candidates to be included in the Fisher algorithm (regardless of their distance to the core and provided they are not saturated, in which case they are excluded). Moreover, among all triggered T5 stations the earliest ones exhibit the best S/B separation as shown in figure 5.5.

Also important is to survey the evolution of the AoP with zenith angle. As shown in figure 5.6 these two parameters are anti-correlated, the S/B discrimination becoming weaker at lower angles. In order to cope with this effect the search angular window $58.5° < \theta < 76.5°$ was split in five sub-regions as indicated by the dashed vertical lines in the figure, and five different Fisher polynomial were trained independently. The first four regions covering the smaller angles

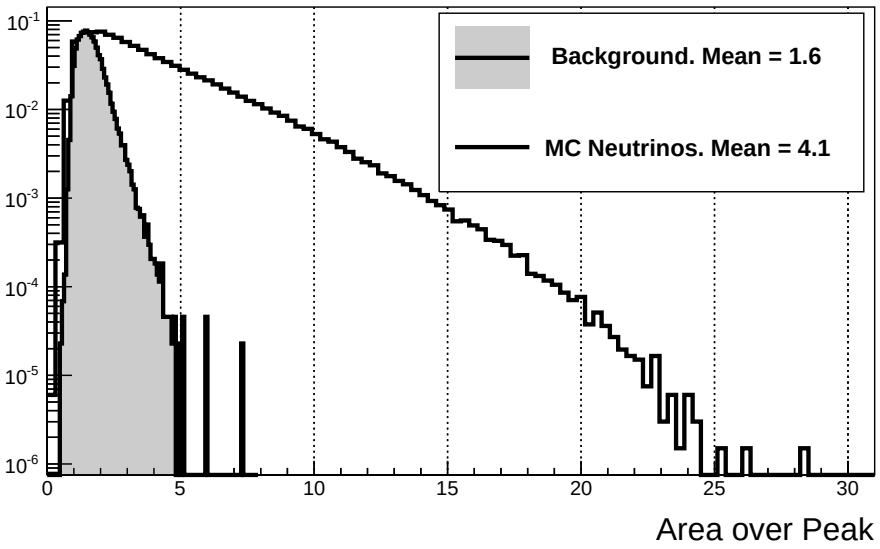

Figure 5.2: Area over Peak distribution for all stations on events passing the pre-selection cuts (inclined + fiducial + young shower criteria described in section 5.2) for the background training sample (full histogram) and for all simulated ν_e CC events (empty histogram).

have a size of 3° whereas the size of the last region is twice this value. The use of five angular regions instead of a single one gives more flexibility to the Fisher algorithms to incorporate the differences observed on the properties of the showers according to their age. This additional degree of freedom certainly increases the performances of the analysis.

On the three regions covering the smaller angles ($58.5° < \theta_{\rm Rec} \leq 67.5°$) where the discrimination becomes more difficult, the first five triggered T5 stations are selected to build the Fisher variables. On contrast, in the higher angular regions ($67.5° < \theta_{\rm Rec} \leq 76.5°$) only the first four T5 stations are used. Finally, the variables selected to be used in the Fisher discriminant analysis are the individual AoP of the selected stations and the product of them. The aim of the product is to break the linearity of the Fisher polynomial allowing a better discrimination power for some of the events. The typical AoP values in the first selected station range between 4 and 6 for deep inclined showers, well above the average value measured in standard nucleonic showers (left-hand panel of figure 5.7). The product of the AoP of the selected stations in the event is also a very good discriminator as shown in the right-hand panel of figure 5.7. The full analysis procedure (pre-selection cuts and Fisher discriminant variables) described in this chapter is summarized in table 5.2.

Once the Fisher variables are defined, the training procedure starts. As earlier described in section 5.1 (see also table 5.1), the signal sample is composed by all Monte-Carlo ν-induced showers whereas the background training sample is made by 20% of the events in the analysed data period (0.81 yr of full Auger SD data). Each individual Monte-Carlo neutrino event is weighted by a factor $\omega = E_{\rm MC}^{-1} \cdot sin(\theta_{\rm MC}) \cdot cos(\theta_{\rm MC})$ which accounts for the different probability of occurrence according to the zenith angle (changes the projection of the detector area in the direction of the shower axis) and the energy (the diffuse neutrino flux and the interaction cross section are function of the primary neutrino energy). In figure 5.8 we show the distributions of the Fisher value $\mathcal{F}$ in the five sub-regions for both, the background training sample and the Monte-Carlo ν showers. An excellent separation is achieved for events in each of the five angular

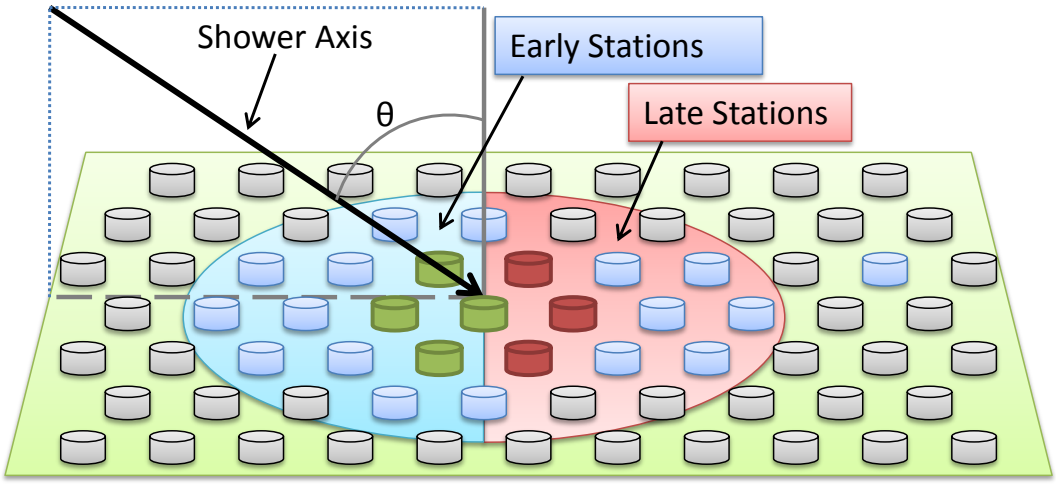

Figure 5.3: Illustration of the footprint of an inclined shower on the SD array. The black line represents the shower axis. The light gray stations are not triggered by the shower and do not participate in the event reconstruction. Stations triggered in the *early* (*late*) stage of the shower development are located before (after) the shower core. Red + green tanks represent the 6T5 stations. Among them, green stations are selected to build the Fisher discriminant.

regions.

5.3.2 Fisher cut and background estimation

The next step after training the Fisher algorithm, is to define a numerical value of the Fisher cut ($\mathcal{F}_{\rm cut}$) that separates neutrino candidates from regular hadronic showers. The criteria adopted in this work was to select the value $\mathcal{F}_{\rm cut}$ such that the number of background events expected after 20 years of data taking with a full Auger SD is 0.2 for each sub-region, i.e. 1 background event expected in the full studied angular region.

In absence of Monte-Carlo background events, the background estimation is done by analysing the shape of the distribution of the largest values of $\mathcal{F}$. The tails of the $\mathcal{F}$ distributions for the five sub-regions shown in figure 5.9 exhibit a clear exponential shape that can be used to

	Region 1	Region 2	Region 3	Region 4	Region 5
Inclined Sel. $\theta_{\rm Rec} \in$	$(58.5°, 61.5°]$	$(61.5°, 64.5°]$	$(64.5°, 67.5°]$	$(67.6°, 70.5°]$	$(70.5°, 76.5°]$
Quality Cuts	6T5 + $\Delta\theta_{\rm Rec} < 3°$				
Young Selection	75% of T5 stations to be ToT				
Fisher Disc. ($\mathcal{F}$)	$\frac{\mathrm{AoP}_n}{\prod_n \mathrm{AoP}_n}$ (n = number of first T5 triggered stations)				
	$n \leq 5$			$n \leq 4$	

Table 5.2: Summary of the pre-selection cuts and variables used to build the Fisher discriminant algorithm in each angular region.

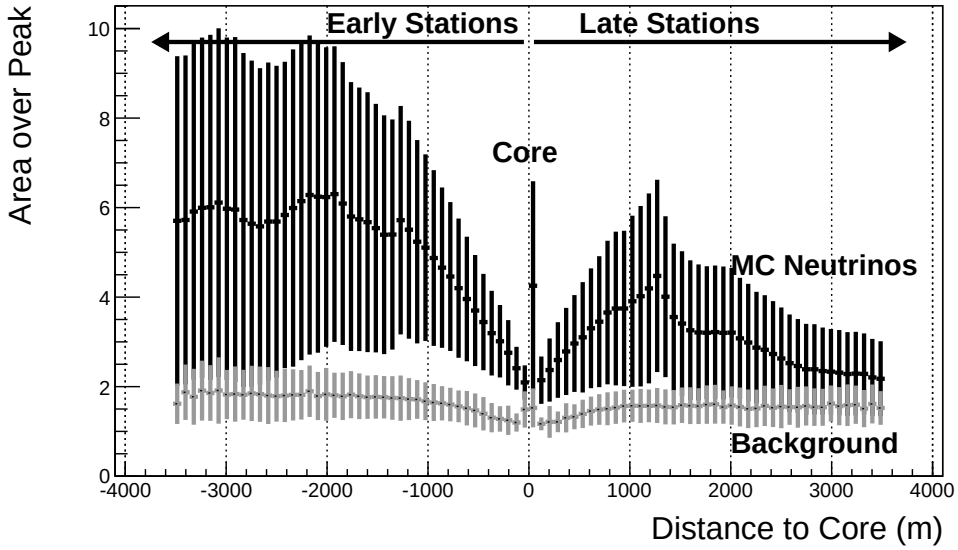

Figure 5.4: Evolution of the AoP of the stations with their distance to the shower core for events fulfilling the pre-selection cuts defined in section 5.2, for the background training sample (light gray) and for all simulated ν_e CC events (black).

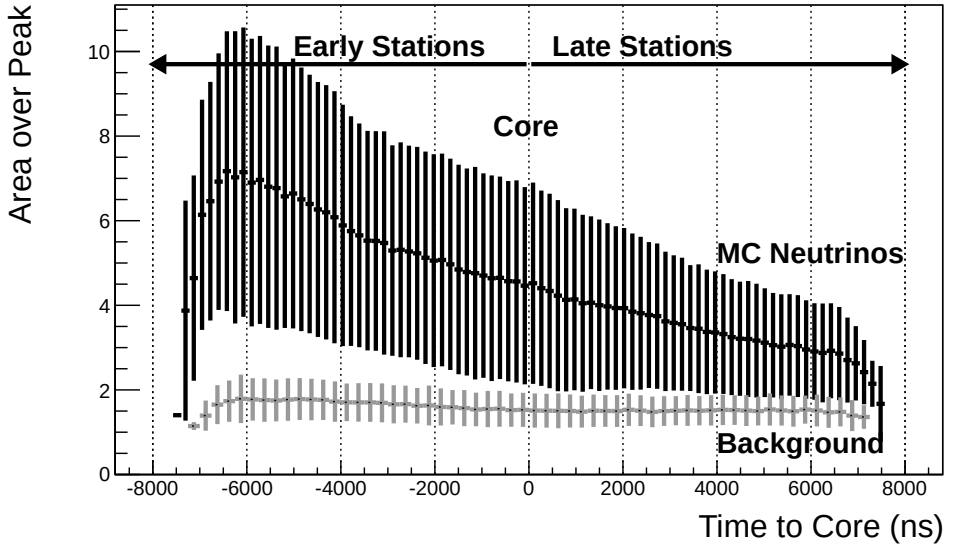

Figure 5.5: Evolution of the AoP of the T5 stations with their relative time to the shower core for events fulfilling the pre-selection cuts defined in section 5.2, for the background training sample (light gray) and for all simulated ν_e CC events (black).

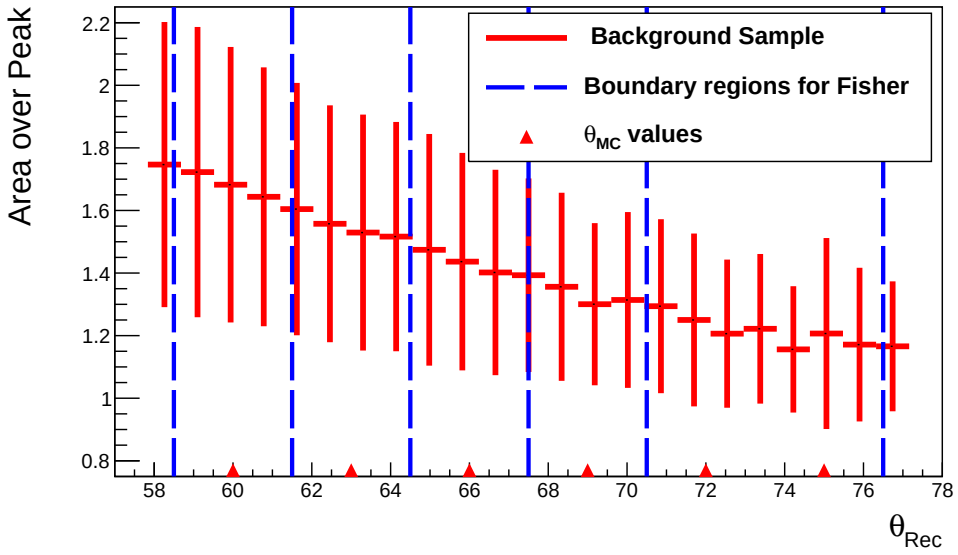

Figure 5.6: Evolution of the AoP of the T5 stations with the reconstructed zenith angle θ_{Rec}. Blue dashed lines delimit the five angular sub-regions in which the analysis is split. The small triangles indicate the θ_{MC} simulated values.

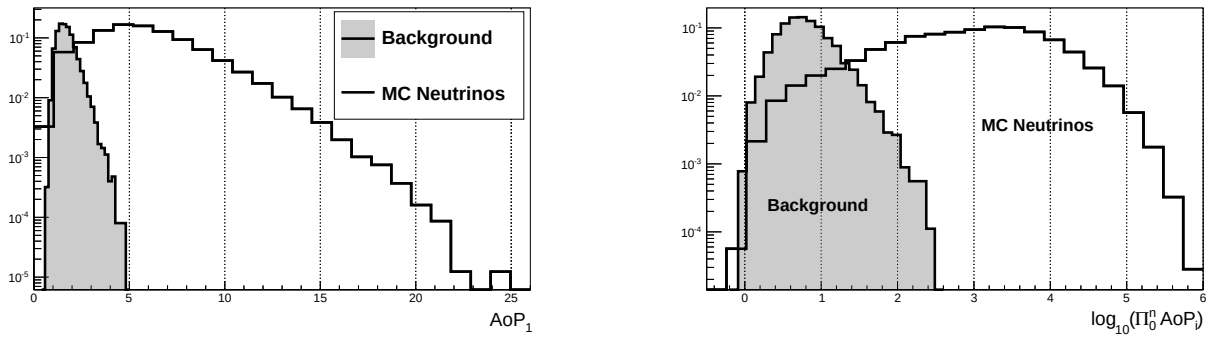

(a) AoP of the first triggered T5 station.

(b) Product of AoP of selected stations.

Figure 5.7: Distribution of the Area over Peak of the first T5 station (left) and of the product of the AoP of the selected stations (right). In each panel we show the distribution of the corresponding variable in background events, i.e. data events in the training sample (full histograms), and in simulated electron neutrino charged current events (empty histograms). These are two of the variables used in constructing the multi-variate Fisher discriminant linear polynomial to optimize the separation between background and neutrino-induced showers.

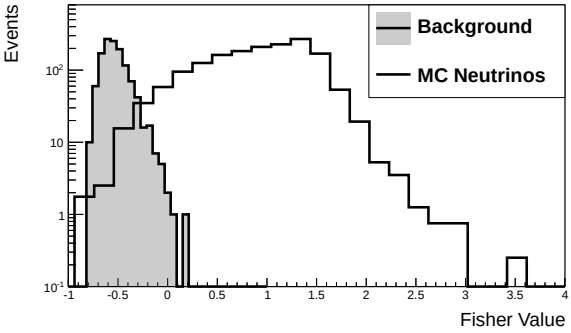

(a) $58.5^\circ < \theta_{\mathrm{Rec}} \leq 61.5^\circ$

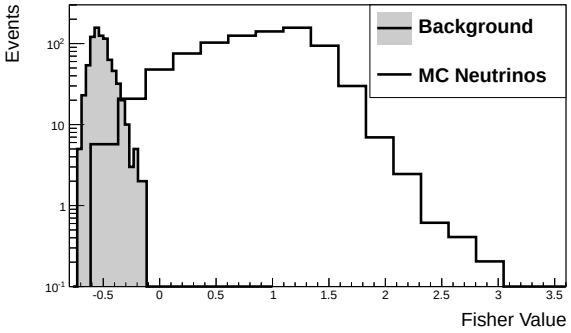

(b) $61.5^\circ < \theta_{\mathrm{Rec}} \leq 64.5^\circ$

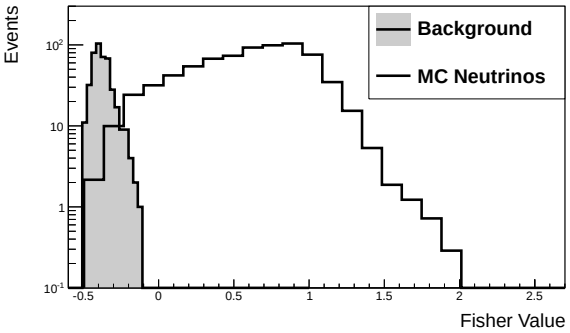

(c) $64.5^\circ < \theta_{\mathrm{Rec}} \leq 67.5^\circ$

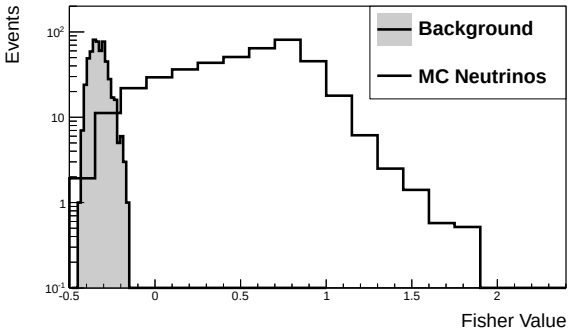

(d) $67.5^\circ < \theta_{\mathrm{Rec}} \leq 70.5^\circ$

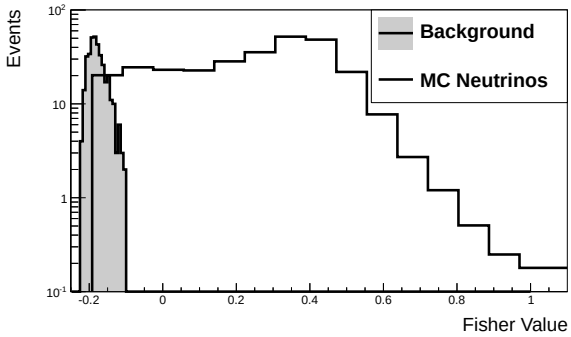

(e) $70.5^\circ < \theta_{\mathrm{Rec}} \leq 76.5^\circ$

Figure 5.8: Distribution of the value of the Fisher polynomial ($\mathcal{F}$, see text for details) for events with reconstructed zenith angle in the five sub-regions. Data in the training period (see Table 5.1) describe the nucleonic background, while Monte-Carlo simulated downward-going neutrinos correspond to the signal.

	Number of events in $\mathcal{F}$ distribution tails: "Observed" - "Predicted"				
	Region 1	Region 2	Region 3	Region 4	Region 5
$\mu + 1\sigma$	277 - 270.3	120 - 110.0	70 - 74.7	121 - 112.7	72 - 71.9
$\mu + 2\sigma$	91 - 89.8	42 - 41.2	25 - 27.4	31 - 35.6	24 - 29.5
$\mu + 3\sigma$	16 - 17.2	12 - 15.4	7 - 10.1	4 - 11.2	2 - 9.0
$\mu + 4\sigma$	4 - 5.7	2 - 3.5	1 - 3.7	0 - 3.5	0 - 3.7
$\mu + 5\sigma$	1 - 1.9	0 - 1.3	0 - 1.4	0 - 1.1	0 - 1.5
$\mu + 6\sigma$	0 - 0.6	0 - 0.3	0 - 0.5	0 - 0.5	0 - 0.6

Table 5.3: Number of events "observed" in the background training sample (full histograms in figure 5.9) and "predicted" by the exponential tail assumption (solid lines in figure 5.9). The reported number of events in each row is computed by integrating the tail of the distributions starting from the value indicated in the first column.

estimate the number of expected background events in each region as function of $\mathcal{F}_{\rm cut}$ and of the years of data taking. In all cases, the training samples lack statistics beyond a certain value of $\mathcal{F}$ (around $\mathcal{F} > -0.1$ in figure 5.9e, for instance) and the exponential fit can be only considered as a reasonable guess of how the tail of the background distribution would behave if more statistics would be added.

In practice, the calculation of the exponential shape is done through a fit to the tail of the distributions in logarithmic scale ($A \cdot \mathcal{F} + B$), starting at the bin located at $\mu + \sigma$ and ending at the last bin containing events (non-empty bin), where μ and σ are the mean and the RMS of the $\mathcal{F}$ distribution. Even though marginally, the histogram bin size can influence the estimated fit parameters due to the low statistics populating the tails. The final bin size assumed in each case was determined by these values minimizing the residual fit. In table 5.3 we give, for the five angular regions, the number of events *observed* in the tail of the background training sample and the number of events *predicted* by the exponential fit. The numbers in each row are computed by integrating the most right part of the $\mathcal{F}$ distribution starting from the value indicated in the first column. The estimation given by the exponential fit is in good agreement when the number of events is high, and slightly overestimates the observed number of events in the extreme regions of highest $\mathcal{F}$ values, where predictions are more difficult due to the absence of statistics.

In order to account also for the uncertainties on the obtained exponential fit parameters (σ_A and σ_B), the tail of the $\mathcal{F}$ distribution is finally assumed to be represented by a function that includes the fit errors, $[A + \sigma_A] \cdot \mathcal{F} + [B + \sigma_B]$, a conservative approach which slightly increases the predicted number of background events. Figure 5.9 shows the $\mathcal{F}_{\rm cut}$ values obtained following the procedure described before for the five sub-samples of background events. The number of expected background events estimated to pass the $\mathcal{F}_{\rm cut}$ cut after 20 years of data taking with a full SD array is 0.2 on each sub-sample.

A two dimensional view of the Fisher values as function of the zenith angle is given in figure 5.10. The contour plot represents the number of Monte-Carlo ν signal events passing the pre-selection cuts, the black dots are the background training events and the horizontal blue lines represent the value of $\mathcal{F}_{\rm cut}$ determined previously. The discontinuities observed in the sub-samples reflect the fact that different Fisher discriminants achieving different selection efficiencies are used at each angular region. As expected, the background events with higher $\mathcal{F}$ value in each region tend to accumulate near the lower angular edge. In other words, the number of background events in a given region is observed to be non-uniformly distributed inside the

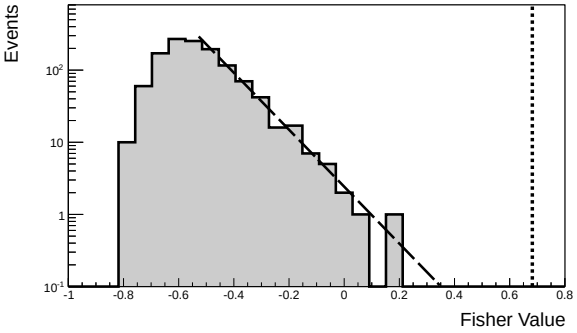

(a) $58.5^\circ < \theta_{\rm Rec} \leq 61.5^\circ$

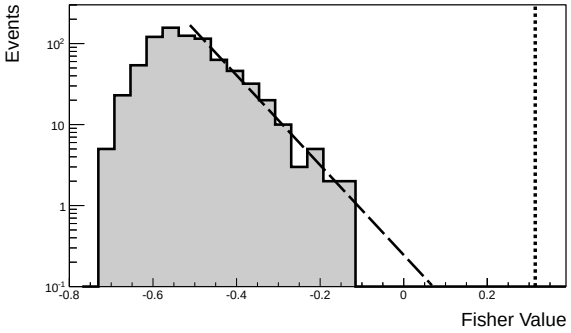

(b) $61.5^\circ < \theta_{\rm Rec} \leq 64.5^\circ$

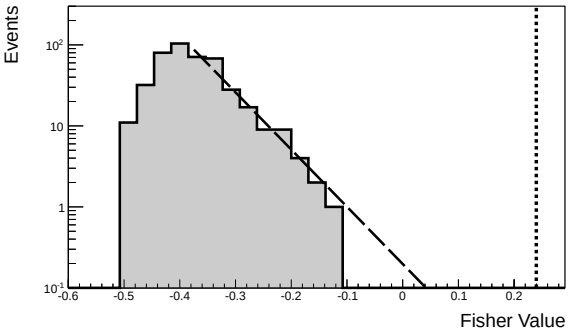

(c) $64.5^\circ < \theta_{\rm Rec} \leq 67.5^\circ$

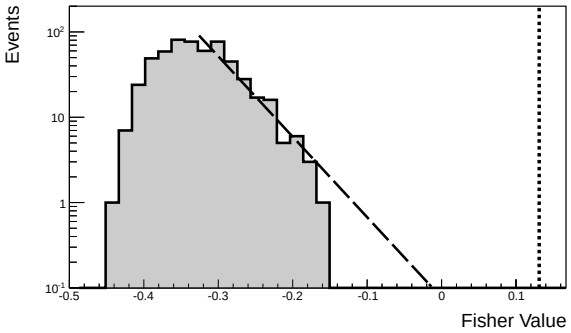

(d) $67.5^\circ < \theta_{\rm Rec} \leq 70.5^\circ$

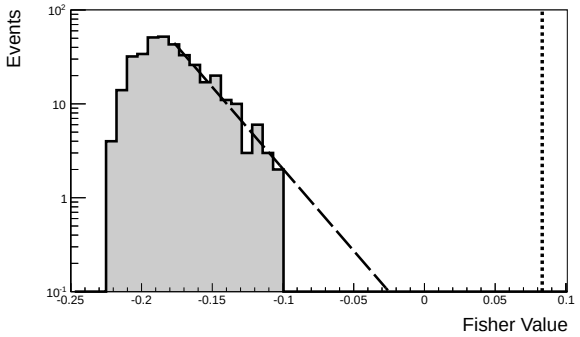

(e) $70.5^\circ < \theta_{\rm Rec} \leq 76.5^\circ$

Figure 5.9: Distribution of the $\mathcal{F}$ value for the background training sample (0.81 yr of full Auger SD data) and exponential fit to the tail (solid line). The vertical dashed lines indicate the value of the Fisher cut ($\mathcal{F}_{\rm cut}$) needed to expect 0.2 events in each sub-sample in 20 years of data taking by a full Auger SD.

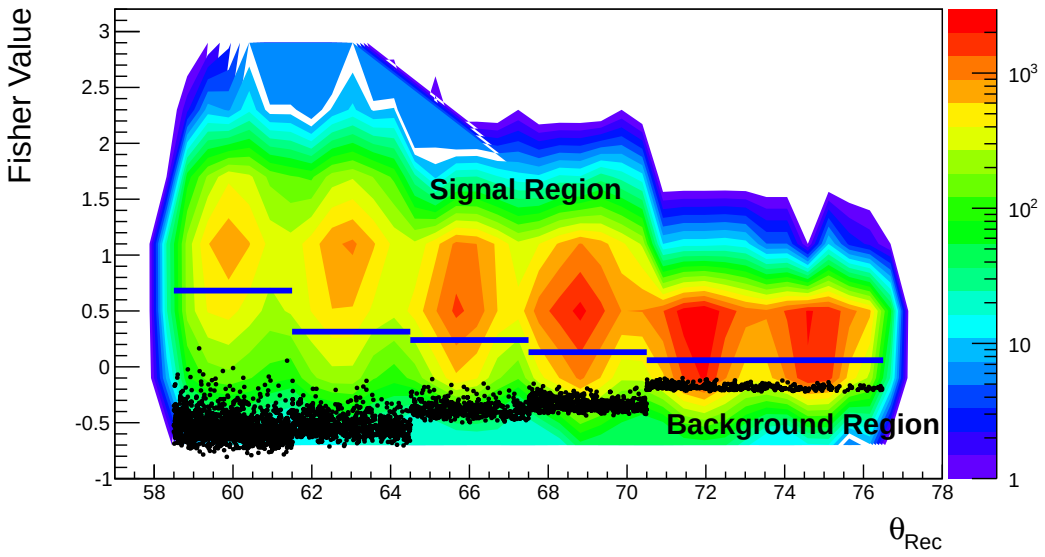

Figure 5.10: Distribution of $\mathcal{F}$ as function of the reconstructed zenith angle. The MC ν events (contour plot), the background events (black dots) and the discrete $\mathcal{F}_{\text{cut}}$ values at each sub-region (blue lines) are displayed.

angular interval.

Rather than a fix $\mathcal{F}_{\text{cut}}$ for each region, a more natural and effective cut results from the lineal interpolation of the five $\mathcal{F}_{\text{cut}}$ values over the full angular region as shown in figure 5.11. The result is a Fisher cut which depends discretely on θ_{Rec}: events above the line will be considered as neutrino candidates. With such a cut, the events on the tails of the background distributions remain roughly at the same distance from the cut line for each region and the expected number of events is almost constant with the angle.

5.3.3 Time stability of the discriminating variables

In this section we report on the time stability of the most relevant variables used in the ν search analysis. Given that the idea behind a blind analysis like the one proposed in this work is to fix the cuts according to the information provided by the training samples and keep the analysis unaltered (i.e. "frozen") until the end of the data taking, any temporal evolution not present or foreseen during the training procedure might have an influence on the results in a long term experiment like Auger. For instance, the appearance of fake neutrino candidates.

The composition of the background training sample chosen in this work minimizes the impact of possible time instabilities that might appear since it contains selected real data events collected by the Observatory in such a way that they randomly spread over the full data taken period where the neutrinos are searched for. Therefore, they should be representative of the search data sample. In any case, a check to the time evolution of the angular reconstruction, the ToT fraction, the AoP and the Fisher value as obtained from the background training sample remains interesting.

The angular reconstruction is very robust against temporal variations. Even in the case of geographical changes of some stations (i.e. Earth-quake, stations replaced, etc) it uses the real position of the station and the estimated angle should be robust enough. Larger changes could be expected in case the reconstruction algorithms were improved. The systematic uncertainty of

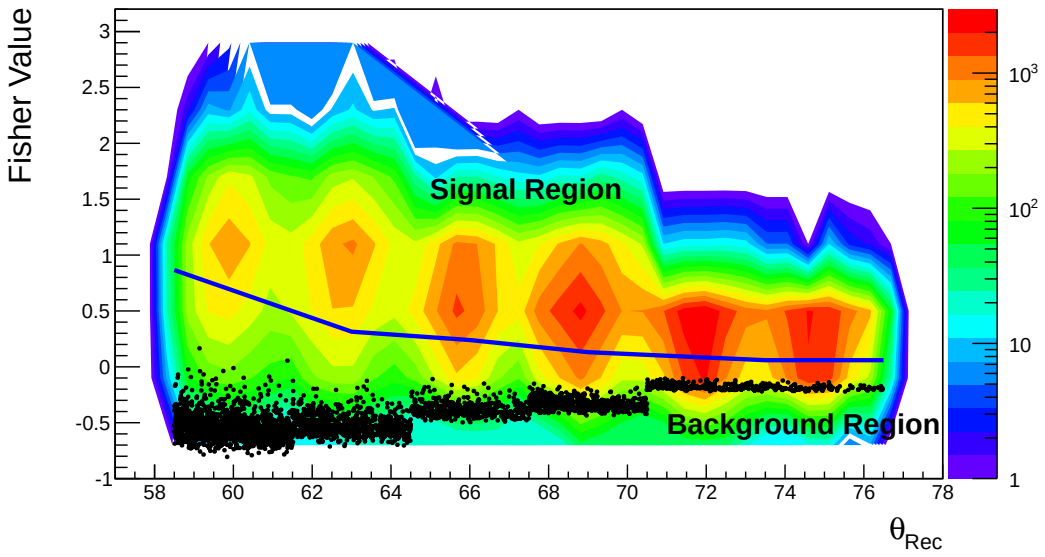

Figure 5.11: Same as figure 5.10 but with continuous $\mathcal{F}_{\text{cut}}$ (blue line) obtained from linear interpolation of discrete values.

different reconstruction procedures is discussed in section 6.2.

The ToT fraction of the T5 triggered station is more likely to be time dependent [165, 166]. Since the ToT criteria is based in a signal threshold, the ToT fraction can be affected by changes in the surface detectors (changes in the liner reflectivity, water absorption length, PMTs and/or electronics ageing, etc). Figure 5.12 shows the ToT fraction of the T5 triggered stations as function of the event ID number. Since event ID numbers are correlative in time, they represent the evolution with time. A decrease with time of the order of 10% in the average value is observed for events taken after 2009. This effect, in case to persist, would degrade the neutrino detection efficiency.

The most important variables on the ν selection are the AoP of the stations (which influences the Fisher) and, of course the Fisher discriminant $\mathcal{F}$. Figures 5.13 and 5.14 show how these two magnitudes behave with time. The AoP shows a smooth modulation which can be related to the already observed effect described in [165, 166]. Nevertheless, this modulation is attenuated in the Fisher variable at low angles and disappears at the highest zenith region. From this result we can conclude that the dependences with time, if any, are very weak and not expected to influence the ν search with the used search data sample.

5.4 Neutrino Identification Efficiency

In table 5.4 we give the summary list of the sequential cuts applied in the analysis and their impact on the selection efficiency of ν_e CC and NC events. Numbers are relative, i.e. computed with respect to the events remaining after the precedent cut in each case. The inclined selection efficiency is calculated with respect to the reconstructed ν events only. The numbers are obtained through Monte-Carlo simulations assuming a full surface detector array (large enough to fully contain all showers, complete and fully operational). In general, the efficiency depends on the neutrino flavour, type of interaction, neutrino energy, zenith angle and slant depth of interaction.

The inclined selection removes $\sim 7\%$ of the reconstructed events in the two channels. These are

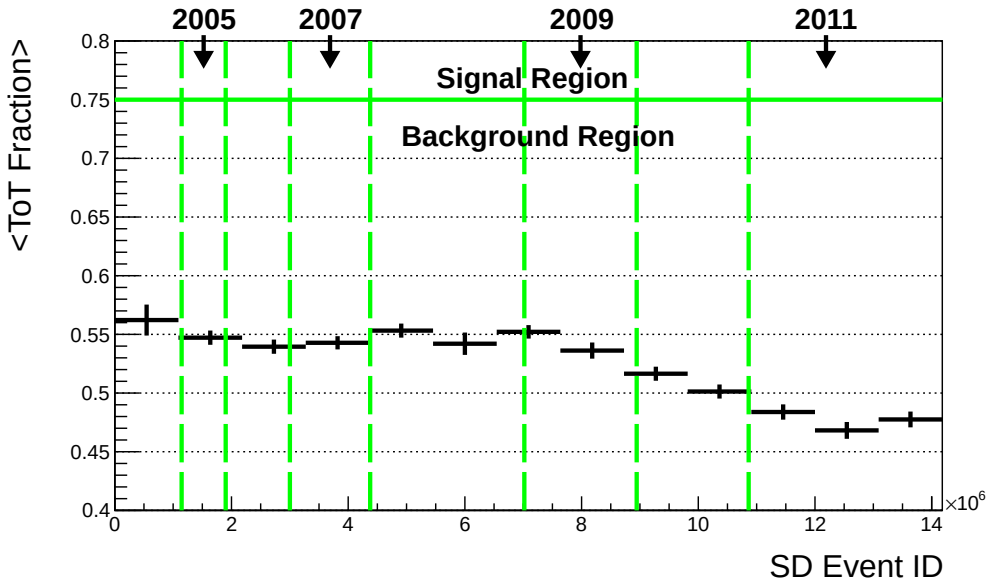

Figure 5.12: Average fraction of T5 stations with ToT trigger in the hexagon as function of the SD event ID. Data from the background training sample.

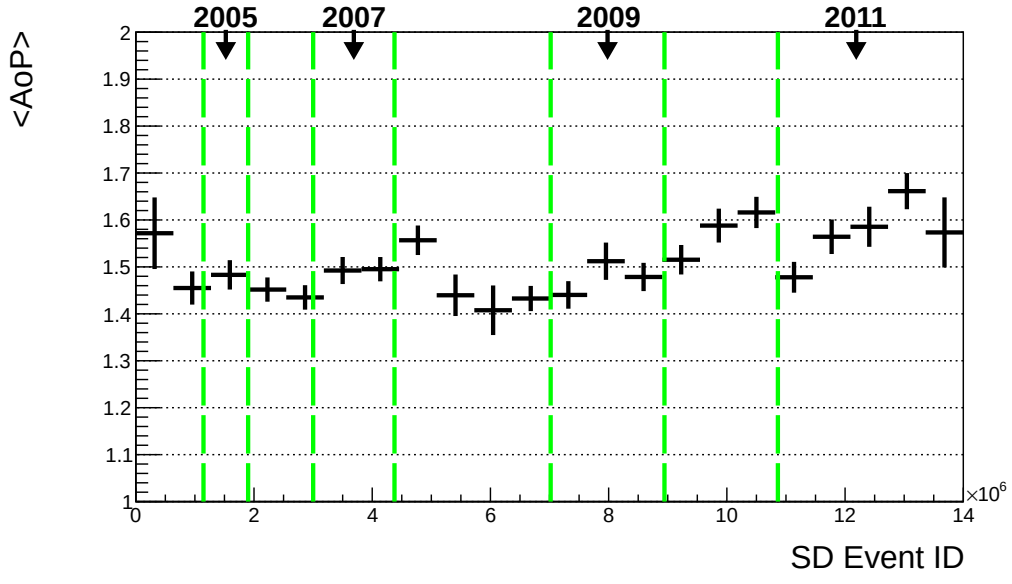

Figure 5.13: Average AoP of the selected Fisher stations as function of the SD event ID. Data from the background training sample.

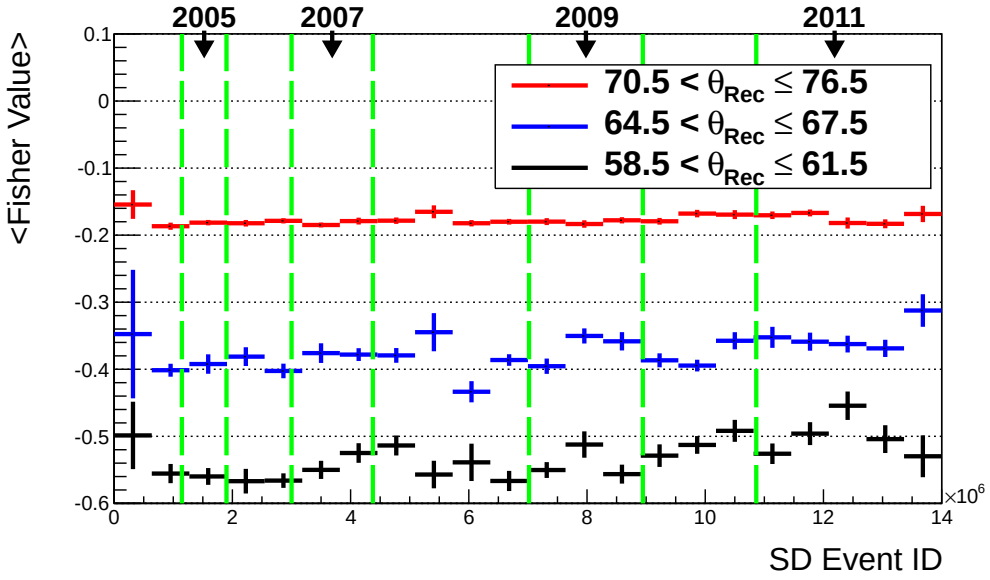

Figure 5.14: Average Fisher value $\mathcal{F}$ as function of the SD event ID. Data from the background training sample.

		Efficiency	
	Cut	CC	NC
Inclined Selection	$58.5 < \theta_{\mathrm{Rec}} \leq 76.5$	94.4%	93.0%
Quality Cuts	6T5 + $\Delta\theta_{\mathrm{Rec}} < 3°$	92.3%	80.4%
Young Shower Selection	75% of T5 stations to be ToT	98.0%	93.6%
Number of T5 triggered Stations	$\geq 5 \; \forall \; \theta_{\mathrm{Rec}} \in (58.5, 67.5]$ $\geq 4 \; \forall \; \theta_{\mathrm{Rec}} \in (67.5, 76.5]$	78.6%	52.7%
Neutrino Selection	Fisher Discriminant $\mathcal{F}_{\mathrm{cut}}$ (linear interpolation in θ_{Rec})	79.6%	40.2%

Table 5.4: Selection efficiencies on Monte-Carlo neutrinos simulated in the charged and neutral current interaction channels (all simulated energies, zenith angles and interaction depths included). Inclined selection efficiency normalized with respect to reconstructed events only. Efficiencies for the other cuts normalized with respect to the events remaining after the precedent cut.

	Relative Efficiency (%)				
Angular Region	$(58.5, 61.5]$	$(61.5, 64.5]$	$(64.5, 67.5]$	$(67.6, 70.5]$	$(70.5, 76.5]$
Quality Cuts	97.8 (97.0)	97.2 (94.9)	95.4 (89.9)	92.0 (80.6)	87.6 (64.7)
T5 Candidates	63.1 (31.0)	62.6 (31.3)	66.3 (31.7)	88.3 (73.9)	91.0 (75.8)
Fisher Selection	71.1 (13.5)	85.1 (33.2)	83.7 (31.6)	84.8 (47.5)	76.0 (44.8)

Table 5.5: Relative efficiency of the three cuts with bigger impact on the ν selection. Values quoted at the five angular regions for ν_e CC (NC) simulated events.

mainly showers interacting very close to ground which populate the tails of the $\theta_{\rm Rec}$ distributions as discussed in section 4.3.

The quality cut on $\Delta\theta_{\rm Rec}$ gives a stronger reduction of NC events than CC events. On average, a clear worsening on the error of the reconstructed angle is observed when the zenith angle increases (figure 5.15a) and also when the shower energy diminishes (figure 5.15b). The tail of the $\Delta\theta_{\rm Rec}$ distribution above the cut (dashed line) is dominated by the contribution from showers for which the reconstruction algorithms are less efficient: low energetic (triggering less stations at ground) and coming at large zenith angles. The quality of the reconstructed showers in terms of $\Delta\theta_{\rm Rec}$ is, however, better for CC than for NC events as shown in table 5.5.

Regarding the requirement on the minimum number of T5 candidate stations, a stronger reduction of surviving events is observed for events below 67.5° due to the more restrictive cut imposed in this low angular region (needed to maintain a small background level). As summarized in table 5.5, the impact of this cut is much stronger in the NC sample due, again, to the smaller number of triggered stations compared to the CC events.

Concerning the Fisher selection cut, the efficiency achieved on the NC channel is about half the obtained on the CC channel. As an example, we compare in figure 5.16a the Fisher distributions for the training sample and for ν_e CC and ν_e NC simulated showers, all in the lower angular region ($58.5^\circ < \theta_{\rm Rec} \leq 61.5^\circ$). The performance of the method to separate the background from NC events is clearly smaller compared to CC events. The $\mathcal{F}$ distribution for the NC sample is sitting between the background and the CC samples. As shown in figure 5.16b, the reason for that can be found on the different behavior of the main variable used to build the Fisher polynomial: the AoP of the stations. Showers in the NC channel exhibit small values of the AoP when initiated in the top of the atmosphere (similar to the values obtained for the background training sample), smoothly increasing for deeply interacting showers. Showers in the CC channel at high zenith angle ($\theta_{\rm MC} > 70^\circ$) exhibit a similar behavior, even though with higher values of AoP (on average) which help on the background discrimination. On the other hand, CC showers at small zenith angles ($\theta_{\rm MC} < 67^\circ$) retain at ground a higher electromagnetic component than more inclined ones, showing an even higher value of AoP (on average) provided the shower is not initiated too deep in the atmosphere.

An example of the efficiency that can be achieved in a full SD array as function of the slant depth of interaction for ν_e CC neutrinos of two energies and zenith angles is shown in figure 5.17. The "T3 trigger + reconstruction" efficiencies almost saturate for $10^{19.5}$ eV showers interacting from the top of the atmosphere up to slant depths of ~ 1800 g cm^{-2}. For primary interaction vertices closer to ground (i.e big values of slant depth) the efficiency dramatically drops since a minimal amount of matter is needed for the ν-induced shower to reach a sufficient lateral expansion which triggers the array and allows an angular reconstruction. On the other hand, the neutrino selection efficiency also drops for $10^{18.5}$ eV showers if the interaction takes place near the top of the atmosphere (low values of slant depth) and the angle is large because the

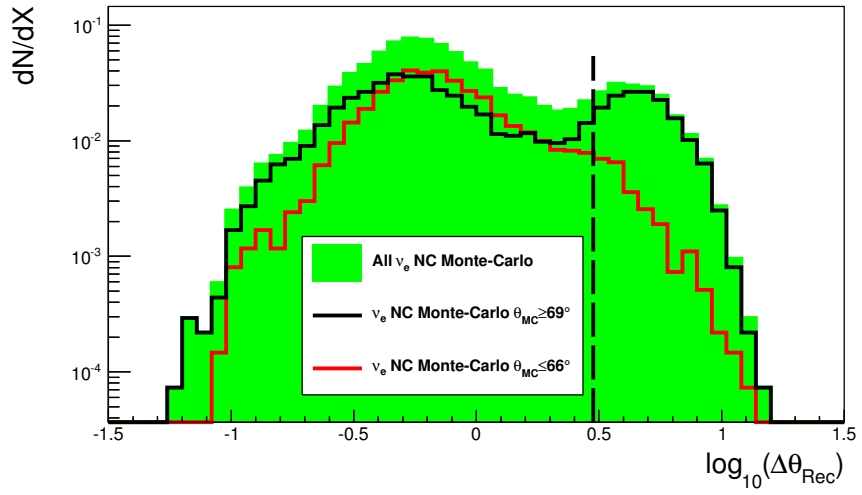

(a) Error on the angular reconstruction for different angles: all ν_e NC showers (full histogram), $\theta_{\mathrm{MC}} \leq 66^\circ$ showers (red histogram) and $\theta_{\mathrm{MC}} \geq 69^\circ$ showers (black histogram).

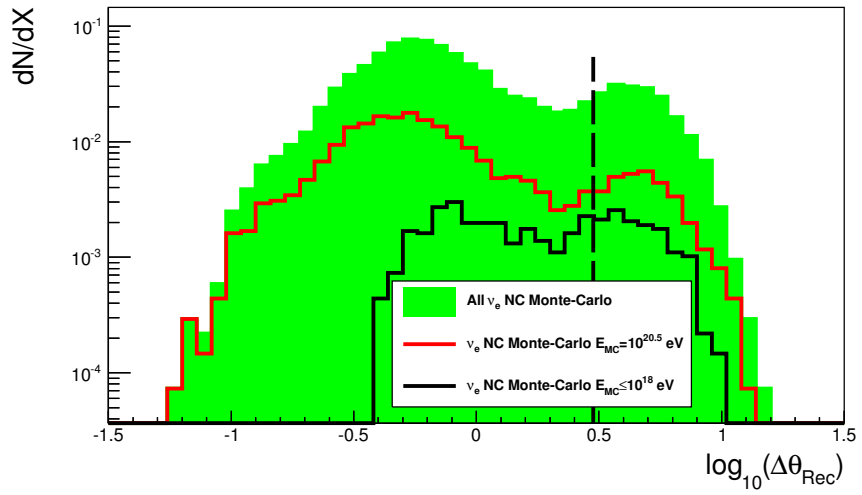

(b) Error on the angular reconstruction for different energies: all ν_e NC showers (full histogram), $E_\nu = 10^{20.5}$ eV showers (red histogram) and $E_\nu \leq 10^{18}$ eV showers (black histogram).

Figure 5.15: Distribution of the absolute error on the reconstructed zenith angle ($\Delta\theta_{\mathrm{Rec}}$) for ν_e NC Monte-Carlo showers for several values of the zenith angle (top) and neutrino energy (bottom).

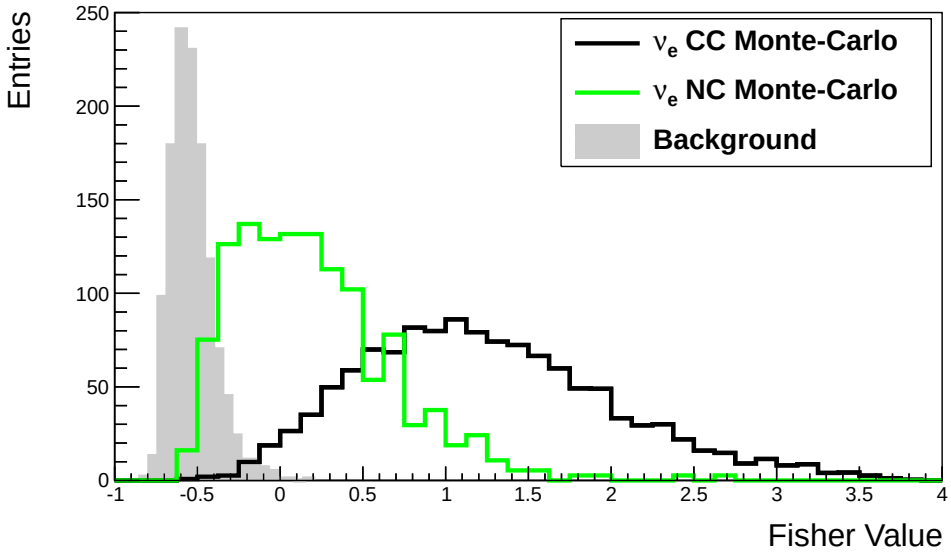

(a) Fisher Value ($58.5° < \theta_{\mathrm{Rec}} \leq 61.5°$).

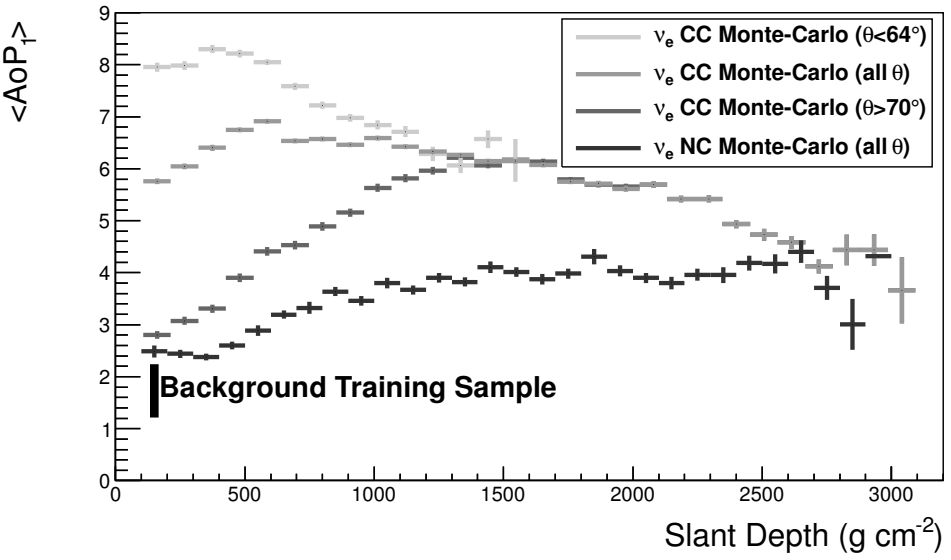

(b) Area over Peak of the first T5 station.

Figure 5.16: Figure 5.16a: Distribution of the Fisher value in the lower angular region for the background training sample (gray shaded histogram), the ν_eNC Monte-Carlo (light histogram) and the ν_e CC Monte-Carlo (black histogram). Figure 5.16b: Average of the AoP of the first T5 station used in the Fisher discriminant as function of the slant depth for all the ν_e NC Monte-Carlo and for the ν_e CC showers in different angular regions. The background has been shifted to 150 g cm^{-2} for a better visualization.

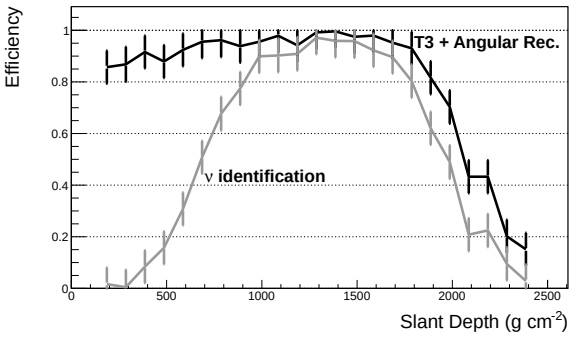

(a) $\log_{10}(E_\nu/\text{eV}) = 19.5$, $\theta_{\text{MC}} = 72°$.

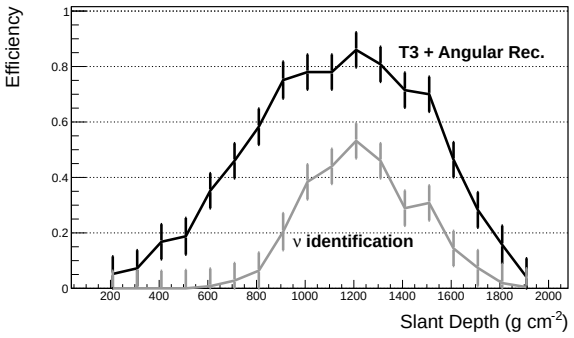

(b) $\log_{10}(E_\nu/\text{eV}) = 18.5$, $\theta_{\text{MC}} = 69°$.

Figure 5.17: Fraction of electron CC neutrinos triggering the array and reconstructed (blue dashed line) and passing all the analysis cuts in table 5.4 (red line) as function of the slant depth of the interaction above the ground. Efficiencies calculated with a full SD array. The top of the atmosphere corresponds to 0 g cm^{-2}. Detector depth at ~ 2500 g cm^{-2}.

electromagnetic component of the shower is almost extinguished at ground level and hence the neutrino cannot be identified with the present criteria. In general, the efficiency as well as the slice of atmosphere where it is different from zero, typically increase with the neutrino energy, and depend on the neutrino flavour and interaction channel. This has an impact on the effective mass of the SD array as discussed in section 6.1.

In figure 5.18 we show the dependence of the ν identification efficiency with the zenith angle for three ν_e CC energies. The increase of the efficiency with energy is clear, reaching maximum values of $\sim 70\%$ for energies above $\sim 10^{19.5}$ eV. The behaviour with zenith angle is smooth in most of the explored range with the peak of efficiency observed at around $\theta_{\text{MC}} \sim 70°$ for all energies. Showers reconstructed with zenith angles above $\sim 73°$ suffer a significant decrease on the ν identification efficiency. This is so because in these very inclined showers the electromagnetic component present on the stations close to the core is smaller than on more vertical ones (it has been partially absorbed), making the discrimination more difficult. In these cases, a better ν identification could be achieved by selecting the earliest triggered stations rather than the T5 ones. As mentioned before in this section, to a lesser extent the drop on efficiency at the highest zenith angles is due to the cut on the reconstruction error $\Delta\theta_{\text{Rec}}$ which removes more signal events at higher zenith angles (we remind here that the angular reconstruction algorithm used in this work is not optimized for very inclined showers). A similar behavior, with a reduced global efficiency, is observed for showers interacting in the NC channel (figure 5.19).

5.5 A look to the showers induced by UHE photons

The same astrophysical and cosmological scenarios predicting the existence of UHEν_s also predict the existence of UHE photons. So far, no UHE photon has been identified in the bulk of data collected by the Pierre Auger Observatory. The most recent comparisons of the upper limits on the integral photon flux to the measured Auger spectrum allow to set stringent upper bounds on the fraction of photons of about 0.4% for energies above 1 EeV [54] (section 1.2.4).

Photons induce EASs mainly trough electromagnetic interaction. Due to the nature of this interaction, photon showers are likely to start deeper than the hadronic induced ones. Moreover, this kind of showers usually exhibit a lower number of muons together with an

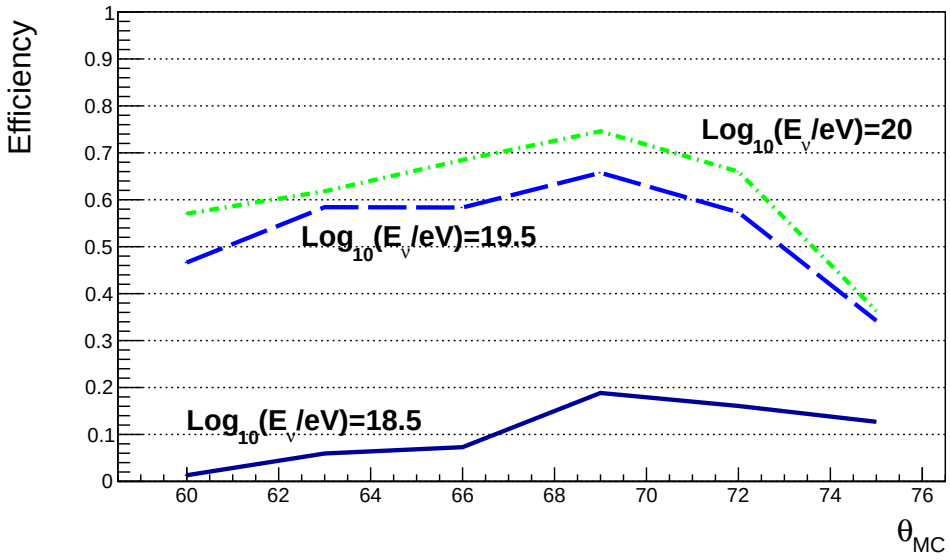

Figure 5.18: Fraction of electron CC neutrinos passing the analysis cuts in table 5.4 as function of the true zenith angle for three neutrino energies.

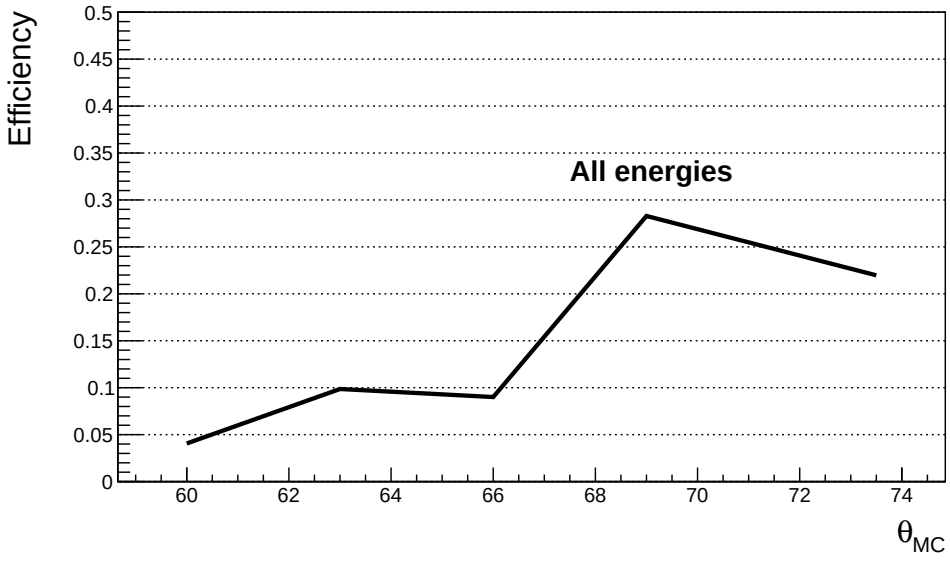

Figure 5.19: Fraction of electron NC neutrinos passing the analysis cuts in table 5.4 as function of the true zenith angle (all neutrino energies included).

important electromagnetic component. For very inclined showers, it is generally believed that the amount of atmosphere is enough to absorb the electromagnetic component, therefore they do not represent and important source of background for neutrino searches. Nevertheless, in the angular region of our study, where the amount of atmosphere becomes smaller than for very inclined showers, photon induced showers exhibit features at ground which can be very similar to the ones characterizing the ν-induced showers, thus representing a potential source of background.

Given that showers induced by photons can be more similar to, for instance, ν_e CC events than to hadronic induced showers, it is interesting to study the response of the neutrino selection described in this chapter to this kind of events. To do so, a specific Monte-Carlo data set of photon induced showers was produced under the GRID technology in a number of 60000 events. The production covers the θ angular region between 60° and 70° following a $(sin\theta \cdot cos\theta)$ distribution, whereas the energy follows a E^{-1} power law in the range from $10^{17.5}$ eV to 10^{20} eV. Photons were simulated without the Landau-Pomeranchuk-Migdal effect [167, 168], so they represent an upper limit to the real expected background. The same reconstruction and selection procedures applied for the ν analysis and described in previous sections is used on the Monte-Carlo photon sample. The same Fisher discriminant is also applied to the reconstructed photons.

In figure 5.20 we compare the Fisher distributions of the background training sample (full histogram), Monte-Carlo neutrinos (gray line) and simulated photons (black line). The photon events are weighted by a E^{-1} power law and the distributions normalized to the events present on the background training sample. The scatter plot of the Fisher values as function of the zenith angle is given in figure 5.21 (there is no normalization in this case, i.e. each event is shown as a point in the graph). Despite the reduced statistics in the higher angular bin, the result confirms the expected behavior: the estimated contribution from photon showers to the background on the UHEν search analysis strongly decreases with the zenith angle.

At the lower angles, photon showers show $\mathcal{F}$ distributions with long tails extending to the region populated by the ν signal events, far from the hadronic background (see figure 5.20a). At zenith angles below $\sim 65°$ a fraction of the photon showers become indistinguishable from neutrinos interacting high in the atmosphere, representing an irreducible background for the current ν analysis. The fraction of photon events passing the Fisher selection is, nevertheless, very small ($\sim$1%). Increasing the angle decreases the photon trigger and selection probability and the pattern of the $\mathcal{F}$ distribution obtained for photon events gets closer to the distribution of the hadronic background, shifting towards smaller values of $\mathcal{F}$ (figure 5.20e). Above $\theta \sim 65°$, the photon selection efficiency drops below 0.2%.

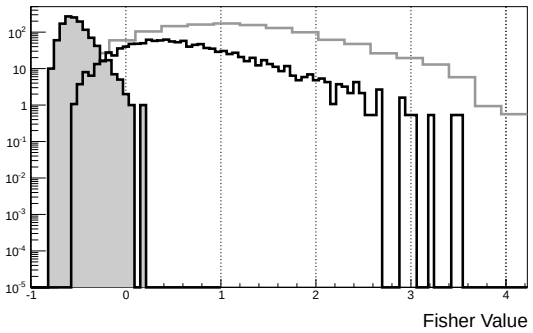

(a) $58.5^\circ < \theta_{\mathrm{Rec}} \leq 61.5^\circ$

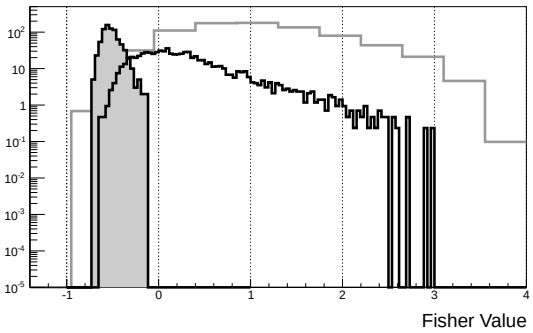

(b) $61.5^\circ < \theta_{\mathrm{Rec}} \leq 64.5^\circ$

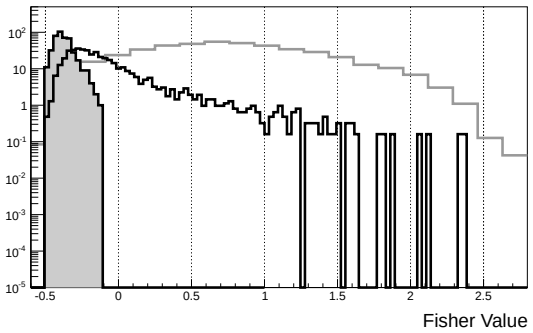

(c) $64.5^\circ < \theta_{\mathrm{Rec}} \leq 67.5^\circ$

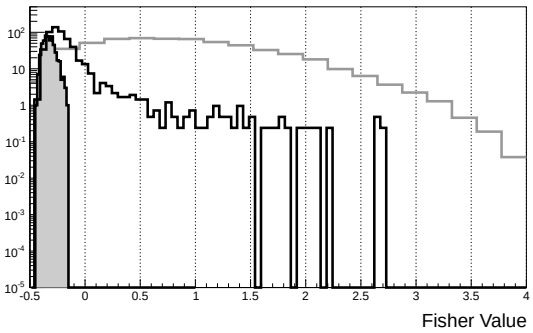

(d) $67.5^\circ < \theta_{\mathrm{Rec}} \leq 70.5^\circ$

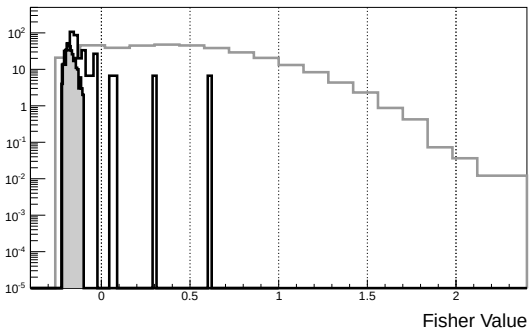

(e) $70.5^\circ < \theta_{\mathrm{Rec}} \leq 76.5^\circ$

Figure 5.20: Distribution of the value of the Fisher polynomial ($\mathcal{F}$) for events in the background training sample (full histogram), neutrino Monte-Carlo showers (gray line) and photon Monte-Carlo showers (black line) with reconstructed zenith angle in the five sub-regions.

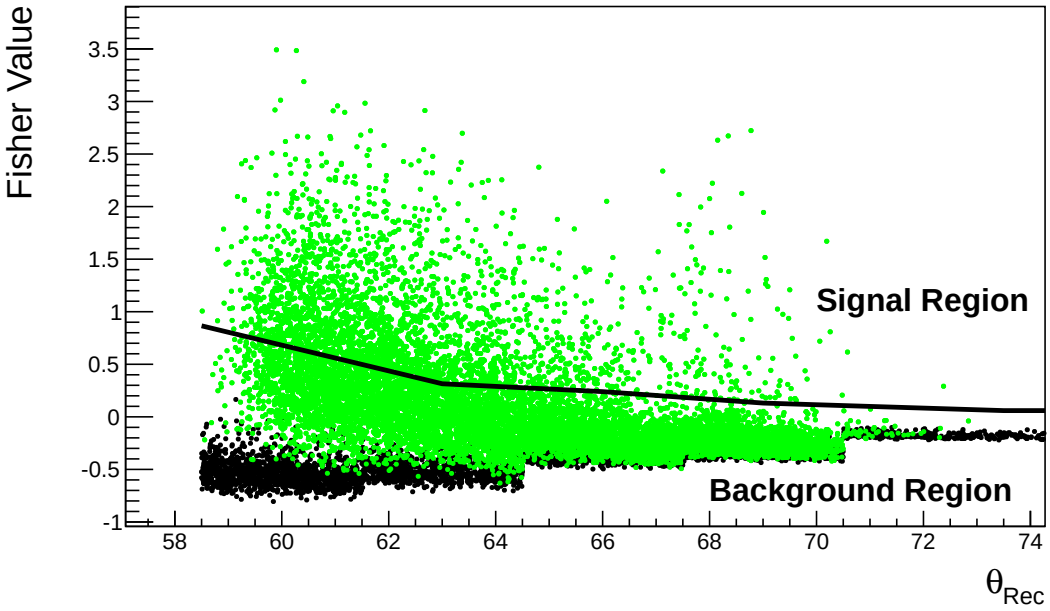

Figure 5.21: Distribution of $\mathcal{F}$ as function of the reconstructed zenith angle for events in the background training sample (black dots) and photon Monte-Carlo showers (light dots). Events above the solid line ($\mathcal{F}_{\text{cut}}$) would pass the neutrino selection cuts.

6
Detector Exposure

In the previous chapter the observables and the methodology defined to identify ν-induced showers with the SD array of the Pierre Auger Observatory were described and the detection efficiencies evaluated. These efficiencies are necessary to estimate the detector exposure and the expected neutrino rates. In the next sections, a study of the contribution of individual neutrino flavours to the calculated exposure is presented (section 6.1) together with a discussion on the systematic uncertainties arising from the method (section 6.2).

6.1 Effective Mass and Exposure

One of the techniques that can be applied to calculate the exposure of the SD array to UHEν_s consists in randomly distributing the simulated neutrino showers over the actual configurations of the array, applying to the showers at ground the trigger and neutrino identification conditions to obtain the active (*effective*) area of the array at every instant t, and as a function of the parameters of the neutrino-induced showers (neutrino energy, zenith angle,...). This is a extremely high CPU time-consuming process given the large number of real detector configurations that have to be taken into account, even in a daily basis. As explain below, a different approach is followed in this work taking advantage of the 6T5 trigger required to the showers as part of the pre-selection cuts.

The *effective aperture* of the SD array can be understood as the effective area which is seen by the incident cosmic neutrino flux and can be calculated geometrically based on the elementary surface detector unit used in our analysis: the 6T5 hexagon. At full efficiency, the detection area of such a elementary detector unit is $A_{6T5} = 1.95$ km^2 [169], correspond to the Brillouin area shaded in figure 6.1. The full SD array (1660 stations covering a geometrical area of about 3000 km^2) contains 1420 hexagons. The *effective acceptance* for UHEν_s with energy E_ν initiating a shower at a slant injection depth D is the convolution of the aperture with the detector identification efficiency calculated in section 5.4. Therefore, the effective acceptance of a single hexagon can be written as:

$$A_{\rm hex}(E_\nu, D) = \int_{\phi=0}^{\phi=2\pi} d\phi \int_{\theta_{\rm min}}^{\theta_{\rm max}} A_{6T5} \cdot \varepsilon(E_\nu, \theta, D) \cdot \sin\theta\cos\theta \cdot d\theta \qquad [\text{cm}^2\ \text{sr}] \qquad (6.1)$$

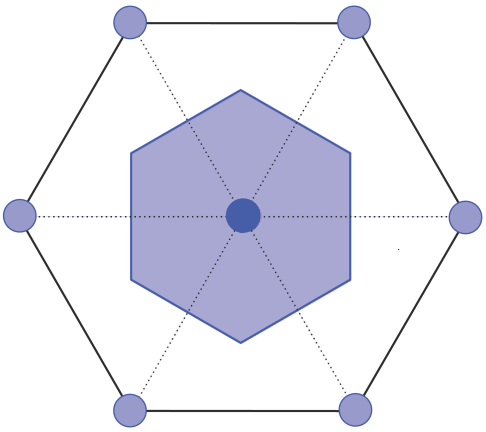

Figure 6.1: Drawing of a 6T5 hexagon of SD stations (represented by circles) and the Brillouin effective area A_{6T5} (shaded hexagon around the central station) for a triangular grid.

where $\varepsilon(E_\nu, \theta, D)$ is the neutrino detection efficiency and the integral over the zenith angle goes from $\theta_{\rm min} = 58.5°$ to $\theta_{\rm max} = 76.5°$.

The *effective mass* inside which if a neutrino interacts it will be identified is obtained by integrating the aperture over the neutrino slant injection depths. In other words, it accounts for all the effective mass target over the hexagon which is effective for neutrino identification in the angular region of search:

$$M_{\rm hex}(E_\nu) = \int_D A_{\rm hex}(E_\nu, D) \cdot dD \qquad [\text{g sr}] \tag{6.2}$$

where the integral over the injection depth runs over the values simulated at each zenith angle (see table 4.1).

Figure 6.2 shows the SD effective mass for ν detection corresponding to a single 6T5 hexagon, for both ν_e CC and NC interaction channels (numerical values also given in table 6.1). The effective mass is a monotonically increasing function of the energy, the expected behaviour since it is directly proportional to the neutrino detection efficiency. The contribution to the effective mass of the CC channel relative to the NC is a factor ~ 10 at 1 EeV, increasing to ~ 20 at 100 EeV due to the much higher detection efficiencies.

During the search period considered in this work, the surface detector array of the Pierre Auger Observatory was growing continuously. Since the number of working stations and their status (they can eventually have periods of instability) are monitored every second, the SD configuration at any instant as well as its evolution with time is known with very good accuracy. In particular $n(t)$, the instantaneous number of active 6T5 hexagons at a given time t.

The calculation of the *exposure* of the Observatory to UHEν_s involves folding the SD array effective mass with the ν interaction probability, and integrating in time. For each neutrino channel (i = CC, NC) and flavour ($\alpha = e, \mu, \tau$) it can be expressed as follows:

$$\xi^{i,\alpha}(E_\nu) = \frac{\sigma^{i,\alpha}(E_\nu)}{m_N} \int_t M^{i,\alpha}_{\rm hex}(E_\nu) \cdot n(t) \cdot dt = \frac{\sigma^{i,\alpha}(E_\nu)}{m_N} \cdot M^{i,\alpha}_{\rm hex}(E_\nu) \cdot N_{\rm hex} \qquad [\text{cm}^2 \text{ sr yr}] \tag{6.3}$$

where $\sigma^{i,\alpha}(E_\nu)$ is the ν-nucleon interaction cross-section [80], m_N is the mass of a nucleon and $N_{\rm hex}$ is the total number of active 6T5 hexagons integrated in time over a data taking period. For the calculation of the exposure, the actual number of active 6T5 hexagons was computed

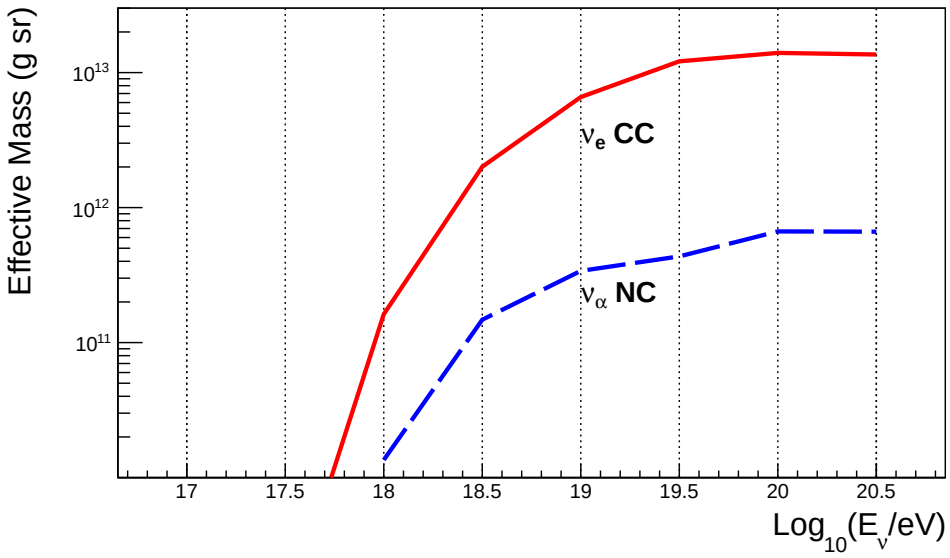

Figure 6.2: Effective mass of one 6T5 hexagon of the SD array to electron neutrinos interacting through CC (red line) and NC (blue dashed line) channels ($\alpha = e, \mu, \tau$).

$\log(E_\nu/\text{eV})$	Effective Mass [g sr] (6T5 hexagon unit)		Exposure [cm^2 s sr] (2 yr full SD array)		
	ν_e CC	ν_α NC	ν_e CC	ν_μ & ν_τ CC	ν_α NC
17.5	8.76×10^{8}	–	3.81×10^{11}	–	–
18.0	1.62×10^{11}	1.35×10^{10}	1.06×10^{14}	8.79×10^{12}	3.51×10^{12}
18.5	2.01×10^{12}	1.48×10^{11}	1.95×10^{15}	1.44×10^{14}	5.74×10^{13}
19.0	6.59×10^{12}	3.40×10^{11}	9.35×10^{15}	4.82×10^{14}	1.93×10^{14}
19.5	1.21×10^{13}	4.35×10^{11}	2.46×10^{16}	8.84×10^{14}	3.56×10^{14}
20.0	1.40×10^{13}	6.66×10^{11}	3.97×10^{16}	1.89×10^{15}	7.88×10^{14}
20.5	1.36×10^{13}	6.63×10^{11}	5.39×10^{16}	2.62×10^{15}	1.05×10^{15}

Table 6.1: Effective mass of one 6T5 hexagon unit and exposure for a data period equivalent to 2 yr of a full SD array, to neutrinos of different studied channels. ν_α stands for the three neutrino flavours.

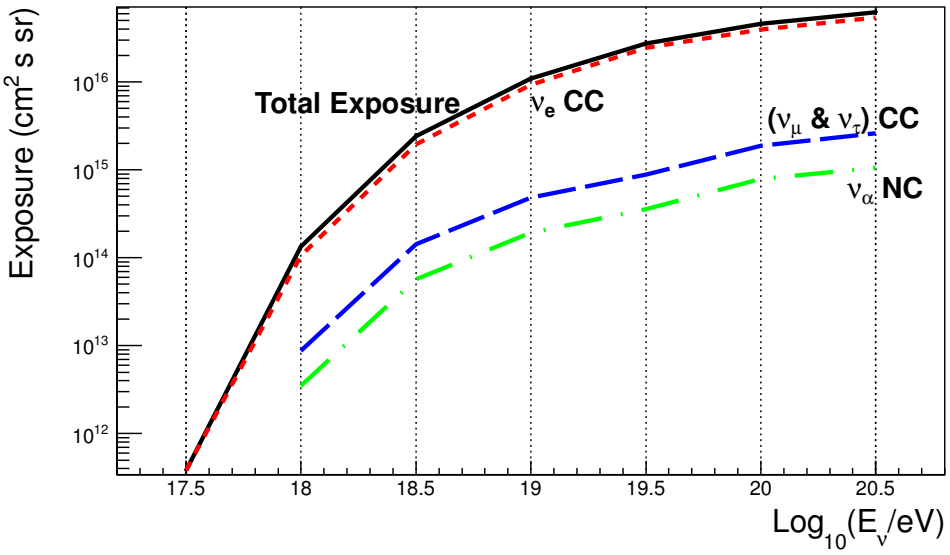

Figure 6.3: Exposure of the Pierre Auger Observatory to downward-going neutrinos in the angular range 58.5° to 76.5° for a data period equivalent to 2 years of full SD array (equation 6.3).

and updated every minute. Overall, the uncertainty on the determination of $n(t)$ amounts to about 1.5% [169].

Assuming a 1:1:1 flavour ratio (as expected due to the effects of neutrino oscillations during propagation from the sources), the total exposure can be written as:

$$\xi(E_\nu) = \sum_i \sum_\alpha \xi^{i,\alpha}(E_\nu) \tag{6.4}$$

The exposures to neutrinos on the different channels obtained for an equivalent period of 2 yr of full SD array are listed in table 6.1 and plotted in figure 6.3. As expected the exposure follows the same behaviour of the effective mass, convoluted with the ν cross-section. We remind here that the possibility that downward-going ν_τ produce double bang showers is not accounted for in the calculation, which underestimates the real exposure of the Observatory to this particular channel.

The contribution of the different channels to the final result is clearly different. The effective mass increases rapidly with energy on the first bins and then slowly saturates. The exposure follows the same pattern but still increases with energy due to the contribution of the cross-section which grows like $\sim E^{1/3}$. The fast rise at the first energy bins is dominated by the increase of the trigger efficiency of the SD which saturates at $10^{18.5}$ eV. On the other hand, the contribution from the NC channel is very small compared to the CC channel due to the much smaller detection sensitivity shown by the analysis to NC showers (see discussion in section 5.4).

In summary, the total quoted exposure of the Observatory to the detection of UHEν induced showers in the explored low zenith angular region is dominated by the ν_e CC channel, which contributes to $\sim 85\%$ of the total exposure. In this channel, the energy carried by the primary particle is fully transferred to the shower. The $\nu_\mu + \nu_\tau$ CC channels follow in importance ($\sim 10\%$ contribution), taking advantage of the higher value of the cross section compared to the ν NC channels ($\sim 5\%$ in total).

In figure 6.4 we show the dependence of the sensitivity to the detection of UHEν_s with the

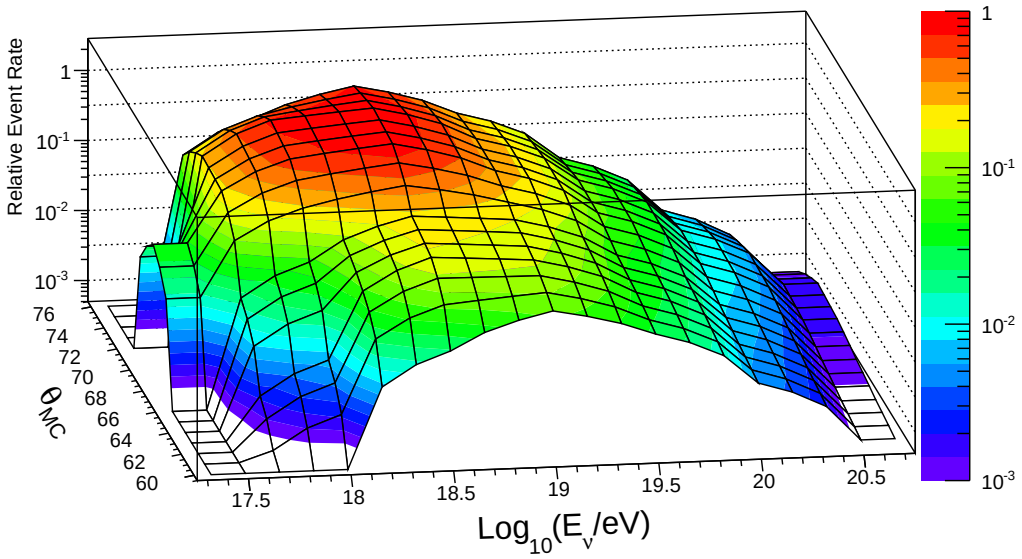

Figure 6.4: Sensitivity to the detection of ν-induced showers in the "energy – zenith angle" parameter space. The number of neutrino events expected to be detected by this analysis (assuming a E_ν^{-2} flux) is shown normalized to the events expected in the maximum bin.

neutrino incident zenith angle and energy. Assuming an incoming flux of neutrinos with power $J(E_\nu) \propto E_\nu^{-2}$, the number of expected events in each (E_ν, θ_{MC}) bin is computed. The peak of sensitivity, corresponding to the bin where most of the events would be detected, is observed around $E_\nu \sim 10^{18.5}$ eV and $\theta_{\mathrm{MC}} \sim 72°$. In figures 6.4 and 6.5, the number of events in each bin (shown in the vertical axis) is normalized with respect to the events computed in the bin with highest sensitivity. Many effects contribute to explain the observed shape of the distribution. For instance, the decrease on sensitivity at the highest energies is driven by the chosen energy spectrum whereas the reduction at the lower energies comes from the small trigger efficiency. On the other hand, the increase of the atmospheric depth with the zenith angle (and hence, the neutrino interaction probability) contributes to enhance the sensitivity with θ.

6.2 Systematic uncertainties

The calculation of the actual exposure for each class of event requires the input of several ingredients, each having its specific uncertainty. Some of these uncertainties are directly related to the Monte-Carlo simulation (generator of first interaction, air shower development, ...) and some come from the limitations on the theoretical models estimating, for instance, the interaction cross section or the hadronic interaction models. On this regime, available parametrisations and the underlying data are not always suitable for the simultaneous description of all kinematic ranges. According to the parameters of which the exposure depends, the systematic uncertainties can arise from the neutrino cross-section or from the detection efficiency since the number of hexagons and the rest of parameters are well determined numbers. The uncertainties on the efficiency mainly depend on the simulation and reconstruction procedure while the uncertainties on cross-section depend on the model used.

A complete and exhaustive evaluation of the systematic uncertainties in the full parameter space, i.e. changing every single ingredient which might modify the detection efficiency $\varepsilon(E_\nu, \theta, D)$,

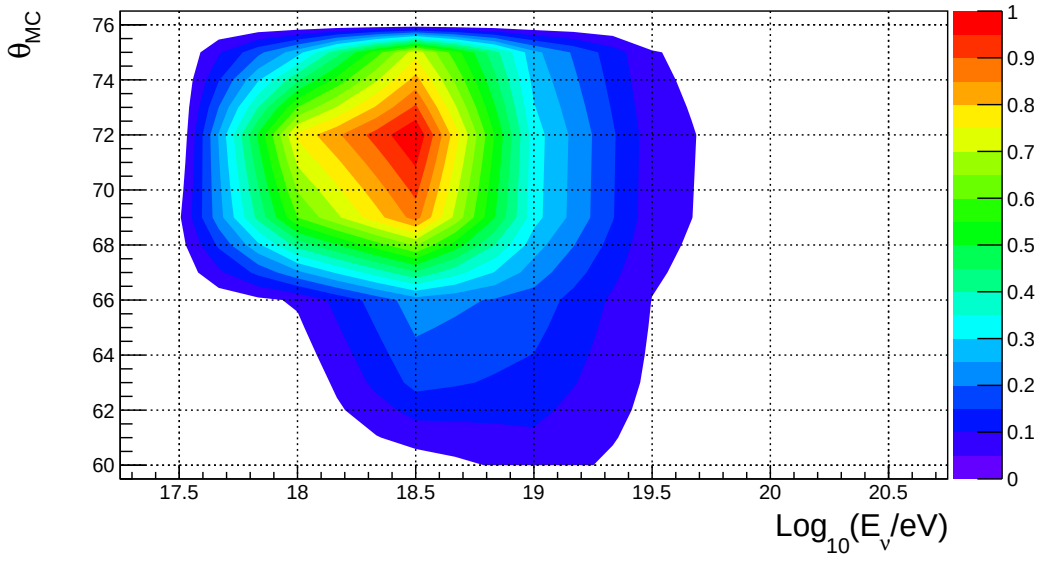

Figure 6.5: Projection of figure 6.4 in the "energy – zenith angle" plane.

would require an unaffordable number of simulated events. Instead, the comparison between models was done in a reduced region of the parameter space [170]. First, the new showers were produced using only electron neutrinos as primary particles interacting through the CC channel, since this is the channel that contributes the most to the total exposure. Concerning the energy of the primary ν_e, three representative values of the energy were re-simulated (0.3 EeV, 1 EeV and 3 EeV). The value of the zenith angle of the incident neutrino is expected to have a marginal impact on the final result since most of the dominant sources of systematic uncertainty (interaction generator, parton distribution functions, cross-section, etc) do not depend on θ. In order to simplify the problem and to facilitate a posterior combination of systematics with the analysis searching for neutrinos at high angle ($75° - 90°$), only showers incident at the highest angle considered in our analysis were simulated. Finally, all injected neutrinos were forced to interact at fixed injection points D, uniformly distributed along the shower axis in steps of 100 g cm^{-2}, i.e. the full range of interaction depths was explored. This ensures a better estimation of systematic changes in the exposure given that $\xi(E_\nu)$ is proportional to the integral of the efficiency with D.

Primary Interaction Generator: Three interaction generators have been compared: PYTHIA [151] and HERWIG, the later in FORTRAN [146] and C++ [171] versions. The reference generator used in this analysis is the HERWIG FORTRAN version. The systematic uncertainties quoted for this source becomes (+2.6%, −3.7%).

Parton distribution function: The differences observed on neutrino showers generated with different PDF were produced with the PYTHIA generator. This program contains several internal PDF functions but also offers the possibility of free choice of external PDFs. No big differences are observed between the different models. The systematic fluctuations are below 5% and at the level of the statistical errors ($< 3\%$) in most of the cases. Taking as reference the MRST98 [148] model used in this analysis, the estimated uncertainty on the exposure is (+4%, −5%).

Hadronic Model: Another source of uncertainty in the shower simulation process arises from

the assumed hadronic model because the accelerator data have to be extrapolated to the shower energies under study. Since the trigger efficiency is mainly sensitive to the muon content and the electromagnetic component of the shower (the most relevant part for neutrino identification) is believed to be better reproduced by simulations, these uncertainties in the hadronic model are expected to have a small effect on the final result. Some of the most popular high energy hadronic models have been compared: QGSJET [152], QGSJETII [172] and SIBYLL [173]. In general, a very good compatibility between them within statistical errors is observed. The highest difference, appearing between QGSJET and QGSJETII remains small: -5.5% with a $\sim 3\%$ statistical error. On the other hand, the measured discrepancy between QGSJETII and SIBYLL (-0.5%) is well below the statistical error. A total systematic uncertainty of -6% is therefore assumed to come from the change of hadronic model.

Shower Simulator and thinning algorithm: Two different atmospheric shower development simulators have been tested in order to quote the uncertainty affecting the exposure: AIRES [174] and CORSIKA (see section 4.1.2). An overall increase of the exposure of $+17\%$ is quoted for showers simulated with AIRES compared to CORSIKA. Regarding the thinning algorithm, a more realistic value of 10^{-7} was also compared with the 10^{-6} value used in the analysis, leading to a contribution of $+7\%$ to the total systematic uncertainty.

Detector simulator version: There are different detector response simulators, nevertheless only the $\overline{\text{Off}}\underline{\text{line}}$ performs a full simulation of the detector using the well tested code GEANT4 [175]. Other simulators infer the total signal from the total length of the muons crossing the detectors. Differences between both treatments have been computed for other analysis and are in agreement within the $\pm 5\%$ in the worst case (see for instance [176]).

Additionally we checked the differences between the simulations performed by the official $\overline{\text{Off}}\underline{\text{line}}$ release used in GRID and the latest trunk version SVN:21443 available when this report was written. No sizeable differences were found between them.

Reconstruction algorithm The basis of the reconstruction algorithm were described in section 4.2.3 but the implementation can be different among different packages. We compared the angular reconstruction of two $\overline{\text{Off}}\underline{\text{line}}$ modules, $LDFFingerKG$ and $HASReconstructionOG$, quoting differences below $\pm 1\%$ in the exposure.

On the other hand, reconstruction algorithms are continuously evolving to account for curvature corrections, improvements on minimization procedures, etc. We contrasted the results between the version used in this analysis and the latest available of the module $LDFFinderKG$ SVN:21443. Again the difference in the exposure is well below 1%.

Systematic uncertainty from neutrino cross-section: In this work we assumed the ν-nucleon cross-section values and uncertainties published in [80], which amount to $\pm 7\%$. Nevertheless, the effective mass given in table 6.1 is independent on the ν-nucleon cross-section allowing to recompute the expected event rate (and neutrino flux limit) for other models if required.

In table 6.2 we give the summary of the different contributions to the systematic uncertainties studied in this work [170] and described in this section. All sources of uncertainty have a contribution smaller than 10%, with the exception of the shower simulator. The total impact on the central value of the exposure computed with the reference Monte-Carlo sample (section 4.1) is $[+21\% , -12\%]$, obtained from the quadratic sum of the individual contributions. As described later in section 7.2.3, the final uncertainty will be incorporated in the value of the limit itself through a semi-Bayesian extension [177] of the Feldman&Cousins approach [178].

Source of uncertainty	
Interaction Generator	+3% −4%
Parton Distribution Function	+4% −5%
Hadronic Model	−6%
Shower Simulator	+17%
Thinning Algorithm	+7%
Detector Simulation	+5% −5%
Reconstruction Algorithm	+1% −1%
ν cross-section	+7% −7%
Total systematic	+21% −12%

Table 6.2: Main sources of systematic uncertainty and their impact on the exposure. The numbers correspond to the maximum positive and negative deviations from the reference exposure.

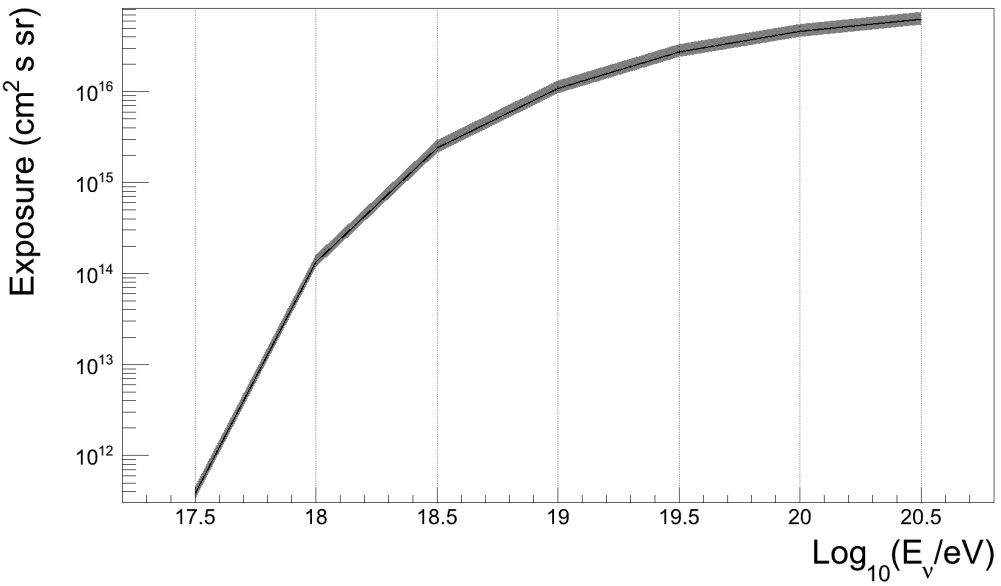

Figure 6.6: Total exposure of the Pierre Auger Observatory for down-going neutrinos in the angular range 58.5° to 76.5° (this analysis) for a data period equivalent to 2 years of full SD array. The central value (solid line) is shown together with the [+21% , −12%] systematic uncertainty band (gray area).

7

Limits to the Diffuse Flux of UHE neutrinos

In the previous chapters the "blind" analysis searching for ν-induced showers at low zenith angle has been defined. It has been characterized by means of a set of pre-selection cuts, which intend to select well reconstructed young showers in the angular range of interest, followed by a Fisher discriminant method based on the AoP values of the selected SD stations. The optimization of the cuts to discriminate neutrino events from ordinary cosmic ray signatures is carried out by training the Fisher algorithm with a sub-sample of data events (flagged as "background" events) and a sample of simulated ν showers (the "signal" events). A final cut on the Fisher variable is set such that 1 background event is expected to be selected by the analysis in 20 years of full Auger data.

In this chapter we show the result of the data unblinding, i.e. we *open the box* (as it is colloquially known) and look for ν candidates in the remaining sub-sample of data events (the "search" sample). This is reported in section 7.1, together with some compatibility checks between the training and search distributions. We anticipate here that no events in the search data sample passed the selection criteria. The absence of neutrino candidates was translated into an upper limit on the incoming flux of UHEν_s. In section 7.2 different statistical approaches are discussed and the final integral and differential limits presented. Finally, a first attempt to the combination of the ν search results obtained in this work with the downward-going ν search at high zenith angle ($\theta \in [75^\circ - 90^\circ]$) [3] is discussed in section 7.3.

7.1 The Data Unblinding: searching for neutrino candidates

As described in section 5.1, the search sample was constructed as a complementary set of the background training sample. It is composed by all events collected by the Observatory in the period 1 January 2004 to 31 May of 2010 except those events whose SD event number is divisible by 5 (already used to build the training sample). The search period corresponds to 2.21 ± 0.03 years of full Auger data (see table 5.1).

After applying to the search sample the full set of cuts listed in table 5.4, **0 events survive the selection**. Figure 7.1 shows the Fisher distribution of the events in the training (black dots) and search (red dots) samples as a function of the zenith angle. The solid line indicates the $\mathcal{F}_{\rm cut}$ value: events above the line would be considered neutrino candidates. Events from the two

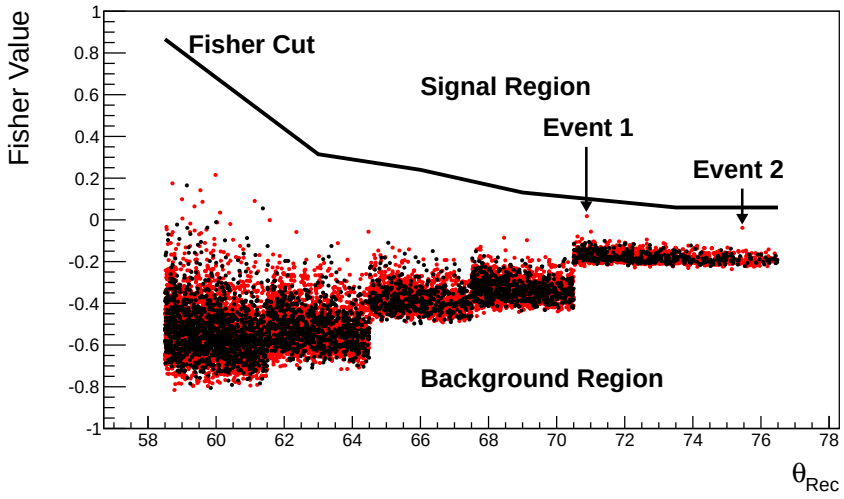

Figure 7.1: Fisher value as function of the reconstructed angle θ_{Rec} for the background training sample (black dots) and the search sample (red dots). The black line represents the Fisher cut. The two events from the search sample with Fisher value closer to $\mathcal{F}_{\mathrm{cut}}$ are indicated (Event 1 with ID 9084924 and Event 2 with ID 1335567).

samples clearly overlap.

The five plots shown in figure 7.2 give the distributions of the Fisher values corresponding to the search (open histograms) and training (full histograms) samples, for each angular region. The dashed line indicates the result of fitting the tail of the training distributions to an exponential function, as described in section 5.3.2. Several conclusions can be drawn out of this result. First, the training and search distributions are compatible within statistical fluctuations. No statistical significant differences on the shapes or systematic shifts between the two distributions are observed. Second, the prediction made by the exponential fit to the training sample describes properly also the tail of the distribution of the search sample. Moreover, the search sample containing about 2.7 times more data than the training one, tends to populate the "holes" (bins with no entries) present in the training sample below the exponential extrapolation. Table 7.1 gives a more quantitative information of the goodness of the exponential tail extrapolation by comparing the number of *observed* events in the search sample and the ones *predicted* by the fit. Both data are compatible within statistical fluctuations and, when compared to numbers from table 5.3, a better agreement on the most extreme bins of the tail is achieved due to the increase of statistics in the search sample. Finally, the two events with $\mathcal{F}$ value closer to $\mathcal{F}_{\mathrm{cut}}$ (with ID numbers 9084924 and 1335567) appear in the last angular region and are still far from the cut value (see figure 7.2e).

The first event, with ID number 9084924, is shown in figure 7.5. The footprint is clearly elongated and it is reconstructed with a zenith angle of 70.9 ± 0.1 degrees. The time residual of the stations nicely fits to a curved shower front. Nevertheless, two out of the four stations selected to build the Fisher have only one active PMT, and one of the remaining stations has two active PMTs. The biggest value of AoP (> 3) arises from station 164, which falls at the edge of the footprint where deflected muons can be delayed with respect to the front shower plane (this can potentially increase the AoP value). A cut on the total fraction of active PMTs in the T5 stations can be envisaged for future analysis upgrades.

Additionally, for this particular event we have obtained the so called muon production

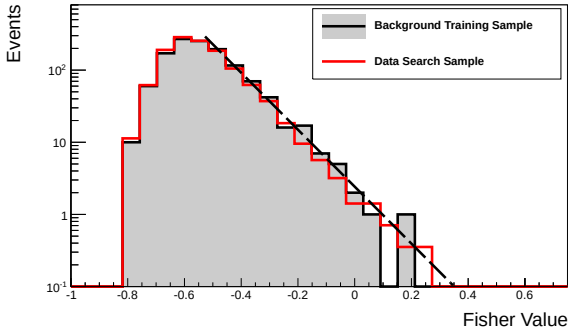

(a) $58.5^\circ < \theta_{\mathrm{Rec}} \leq 61.5^\circ$.

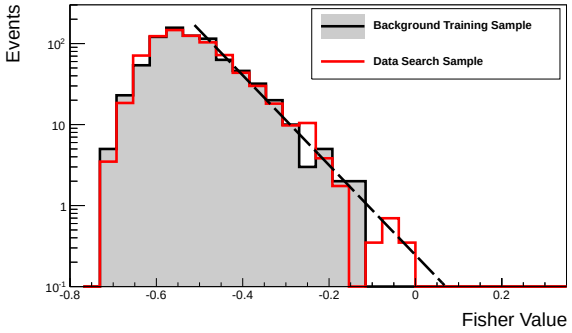

(b) $61.5^\circ < \theta_{\mathrm{Rec}} \leq 64.5^\circ$.

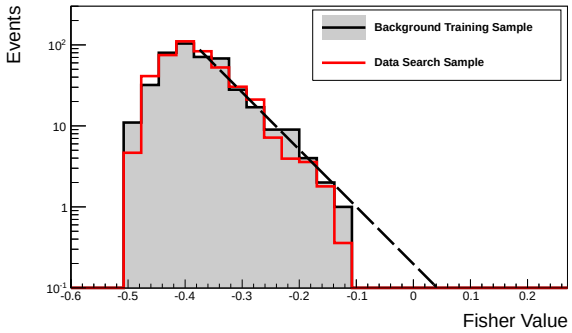

(c) $64.5^\circ < \theta_{\mathrm{Rec}} \leq 67.5^\circ$.

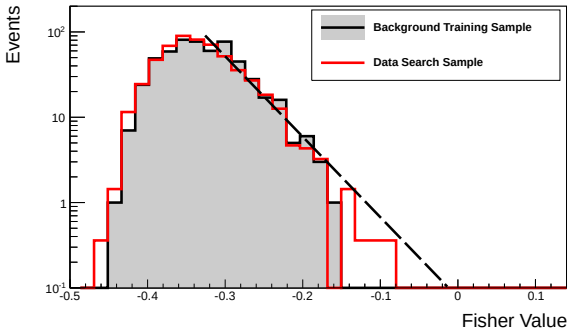

(d) $67.5^\circ < \theta_{\mathrm{Rec}} \leq 70.5^\circ$.

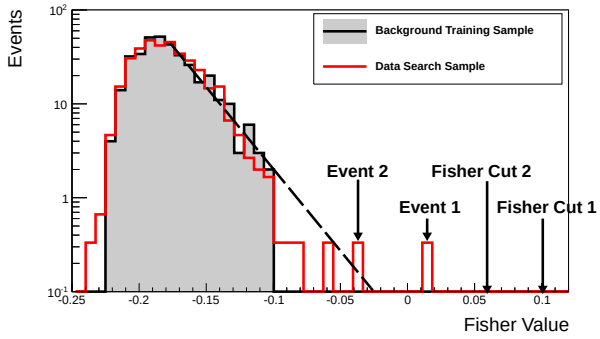

(e) $70.5^\circ < \theta_{\mathrm{Rec}} \leq 76.5^\circ$.

Figure 7.2: Comparison of the $\mathcal{F}$ distributions for the background training and search data samples. Both distributions are compatible within statistical errors. The dashed line corresponds to the exponential fit and extrapolation used to estimate the behaviour of the distribution tail. The two events with $\mathcal{F}$ value closer to the corresponding $\mathcal{F}_{\mathrm{cut}}$ are indicated in the bottom figure.

	Number of events in $\mathcal{F}$ distribution tails: "Observed" - "Predicted"				
	Region 1	Region 2	Region 3	Region 4	Region 5
$\mu + 1\sigma$	245.6 - 270.3	118.9 - 110.0	68.4 - 74.7	108.3 - 112.7	72.5 - 71.9
$\mu + 2\sigma$	78.2 - 89.8	45.3 - 41.2	38.0 - 45.3	27.4 - 35.6	13.0 - 22.0
$\mu + 3\sigma$	22.6 - 29.9	7.0 - 9.4	9.7 - 16.6	5.8 - 11.2	3.7 - 9.0
$\mu + 4\sigma$	7.4 - 9.9	1.4 - 3.5	2.1 - 6.1	1.1 - 3.5	1.0 - 2.8
$\mu + 5\sigma$	2.8 - 3.3	1.0 - 1.3	0.0 - 2.2	0.0 - 1.1	0.7 - 1.1
$\mu + 6\sigma$	0.7 - 1.0	0.0 - 0.3	0.0 - 0.8	0.0 - 0.5	0.3 - 0.5

Table 7.1: Number of events "observed" in the search sample (empty histograms in figure 7.2) normalized to the background training sample (full histograms in figure 7.2) and "predicted" by the exponential tail assumption (dashed lines in figure 7.2). The reported number of events in each row of the table is computed by integrating the tail of the search sample distributions starting from the value indicated in the first column.

distribution (MPD) (see figure 7.3). This observable is defined as the distribution of produced muons as a function of the slant depth measured along the shower axis [179]. This parameter can be computed using the information of the SD with the method described in [53], where it is also shown that the maximum of this distribution, $X^{\mu}_{\max}$, contains valuable information related to the primary mass composition. The value of $X^{\mu}_{\max}$ extracted from the fit to a Gaisser-Hillas function is around 680 g cm^{-2}. Figure 7.4 shows how this value compares to the MPD elongation rate for protons and irons. Although uncertainties in $X^{\mu}_{\max}$ are large, at the given energy ($E = 6.3 \cdot 10^{19}$ eV), this event is most likely classified as a light and deep primary.

The display of the second event with ID 1335567 is shown in figure 7.6. It falls at the edge of the array, with part of the footprint probably lost outside the SD sensitive area. The reconstructed core has a large uncertainty in the direction of the shower axis suggesting that what was detected is indeed only a fraction of the complete shower whose real core would be located outside the array. We remind here that the position of the core defines the selected T5 stations. A cut on the uncertainty on the core position can be envisaged for future analysis upgrades.

Besides these 2 events, the 10 events of the search sample with bigger Fisher value in each angular region were carefully scanned and no special pathology, no particular feature was found in any of them.

7.2 Diffuse Limit to the UHE neutrino flux

Given that no neutrino candidates are found in data, we can compute an upper limit to the flux of incoming UHEν_s $J(E_\nu) = \frac{dN}{dE}$. This magnitude is usually given in units of [GeV^{-1} cm^{-2} s^{-1} sr^{-1}]. The expected number of detected neutrinos can be computed as:

$$N_{\text{Expected}} = \int_{E_{\nu\min}}^{E_{\nu\max}} J(E_\nu) \cdot \xi(E_\nu) \cdot dE_\nu \tag{7.1}$$

where $\xi(E_\nu)$ is the exposure defined in equation 6.4 and showed in figure 6.3. We recall here that the contribution of the three neutrino flavours is added, assuming the same differential flux for the three channels and a $\nu_e : \nu_\mu : \nu_\tau \equiv 1 : 1 : 1$ relative ratio on Earth. Under the assumption

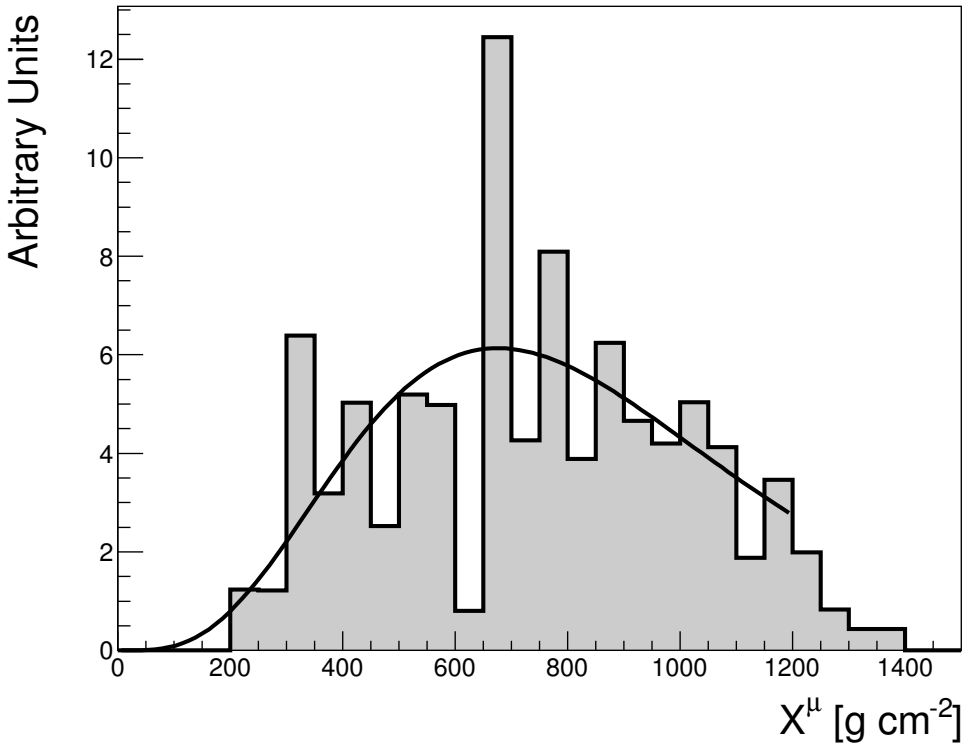

Figure 7.3: Muon production depth distribution (MPD) extracted from the SD event ID 9084924. The line shows the fit to a Gaisser-Hillas fuction from which the $X^{\mu}_{\rm max}$ is extracted.

that the UHEν flux behaves with energy as $J(E_\nu) = k \cdot E_\nu^{-2}$, the integrated upper limit on the value of k is:

$$k_{\rm Up} = \frac{N_{\rm Up}}{\int_{E_{\nu\rm min}}^{E_{\nu\rm max}} E_\nu^{-2} \cdot \xi(E_\nu) \cdot dE_\nu} \tag{7.2}$$

where the actual value of the upper limit on the signal events $N_{\rm Up}$ at a given confidence level (C.L.) depends on the number of events observed in data and on the number of events expected from background. Moreover, given that the problem of quoting a confidence interval or an upper limit for a parameter given a measure of a related observable in the presence of background can be confronted from several approaches, different *statistical methods* can lead to different values of $N_{\rm Up}$ as discussed in the next sections. Among all the possible elections we will use the Feldman and Cousins treatment [178] and extensions to it which incorporate the systematic uncertainty on the exposure, in consistency with what is commonly used in UHEν experiments. It is important to stress that other alternative treatments exist in the literature.

7.2.1 The Feldman&Cousins treatment

When a parameter estimate is not significantly far away from the boundary, it is natural to report a one-sided confidence interval (often an upper limit). If, however, the data come out such that the parameter estimate is not so close to the boundary, one might wish to report a central (two-sided) confidence interval. As pointed out by Feldman&Cousins [178], if the decision to report an upper limit or a two-sided interval is made by looking at the data ("flip-flopping"), then in general there will be parameter values for which the resulting intervals have a coverage

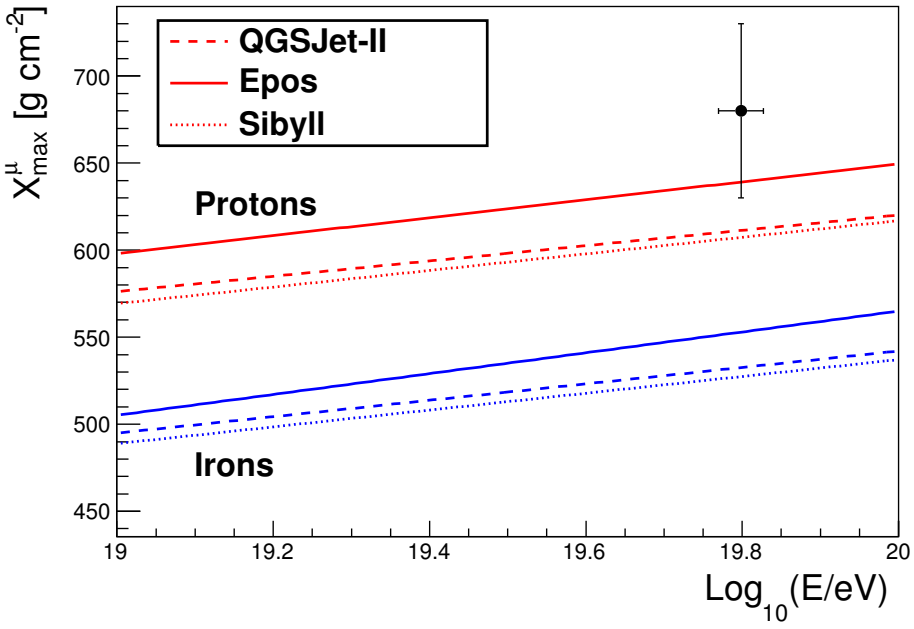

Figure 7.4: Evolution of $X^{\mu}_{\max}$ with the energy. The predictions for proton and iron primaries following different hadronic models (lines) is shown together with the value obtained for the SD event ID 9084924 (point).

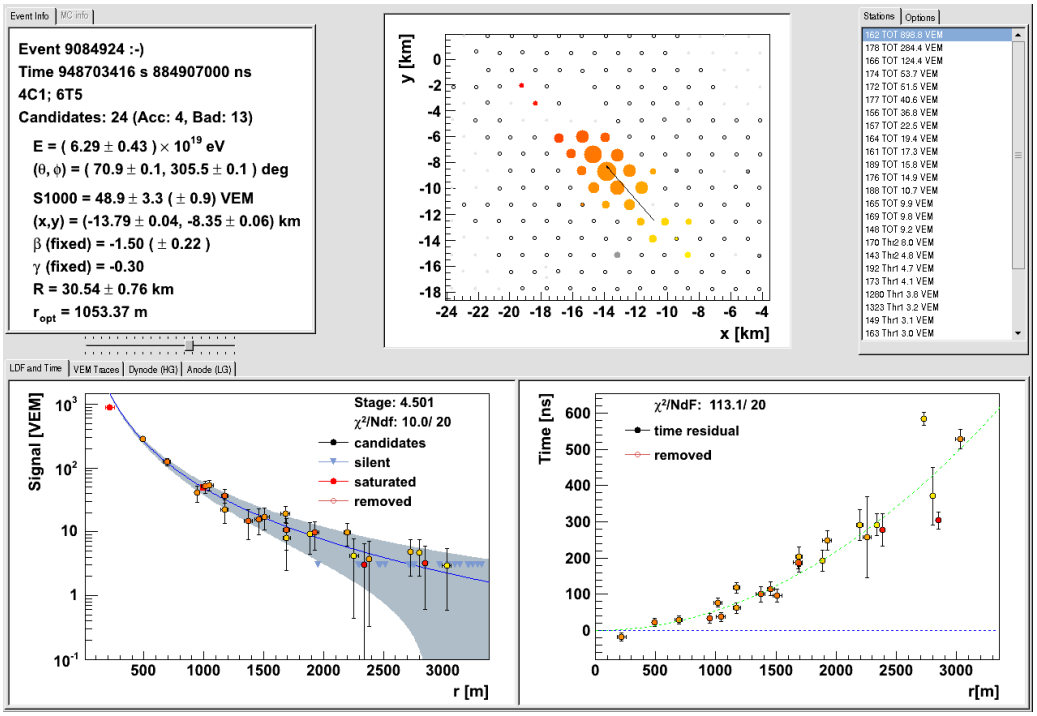

Figure 7.5: Display of SD event ID 9084924, recorded on January, 28th 2010 (before noon). The selected Fisher stations have ID numbers 162, 164, 166 and 172.

probability less than the expected. With the confidence intervals suggested by Feldman&Cousins, the prescription determines whether the interval is one- or two-sided in a way which preserves the coverage probability. Interval constructions having this property and avoiding the problem of null intervals are said to be unified. For a given choice of confidence level, if the parameter estimate is sufficiently close to the boundary, the method gives a one-sided limit. For parameter estimates increasingly far away from the boundary, the interval makes a smooth transition from one- to two-sided, and far away from the boundary, one obtains a central interval.

A potential difficulty with unified intervals arises if, for example, one constructs such an interval for a Poisson parameter s of some yet to be discovered signal process with, say, C.L. = 0.9. If the true signal parameter is zero, or in any case much less than the expected background, one will usually obtain a one-sided upper limit on s. However, in a certain fraction of experiments, a two-sided interval for s will result. Since, however, one typically chooses C.L. to be only 0.9 or 0.95 when setting limits, the value $s = 0$ may be found below the lower edge of the interval before the existence of the effect is well established. It must then be communicated carefully that in excluding $s = 0$ from the interval, one is not necessarily claiming to have discovered the effect. This situation can arise if one neutrino candidate is found in the future in the Auger data. This issue is solved when the background and the signal sample are considered to be affected by statistical errors (see section 7.2.2).

The Feldman&Cousins approach is implemented in a ROOT [180] class named TFeldman-Cousins [181] which was used for this analysis. If no neutrino events are observed, for a 90% C.L. coverage interval and with the conservative assumption of zero background, the upper and lower limits to the number of signal events are $N_{\mathrm{Up}}^{90\%\mathrm{CL}} = 2.44$ and $N_{Low}^{90\%\mathrm{CL}} = 0$, respectively. In case 1 signal event is found, this belt becomes [4.36, 0.11]. Note that in this case the lower limit is not zero (in spite of which and in the presence of a Poisson background it would not mean a

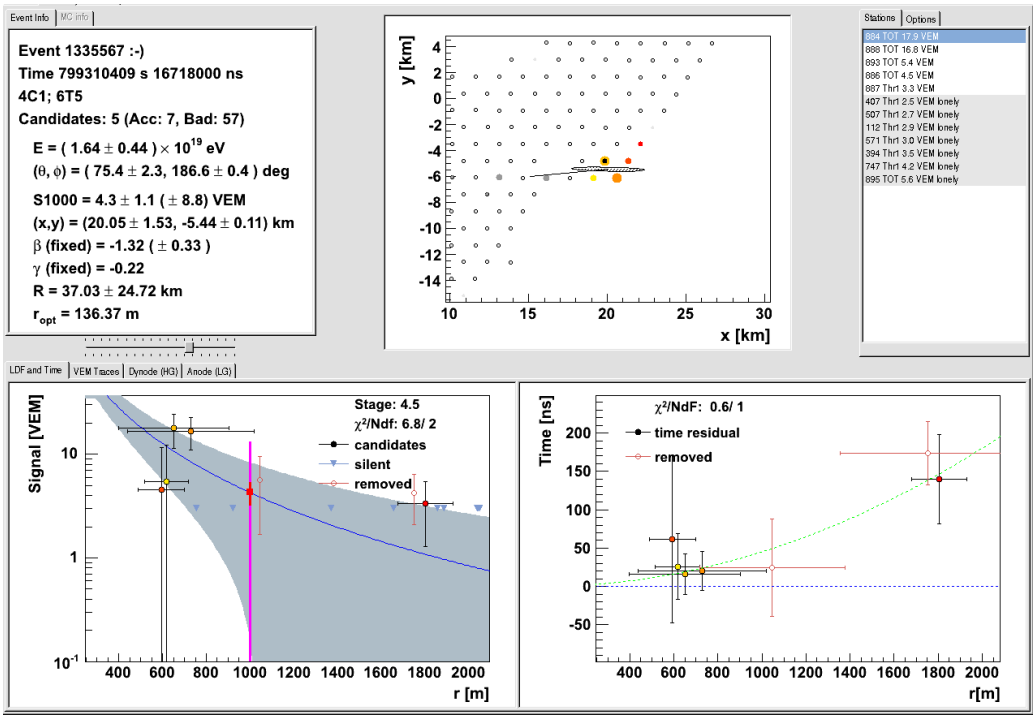

Figure 7.6: Display of SD event ID 1335567, recorded on May, 5th 2005 (before noon). The selected Fisher stations have ID numbers 884, 886, 888 and 893.

discovery).

7.2.2 Including statistical uncertainties: The Rolke approach

The Feldman&Cousins treatment needs to have a fairly precise knowledge of the background rate, which can be estimated either from the data or through Monte-Carlo simulations. Indeed, in many cases it is not possible to ignore the uncertainty in the background estimation and the method can fail if this uncertainty is high [182]. The extension of the problem to the case of a signal with a Poisson distribution, a background with either a Poisson or a Gaussian distribution and an efficiency with either a Binomial or a Gaussian distribution has been studied by Rolke and others [183].

The method is implemented in a ROOT class [184]. For no signal observed and with the assumption of zero background, the 90% confidence belt on the number of signal events is [2.21, 0], assuming a Poisson distribution for both, signal and background.

It is worth to mention that despite the fact that this method has an additional uncertainty, the upper limit is smaller than the one obtained by the Feldman&Cousins treatment. This apparent paradox is explained if one considers the question whether a single detected event observed in the signal region is a signal or a background event. Using the Feldman&Cousins the answer is clear: having assumed zero background, the event has to be signal. In fact, the treatment also quotes a lower limit greater than 0. On the other hand, in the Rolke approach zero background has to be understood as a Poisson number. It is therefore still possible that the event in the signal region is in fact a background event. Then, it should come as no surprise that in those cases the method quotes smaller upper (and lower) limits than the Feldman&Cousins. This effect is even more clear if one candidate were found in the data sample, in which case the confident belt would become [3.65, 0]. Note that with this treatment one candidate is still compatible with no signal.

7.2.3 Including systematic uncertainties: The Conrad approach

Neither the Feldman&Cousins nor the Rolke method account for systematic uncertainties both in the signal and background efficiencies as well as theoretical uncertainties in the background prediction. The method proposed by Conrad [177] accounts for them by integrating over the probability density functions parametrizing the uncertainties. The method is based in the likelihood ratio ordering (proposed by Feldman&Cousins) and allows one to use newer ordering schemes. It is, therefore, a semi-Bayesian extension of the Feldman&Cousins treatment.

The systematic uncertainty on the neutrino exposure was estimated in this work to [−12%, +21%] as reported in table 6.2. Assuming zero signal and no expected background events, the upper and lower limits at 90% C.L. are:

$$\begin{aligned} N_{\mathrm{Up}}^{90\%\mathrm{CL}} &= 2.37 \\ N_{\mathrm{Low}}^{90\%\mathrm{CL}} &= 0.00 \end{aligned} \tag{7.3}$$

These numbers are obtained under the assumption of a uniform PDF function to characterize the exposure and a Gaussian PDF to characterize the background. Since the positive systematic on the exposure is bigger in absolute value than the negative one, the upper limit is smaller than the one quoted by following the Feldman&Cousins method. In the case 1 candidate event is assumed, the confident belt becomes [4.14, 0.11].

7.2.4 Calculation of the Integral and Diffuse Limits to the flux

Once the confident belt for the expected number of events is computed by the Conrad procedure described above, the limit to the constant k of the incoming flux can be easily computed by resolving equation 7.2. A relevant information that has to be computed together with the central value of $k_{\rm Up}^{90\%\rm CL}$ concerns its *range of validity*. Even though the integration in equation 7.2 is performed between $E_{\rm min}$ ($10^{17.5}$ eV) and $E_{\rm max}$ ($10^{20.5}$ eV), the $k_{\rm Up}^{90\%\rm CL}$ limit will be valid in a smaller energy window. Indeed, one could extend the integration to smaller (up to zero) or bigger (up to infinity) values of the energy, but this would not change significantly the final limit since the contribution of the extended energy range becomes negligible given the E_ν^{-2} factor and the fact that $\xi(E_\nu)$ rapidly decreases for small energy values. The adopted criteria to define the applicability of the $k_{\rm Up}^{90\%\rm CL}$ limit consists on finding the energy range over which 90% of the events are expected for a neutrino flux $J(E_\nu) \propto E_\nu^{-2}$.

The quoted value on the integral limit to the diffuse flux of UHEν_s at 90% C.L., for zero candidates found and assuming zero background events, is:

$$k_{\rm Up}^{90\%\rm CL} = 6.3 \times 10^{-7} \qquad \text{GeV cm}^{-2}\ \text{s}^{-1}\ \text{sr}^{-1} \tag{7.4}$$

$$\text{for the energy range } \; E_\nu \in [1.9 \times 10^{18} - 2.0 \times 10^{20}] \text{ eV}$$

This result is indicated in figure 7.7 by the horizontal black line, which extends over the energy range covering the 90% of the events as mentioned above. Dashed lines represent theoretical predictions for cosmogenic and astrophysical neutrinos.

Another standard way of presenting the results on neutrino searches is the so called *differential limit*. In this less model dependent format, it is assumed that the diffuse neutrino flux follows a E_ν^{-2} dependence within energy bins of given width on a given energy scale. In our case, the bin width is 0.5 on decimal logarithmic scale ($\Delta \log_{10}(\rm E_\nu/eV) = 0.5$). Therefore, the 90% C.L. differential limit on the neutrino flux (no candidates found and zero background expected) for the *i-th* energy bin is:

$$\begin{matrix}\text{differential limit} \\ \text{(i-th } E_\nu \text{ bin)}\end{matrix} = \frac{N_{\rm Up}}{\displaystyle\int_{\log_{10}(E^i-(\Delta \log_{10} E)/2)}^{\log_{10}(E^i+(\Delta \log_{10} E)/2)} E_\nu^{-1} \cdot \xi(E_\nu) \cdot \ln(10) \cdot d(\log_{10}(E_\nu))} \tag{7.5}$$

Alternatively, a rough estimate of the differential upper limit can be obtained in a more simplistic way by assuming that both the E_ν^{-2} flux and the exposure are constant in each energy interval. Under this approximation the differential limit is given by:

$$\begin{matrix}\text{Approx. differential limit} \\ \text{(i-th } E_\nu \text{ bin)}\end{matrix} = \frac{N_{\rm Up}}{E_\nu^{-1} \cdot \xi_{(E_\nu)} \cdot \ln(10) \cdot \Delta(\log_{10}(E_\nu))} \tag{7.6}$$

The differential limit obtained including systematic uncertainties is shown in figure 7.7 (small horizontal black lines) together with some theoretical predictions on UHEν fluxes.

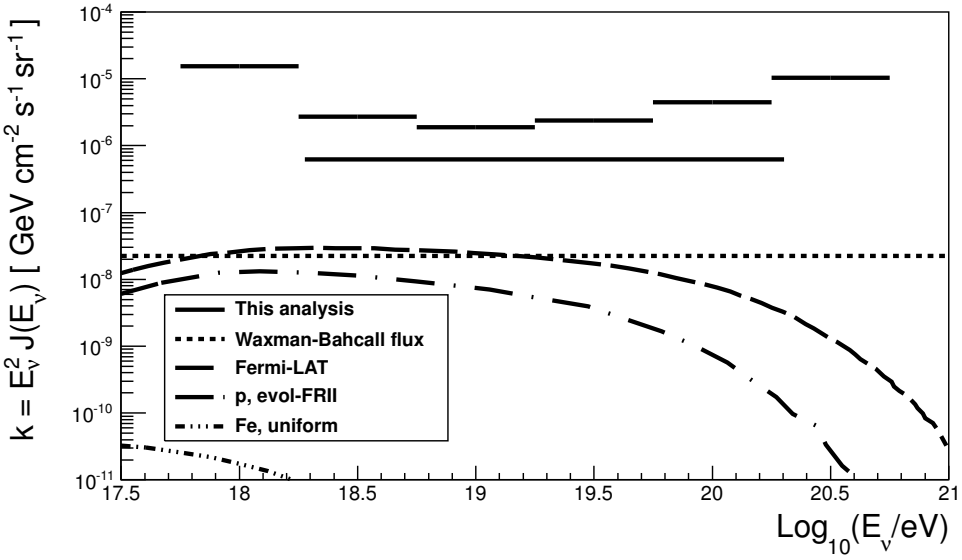

Figure 7.7: Differential (sort lines) and integral upper limits (90% C.L.) for a diffuse flux of down-going ν in the period from 1 Jan 2004 to 31 May 2010 scanning the angular region $58.5° < \theta_{\rm Rec} \leq 76.5°$. Predictions of three calculations of cosmological flux [56, 57] together with the astrophysical Waxman-Bahcall [68] flux are also plotted.

7.3 On the combination of the *low* and *high* zenith angle neutrino analyses

In this section we present a first attempt for the combination of the *low angle* analysis ($\rm DG_{low}$ hereafter) described in this Ph.D. thesis and designed to search for UHEν_s in the region $\theta \sim 60° - 75°$, with the *high angle* analysis [3] ($\rm DG_{high}$ in the following) optimized in the $75° - 90°$ zenith angular range. Several questions have to be addressed when combining the two analyses. For instance, how to deal with the (tiny) angular region shared by them, the use of a common angular reconstruction algorithm, the estimation of the background, or the calculation of the common systematics to be included in the limit calculation. All these considerations are currently under careful investigation inside the Auger Collaboration.

7.3.1 Brief summary of the $\rm DG_{high}$ neutrino analysis

The search for UHEν_s with the Pierre Auger Observatory in the $\theta \in [75° - 90°]$ angular range is described with detail in [3]. The analysis is based in the selection of very inclined young showers. The selection of nearly horizontal showers is made by requesting a reconstructed zenith angle larger than 75° and in the same way, putting an upper bound of 0.313 m ns^{-1} on the mean ground speed of the shower front ($\langle V \rangle$). As an extra quality cut the event is rejected if the relative spread of its ground speed is larger than 0.08%. Also the "footprint" (configuration of triggered stations on ground) is requested to be elongated. For this purpose an inertia tensor with the position of the stations weighted by their signal is constructed. Both eingenvalues of the tensor correspond to magnitudes which are proportional to the length L and the width W of the footprint, and a cut on the minimum value of L/W is imposed. The neutrino selection is based in a Fisher discriminant method using the AoP of the first four stations, an asymmetry

	DG_{low} cuts	DG_{high} cuts
Inclined Selection	$58.5° < \theta_{Rec} \leq 76.5°$	$\theta_{Rec} > 75°$ $\langle V \rangle < 0.313$ m ns^{-1} RMS(V)/ $\langle V \rangle < 0.08\%$ $L/W > 3$
Young Shower Selection	ToT fraction	Fisher AoP
Neutrino Selection	Fisher AoP of T5 stations	of early stations

Table 7.2: Summary of the selection cuts applied on the two downward-going neutrino analyses.

variable between the AoP of the first and the last stations and combinations of the AoP. Three independent Fishers are trained depending on the multiplicity (number of triggered stations) of the event. Table 7.2 summarizes the whole selection procedure of the DG_{high} analysis.

7.3.2 Combined Exposure and Limit

The *low* and *high* angular regions exhibit a *target mass* for the interaction of neutrinos which is clearly favourable to the second region. We remind here that the effective target mass of the SD array to the neutrino detection is computed by integrating not only on the zenith angle (equation 6.1) but also on the interaction depth D (equation 6.2), which extends over much larger distances in the *high* angular region. A rough calculation assuming full efficiency to neutrino detection in the range of injection depths where Monte-Carlo neutrinos were simulated for the two analyses gives a factor 2 more target mass for the *high* region as compared to the *low* region.

The unified analysis should clearly ensure that no overlapping is produced between the two analyses, i.e. should exclude any over-counting of events that can appear in the (very small) shared angular region, close to the border at $\theta \sim 75°$ and which could artificially overestimate the final exposure. This is achieved by applying to each event the DG_{high} *inclined selection*: if the event passes the cuts, it is then processed (only) through the DG_{high} neutrino selection; otherwise, the DG_{low} inclined selection is applied. At this point it is worth noticing that the two different reconstruction algorithms are currently used on the two analyses. On the DG_{low} selection, the standard reconstruction for vertical showers implemented in the $\overline{\text{Off}}\underline{\text{line}}$ package is used, whereas a dedicated reconstruction algorithm optimized for neutrino detection at very high angle is adopted in the DG_{high} selection. Tests on differences between the two methods are under study in view of defining a common angular reconstruction.

Following this approach, table 7.3 gives the quoted exposures for the search period up to 31 May 2010, for the two independent analyses and for the combination (see also figure 7.8). Values on the DG_{high} column have been recomputed by us by re-scaling the numbers published in [3] with the ν interaction cross-section proposed in [80] (the reference used in this thesis). As discussed in section 6.1 the DG_{low} exposure is strongly suppressed at the lower energies but exhibits a significant contribution above $\sim 10^{19.5}$ eV, extending the sensitivity of the detector at the highest energies. The exposure of the DG_{high} analysis at low energy is enhanced thanks to the contribution of low energy showers producing long elongated patterns at very high angles triggering the array.

Before computing the combined limit, a consideration can be done on the background estimation. For a combined analysis it is desirable, even though not mandatory, that the two searches apply the same convention to estimate the contribution from background events and even the final number on the estimated background to be similar. In our case, the two analyses use

$log_{10}(E_\nu/eV)$	Exposure (cm^2 s sr)		
	DG_{low} $60^\circ < \theta_{Rec} \leq 75^\circ$	DG_{high} $75^\circ < \theta_{Rec} \leq 90^\circ$	Combined $60^\circ < \theta_{Rec} \leq 90^\circ$
16.75	–	$1.68 \cdot 10^{13}$	$1.68 \cdot 10^{13}$
17.0	–	$8.76 \cdot 10^{13}$	$8.76 \cdot 10^{13}$
17.5	$3.81 \cdot 10^{11}$	$9.21 \cdot 10^{14}$	$9.21 \cdot 10^{14}$
18.0	$1.34 \cdot 10^{14}$	$4.55 \cdot 10^{15}$	$4.68 \cdot 10^{15}$
18.5	$2.39 \cdot 10^{15}$	$1.28 \cdot 10^{16}$	$1.52 \cdot 10^{16}$
19.0	$1.09 \cdot 10^{16}$	$2.55 \cdot 10^{16}$	$3.62 \cdot 10^{16}$
19.5	$2.73 \cdot 10^{16}$	$4.18 \cdot 10^{16}$	$6.88 \cdot 10^{16}$
20.0	$4.57 \cdot 10^{16}$	$6.62 \cdot 10^{16}$	$1.11 \cdot 10^{17}$
20.5	$6.20 \cdot 10^{16}$	–	$6.20 \cdot 10^{16}$

Table 7.3: Exposure of the surface detector array on the data search period (up to 31 May 2010) to downward-going neutrinos on the DG_{low}, DG_{high} and combined analysis accounting for all neutrino channels. DG_{high} data from [3] rescaled by us using ν interaction cross sections from [80].

Analysis (statistical method)	DG_{low} $60^\circ < \theta_{Rec} \leq 75^\circ$ Conrad	DG_{high} $75^\circ < \theta_{Rec} \leq 90^\circ$ Conrad	Combined $60^\circ < \theta_{Rec} \leq 90^\circ$ Feldman&Cousins
Limit $k_{Up}^{90\%CL}$ (GeV cm^{-2} s^{-1} sr^{-1})	$< 6.3 \cdot 10^{-7}$	$< 1.54 \cdot 10^{-7}$	$< 1.15 \cdot 10^{-7}$
Energy range (EeV) $\sim$	[1.9, 200]	[0.13, 50]	[0.16, 75]

Table 7.4: Summary of integral limits at 90% C.L. to the diffuse flux of UHEνs (single flavour assuming equipartition) for the DG_{low}, DG_{high} and combined analysis in the search period (up to 31 May 2010). The energy range where the limits apply are indicated in the last row.

an exponential extrapolation to estimate the behaviour of the tail of the background distribution (see figure 7.2). On the other hand, the predicted number of events in 20 years of full Auger data is 1 for DG_{low} and 3 for DG_{high}.

The numerical values of the 90% C.L. limit to the normalization k of a diffuse flux of UHEν_s assumed to behave with energy as $J(E_\nu) = kE_\nu^{-2}$ are shown in table 7.4. In the last row we indicate the energy range where the limits apply, typically the energy interval where 90% of the events are expected. In the case of the DG_{low} and DG_{high} limits, the systematic uncertainties are included in the value of the limit following in both cases the semi-Bayesian approach described in section 7.2.3. Even though the two analyses suffer from common systematic uncertainties, in absence of a precise estimation of the combined analysis systematic and cross-correlations (this is currently the subject of study inside the Collaboration), the combined limit has been computed following the Feldman&Cousins approach described in section 7.2.1. Regardless of the moderate improvement on the absolute value of $k_{Up}^{90\%CL}$ ($\sim$30%), the contribution of the DG_{low} analysis on extending the sensitivity of the Pierre Auger Observatory to the detection of UHEν_s at the highest energies is notable. As a consequence, the sensitivity to neutrino fluxes with spectral index γ smaller than -2 assumed here ($J(E_\nu) \propto E_\nu^{-\gamma}$) is also enhanced.

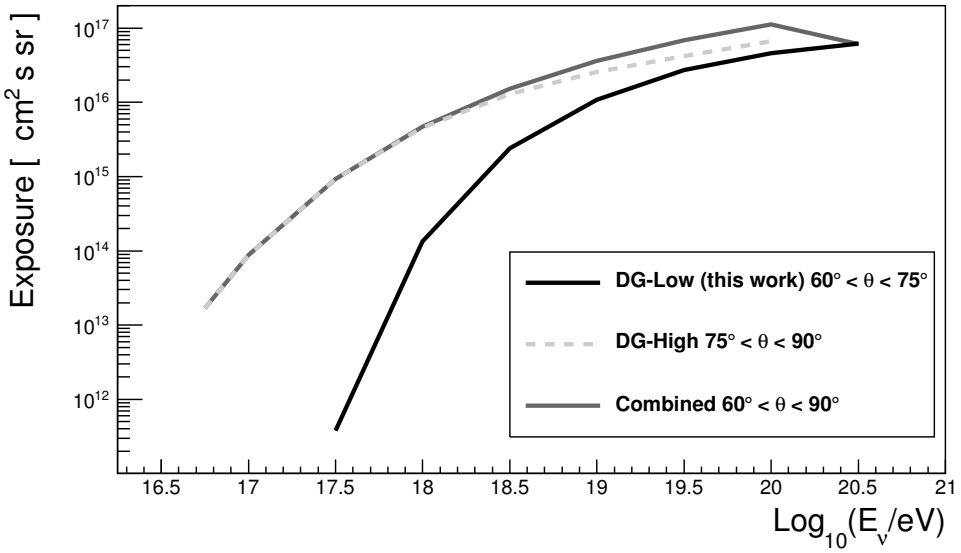

Figure 7.8: Exposure of the surface detector array on the data search period (up to 31 May 2010) to downward-going neutrinos on the DG_{low}, DG_{high} and combined analysis accounting for all neutrino channels (see also table 7.3).

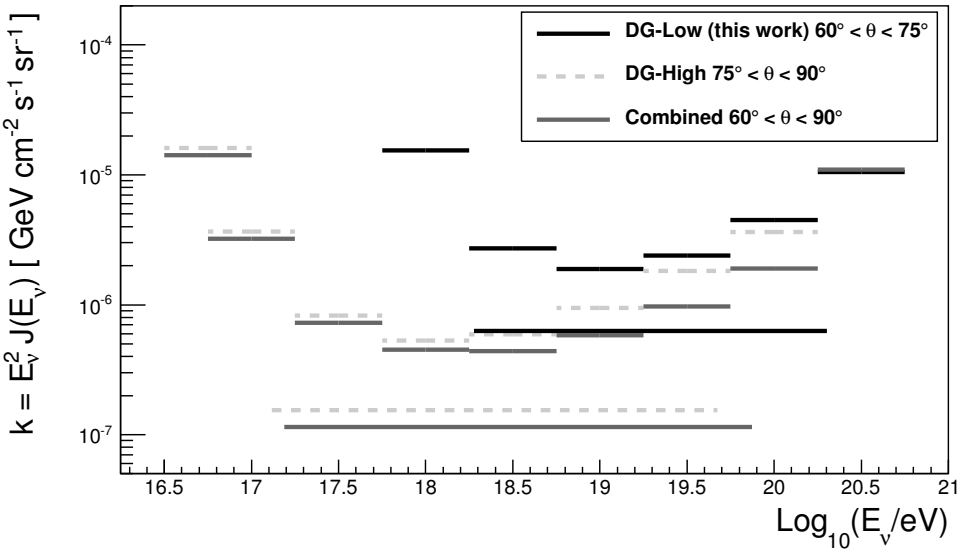

Figure 7.9: Differential (sort lines) and integral upper limits at 90% C.L. to the diffuse flux of UHEνs (single flavour assuming equipartition) from the DG_{low}, DG_{high} and combined analysis in the search period (up to 31 May 2010).

Part III

Sensitivity to Point Sources from downward-going and Earth-skimming neutrinos

8

Improved Limit on the Diffuse Flux of Earth-skimming Tau Neutrinos

The Pierre Auger Collaboration published in PRL [185] and PRD [4] an analysis to search for UHE tau neutrinos entering the Earth just below the horizon (the so called Earth-skimming ν_τ channel). No τ neutrino candidates were found by this analysis in data collected from 1 January 2004 to 30 April 2008 and a limit to the diffuse neutrino flux was computed.

In this chapter we present an update of the results obtained on the search for Earth-skimming tau neutrinos in a larger data sample which extends from 1 January 2004 until 31 May 2010, i.e. 3.5 years of full Auger equivalent time. The same analysis cuts defined in [4] are used here. On contrary, the treatment of the tau polarization is revised: tau leptons simulated in this work are fully polarized according to its electrical charge. We anticipate here that no events pass the selection cuts in the new search sample. In section 8.1 a short review on the published Earth-skimming analysis is presented, whereas the discussion on the time evolution of the Auger exposure to ν_τ events and the obtained limits to the flux is given in section 8.2.

It is worth mentioning here that the sensitivity of the Auger SD array to the detection of UHE tau neutrinos coming from point-like sources was also evaluated in this work (see chapter 9). This novel study, complementary to the downward-going analysis presented in the same chapter, extends the point source search to zenith angles below the horizon ($\theta \in 90°$–$95°$). The results on the search for point-like sources of UHE tau neutrinos together with the improved limit on the diffuse flux with the extended statistics presented in this Ph.D. thesis were recently published in [106].

8.1 Brief summary of the Earth-skimming ν_τ analysis

The Earth-skimming ν_τ diffuse search analysis is explained with detail in PRL [185] and PRD [4]. The simulation of astrophysical neutrino events is essential for the determination of the signal detection efficiency and thereby for the calculation of flux limits or detected fluxes. Three separate calculations based on Monte-Carlo techniques can be identified. The first one deals with incident neutrinos entering the Earth which may interact by NC or CC. If the later occurs, the generated τ lepton can emerge from Earth and its energy, direction and decay position are stored. The second one involves the tau decay in flight and the development of an up-going

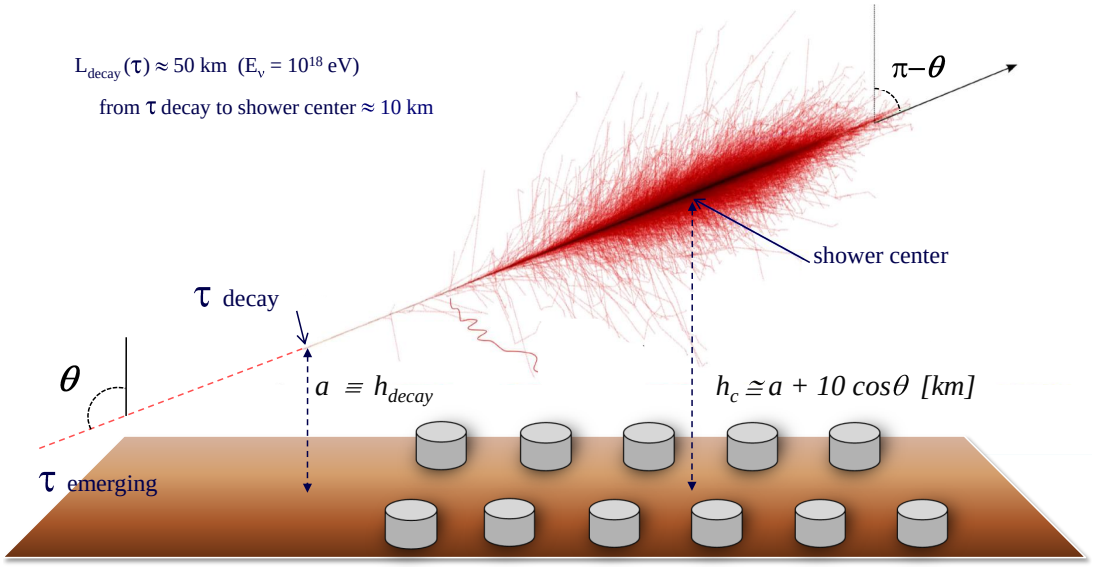

Figure 8.1: Sketch with the geometry of the induced τ shower. The definitions of the τ decay height (a) and shower center (h_c) as well as their relation with the zenith angle (θ) are also given.

atmospheric shower (figure 8.1). And finally, a third one dedicated to simulate the tank response to the through-going particles.

The applied *selection criteria* are summarized in table 8.1. Note that the ToT cut in the young shower selection is defined by requiring that the signal after cleaning of the FADC trace has at least 13 bins above 0.2 VEM and the ratio of the integrated signal over the peak height exceeds by a factor 1.4 the average ratio observed in signals of isolated particles.

Inclined shower selection:
Number of stations ≥ 3
0.29 m ns^{-1} < "average ground signal speed" < 0.31 m ns^{-1}
r.m.s. ground speed < 0.08 m ns^{-1}
shower footprint (Length / Width) > 5
Young shower selection:
Fraction of triggered stations with Offline ToT > 0.6
For closest station to barycenter: first crown with > 4 active stations
≤ 3 speeds between pairs of ToT stations satisfying: 0.285 m ns^{-1} < v_{ij} < 0.31 m ns^{-1}

Table 8.1: Summary of the Earth-skimming ν_τ analysis cuts [4].

Regarding the calculation of the *exposure* to ν_τ-induced showers, the geometry considered in the Earth-skimming simulations is depicted in figure 8.2. For a parallel flux of $N_{\rm sim}$ mono-energetic neutrinos crossing the Earth with equal probability in terms of $\sin^2\theta$, the simulations provide a realisation of the differential probability of an emerging τ as a function of tau

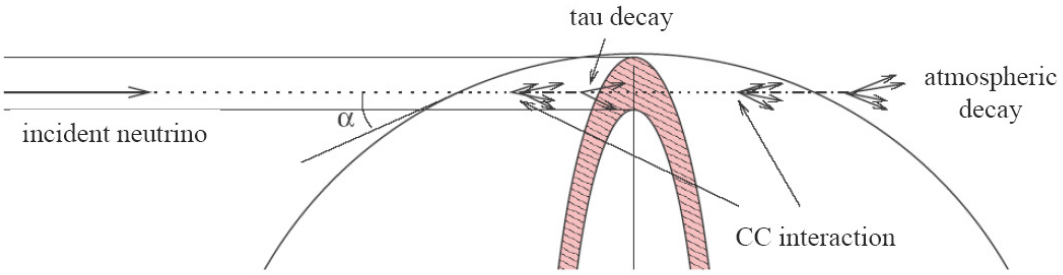

Figure 8.2: Geometry considered in the Earth-skimming ν_τ simulations.

energy E_τ, tau decay altitude a and $\sin^2\theta$. In the following, this differential probability is denoted by $d^3p_\tau/dE_\tau d\sin^2\theta da$, while the realisation provided by the simulations is denoted by $d^3p_\tau^{\rm MC}/dE_\tau d\sin^2\theta da$. The relationship between both expressions is:

$$\frac{d^3p_\tau}{dE_\tau d\sin^2\theta da} \simeq \frac{1}{N}\frac{d^3p_\tau^{\rm MC}}{dE_\tau d\sin^2\theta da} \tag{8.1}$$

where N is the total number of injected neutrinos crossing the Earth. Actually, since any incoming neutrinos with an incident angle α greater than $\alpha_m = 0.3$ rad has no chance to produce an emerging τ that produces an observable shower at ground level, incident angles in simulations are restricted between 0 and α_m so that the effective number of events normalising the realisation is $N = N_{\rm sim}/\sin^2\alpha_m$ where $N_{\rm sim}$ is the actual number of injected neutrinos crossing the Earth crust between 0 and α_m:

$$\frac{d^3p_\tau}{dE_\tau d\sin^2\theta da} \simeq \frac{\sin^2\alpha_m}{N_{\rm sim}}\frac{d^3p_\tau^{\rm MC}}{dE_\tau d\sin^2\theta da} \tag{8.2}$$

The directional exposure[1] $\xi(E_\nu,\theta)$ to ν_τ-induced showers with energy E_ν and zenith angle θ is obtained by folding these simulations to the effective detection surface $S_{\rm eff}$ of the SD array:

$$\xi(E_\nu,\theta) = \int_0^{E_\nu} dE_\tau \int_0^\infty da\, \frac{d^3p_\tau}{dE_\tau\, da\, d\sin^2\theta}\, S_{\rm eff}(E_\tau,\theta,a) \tag{8.3}$$

$$\simeq \frac{\sin^2\alpha_m}{N_{\rm sim}}\frac{1}{\sin 2\theta}\int_0^{E_\nu} dE_\tau \int_0^\infty da\, \frac{d^3p_\tau^{\rm MC}}{dE_\tau\, da\, d\theta}\, S_{\rm eff}(E_\tau,\theta,a) \tag{8.4}$$

The effective detection surface $S_{\rm eff}$ accounts for the evolution of the SD array with time as well as the instabilities of each station, by integrating the probability ϵ to identify a τ (including the detection efficiency which depends on E_τ and θ) over the position of the shower in the array (x,y) and on the instantaneous configuration of the array at time t (denoted below as $SD(t)$):

$$S_{\rm eff}(E_\tau,\theta,a) = \int_{\Delta T} dt \int_S dx\, dy\, \epsilon(E_\tau,\theta,a;x,y,SD(t)) \tag{8.5}$$

[1]Here, we assume a constant exposure in terms of the azimuthal angle so that we drop the azimuth label.

Actually, it is observed that the SD detection efficiency as function of the height of the shower center[2] (h_c) shows a common dependence for any fixed zenith (θ) or height of the τ decay (a). Moreover, as pointed out in [186] the altitude of the shower center can be written as:

$$h_c = a + \cos(\theta) \cdot 10 \text{ km} \tag{8.6}$$

Therefore, there is effectively only one relevant geometrical parameter determining the efficiency of trigger and identification. The procedure to calculate the exposure $\xi(E_\nu)$ in the case of *diffuse neutrino fluxes* has been described with detail in [185, 4]. We remind here that in order to add contributions from the whole sky, an integration in solid angle has to be performed:

$$\begin{aligned}
\xi(E_\nu) &= 2\pi \int_{\pi/2+\alpha_m}^{\pi/2} d\theta \, \cos\theta \, \sin\theta \int_0^{E_\nu} dE_\tau \int_0^{\infty} dh_c \, \frac{1}{\sin 2\theta} \frac{d^3 p_\tau}{dE_\tau \, dh_c \, d\theta} \left| \frac{\partial(E_\tau, \theta, h_c)}{\partial(E_\tau, \theta, a)} \right| S_{\text{eff}}(E_\tau, h_c) \\
&= \pi \int_0^{E_\nu} dE_\tau \int_0^{\infty} dh_c \, \frac{d^2 p_\tau}{dE_\tau \, dh_c} \, S_{\text{eff}}(E_\tau, h_c) \\
&\simeq \frac{\pi \sin^2 \alpha_m}{N_{\text{sim}}} \int_0^{E_\nu} dE_\tau \int_0^{\infty} dh_c \, \frac{d^2 p_\tau^{\text{MC}}}{dE_\tau \, dh_c} \, S_{\text{eff}}(E_\tau, h_c) \\
&\simeq \frac{\pi \sin^2 \alpha_m}{N_{\text{sim}}} \sum_{i=1}^{N_{\text{success}}} S_{\text{eff}}(E_\tau^i, h_c^i)
\end{aligned} \tag{8.7}$$

As mentioned in the introduction of this chapter, the sensitivity of Auger to point-like neutrino sources on the Earth-skimming channel has been also explored for the first time. The details of such analysis are given in chapter 9 of this document.

8.2 Exposure and Limit to the Diffuse ν_τ Flux

In [4], the central values of the exposures for Earth-skimming ν_τ detection were computed using not polarized tau leptons. The choice of the tau polarization influences the energy distribution among the tau decay products and hence the final detection efficiency. The most and least favourable cases in the range of possible polarizations were used in [4] to estimate the uncertainty associated to this parameter, resulting on a fluctuation on the final exposure not larger than $^{+17\%}_{-10\%}$.

The updated work presented in this Ph.D. thesis considers fully polarized tau events according to its electrical charge, removing from the systematic calculation any contribution related to the tau polarization uncertainty.

In order to evaluate the impact of the τ polarization on the final integral diffuse limit, we have recomputed the limits for the same search periods of the PRL [185] and PRD [4] publications, but with fully polarized taus ($\tau_{\text{polarized}}$). The comparative result is shown in the first two columns of figure 8.3. As expected, the total systematic uncertainty[3] quoted for the not polarized scenario contains the central limit value of the fully polarized scenario. Moreover, the full polarization case gives a small worsening of the limit.

[2] The shower center is very close to the maximal lateral extension of the tau decay shower for the energies relevant in this analysis.

[3] Several sources of systematic uncertainty are considered: shower simulation, topography, neutrino interaction cross section, tau energy losses, etc.

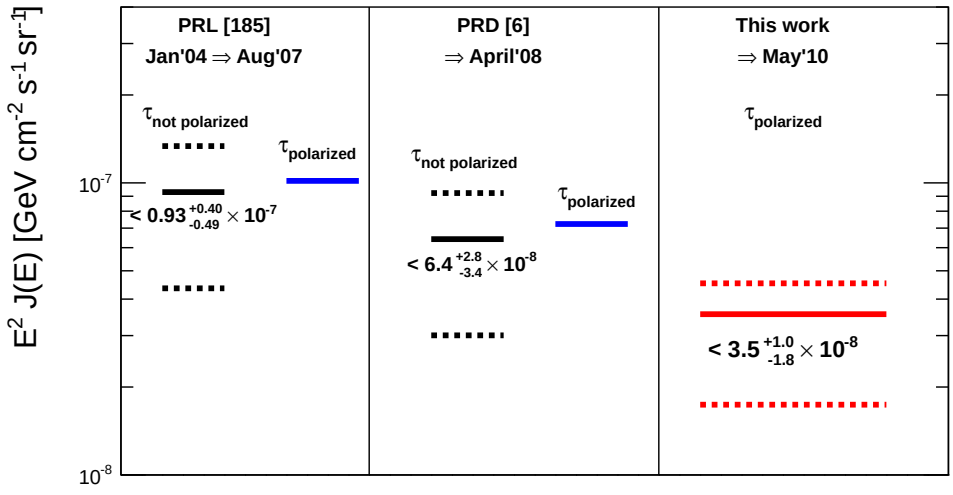

Figure 8.3: Comparison of diffuse Earth-skimming ν_τ integral limits: PRL [185] and PRD [4] computed with not polarized taus; fully polarized taus ($\tau_{\text{polarized}}$) recomputed in this work for the same search data periods; and update of the limit until May 2010 with fully polarized taus (Nov'04 and Dec'04 search sample excluded). Solid lines refer to central limit values while dotted lines indicate the upper and lower total systematic bounds.

8.2.1 The SD Exposure

In this work, the neutrino *search period* has been extended from 1 January 2004 until 31 May 2010 with negative result: no events in the Auger SD data pass the selection cuts.

Due to the fact that the SD array has a dynamic configuration (detector incomplete and growing until 2008, blank tanks, instability periods, etc.) the 75 months covered by the search period[4] correspond to a smaller sample if one normalizes to the so called *full Auger* detector, i.e. to a complete and fully operational SD array.

In table 8.2 the 1 year full Auger exposure (third column) is compared to the search period accumulated exposure for each neutrino energy bin. The values are also plot in figure 8.4. The distance between the two sets of points is an almost constant factor close to 3.5, giving a first hint on the value of full Auger accumulated time ($\mathtt{T}_{\mathtt{full\ Auger}}$).

The time evolution of the exposure from 2004 until 2010 is shown in figure 8.5 where a quick increase of the exposure is appreciated in the first years of data taking due to the fast growing of the SD array. On the other hand, the 2009 contribution to the exposure appears to be smaller than expected because of a big period of instabilities in the SD.

The increase of the SD array active surface with time and how it affects the tau acceptance is even more clear from figure 8.6. In this plot, the value obtained for the second month of each year is divided by the value obtained for one month with an ideal full Auger detector (taken as reference). Despite statistical fluctuations, an increase on the acceptance of about a factor 2 per year is observed until 2008, when the detector was completed. Then, a saturation is reached. The top triangles in the graph trace the maximum reachable value in ideal conditions. As expected, data points beyond 2008 approach this optimal value at the highest energies (above $\sim 10^{18}$ eV) where the event tank multiplicity is higher and the ν detection efficiency less affected by missing stations.

[4]Note that November and December 2004 were used as training sample to define the selection cuts and are therefore excluded from the exposure calculation.

$\log_{10}(\mathbf{E_\nu}$ / eV)	$\mathbf{E_\nu}$ [EeV]	**Full Auger Exposure** (1 year) [cm^2 s sr]	**Current Auger Exposure** (Jan 04 – May 10) [cm^2 s sr]	**Current Auger Differential limit** ($E^2 \cdot \frac{dN}{dE}$) (Jan 04 – May 10) [GeV cm^{-2} s^{-1} sr^{-1}]
17.0	0.1	9.4×10^{13}	30.9×10^{13}	5.3×10^{-7}
17.5	0.316	1.6×10^{14}	53.3×10^{14}	1.3×10^{-7}
18.0	1.0	5.4×10^{15}	19.1×10^{15}	1.2×10^{-7}
18.5	3.16	10.9×10^{15}	38.8×10^{15}	1.8×10^{-7}
19.0	10.0	16.7×10^{15}	59.9×10^{15}	3.5×10^{-7}
19.5	31.6	20.8×10^{15}	75.1×10^{15}	8.7×10^{-7}
20.0	100.0	22.1×10^{15}	79.8×10^{15}	2.5×10^{-6}
20.5	316.0	22.5×10^{15}	81.3×10^{15}	1.2×10^{-5}

Table 8.2: Accumulated exposure to Earth-skimming ν_τ events integrated over time for a full SD array (1 year) and for the real detector over the search period (from 1 January 2004 until 31 May 2010). The last column gives the obtained differential limit assuming a E_ν^{-2} flux (eq. 7.5).

8.2.2 Integral and Differential limits

Based on the computed exposures reported in table 8.2, a limit on the neutrino diffuse flux can be derived (see equation 7.2). Since zero candidates are found and assuming zero background events, the upper limit on the number of signal events is $N_{\rm Up} = 2.44$ at 90% C.L. following the Feldman&Cousins treatment described in section 7.2.1. Changing to a logarithmic binning, $dE = E \cdot \ln(10) \cdot d(\log_{10}(E))$, the upper limit on the value of k is:

$$k_{\rm Up}^{90\%\rm CL} < \frac{2.44}{\int_{\log_{10}(E_{\rm min})}^{\log_{10}(E_{\rm max})} E_\nu^{-1} \cdot \xi(E_\nu) \cdot \ln(10) \cdot d(\log_{10}(E_\nu))} \tag{8.8}$$

The denominator is computed with a multidimensional numerical integration algorithm which uses importance sampling for variance reduction [187]. The exposure as function of the energy has been estimated from the eight data points (table 8.2) using a combination of two kinds of interpolations in a ($\log_{10}(\xi(E_\nu))$, $\log_{10}(E_\nu)$) plane:

1. *Linear interpolation* (small blue dots in figure 8.4). This simple interpolation gives a good description of the exposure for energies above ∼1 EeV, where the behaviour is smooth. On contrary, straight lines seem to underestimate the exposure at the lowest energies, specially on the region between the first and second energy points (0.1–0.5 EeV).

2. *Exponential interpolation* (dashed line in figure 8.4). In order to improve the estimation of the exposure on the low energy region, the first three data points were fit to an exponential function[5] and the obtained parameters used as interpolator in the region between 0.1 and 1 EeV. For energies above 1 EeV the linear interpolation was used.

[5] $\xi(E_\nu) = \mathrm{a} - \mathrm{b} \cdot e^{(-\mathrm{c} \cdot E_\nu)}$

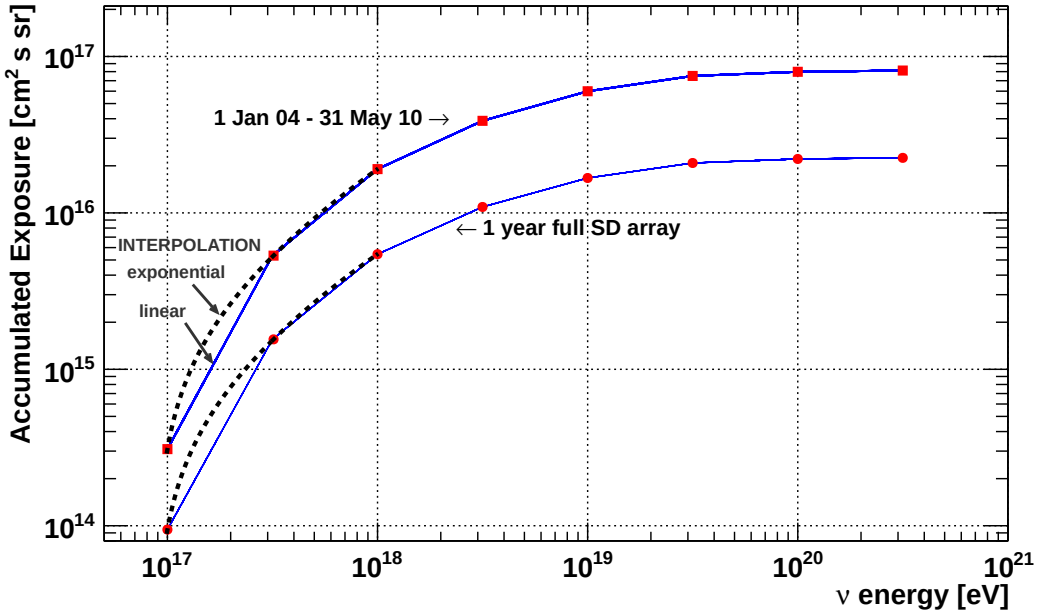

Figure 8.4: Earth-skimming ν_τ accumulated exposure expected for a full Auger SD array in 1 year of data taking (dots) and computed for a dynamic real array from 1 January 2004 to 31 May 2010 (squares). Values computed at the eight scanned energy bins (table 8.2). Two kinds of linear interpolations between data points are used: linear (small blue dots) and from an exponential function fit (dashed line).

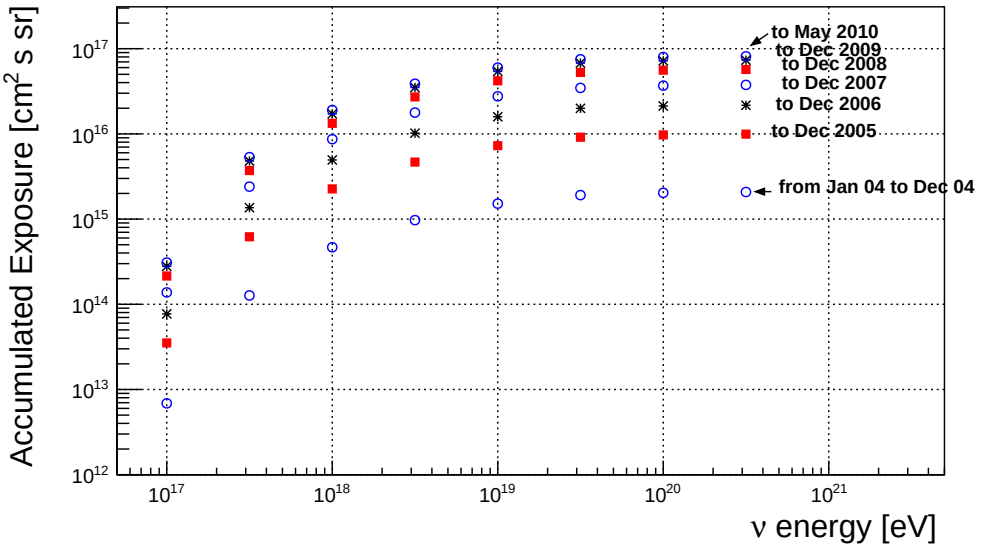

Figure 8.5: Earth-skimming ν_τ accumulated exposure as function of the energy computed for a dynamic real array from 1 January 2004 adding up annual contributions until 31 May 2010.

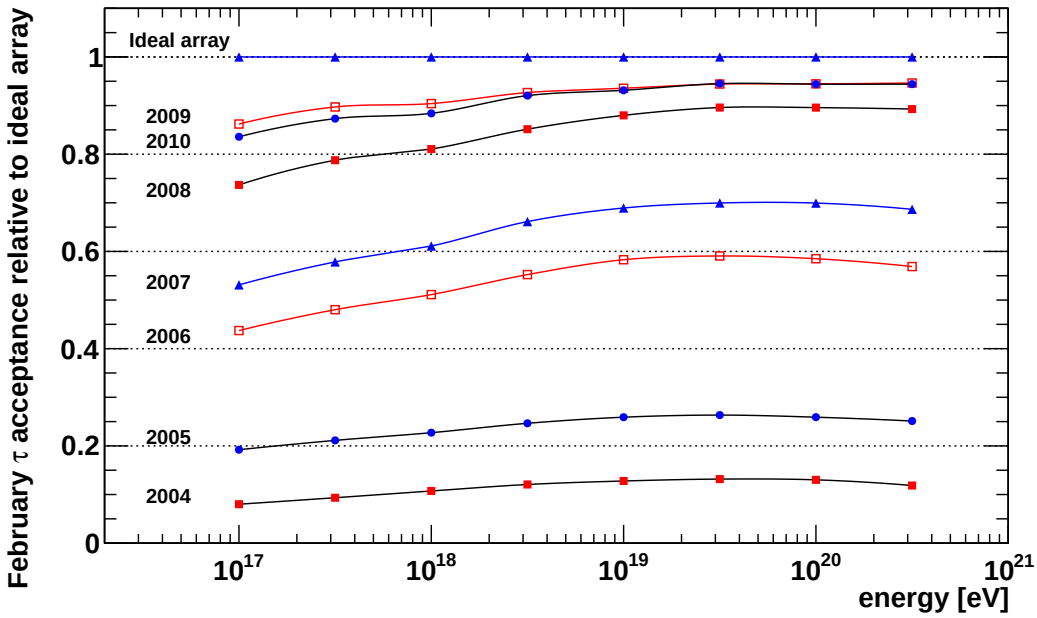

Figure 8.6: One month tau acceptance (February) for different years divided by the 1 month full Auger SD array acceptance for each energy bin.

The use of this combined interpolation (exponential below and linear above 1 EeV) slightly increases the estimated exposure at the lower energies as compared to the simple linear interpolation in the whole energy range, improving the final limit on $k_{\rm Up}^{90\%\rm CL}$ by a $\sim$7%.

Table 8.3 summarizes the diffuse integral limits (upper bounds in $k_{\rm Up}^{90\%\rm CL}$) obtained for an ideal full SD array in 1 year of data taking (which gives the *sensitivity* of the detector), and the one reached after the integration over the search period for a real dynamic SD array (which gives the *real* limit). In both cases, the central limit value is shown together with the most pessimistic and optimistic scenarios given by the upper and lower contributions of the systematic uncertainties of the analysis.

The way we compute the *equivalent period in units of full Auger years* ($\mathtt{T}_{\mathtt{full\ Auger}}$) is the following: we first quote the 1 year sensitivity of the SD array by computing the diffuse limit with a 1 year full Auger configuration $k_{\rm full\ Auger}^{90\%\rm CL}$. Then, for a given diffuse limit, obtained through the search period time integration with the real dynamic SD configuration ($k_{\rm current\ Auger}^{90\%\rm CL}$), the equivalent period is simply:

$$\mathtt{T}_{\mathtt{full\ Auger}} = \frac{k_{\rm full\ Auger}^{90\%\rm CL}}{k_{\rm current\ Auger}^{90\%\rm CL}} \qquad [\text{years}] \tag{8.9}$$

The ratio between the two central limit values results in a *search period equivalent to 3.5 full Auger years*. The error on this number, found to be below 3%, is estimated through the comparison of a number of $k_{\rm full\ Auger}^{90\%\rm CL}$ limits calculated over several years. Even though the detector configuration remains the same (full SD), the final value of the limit might slightly vary between simulations due to the randomization of several parameters inside the exposure calculation procedure (the position of the shower core at ground, for instance).

		$k_{\rm Up}^{90\%\rm CL}$ limit [GeV cm^{-2} s^{-1} sr^{-1}]	
Full Auger (1 year)	Upper systematics	$< 16.0 \times 10^{-8}$	
	Central	$< 12.4 \times 10^{-8}$	$\Rightarrow < 12.4\,^{+3.6\,(\equiv+29\%)}_{-6.3\,(\equiv-51\%)} \times 10^{-8}$
	Lower systematics	$< 6.1 \times 10^{-8}$	
Current Auger ICRC'11 (Jan 04 – May 10)	Upper systematics	$< 4.53 \times 10^{-8}$	
	Central	$< 3.55 \times 10^{-8}$	$\Rightarrow < 3.55\,^{+0.98\,(\equiv+28\%)}_{-1.81\,(\equiv-51\%)} \times 10^{-8}$
	Lower systematics	$< 1.74 \times 10^{-8}$	
	semi-Bayesian		$\Rightarrow < 3.2 \times 10^{-8}$

Table 8.3: Earth-skimming ν_τ integrated diffuse limits calculated in this work for a 1 year full SD array configuration (full Auger) and for the real SD configuration along the search period (Current Auger). In the later case, the limit obtained with the semi-Bayesian [177] extension of the Feldman&Cousins [178] approach to include uncertainties in the exposure is also given.

In summary, the new updated limit computed from 1 Jan 2004 to 31 May 2010 equivalent to 3.5±0.1 full Auger years (labelled "This work" in figure 8.3) is:

$$k_{\rm Up}^{90\%\rm CL} < 3.5\,^{+1.0}_{-1.8} \times 10^{-8}\ \ {\rm GeV\,cm^{-2}\,s^{-1}\,sr^{-1}} \tag{8.10}$$

$$\text{for the energy range}\ \ E_\nu \in [1.6 \times 10^{17} - 20.8 \times 10^{18}]\ {\rm eV}$$

The upper ($\sim 30\%$) and lower ($\sim 50\%$) errors in the above limit come from several sources of systematic uncertainties that affect the analysis (see reference [4] for a detailed discussion). The new bounds in equation 8.10 and table 8.3 come from a recalculation of the systematics where the contribution from the tau polarization uncertainty has been removed. This result, together with other experimental limits, is presented in figure 8.7. The Auger Earth-skimming neutrino limit remains the strongest constraint to date on the cosmogenic UHEν flux at energies above $\sim 6 \times 10^{18}$ eV. Below this energy, the recent IceCube-40 results[6] improve the model independent limit down to 1.2×10^{-8} GeV cm^{-2} s^{-1} sr^{-1}.

Based on the results quoted in equation 8.10, the upper limit on the diffuse neutrino flux can be recomputed using a the semi-Bayesian extension of the Feldman&Cousins approach to include uncertainties in the exposure (section 7.2.3). If zero background events are assumed, the upper limit on the number of signal expected events results to be 2.24 at 90% C.L. (instead of 2.44) and the limit translates into:

$$k_{\rm Up}^{90\%\rm CL} < 3.2 \times 10^{-8}\ \ {\rm GeV\,cm^{-2}\,s^{-1}\,sr^{-1}} \tag{8.11}$$

It is also interesting to observe the evolution of the Auger integral limit with time. Figure 8.8 shows how the upper bound in the diffuse flux has been smoothly decreasing since 2004, following the increase on the number of tanks in the field and data statistics. As indicated by the dashed line, the 1 year ideal full Auger limit was reached after the first ~ 3 years of data taking.

In the same way, the differential limit as defined in section 7.2.4 is plot in figure 8.9 and detailed in the last column of table 8.2.

[6] Data collected between April 2008 and May 2009 with half of the completed IceCube array. Absence of signal candidate events in the sample of 333.5 days of lifetime.

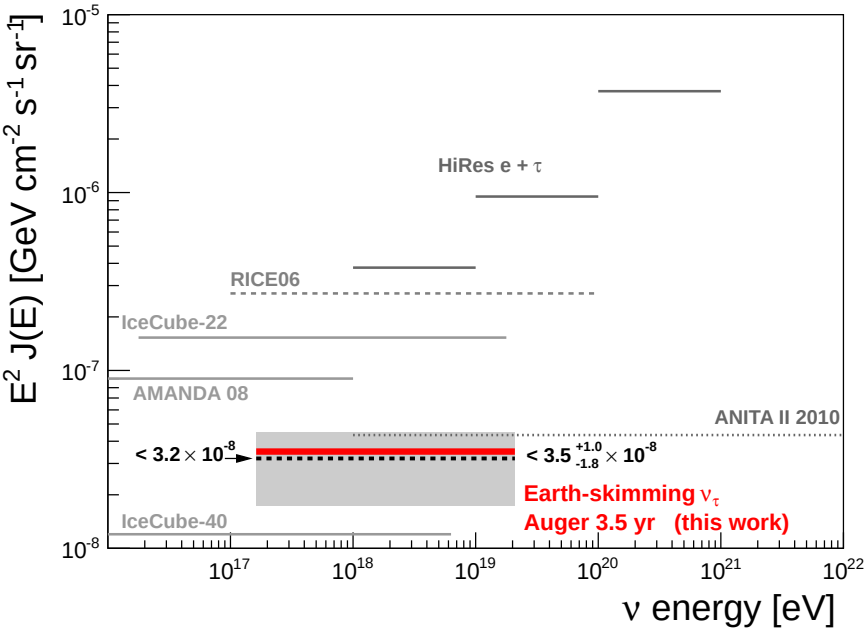

Figure 8.7: Earth-skimming ν_τ integrated upper limit at 90% C.L. for a diffuse neutrino flux as obtained in the search period from 1 January 2004 to 31 May 2010. Limits from other experiments [188, 189, 190, 191, 192, 193, 194] are also plotted: ANITA II and IceCube recomputed by us from *all* to *single* flavour limits (factor $\times\frac{1}{3}$). RICE 06 recomputed by us from 95% to 90% C.L.

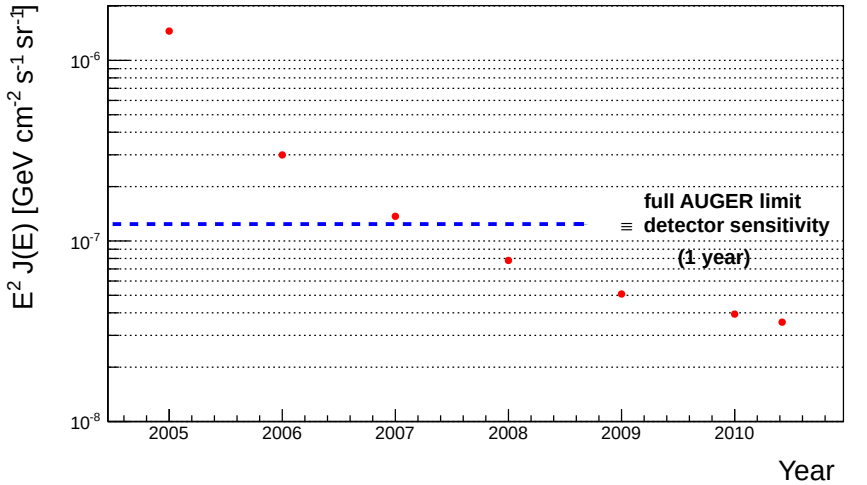

Figure 8.8: Dots: time evolution of the Auger Earth-skimming ν_τ integral upper limit on the diffuse neutrino flux (90% C.L.) from December 2004 until May 2010. The 1 year full detector limit is reached early in 2007 (dashed line).

The differential limit format is useful to demonstrate explicitly that the sensitivity of the Pierre Auger Observatory to Earth-skimming neutrinos peaks in a narrow energy range close to where the GZK neutrinos are expected. This is clearly shown in figure 8.10 where differential and integral limits are shown together with some theoretical diffuse flux predictions in the EeV range [3]. In table 8.4 (left) the expected event rates from these models after folding the fluxes with the Earth-skimming (table 8.2) exposure are given. In all cases, the spectral shape and flux strength are sensitive to parameters with unknown value so the predicted final number of expected events can vary substantially in a model if the assumed values are changed. As an example, two predictions from [56, 59] are given. Models labelled as GZK [56, 57] consider cosmogenic neutrinos and represent the so called "guaranteed" source of neutrinos. Predictions from [69] and [195] come from neutrinos produced in accelerating sources while [59] are examples of fluxes from neutrinos of exotic origin.

Diffuse Model		$\mathbf{N}_{\text{expected}}$
GZK-Fermi	[56]	4.0
	[56]	0.6
GZK-evolFRII	[57]	1.4
MPR-max	[69]	12.1
BBR	[195]	5.1
TD-Necklaces	[59]	3.0
	[59]	0.6
Z-Burst	[59]	7.0

Table 8.4: Expected number of Earth-skimming ν_τ events predicted by several diffuse neutrino flux models.

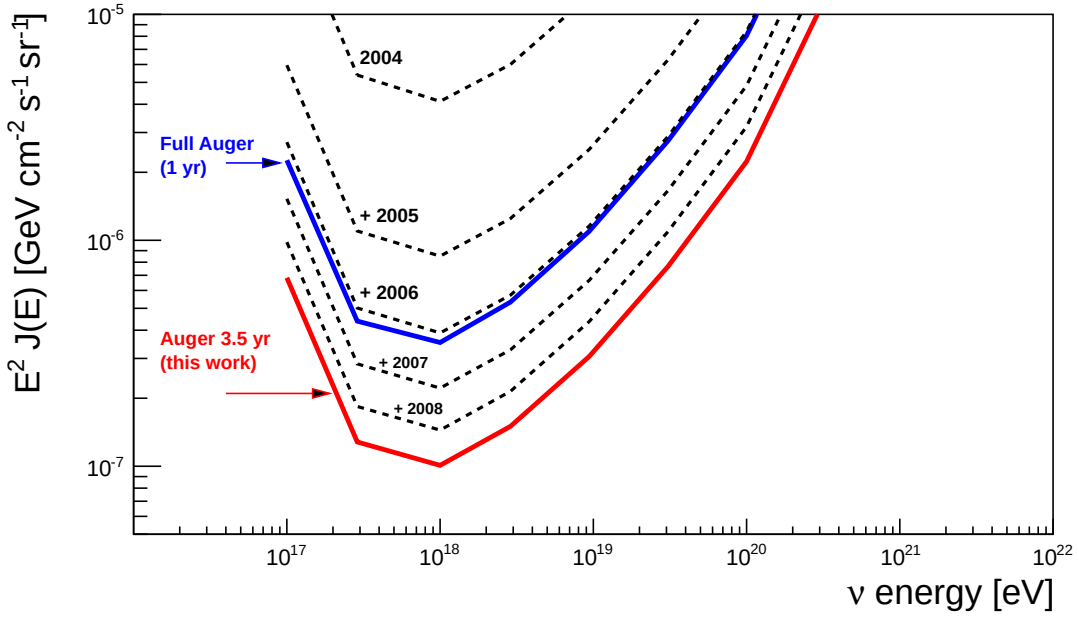

Figure 8.9: Earth-skimming ν_τ differential upper limit at 90% C.L. for a diffuse neutrino flux as obtained for the search period from 1 January 2004 to 31 May 2010 (solid red line). The limit improvement when increasing data statistics is shown by the dashed lines (2004 means 2004 data only, +2005 adds 2005 data, etc.). The limit obtained for an ideal full SD array after 1 year of data taking corresponds to the blue solid line.

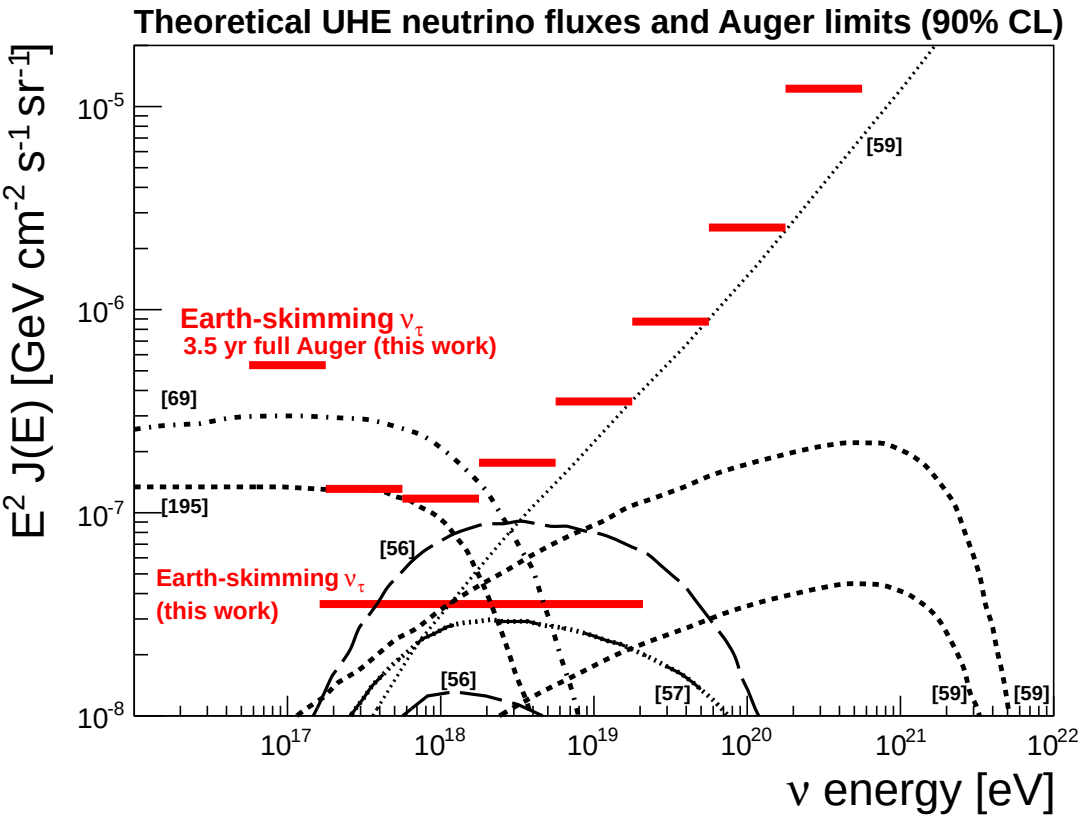

Figure 8.10: Earth-skimming ν_τ differential (sort segments) and integral upper limit at 90% C.L. for a diffuse neutrino flux as obtained in the search period from 1 January 2004 to 31 May 2010 (red curve). The limit is shown together with several theoretical calculations [56] [57] [69] [195] [59].

9

Sensitivity to Point-like Sources of UHEνs from the Downward-going and Earth-skimming channels

One of the most exciting topics in astronomy is the search for neutrino sources in the sky map. The detection of UHEν_s coming from cosmic objects is crucial in order to understand the most energetic processes of the universe. A positive result would mean a tremendous breakthrough in the studies about the origin of cosmic rays and also in the understanding of the γ-ray production processes at high energies. Moreover, the detection of unknown sources invisibles with other techniques is not discarded.

In this chapter the sensitivity of the SD array to the detection of ν events coming from single point sources in the sky is studied. The analysis is performed for the downward-going ν selection at low zenith angle $\mathrm{DG_{low}}$ (presented in section 5.3 and sensitive to the region $\theta \in [58.5°–76.5°]$) and also for the Earth-skimming ν_τ selection (which covers the range $\theta \sim [90°–95°]$ as described in chapter 8). The final goal of this study is to quote, for the two analyses, a limit on the neutrino flux as function of the source declination given that zero neutrino candidates are found in data. To do so the SD exposure from each channel as function of energy, declination δ and right ascension α (Equatorial coordinates) is computed using Monte-Carlo simulations. In section 9.1 we introduce the principles and methodology for a discrete search of neutrinos in the sky. Then, in section 9.2 the final results for the downward-going and Earth-skimming analyses are reported. This study was published in reference [106].

9.1 Methodology of the point-like sources analysis

The procedure followed to estimate the sensitivity of the Pierre Auger Observatory to the detection of neutrinos coming from point-like sources can be summarized in three steps:

1. For each source declination δ, the fraction of time t in 1 sidereal day the source is *visible*, i.e. within the field of view of the analysis ($\theta \in [\theta_{\mathrm{min}}, \theta_{\mathrm{max}}]$), is calculated. Then, for the current declination the SD exposure $\xi(E_\nu, \delta)$ is evaluated using the detection efficiency as function of zenith angle and the time spent by the source at each zenith angle (relationship between θ, δ and t shown in equation 9.1).

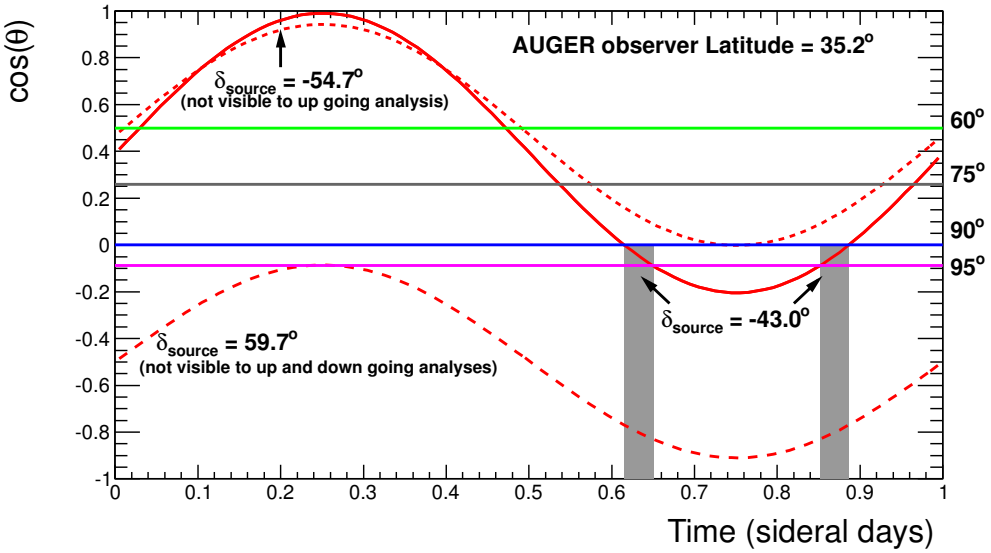

Figure 9.1: Point source analysis: for an observer located at the Auger latitude, the curves indicate the change on zenith angle ($\cos(\theta)$) of three point sources with declinations $\delta_{\rm source}$, as function of time along 1 sidereal day (eq. 9.1). The horizontal lines mark the regions where the $\rm DG_{low}$ ($\theta \sim [60°–75°]$) and Earth-skimming ($\theta \sim [90°–95°]$) neutrino search analyses are sensitive. The gray vertical bands show the segments on the sidereal day in which a source at $\delta = -43°$ would be within the Earth-skimming analysis field of view.

2. Given that no candidates are found and assuming a neutrino flux $J(E_\nu) = k \cdot E_\nu^{-2}$, a limit on $k_{\rm PS}^{90\%\rm CL}(\delta)$ is derived.

3. Steps 2 and 3 are repeated for all declinations in the sky.

Time a source is visible in the sky

For a given source at a declination δ (in Equatorial coordinates) the zenith angle at which it is visible from the SD is a periodic function $\theta(t)$ depending on the sidereal time. Hence, for a source at declination δ, the dependency of the zenith angle θ of the source at a certain time t is given by the equation:

$$\cos\theta(t) = \sin\lambda\sin\delta + \cos\lambda\cos\delta\sin(2\pi t/T - \alpha) \tag{9.1}$$

where λ is the latitude of the observer, T is the duration of one sidereal day, and α is the right ascension in Equatorial coordinates.

Figure 9.1 shows this relation for the case of an observer located at the Pierre Auger Observatory (coordinates $\sim 35°\ 28'$ S – $69°\ 18'$ W). The horizontal lines indicate the field of view of the downward-going $\rm DG_{low}$ ($\theta \sim [60°–75°]$) and Earth-skimming ($\theta \sim [90°–95°]$) neutrino search analyses: sources placed at declinations crossing these regions at any time along 1 sidereal day are visible. The result for $\delta = -43°$ (Centaurus A) is given by the solid line. Larger (smaller) declination values would move the curve down (up) in the graph.

Figure 9.2 gives the information on the fraction of 1 sidereal day the sources are visible for $\rm DG_{low}$ and Earth-skimming searches. This fraction of time depends only on the source declination. For both analyses the data structure is similar: zero sensitivity in the corners, i.e.

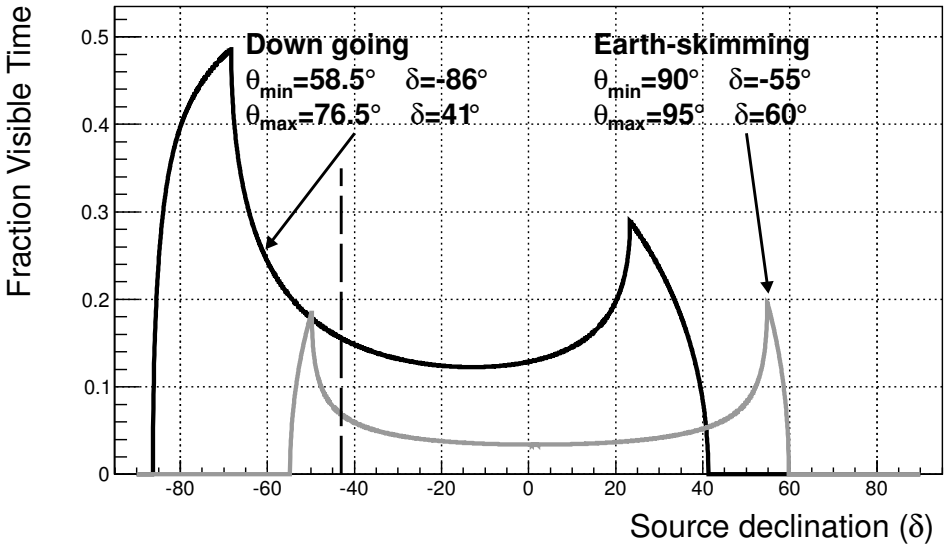

Figure 9.2: Fraction of time a source (δ) is within the field of view of the DG_{low} (black) and Earth-skimming (light gray) neutrino analyses. The extreme values of declinations beyond which the analyses are not sensitive are indicated in the figure.

above and beyond a certain δ value; a *plateau* in the central part; and two *horns* indicating the most sensitive declination values, which are a consequence of the relative smaller rate of variation of zenith angle with time for directions near the edges of the range accessible to this analysis. At the latitude of the Pierre Auger Observatory ($\lambda = -35.2°$), the *field of view* of the DG_{low} analysis covers a range in declination from about $-85°$ to $+40°$, whereas the Earth-skimming analysis is sensitive to sources with declinations in a window from about $-55°$ to $+50°$. As expected, for a given declination the fraction of visible time is in general higher for DG_{low} than for the Earth-skimming analysis since the angular sensitivity window of the former is three times larger than for the later. As an example, the declination of Centaurus A, which is shown as a vertical black dashed line in figure 9.2, is visible a $\sim 16\%$ ($\sim 7\%$) of one sidereal day in the DG_{low} (Earth-skimming) analysis.

Exposure Calculation

The exposure of the SD as function of the neutrino energy E_ν and the source position in the sky δ is evaluated in the same way to that used for the calculation of the diffuse flux, except for the solid angle integration over the sky. The way in which the exposure is computed for each analysis is slightly different. For the DG_{low} selection, where the 6T5 trigger is required, the exposure is given by:

$$\xi(E_\nu, \delta) = \sum_i \frac{\omega_i \sigma(E_\nu)^i}{m_N} \int_t \int_D \varepsilon(E_\nu, \theta(t), D)\, A_{6T5}\, n(t)\, dt\, dD \tag{9.2}$$

where the integration is performed over the interaction depth D an the search period t. The dependency on δ comes from $\theta(t)$ as obtained from equation 9.1. Changes in the number of hexagons as function of the time can induce a dependence of the exposure with the right ascension. Since the search is performed over a large period, the overall effect is expected to

be small, providing that the average number of hexagons in the period of one sidereal day is roughly a flat distribution with random fluctuations.

For the Earth-skimming analysis, the exposure is given by:

$$\xi(E_\nu, \alpha, \delta) = \frac{1}{4\pi} \int_{2\pi} dt \; cos\theta(\frac{2\pi t}{T} - \alpha, \delta) \; \xi(E_\nu, \theta(\frac{2\pi t}{T} - \alpha, \delta)) \tag{9.3}$$

and averaging the exposure over a full sidereal day, the time integral is equivalent to integrate over right ascension:

$$\xi(E_\nu, \delta) = \frac{1}{4\pi} \int_{2\pi} d\alpha \; cos\theta(\alpha, \delta) \; \xi(E_\nu, \theta(\alpha, \delta)) \tag{9.4}$$

where $\xi(E_\nu, \theta(\alpha, \delta))$ is defined in equation 8.3 by adding the θ dependency of equation 9.1.

In both cases, when integrating over time only those periods when the source is within the zenith angle range of the neutrino selection are considered. Changes in the detector configuration during data taking, due to the dead times of the SD stations, and to the increase of the array size during the construction phase, may introduce a dependence of the exposure on the right ascension. In particular, fluctuations in the number of stations cause a small diurnal variation, but this effect is only apparent in solar time. When averaged over a large number of sidereal days, as in this analysis, the modulation in right ascension caused by this effect is less than 1% [196]. For this reason, the dependence of the exposure on α has been neglected in the evaluation of the upper limits.

9.2 Limits to the neutrino flux from point-like sources

Using a similar approach than the one applied on the calculation of the limits to the diffuse ν flux (equation 7.2), under the assumption that the UHEν flux from a given source at declination δ behaves with energy as $J(E_\nu) = k \cdot E_\nu^{-2}$, the integrated upper limit on the value of k from each particular source is:

$$k_{\rm PS}^{90\%\rm CL}(\delta) = \frac{N_{\rm Up}}{\int_{E_{\nu\rm min}}^{E_{\nu\rm max}} E_\nu^{-2} \, \xi(E_\nu, \delta) \, dE_\nu} \tag{9.5}$$

Notice that, since no integration in solid angle is performed, $k_{\rm PS}^{90\%\rm CL}$ is expressed in units of [GeV cm^{-2} s^{-1}].

As reported in section 8.2, the search for UHEν_s in the Earth-skimming channel over the whole sky has produced negative results: no events pass the selection cuts in the search period (from 1 January 2004 to 31 May 2010). This has allowed to set stringent limits on the *diffuse* neutrino flux as shown in figure 8.10. The exposure for each declination has been computed using equation 9.4. As an example, figure 9.3 gives the exposures obtained at the Centaurus A and Galactic Center declinations as function of the neutrino energy for the search data period.

In Figure 9.4, the 90% C.L. upper limits on $k_{\rm PS}$ derived from the Earth-skimming and DG$_{\rm low}$ analyses are shown as a function of source declination (search period from 1 January 2004 to 31 May 2010). A E_ν^{-2} flux from any point-like source at a declination δ is assumed. The shape of the declination-dependent upper limits is largely dominated by the fraction of time a source is within the field of view of the analyses (see figure 9.2) but in an inverted form as expected (the larger the time a source is *seen* by the analysis, the higher the exposure and the better the limit), and, to a lesser extent, by the zenith angle dependence of the exposure.

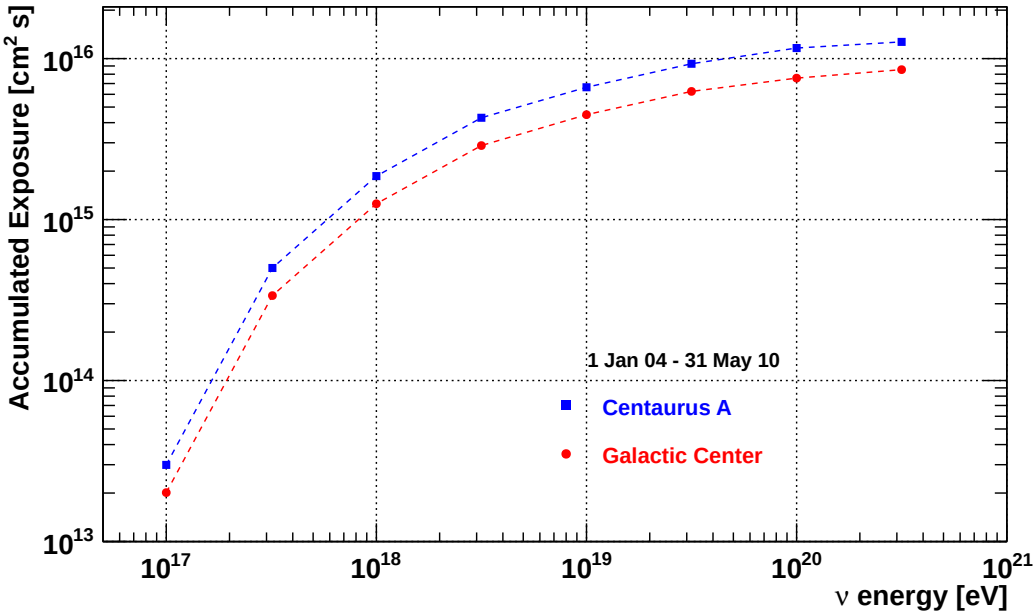

Figure 9.3: Point source Earth-skimming ν_τ analysis: accumulated exposure in the real SD array from 1 January 2004 to 31 May 2010 for Centaurus A ($\delta = -43°$) and the Galactic Center ($\delta = -29°$). The dashed line connecting points corresponds to a linear interpolation.

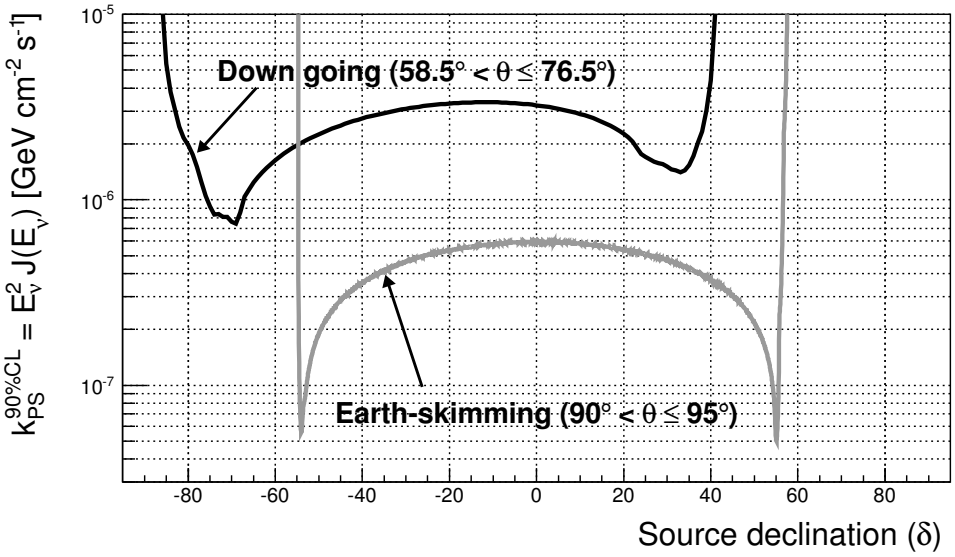

Figure 9.4: Upper limits at 90% C.L. on a single flavour E_ν^{-2} flux from a specific point-like source as function of the source declination (search period from 1 January 2004 to 31 May 2010).

The upper limits are derived for neutrinos in the energy range $\sim 1.6 \times 10^{17}$ eV – 2.0×10^{19} eV for the Earth-skimming analysis, and in the range $\sim 2.0 \times 10^{18}$ eV – 2.0×10^{20} eV for the $\mathrm{DG_{low}}$ analysis, with a negligible dependence of these energy intervals on the source declination.

As compared to figure 9.2, data points show a similar but inverted distribution: a smaller upper bound in $k_{\mathrm{PS}}^{90\%\mathrm{CL}}$ is obtained for declinations expending longer time within the Earth-skimming search field of view (*horns* in figure 9.2). The highest sensitivity is reached by the Earth-skimming analysis close to $-50°$ and $+55°$ where limits around 5×10^{-8} GeV cm^{-2} s^{-1} are obtained. In the broad *plateau* region ($\delta \in [-40°, +40°]$), the limit increases by a factor $\sim$6–10.

The correlation between the flux upper limit and the time spent by the source is even more evident in figure 9.5 where the decimal logarithm of $k_{\mathrm{PS}}^{90\%\mathrm{CL}}$ is plotted as a function of the declination for the Earth-skimming analysis. These values are also shown in figure 9.6 in the form of a sky map. The limits (z-axis) are drawn in a (δ, α) Equatorial coordinates plane using the *Aitoff*-projection. The black dots in the graph indicate the location of some pre-defined source candidates of neutrinos (listed in table 9.1 together with their respective flux limit).

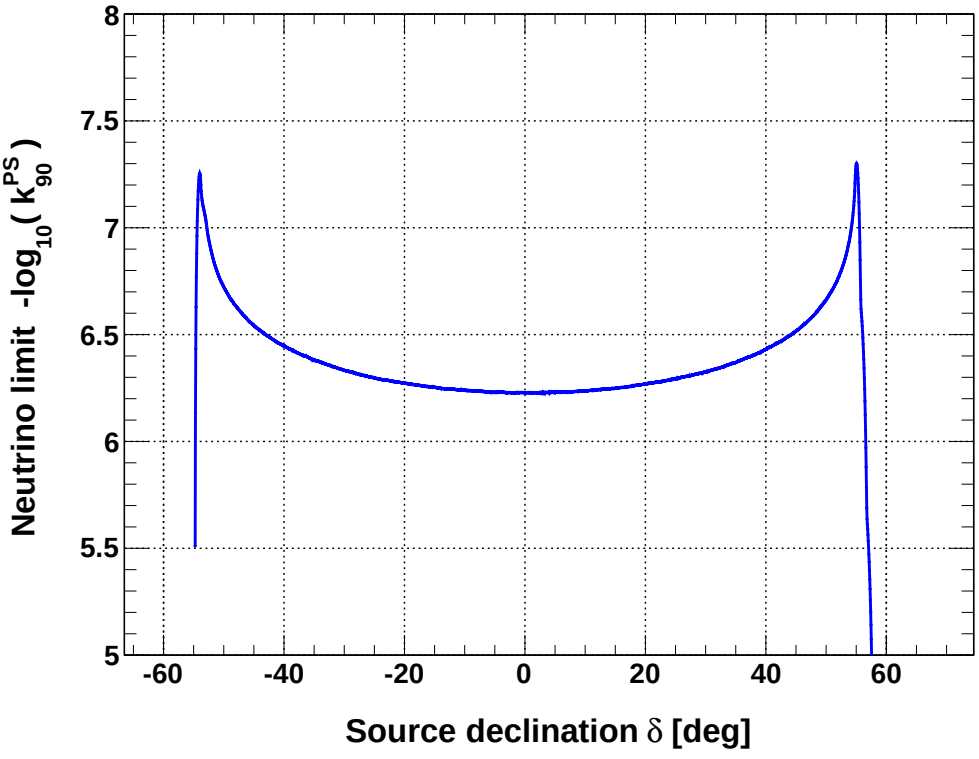

Figure 9.5: Same as Earth-skimming limit in figure 9.4 in units of $-\log_{10}(k_{\mathrm{PS}}^{90\%\mathrm{CL}})$.

As a cross-check, a *diffuse limit* can be computed from the results obtained in the point source analysis by double integration of the exposure $\xi(E_\nu, \delta)$ in declination angle and energy (eq. 9.4):

$$k_{\rm PS}^{90\%\rm CL} < \frac{N_{\rm Up}}{\int_{\log_{10} E_{\rm min}}^{\log_{10} E_{\rm max}} \int_{-\pi/2}^{+\pi/2} 2\,\pi \cdot cos(\delta) \cdot E_\nu^{-1} \cdot \xi(E_\nu, \delta) \cdot \ln(10) \cdot d(\log_{10}(E_\nu)) \cdot d\delta} \tag{9.6}$$

The resulting diffuse limit from the point source analysis is:

$$k_{\rm PS}^{90\%\rm CL} < 3.6\ \times 10^{-8}\ \ {\rm GeV\,cm^{-2}\,s^{-1}\,sr^{-1}} \tag{9.7}$$

in good agreement with the one quoted in eq. 8.10.

Note that a second (faster but less precise) cross check between the diffuse and the point source results can be done by comparing the quoted exposures or final limits after correcting by the solid angle and the fraction of time the source is visible. The exposure for a given point source could be estimated as the ratio between the diffuse exposure (figure 8.4) and the solid angle covered by the diffuse analysis ($\sim 2\pi \cdot \cos(95^\circ)$), multiplied by the fraction of time the source is visible. For instance, in the case of Centaurus A (visible $\sim$ 6.8% of the time) the rough estimated exposure at 10^{18} eV would give a value of $\sim 2.3 \times 10^{15}$ cm^2 s, to be compared with the one quoted in figure 9.3. The same kind of quick comparison could be done between the DG$_{\rm low}$ and the Earth-skimming limits since the ratio between the two limits for a given point source should be close to the ratio between the respective diffuse limits weighted by the solid angles and by the fraction of time the source is visible to each analysis.

Limits for the particular case of the active galaxy Centaurus A, a potential source of UHECRs, are shown in figure 9.7, together with constraints from other experiments. The predicted fluxes for two theoretical models of UHEν production (in the jets [197] and close to the core of Centaurus A [198]) are also shown for comparison. The expected number of events in our blind search samples for a flux like in [197] is about 0.1 and 0.02 for the Earth-skimming and DG$_{\rm low}$ selection respectively, the expected number for [198] being one order of magnitude smaller.

As a conclusion, even though the sensitivity window of the Earth-skimming and DG$_{\rm low}$ analyses in zenith angle is tiny, it allows a potential point source survey in a broad range in declination angles spanning more than 100° in the sky.

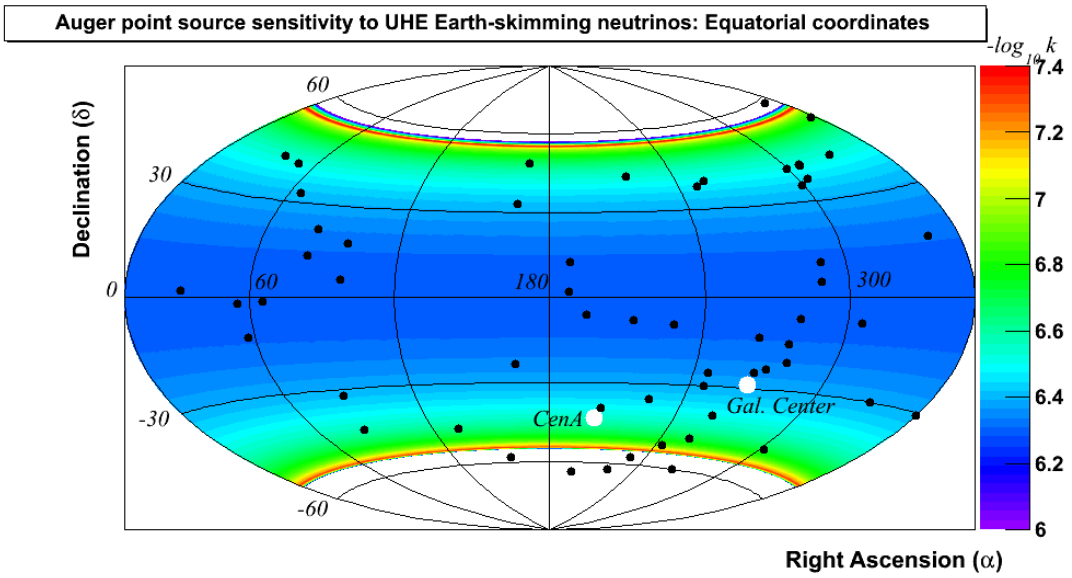

Figure 9.6: Sky map in Equatorial coordinates (declination δ vs. right ascension α) with the Earth-skimming ν_τ point source limits at 90% C.L. in units of $-\log_{10}(k_{\rm PS}^{90\%\rm CL})$. Positions of sources listed in table 9.1 are also shown (black dots).

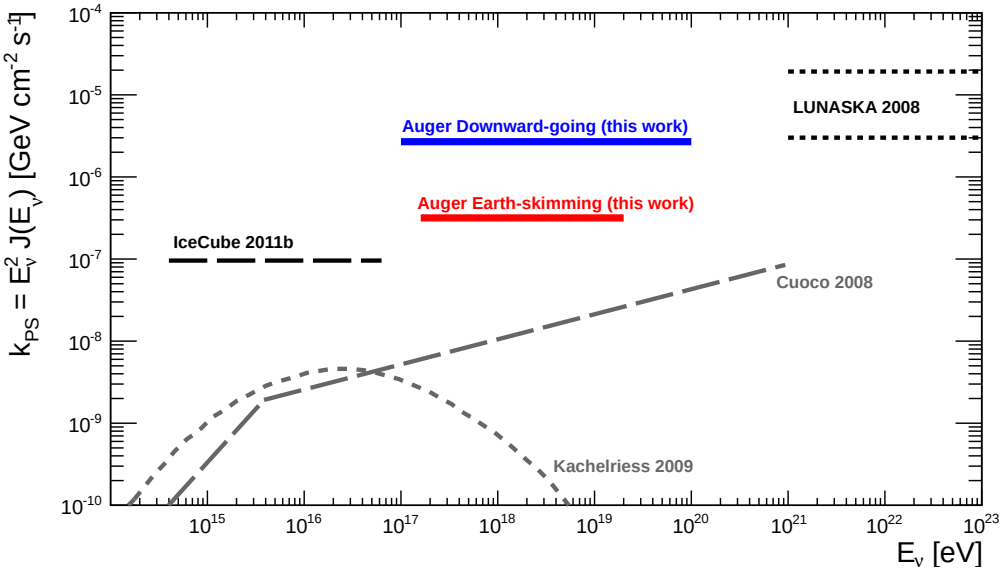

Figure 9.7: Upper limits at 90% C.L. on a single flavour E_ν^{-2} flux from the active galaxy Centaurus A from the Earth-skimming and $\rm DG_{low}$ neutrino analyses, together with bounds from the IceCube Neutrino Observatory [199] and LUNASKA [200]. The predictions for two models of UHEν production also shown.

Object	Dec. δ [°]	R.A. α [°]	$k_{\mathrm{PS}}^{90\%\mathrm{CL}}$ $\times 10^7$	**Object**	Dec. δ [°]	R.A. α [°]	$k_{\mathrm{PS}}^{90\%\mathrm{CL}}$ $\times 10^7$
Cas A	58.8	350.8	5976	HESS J1833-069	-6.9	279.4	5.82
1ES 2344+514	51.7	356.8	1.80	PKS 2023-07	-7.6	306.4	5.81
XTE J1118+480	48.0	169.5	2.56	PKS 1406-076	-7.9	212.2	5.79
3C 661	43.0	37.7	3.33	PKS 1510-089	-9.1	228.2	5.78
H 1426+428	42.7	217.1	3.37	1ES 0347-121	-12.0	57.3	5.69
QSO B2200+420	42.3	330.7	3.41	PKS 1730-130	-13.1	263.3	5.66
NGC 1275	41.5	50.0	3.52	LS 5039	-14.8	276.6	5.58
Cyg OB2	41.3	308.3	3.54	PKS 1830-21	-21.1	278.4	5.25
Cyg X-3	41.0	308.1	3.58	W28	-23.3	270.4	5.14
Cyg A	40.7	299.9	3.61	1ES 1101-232	-23.5	165.9	5.13
Mrk 501	39.8	253.5	3.73	PKS 1622-253	-25.5	246.4	5.01
4C 38.41	38.1	248.8	3.93	Sgr A* (Gal.Cent.)	-29.0	266.4	4.71
MGRO J2019+37	36.8	304.8	4.07	PKS 1622-297	-29.9	246.5	4.65
Cyg X-1	35.2	299.6	4.24	PKS 2155-304	-30.2	329.7	4.62
Mrk 421	33.2	166.1	4.43	H 2356-309	-30.6	359.8	4.59
GRO J0422+32	32.9	65.4	4.46	PKS 0548-322	-32.3	87.7	4.41
Crab Nebulae	22.0	83.6	5.28	PKS 1454-354	-35.6	224.4	4.09
Geminga	17.8	98.5	5.51	RX J1713.7-3946	-39.8	258.2	3.59
3C 454.3	16.4	343.5	5.58	Centaurus A	-43.0	201.4	3.17
PKS 0528+134	13.5	82.7	5.67	PKS 0537-441	-44.1	84.7	3.01
M87	12.4	187.7	5.71	RX J0852.0-4622	-46.4	133.0	2.62
GRS 1915+105	10.9	288.8	5.77	GX 339	-48.8	255.7	2.17
HESS J0632+57	5.8	98.2	5.88	PKS 2005-489	-48.8	302.4	2.17
SS 433	5.0	288.0	5.91	HESS J1615-518	-51.8	243.6	1.38
3C 273	2.1	187.3	5.92	CIR X-1	-57.2	230.2	–
RGB J0152+017	1.8	28.2	5.91	HESS J1023-575	-57.8	155.8	–
PKS 0420-014	-1.3	65.8	5.89	ESO 139-G12	-59.9	264.4	–
PKS 0336-019	-1.8	54.9	5.92	RCW 86	-62.5	220.7	–
3C279	-5.8	194.1	5.88	PSR B1259-63	-63.8	195.7	–

Table 9.1: Earth-skimming ν_τ limits in units of [GeV cm^{-2} s^{-1}] for predefined point source neutrino candidates.

Summary and Conclusions

Although the Pierre Auger Observatory was conceived to detect Ultra High Energy Cosmic Rays (UHECRs), it has been shown that Ultra High Energy Neutrinos (UHEν_s) can also be identified with the surface detector array (SD). UHEν_s play a key role in the understanding of the sources and acceleration mechanisms of UHECRs. Their observation should open a new window to the universe. Unlike cosmic rays, neutrinos point directly to the source where they were produced, without being deflected by Galactic and extragalactic magnetic fields. Unlike photons, they travel undisturbed from the sources carrying a footprint of the production model. Predicted by different astrophysical and cosmological models, they are expected to be produced in the same sources where UHECRs are thought to be accelerated, as well as during the propagation of UHECRs through the cosmic microwave background radiation. Their detection or absence would either confirm or exclude these models.

The idea behind the detection of UHEν_s with a ground detector like the SD is that, having very small cross-sections, they can interact at any point along their trajectories, while protons, nuclei or photons interact shortly after entering the atmosphere. Downward-going neutrinos of all flavours can induce Extensive Air Showers (EASs) close to ground ("young" showers) which present a large electromagnetic component (i.e. photons, electrons and positrons). When looking at high zenith angles ($\theta > 75^\circ$) the atmosphere is thick enough (thicker than about three vertical atmospheres) so that the cosmic rays interacting high in the atmosphere have shower fronts dominated by muons at ground ("old" shower front). A very inclined neutrino interacting deep will present a young shower front and, consequently, can be distinguished.

However, when considering more vertical showers, even the ones initiated by protons or heavy nuclei have a considerable amount of electromagnetic component at ground and the differences between EASs induced by neutrinos gradually become less evident. Up to now the identification of UHEν_s in Auger through the EASs they induce has been restricted to very inclined showers ($\theta > 75^\circ$) [3]. The work presented in this document demonstrates that a search for UHEν_s with the surface detector array of the Pierre Auger Observatory in the region of lower zenith angles ($60^\circ \leq \theta \leq 75^\circ$) is also feasible.

The most relevant contributions presented in this Ph.D. thesis are summarized in what follows:

■ Search for UHEν_s in the region of low zenith angle.

We have presented a new analysis aiming at detecting downward-going ν-induced showers impinging the surface detector array of the Pierre Auger Observatory at low zenith angles, in the region $\theta \sim [60^\circ - 75^\circ]$.

The essential point for the identification of ν-induced showers is the definition and choice of the observables which select inclined–young showers in the overwhelming background of normal showers induced by cosmic rays. The analysis is based on a blind search approach to avoid any artificial bias on the choice of the discriminating variables and on the final values of the cuts. The procedure includes an end to end simulation chain to reproduce the EASs generated by

UHEν_s in the atmosphere and the signals recorded in the water Cherenkov stations at ground. These Monte-Carlo neutrinos (signal sample) together with a fraction of the data collected by the Observatory (background sample) are used to tune the selection algorithms, to find the most discriminating variables, and to build and to train a Fisher discriminant polynomial. The reconstructed zenith angle is used to filter inclined showers, and the young selection is done by requiring a high fraction of T5 stations with Time-over-Threshold trigger (ToT) trigger. The Fisher polynomial is built with the Area over Peaks (AoPs) of the selected stations. The final neutrino selection is based in a cut on the Fisher value for each event, $\mathcal{F}_{\rm cut}(\theta)$.

Once the selection criteria were fixed, the remaining fraction of data in the period from 1 Jan 2004 to 31 May 2010 was unblinded and used as search sample. No neutrino candidates were selected using the analysis described in this work. Assuming a differential spectrum $J(E_\nu) = dN_\nu/dE_\nu = k \cdot E_\nu^{-2}$ for the diffuse flux of UHEν_s, a (1:1:1) flavour neutrino ratio and zero background, a 90% C.L. upper limit on the integrated flux of UHE neutrinos was derived. Using a semi-Bayesian extension of the Feldman&Cousins approach which allows to incorporate in the calculation the systematic uncertainties on the exposure, the quoted limit to the normalization k on the diffuse flux is:

$$k_{\rm Up}^{90\%\rm CL} < 6.3 \times 10^{-7} \ \ \text{GeV cm}^{-2}\ \text{s}^{-1}\ \text{sr}^{-1} \quad \text{(Downward-going } \nu \text{ low angle)}$$

valid in the energy range $E_\nu \in [1.9 \times 10^{18} - 2.0 \times 10^{20}]$ eV, where $\sim 90\%$ of the neutrino events would be detected for an E_ν^{-2} flux.

The new selection described in this thesis intends to complement the existing ν search at high zenith angles [3]. A first attempt to combine the two analyses is discussed in this thesis. The results from this work show a significant contribution to the exposure from the low angle analysis at the highest energies, extending the sensitivity of the Observatory to the most energetic neutrinos. Despite the fact that the linear sum of the SD exposures in the whole energy range gives a similar number for the two selections, the contribution from the low angle analysis to the absolute value of the combined limit is moderate due to the assumed behavior of the flux ($\propto E_\nu^{-2}$) which penalizes the highest energies. The definition of a unified criteria to combine the three existing analysis searching for UHEνs in Auger is currently the subject of work inside the Auger Collaboration.

■ Improved limit on the diffuse search of Earth-skimming tau neutrinos.

The analysis searching for Earth-skimming tau neutrinos in Auger has been revisited, specially on what concerns the treatment of the tau polarization having an impact on the estimated systematic uncertainty. Moreover, the search data period has been extended by about 2 years with respect to the latest Auger publication [4], going from 1 January 2004 until 31 May 2010. No candidate events are found in data. In order to derive a limit on the diffuse neutrino flux, the exposure as a function of the energy and zenith angle have been re-calculated in the new data search period. Assuming a differential spectrum $J(E_\nu) = k \cdot E_\nu^{-2}$ for the diffuse flux of UHEν_s and zero background, the following 90% C.L. upper limit on the integrated flux of tau neutrinos is derived:

$$k_{\rm Up}^{90\%\rm CL} < 3.2 \ \times 10^{-8} \ \ \text{GeV}\,\text{cm}^{-2}\,\text{s}^{-1}\,\text{sr}^{-1} \quad \text{(Earth-skimming } \nu_\tau \text{ channel)}$$

valid in the energy range $E_\nu \in [1.6 \times 10^{17} - 20.8 \times 10^{18}]$ eV, where $\sim 90\%$ of the neutrino events would be detected for an E_ν^{-2} flux. The results of this work were published in [106].

Note that the maximum sensitivity shown by the downward-going and the Earth-skimming analyses, obtained for $E_\nu \sim 10^{18} - 10^{19}$ eV, matches well the region where Greisen-Zatsepin-Kuzmin (GZK) models predict the strongest fluxes of cosmogenic neutrinos. Therefore, although not excluded that future theoretical predictions may shift the predicted fluxes down, with the current selection criteria the exposure accumulated in ∼10 more years with the Pierre Auger Observatory can be sufficient to clearly identify a neutrino candidate. On the other hand, the absence of neutrino candidates should strongly constraint some neutrino production models.

■ **Sensitivity to point-like sources of UHE neutrinos.**

Based on the negative result obtained on the search for UHEν_s reported in this work, the sensitivity of the SD detector to neutrinos coming from point-like sources was evaluated. The methodology to compute the exposures to Earth-skimming and downward-going neutrinos at low zenith angles is described and the sensitivity calculated as a function of the energy and declination δ of the source. In absence of neutrino candidates in data collected through 31 May 2010, upper limits on the neutrino fluxes from point-like sources as function of the source position in the sky $k_{\rm PS}^{90\%{\rm CL}}(\delta)$ were derived and published in [106].

The Earth-skimming analysis places limits which are currently the most stringent at energies around and above 1 EeV in a large fraction of the sky spanning more than 100° in declination. The declination-dependent upper limit is found to have a minimum value around 5×10^{-8} GeV cm^{-2} s^{-1} close to −50 and +55 degrees, smoothly degrading for declinations between these two values up to $\sim 6 \times 10^{-7}$ GeV cm^{-2} s^{-1}. Even though the limits quoted from the downward-going analysis at low angle are modest as compared to the Earth-skimming channel, exploring the $\theta \in [60°, 75°]$ angular window extends by about 30° the field of view of the Observatory at negative declinations. Moreover, the downward-going search at low angle shows the maximum sensitivity to sources located at declinations from about −80° to −60°, a portion of the sky hidden to the Earth-skimming analysis.

Resumen y Conclusiones

Aunque el observatorio Pierre Auger fue concebido para la detección de UHECRs, tiene la capacidad de detectar UHEνs usando la información proporcionada por el detector de superficie. Los UHEνs juegan un papel clave en la comprensión de las fuentes y los mecanismos de aceleración de los UHECRs. Su detección puede abrir una nueva ventana al universo ya que, al contrario que los UHECRs, los neutrinos apuntan directamente a las fuentes que los produjeron sin ser desviados por los campos magnéticos galácticos ni extragalácticos. Por otro lado, al contrario que los fotones, la información que los neutrinos portan sobre su modelo de producción no se ve alterada hasta el momento de su detección. Diferentes modelos astrofísicos y cosmológicos predicen la producción de neutrinos tanto en las fuentes de UHECRs como en la interacción de estos con el fondo cósmico de microondas durante su propagación. La detección de neutrinos puede confirmar o excluir estos modelos.

La idea original de detección de UHEνs con un detector de superficie como el de Auger se basa en el hecho de que, con los valores tan pequeños de sección eficaz de los neutrinos, estos pueden interaccionar en cualquier punto a lo largo de su trayectoria en la atmósfera, mientras que los protones, nucleos o fotones interaccionan solo en las capas más altas de la atmósfera. Los neutrinos de cualquier sabor que interaccionan en la atmósfera ("downward-going") pueden inducir "lluvias extensas" cerca del detector de superficie ("lluvias jóvenes") que presentan una gran cantidad de componente electromagnética (fotones, electrones y positrones). Cuando la búsqueda se centra en ángulos cenitales altos ($\theta > 75^\circ$) la atmósfera es suficientemente gruesa como para absorber la componente electromagnética de los rayos cósmicos que interaccionan en las primeras capas y por lo tanto el frente de la lluvia está dominado por la componente muónica a su llegada al detector de superficie ("lluvias viejas"). Una lluvia muy inclinada provocada por un neutrino profundo puede presentar las características de una lluvia joven y puede por lo tanto ser discriminada.

Sin embargo, cuando se analizan lluvias menos inclinadas, incluso las iniciadas por protones o núcleos en las primeras capas de la atmósfera pueden presentar una parte importante de componente electromagnética, provocando que las diferencias con las lluvias iniciadas por neutrinos sean cada vez menos evidentes. Hasta ahora, los estudios de neutrinos realizados en el Observatorio Pierre Auger han considerados solo lluvias muy inclinadas ($\theta > 75^\circ$). El trabajo presentado en esta tesis demuestra que es posible identificar lluvias inducidas por neutrinos a ángulos menores, concretamente en la región angular ($60^\circ \leq \theta \leq 75^\circ$).

Las contribuciones más relevantes presentadas en este documento son las siguientes:

■ Búsqueda de Ultra High Energy Neutrinos (UHEν_s) en la región de bajo ángulo cenital.

Se ha presentado un nuevo análisis que pretende la detección de "lluvias extensas" inducidas por neutrinos interaccionando en la atmósfera en la región angular $\theta \sim [60^\circ - 75^\circ]$.

La clave para la identificación de lluvias inducidas por neutrinos recae en la elección de las variables que permiten seleccionar las lluvias jóvenes inclinadas de entre todo el fondo provocado

por los rayos cósmicos. El análisis se basa en una búsqueda "blindada" para eliminar cualquier posible sesgo en la definición y elección de las variables de selección así como en sus valores de corte. El procedimiento incluye una cadena de simulación de las lluvias inducidas por UHEνs y de las señales inducidas en los detectores Cherenkov de superficie. Este Monte-Carlo de neutrinos (muestra de señal), junto con un subconjunto de datos recolectados por el Observatorio (muestra de fondo) se han usado para ajustar los algoritmos de selección, encontrar las mejores variables de discriminación y construir y entrenar un polinomio de discriminación basado en un discriminante Fisher. El ángulo reconstruido de la lluvia se usa para filtrar las lluvias inclinadas mientras que la selección de lluvias jóvenes se hace exigiendo que una alta fracción de las estaciones usadas para definir el máximo nivel de calidad de cada evento tenga señales de larga duración. El polinómio Fisher es entrenado usando una variable definida como la señal integrada en tiempo dividida por su valor de pico para cada estación seleccionada. La decisión final sobre si un evento es o no provocado por un neutrino, se basa en un corte en su valor Fisher que depende del ángulo del eje de la "lluvia".

Solo una vez que los criterios de selección e identificación están fijados, los datos no usados como muestra de entrenamiento en el periodo comprendido entre el 1 de Enero de 2004 y el 31 de Mayo de 2010 son usados como muestra de búsqueda. No se ha encontrado ningún candidato a neutrino. Por lo tanto, asumiendo un flujo difuso de UHEνs en la forma $J(E_\nu) = dN_\nu/dE_\nu = k \cdot E_\nu^{-2}$, una fracción de sabor (1:1:1) y cero fondo esperado, se ha calculado un límite superior al flujo al 90 % C.L. Usando una extensión semi-Bayesiana del tratamiento de Feldman&Cousins, que permite incorporar las incertidumbres sistemáticas en la exposición del detector a neutrinos, el límite para la constante de normalización k del flujo es:

$$k_{\rm Up}^{90\,\%{\rm CL}} < 6{,}3 \times 10^{-7}\ \ {\rm GeV\ cm^{-2}\ s^{-1}\ sr^{-1}} \quad \text{(Downward-going } \nu \text{ bajo ángulo)}$$

válido en el rango energético $E_\nu \in [1{,}9 \times 10^{18} - 2{,}0 \times 10^{20}]$ eV, donde el $\sim 90\,\%$ de los neutrinos emitidos con un flujo de la forma E_ν^{-2} serían detectados.

Este nuevo análisis complementa al publicado anteriormente por la colaboración Pierre Auger a ángulos mayores [3]. En este documento se describe un primer intento de combinación de ambos análisis. Los resultados de este trabajo muestran una contribución significativa a la exposición a neutrinos, especialmente a las mayores energías, extendiendo la sensibilidad del Observatorio a neutrinos más energéticos. A pesar del hecho de que la combinación lineal de la exposición a neutrinos en todo el rango energético es similar para el análisis a alto y bajo ángulo, la contribución final al límite del segundo es moderada debido al comportamiento asumido del flujo ($\sim E_\nu^{-2}$) que penaliza las energías más altas. Actualmente la colaboración Pierre Auger trabaja para combinar los tres análisis existentes para la búsqueda de neutrinos.

■ Mejora del límite al flujo difuso de neutrinos tau interaccionando en la corteza terrestre.

El análisis basado en la búsqueda de neutrinos interaccionando en la corteza terrestre ha sido actualizado y revisado, especialmente en lo que concierne al tratamiento de la polarización del tau y su impacto en las incertidumbres sistemáticas. Además, el periodo analizado por este análisis se ha extendido hasta el 31 de Mayo de 2010. No se han encontrado candidatos a neutrino en los datos. La exposición a neutrinos con este análisis se ha recalculado en el nuevo periodo de búsqueda y de nuevo, asumiendo un flujo difuso de UHEνs de la forma $J(E_\nu) = dN_\nu/dE_\nu = k \cdot E_\nu^{-2}$, y cero fondo esperado, se ha calculado un límite superior al flujo al 90 % C.L.

$$k_{\rm Up}^{90\,\%{\rm CL}} < 3{,}2\ \times 10^{-8}\ \ {\rm GeV\,cm^{-2}\,s^{-1}\,sr^{-1}} \quad \text{(Canal Earth-skimming } \nu_\tau)$$

válido en el rango energético $E_\nu \in [1{,}6 \times 10^{17} - 20{,}8 \times 10^{18}]$ eV, donde el $\sim 90\,\%$ de los neutrinos emitidos con un flujo de la forma E_ν^{-2} serían detectados. Los resultados de este trabajo han sido publicados en [106].

Es importante remarcar que la máxima sensibilidad de los análisis presentados en este trabajo coincide con la región energética en la que los modelos de producción de neutrinos cosmológicos (neutrinos GZK) predicen el mayor flujo. Por lo tanto, la exposición acumulada en ~ 10 años de toma de datos podría ser suficiente para detectar un candidato a neutrino, suponiendo que los modelos teóricos no reduzcan sus predicciones en el futuro. Por otra parte, la ausencia de candidatos en ese periodo podría restringir algunos modelos de producción.

■ **Sensitividad a fuentes puntuales de UHEνs.**

Basado en el resultado negativo de la búsqueda de UHEνs documentada en este trabajo, se ha evaluado la sensibilidad a fuentes puntuales de producción de neutrinos. Se ha descrito el método utilizado para evaluar la exposición de cada análisis como función de la energía y la declinación de cada fuente. Con la ausencia de candidatos, se ha calculado un límite superior al flujo proveniente de cada declinación ($k_{\rm PS}^{90\%CL}$) al 90 % C.L. El cual ha sido publicado en [106].

El análisis de neutrinos interaccionando en la corteza terrestre consigue los límites más restrictivos para energías mayores de 1 EeV y para una región angular de más de 100° de declinación. El límite al flujo como función de la declinación consigue un valor mínimo cercano a 5×10^{-8} GeV cm^{-2} s^{-1} cerca de los -50° y los +55°, decreciendo suavemente para declinaciones entre esos dos valores hasta $\sim 6 \times 10^{-7}$ GeV cm^{-2} s^{-1}. Aunque los límites al flujo conseguidos por el análisis a bajo ángulo son modestos en comparación con los conseguidos por el análisis de "Earth-skimming", el primero extiende las declinaciones visibles hasta los $-80°$, una región del cielo que el análisis "Earth-skimming" no puede observar.

A

The Fisher Discriminant: Polynomial and Cut

The Fisher discriminant was trained using the *Toolkit for Multivariate Data Analysis with ROOT* (TMVA) package which allows to define different data sets (categories) with specific characteristics. Five different categories (one for each angular region) were trained in this analysis. The package treats each category in an independent way providing a Fisher Polynomial for each region. Prior the training process TMVA performs automatically some transformations of variables, namely, decorrelation, gaussanization, normalization and principal component analysis. For an explanation on each procedure see the TMVA handbook [164].

In our analysis, the Fisher polynomial is defined as:

$$\mathcal{F} = C_0 + C_1 \cdot AoP_1 + C_2 \cdot AoP_2 + C_3 \cdot AoP_3 + C_4 \cdot AoP_4 + C_5 \cdot AoP_5 + C_p \prod_{i=1}^{5} AoP_i \qquad \text{(A.1)}$$

for angular regions using five stations, and by:

$$\mathcal{F} = C_0 + C_1 \cdot AoP_1 + C_2 \cdot AoP_2 + C_3 \cdot AoP_3 + C_4 \cdot AoP_4 + C_p \prod_{i=1}^{4} AoP_i \qquad \text{(A.2)}$$

for angular regions using only four stations for the Fisher. Table A.1 shows the Fisher coefficient C_i for each angular region. It is worth to remind that numbers quoted in the table have been rounded off. Hence, it is recommended to use the TMVA weight file containing the polynomial function together with the *classification application script*, both provided by the TMVA application, to compute the Fisher value for each event.

The TMVA package provides some additional information related to the result of the training procedure, in particular it gives a classification of the relevance of the input variables for the discrimination. In our case, the most valuable variable for discrimination is the Area over Peak (AoP) of the first station, followed by the AoP of the remaining stations (showing a similar discrimination power) and finally the product of the AoP.

Table A.2 gives the values of the coefficients obtained by fitting the tail of the $\mathcal{F}$ distribution of the background training sample (0.81 years of full Auger data) to an exponential function

	Region 1	Region 2	Region 3	Region 4	Region 5
C_0	-1.37	-1.21	$-8.42 \cdot 10^{-1}$	$-7.71 \cdot 10^{-1}$	$-4.08 \cdot 10^{-1}$
C_1	$9.10 \cdot 10^{-2}$	$1.04 \cdot 10^{-1}$	$9.11 \cdot 10^{-2}$	$1.29 \cdot 10^{-1}$	$7.62 \cdot 10^{-2}$
C_2	$7.46 \cdot 10^{-2}$	$6.30 \cdot 10^{-2}$	$4.77 \cdot 10^{-2}$	$5.80 \cdot 10^{-2}$	$2.58 \cdot 10^{-2}$
C_3	$1.36 \cdot 10^{-1}$	$1.33 \cdot 10^{-1}$	$9.39 \cdot 10^{-2}$	$8.66 \cdot 10^{-2}$	$5.16 \cdot 10^{-2}$
C_4	$8.13 \cdot 10^{-2}$	$5.89 \cdot 10^{-2}$	$3.28 \cdot 10^{-2}$	$5.80 \cdot 10^{-2}$	$3.56 \cdot 10^{-2}$
C_5	$8.08 \cdot 10^{-2}$	$6.46 \cdot 10^{-2}$	$4.18 \cdot 10^{-2}$	–	–
C_p	$-3.16 \cdot 10^{-5}$	$-3.30 \cdot 10^{-5}$	$-2.92 \cdot 10^{-5}$	$-3.78 \cdot 10^{-4}$	$-2.71 \cdot 10^{-4}$

Table A.1: Fisher Coefficients for each angular region.

	Region 1	Region 2	Region 3	Region 4	Region 5
a	-9.1 ± 0.4	-12.8 ± 0.8	-16.3 ± 1.2	-21.7 ± 1.4	-40.2 ± 3.9
b	0.9 ± 0.2	-1.4 ± 0.3	-1.6 ± 0.4	-2.6 ± 0.4	-3.3 ± 0.6

Table A.2: Coefficients obtained from the exponential fit to the tail of the background training distribution ($y = e^{a \cdot x + b}$).

($y = e^{a \cdot x + b}$). These functions are used to give an estimate of the expected number of background events passing the cuts on each region.

We remind here that the $\mathcal{F}$ cut is placed to allow 0.2 events in 20 years using the most conservative extrapolation (i.e. including the errors in the coefficients). In table A.3 we give the central values of $(\theta, \mathcal{F}_{cut})$ for each angular region. The final Fisher cut as function of θ is obtained by linear interpolation between these points.

Finally, the most relevant data and results obtained on the search for UHEνs in the framework of this Ph.D. thesis have been compiled in a ROOT file and made available to the Pierre Auger collaborators [201], in order to facilitate the foreseen combination of the ν search analyses or any future revision of the selection criteria.

	Region 1	Region 2	Region 3	Region 4	Region 5
$(\theta, \mathcal{F}_{cut})$	$(60°, 0.68)$	$(63°, 0.31)$	$(66°, 0.24)$	$(69°, 0.13)$	$(73.5°, 0.06)$

Table A.3: Pairs $(\theta, \mathcal{F}_{cut})$ used to construct the Fisher cut function by lineal interpolation.

B

Contributions to Offline Package

The Offline package [145] has been designed to provide an infrastructure to support a variety if distinct computational tasks necessary to analyse the data collected by the Pierre Auger Observatory. The requirements of this project place rather strong demands on the software framework underlying data analysis. The framework must be flexible and robust enough to support the collaborative effort of a large number of physicists developing a variety of applications over the projected lifetime of the experiment. Specifically, the software supports simulation and reconstruction of events using surface, fluorescence and hybrid methods, as well as simulation of calibration techniques and other ancillary tasks such as data preprocessing. Further, as the experimental run will be long, it is essential that the software be extensible to accommodate future upgrades to the Observatory instrumentation.

To fulfil all these requirements the Offline framework comprises three principal parts: a collection of processing modules which can be assembled and sequenced through instructions provided in an eXtensible Markup Language (XML) file, an event data model through which modules can relay data to one another and which accumulates all simulation and reconstruction information, and a detector description which provides a gateway to data describing the configuration and performance of the Observatory as well as atmospheric conditions as a function of time.

To perform the analyses described in this Ph.D. thesis, some new Offline modules were developed in order to adapt the standard analysis procedure to the special features of a neutrino search. In the following sections we give a brief description of the contributions to the Offline package.

B.1 SdAccidentalSignalInyectorGP

As already discussed in section 4.2.2, accidental signals can have a pernicious effect on data quality. Therefore, it is recommended to include the effect of the accidentals, naturally present in real data, in the Monte-Carlo simulated air showers in order to evaluate their impact on the different physics analyses. The use of a realistic accidental background estimation is specially needed when searching for rare events (e.g. photons or neutrinos), selected from the shape of the traces. Some modules for the Offline were developed to simulate accidental signals based mainly in parametrizations of the atmospheric muon flux model (for instance [202]). However, as

mentioned in section 4.2.2, atmospheric muons are not the only source of accidental signals.

The characterization of accidental signals from real data published in [161] was a turning point for the simulation of such signals. Since those signals were selected from real data they include all possible effects (not only atmospheric muons) in a model independent way, providing a fair unbiased sample of the background to the event simulation. It may also account for long term variations or periodic oscillations of these fluxes.

Taking advantage of the set of real accidental signals, an Offline module has been developed to include them in the detector simulation. The module randomly selects an accidental signal from the sample and introduces the signal directly in the trace of each photomultiplier (PMT). The user can chose the time window around the shower front plane arrival time where the accidental signal will be injected. For each station the module computes the appropriate number of accidental signals to be inserted assuming Poisson distributions and the signal rates computed in [161].

The module provides the user some freedom to select the stations were accidental signals will be injected. By default, detectors triggered by at least one simulated particle from the simulated shower are always considered. Additional stations can be also considered crown by crown around the footprint as well as the full array.

A detailed description of the module and the use can be found in the Auger internal note [203].

B.2 SdTopDownSignalRejectorUGR

Despite the importance of the accidental signals, the Offline package does not provide any treatment against them. The *SdTopDownSignalRejectorUGR* module was specially developed to clean the traces of the surface detectors identifying accidental signals and rejecting them. The module can operate in two modes:

Only Accidental treatment In this mode the module only performs accidental signals rejection. The treatment is inspired in the accidental signal identification method already published in [159]. The module identifies segments of signals with criteria defined by the user. If two or more segments are found the election of the good one is made based in three user eligible criteria, namely, the one with biggest signal, the one with biggest AoP or the one with the biggest product of Signal $\times$ "number of bins of the segment". Following the Offline philosophy, all the parameters defined in [159] can be customized using an XML file. With this treatment almost all accidental signals are properly identified and rejected.

Top Down Selector The accidental signal rejection described above is powerful enough for most of the analyses that could be performed in Auger. Nevertheless, some stations are triggered only by an accidental signal fulfilling the criteria of a true shower signal. Moreover, the triggered station can be situated near the triggered stations of a real event fulfilling the geometrical compactness criteria. This signals can not be identified with the previous treatment. Therefore, an advanced algorithm has been developed to identify these signals. The algorithm is based in a "top down" selection criteria [160] and works as follows:

1. First it selects *elementary segments* with a looser criteria than the one specified in [159]. The segment together with the geographical position of the station and other parameters of interest are stored and piled up. It allows to treat each segment as an independent station.
2. A top down procedure as the one published in [160] is applied over the segments instead of over the stations. All the segments are sorted by increasing signal and

the top down procedure tries to find a compatible pattern with a front plane shower propagating at speed of light with certain user defined tolerance. It recursively rejects station by station until a pattern is accepted. The algorithm automatically selects the proper segments, rejecting the accidental ones.

3. The stations with all segments rejected are flagged as accidental stations. For the stations with two or more segments selected, the one with the biggest residual time to the expected front plane shower fit is rejected.
4. The Flash Analog to Digital Converter (FADC) trace of all accepted stations is scanned. If any segment after the selected one fulfils the criteria of [159] it is also accepted.
5. Finally, for each selected station, the start bin (start time) and the end bin (end time) together with some common variables (i.e. rise time, fall time, AoP) are computed and properly stored in the $\overline{\text{Off}}\underline{\text{line}}$ event class.

Note that this option performs both accidental signal rejection and candidate station selection through a top down procedure.

This module plays a key role in the rejection of background, and rejecting most of the fake neutrino candidates due to bad angular reconstruction induced by spoil signals. The XML configuration of the module is given below:

```
<SdTopDownSignalSelectorUGR>

  <Verbose> 4 </Verbose>

  <!-- Select procedure for Accidental Rejection -->
  <!-- 0=Signal, 1=SignalQuality, 2=AoP, 3=AoPQuality, 4=TopDownSelection -->
  <RejectionProcedure> 4 </RejectionProcedure>

  <!-- Only Accidental Rejection -->
  <!-- For a full description of the  parameters see GAP 2005-074 from Pierre Billor -->
  <SignalThreshold> 0.015 </SignalThreshold>
  <Nmin > 10 </Nmin>
  <Smin > 1.0 </Smin>
  <N0 > 20 </N0>

  <MinStationSignal> 3 </MinStationSignal>
  <MinNumberOfStationForSignalCut> 5 </MinNumberOfStationForSignalCut>
  <AnodeSignalFactor> 32 </AnodeSignalFactor>


  <!-- Accidental + Station selection -->
  <!-- Top Down signal selection parameters -->
  <PreSignalThreshold> 0.015 </PreSignalThreshold>
  <PreNmin > 3 </PreNmin>
  <PreSmin > 0.3 </PreSmin>
  <PreN0 > 0 </PreN0>
```

```
  <RejectNonT4Events> 0 </RejectNonT4Events>
  <MinNumberStations> 3 </MinNumberStations>
  <MaxNumberStations> 20 </MaxNumberStations>
  <MaxRejectedSignals> 8 </MaxRejectedSignals>
  <BaryPower> 1 </BaryPower>
  <TimeResidualTolerance> 190 </TimeResidualTolerance>
  <MTimeResidualTolerance>  230 </MTimeResidualTolerance>
  <IsolatedDistance1> 4700 </IsolatedDistance1>
  <IsolatedDistance2> 6200 </IsolatedDistance2>
  <IsoTime1> 15700 </IsoTime1>
  <IsoTime2> 20700 </IsoTime2>
  <Curv0> 0.00014 </Curv0>
  <AreaMin> 0.2e6 </AreaMin>
  <AreaMax> 1.2e6 </AreaMax>
  <DistMax> 2800 </DistMax>
  <Ana3RatMin> 1.6 </Ana3RatMin>

</SdTopDownSignalSelectorUGR>
```

The official XML file provides explanations (omitted here) for each parameter. An internal Auger document with the detail description of the module is in preparation.

B.3 SdFootprintAnalyzerOG

The original Offline framework does not provide any module to compute variables commonly used in neutrino analyses. This prevents, for instance, to reproduce in an easy way the results of the already published analyses. The *SdFooprintAnalyzerOG* module is designed to allow any Auger collaborator to run the DG_{low} neutrino analysis in an easy way. Moreover, the module computes the variables used in other ν analyses and add to the Offline event class the proper containers for such variables to store the data. The module is highly customizable, allowing the user to add new variables that could appear in future analyses. Some of the currently implemented variables are:

Length: Computed as the first eigenvalue of the tensor constructed with the signal weighted station positions at ground as defined in [4]. This variable is proportional to the length of the major axis of the ellipse formed by the footprint.

Width: The complementary variable to the Length extracted from the second eigenvalue of the tensor.

Speed: Mean of all the apparent speeds of the shower front plane moving between pairs of stations. The parameter is defined in [4]. The criteria established to use a pair of stations for the speed histogram computation can be user defined.

Speed Standard Deviation: The standard deviation of apparent speed histogram. All accepted pairs of stations correspond to an entry in the histogram.

Time over Threshold fraction: The fraction of triggered stations with AoP above an user definable threshold which have a Time-over-Threshold trigger (ToT) local trigger. This variable is used in [4, 185].

Area over Peak Asymmetry: Asymmetry between the mean value of the AoP of the first and the last triggered stations.

Alignment: Computes whether or not a surface event has all the triggered stations aligned. The algorithm also returns the status "ill" when all stations are aligned and one of them is not. This parameter is used on the DG_{high} analysis [3].

B.4 T2StatFileManager

The surface array of the Pierre Auger Observatory has a dynamic behaviour in the sense that stations can connect and disconnect independently at any time. Thus, the effective area of the surface array can be different at any time. To account for the status of the stations at each instant of time a monitoring files are produced. The format of those files has been changed with time. The *T2StatFileManager* was created to read the monitoring files in "T2Stat" format [204]. The module also allows for corrections of the "comms-crisis" period [205], a period of high instability and communication problems of the surface detectors (SD) during 2009. An station delays for 120 seconds in sending the data of an event to the Central Data Acquisition System (CDAS). Consequently, to consider an station alive at a certain time, it should be also alive during the next 120 seconds. The probability of an station failing within the 120 seconds after an event is low, except for the "coms-crisis" period. The module allows the user to account for this effect activating a flag. This module was the first $\overline{\text{Off}}\underline{\text{line}}$ module accounting for this effect and it is currently included in the official production release of the framework.

List of used Acronyms

AERA Auger Engineering Radio Array

AGN Active Galactic Nucleus

AMBER Air-shower Microwave Bremsstrahlung Experimental Radiometer

AMIGA Auger Muons and Infill for the Ground Array

AoP Area over Peak

C.L. confidence level

CC charged current

CDAS Central Data Acquisition System

CMB Cosmic Microwave Background

CORSIKA COsmic Ray SImulations for KAscade

CR Cosmic Ray

DAQ Data Acquisition

EAS Extensive Air Shower

EASIER Extensive Air Shower Identification using Electron Radiometer

FADC Flash Analog to Digital Converter

FD fluorescence detectors

GRB Gamma Ray Burst

GZK Greisen-Zatsepin-Kuzmin

HEAT High Elevation Auger Telescopes

ID identification number

IR infra-red

LDF Lateral Distribution Function

LIDAR light detection and ranging

MC Monte-Carlo

MIDAS Microwave Detection of Air Showers

MPD muon production distribution

NC neutral current

NKG Nishimura-Kamata-Greisen

PDF parton distribution function

PMT photomultiplier

QCD quantum chromodynamics

RNB relic neutrino background

SD surface detectors

SNR supernova remnant

TH Threshold trigger

TMVA *Toolkit for Multivariate Data Analysis with ROOT*

ToT Time-over-Threshold trigger

UHE Ultra High Energy

UHEν Ultra High Energy Neutrino

UHECR Ultra High Energy Cosmic Ray

UV ultraviolet light

VEM Vertical Equivalent Muon

XML eXtensible Markup Language

List of Figures

List of Tables

Bibliography

[1] K. Greisen. Cosmic ray showers. *Annual review of nuclear science*, 10(1):63–108, 1960.

[2] J. Abraham et al. Properties and performance of the prototype instrument for the Pierre Auger Observatory. *Nucl.Instrum.Meth.*, A523:50–95, 2004.

[3] P. Abreu et al. A Search for Ultra-High Energy Neutrinos in Highly Inclined Events at the Pierre Auger Observatory. *Phys.Rev.*, D84:122005, 2011.

[4] J. Abraham et al. Limit on the diffuse flux of ultra-high energy tau neutrinos with the surface detector of the Pierre Auger Observatory. *Phys.Rev.*, D79:102001, 2009.

[5] P. Auger, P. Ehrenfest, R. Maze, J. Daudin, and R.A. Fréon. Extensive cosmic-ray showers. *Reviews of Modern Physics*, 11(3-4):288–291, 1939.

[6] K.H. Kampert and M. Unger. Measurements of the Cosmic Ray Composition with Air Shower Experiments. 2012.

[7] R.U. Abbasi, T. Abu-Zayyad, J.F. Amman, G.C. Archbold, J.A. Bellido, K. Belov, J.W. Belz, D.R. Bergman, Z. Cao, R.W. Clay, et al. Monocular measurement of the spectrum of uhe cosmic rays by the fadc detector of the hires experiment. *Astroparticle Physics*, 23(2):157–174, 2005.

[8] J. Abraham et al. Measurement of the energy spectrum of cosmic rays above 10^{18} eV using the Pierre Auger Observatory. *Phys.Lett.*, B685:239–246, 2010.

[9] J. Abraham et al. Upper limit on the cosmic-ray photon fraction at EeV energies from the Pierre Auger Observatory. *Astropart.Phys.*, 31:399–406, 2009.

[10] E. Fermi. On the origin of the cosmic radiation. *Physical Review*, 75(8):1169, 1949.

[11] W.I. Axford. The Origins of high-energy cosmic rays. 1994.

[12] E.G. Berezhko and G.F. Krymsky. Acceleration of cosmic rays by shock waves. *Sov.Phys.Usp.*, 31:27–51, 1988.

[13] A.A. Penzias and R.W. Wilson. A Measurement of Excess Antenna Temperature at 4080 Mc/s. *Astrophysical Journal*, 142:419–421, jul 1965.

[14] C.E. Fichtel and D.V. Reames. Cosmic-ray propagation. *Physical Review*, 175(5):1564, 1968.

[15] J.W. Cronin. The highest-energy cosmic rays. *Nuclear Physics B-Proceedings Supplements*, 138:465–491, 2005.

[16] K. Greisen. End to the cosmic-ray spectrum? *Physical Review Letters*, 16(17):748–750, 1966.

[17] G.T. Zatsepin and V.A. Kuz'Min. Upper limit of the spectrum of cosmic rays. *JETP Lett.(USSR)(Engl. Transl.)*, 4, 1966.

[18] J.L. Puget, F.W. Stecker, and J.H. Bredekamp. Photonuclear Interactions of Ultrahigh-Energy Cosmic Rays and their Astrophysical Consequences. *Astrophys.J.*, 205:638–654, 1976.

[19] G.R. Blumenthal. Energy loss of high-energy cosmic rays in pair-producing collisions with ambient photons. *Phys.Rev.*, D1:1596–1602, 1970.

[20] F.W. Stecker and M.H. Salamon. Photodisintegration of ultrahigh-energy cosmic rays: A New determination. *Astrophys.J.*, 512:521–526, 1999.

[21] L.N. Epele and E. Roulet. On the propagation of the highest energy cosmic ray nuclei. *JHEP*, 9810:009, 1998.

[22] M.C. Allcock and J. Wdowczyk. The attenuation length for high-energy gamma-rays in the relict radiation. *Nuovo Cim.*, B9:315–320, 1972.

[23] R.J. Protheroe and P.L. Biermann. A New estimate of the extragalactic radio background and implications for ultrahigh-energy gamma-ray propagation. *Astropart.Phys.*, 6:45–54, 1996.

[24] P. Bhattacharjee and G. Sigl. Origin and propagation of extremely high-energy cosmic rays. *Physics Reports*, 327(3):109–247, 2000.

[25] G. Sigl, S. Lee, P. Bhattacharjee, and S. Yoshida. Probing grand unified theories with cosmic ray, gamma-ray and neutrino astrophysics. *Phys. Rev.*, D59:043504, 1999.

[26] S. Yoshida and M. Teshima. Energy spectrum of ultrahigh-energy cosmic rays with extragalactic origin. *Prog.Theor.Phys.*, 89:833–845, 1993.

[27] R.J. Protheroe and P.A. Johnson. Propagation of ultrahigh-energy protons over cosmological distances and implications for topological defect models. *Astropart. Phys.*, 4:253, 1996.

[28] G.R. Farrar and P.L. Biermann. Correlation between compact radio quasars and ultrahigh-energy cosmic rays. *Phys.Rev.Lett.*, 81:3579–3582, 1998.

[29] S.R. Coleman and S.L. Glashow. High-energy tests of Lorentz invariance. *Phys.Rev.*, D59:116008, 1999.

[30] S.R. Coleman and S.L. Glashow. Evading the GZK cosmic ray cutoff. 1998.

[31] L. Gonzalez-Mestres. Physics opportunities above the Greisen-Zatsepin-Kuzmin cutoff: Lorentz symmetry violation at the Planck scale. 1997.

[32] L. Gonzalez-Mestres. Deformed Lorentz symmetry and ultrahigh-energy cosmic rays. 1999.

[33] M. Amenomori, Z. Cao, B.Z. Dai, L.K. Ding, Y.X. Feng, Z.Y. Feng, K. Hibino, N. Hotta, Q. Huang, A.X. Huo, et al. The cosmic-ray energy spectrum between 10 14.5 and 10 16.3 ev covering the"knee"region. *The Astrophysical Journal*, 461:408, 1996.

[34] J.R. Hoerandel. On the knee in the energy spectrum of cosmic rays. *Astroparticle Physics*, 19(2):193–220, 2003.

[35] D.J. Bird, S.C. Corbato, H.Y. Dai, B.R. Dawson, J.W. Elbert, T.K. Gaisser, K.D. Green, M.A. Huang, D.B. Kieda, S. Ko, et al. Evidence for correlated changes in the spectrum and composition of cosmic rays at extremely high energies. *Physical review letters*, 71(21):3401–3404, 1993.

[36] P. Abreu et al. The Pierre Auger Observatory I: The Cosmic Ray Energy Spectrum and Related Measurements. 2011.

[37] R.U. Abbasi et al. Observation of the GZK cutoff by the HiRes experiment. *Phys. Rev. Lett.*, 100:101101, 2008.

[38] N. Sakaki et al. . *Proc. 27th ICRC*, 2011.

[39] Y. Tsunesada et al. . *Proc. 27th ICRC*, 2011.

[40] T. Abu-Zayyad, R. Aida, M. Allen, R. Anderson, R. Azuma, et al. The Cosmic Ray Energy Spectrum Observed with the Surface Detector of the Telescope Array Experiment. 2012.

[41] J. Abraham et al. Correlation of the highest energy cosmic rays with nearby extragalactic objects. *Science*, 318:938–943, 2007.

[42] J. Abraham et al. Correlation of the highest-energy cosmic rays with the positions of nearby active galactic nuclei. *Astropart.Phys.*, 29:188–204, 2008.

[43] P. Abreu et al. Update on the correlation of the highest energy cosmic rays with nearby extragalactic matter. *Astropart.Phys.*, 34:314–326, 2010.

[44] M.P. Veron-Cetty and P. Veron. A catalogue of quasars and active nuclei: 12th edition. *Astron. Astrophys.*, 455:773–777, 2006.

[45] T. Abu-Zayyad et al. Search for Anisotropy of Ultra-High Energy Cosmic Rays with the Telescope Array Experiment. 2012.

[46] P. Abreu et al. Search for signatures of magnetically-induced alignment in the arrival directions measured by the Pierre Auger Observatory. *Astropart.Phys.*, 35:354–361, 2012.

[47] J. Abraham et al. Measurement of the Depth of Maximum of Extensive Air Showers above 10^{18} eV. *Phys.Rev.Lett.*, 104:091101, 2010.

[48] P. Abreu et al. The Pierre Auger Observatory II: Studies of Cosmic Ray Composition and Hadronic Interaction models. 2011.

[49] R.U. Abbasi et al. Indications of Proton-Dominated Cosmic Ray Composition above 1.6 EeV. *Phys. Rev. Lett.*, 104:161101, 2010.

[50] Y. Tameda. Measurement of UHECR composition by TA. *AIP Conf. Proc.*, 1367:110–113, 2011.

[51] C.C.H. Jui. Cosmic Ray in the Northern Hemisphere: Results from the Telescope Array Experiment. 2011.

[52] D. Garcia-Gamez. *Muon Arrival Time distributions and its relationship to the mass composition of Ultra High Energy Cosmic Rays: An application to the Pierre Auger Observatory.* PhD thesis, Dpto. de Física Teórica y del Cosmos & CAFPE. Universidad de Granada, October 2010.

[53] D. Garcia Gamez. Measurement of atmospheric production depths of muons with the Pierre Auger Observatory. *Proc. 32nd ICRC*, 2:109, 2011.

[54] P. Abreu et al. The Pierre Auger Observatory III: Other Astrophysical Observations. 2011.

[55] V.S. Berezinsky and G.T. Zatsepin. Cosmic rays at ultra high energies (neutrino?). *Phys. Lett.*, B28:423–424, 1969.

[56] M. Ahlers, L.A. Anchordoqui, M.C. Gonzalez-Garcia, F. Halzen, and S. Sarkar. GZK Neutrinos after the Fermi-LAT Diffuse Photon Flux Measurement. *Astropart. Phys.*, 34:106–115, 2010.

[57] K. Kotera, D. Allard, and A.V. Olinto. Cosmogenic Neutrinos: parameter space and detectabilty from PeV to ZeV. *JCAP*, 1010:013, 2010.

[58] M. Ave, N. Busca, A.V. Olinto, A.A. Watson, and T. Yamamoto. Cosmogenic neutrinos from ultra-high energy nuclei. *Astropart.Phys.*, 23:19–29, 2005.

[59] G. Gelmini, O.E. Kalashev, and D.V. Semikoz. GZK photons as ultra high energy cosmic rays. *J.Exp.Theor.Phys.*, 106:1061–1082, 2008.

[60] W.C. Haxton and B.R. Holstein. Neutrino physics. *Am.J.Phys.*, 68:15–32, 2000.

[61] W.C. Haxton and B.R. Holstein. Neutrino physics: An Update. *Am.J.Phys.*, 72:18–24, 2004.

[62] J.N. Bahcall. *Neutrino Astrophysics.* Number 587p. Cambridge University Press, 1989. CAMBRIDGE, UK: UNIV. PR. (1989) 567p.

[63] W.C. Haxton. Neutrino Astrophysics. *Internal Publication*, 2008.

[64] Y. Fukuda, T. Hayakawa, E. Ichihara, K. Inoue, K. Ishihara, H. Ishino, Y. Itow, T. Kajita, J. Kameda, S. Kasuga, et al. Evidence for oscillation of atmospheric neutrinos. *Physical Review Letters*, 81(8):1562–1567, 1998.

[65] M.H. Ahn et al. Search for electron neutrino appearance in a 250 km long baseline experiment. *Phys.Rev.Lett.*, 93:051801, 2004.

[66] S.N. Ahmed et al. Measurement of the total active B-8 solar neutrino flux at the Sudbury Neutrino Observatory with enhanced neutral current sensitivity. *Phys.Rev.Lett.*, 92:181301, 2004.

[67] H. Athar, M. Jezabek, and O. Yasuda. Effects of neutrino mixing on high-energy cosmic neutrino flux. *Phys. Rev.*, D62:103007, 2000.

[68] E. Waxman and J.N. Bahcall. High energy neutrinos from astrophysical sources: An upper bound. *Phys. Rev.*, D59:023002, 1999.

[69] K. Mannheim, R.J. Protheroe, and J.P. Rachen. On the cosmic ray bound for models of extragalactic neutrino production. *Phys. Rev.*, D63:023003, 2001.

[70] R. Engel, D. Seckel, and T. Stanev. Neutrinos from propagation of ultra-high energy protons. *Phys. Rev.*, D64:093010, 2001.

[71] J.N. Bahcall and E. Waxman. High energy astrophysical neutrinos: The upper bound is robust. *Phys. Rev.*, D64:023002, 2001.

[72] T.K. Gaisser and T. Stanev. Neutrinos and cosmic rays. 2012.

[73] K.S. Hirata et al. Real time, directional measurement of B-8 solar neutrinos in the Kamiokande-II detector. *Phys. Rev.*, D44:2241, 1991.

[74] K.S. Hirata et al. Observation of a Neutrino Burst from the Supernova SN 1987a. *Phys. Rev. Lett.*, 58:1490–1493, 1987.

[75] P.A. Cherenkov. Radiation of ultralight speed charged particles and its utilization in the physics of high-energy particles. 1962.

[76] R. Gandhi, C. Quigg, M.H. Reno, and I. Sarcevic. Neutrino interactions at ultrahigh-energies. *Phys. Rev.*, D58:093009, 1998.

[77] R. Gandhi, C. Quigg, M.H. Reno, and I. Sarcevic. Ultrahigh-energy neutrino interactions. *Astropart. Phys.*, 5:81–110, 1996.

[78] L.A. Anchordoqui, A.M. Cooper-Sarkar, D. Hooper, and S. Sarkar. Probing low-x QCD with cosmic neutrinos at the Pierre Auger Observatory. *Phys. Rev.*, D74:043008, 2006.

[79] I. Sarcevic. Ultrahigh energy cosmic neutrinos and the physics beyond the standard model. *J. Phys. Conf. Ser.*, 60:175–178, 2007.

[80] A. Cooper-Sarkar, P. Mertsch, and S. Sarkar. The high energy neutrino cross-section in the Standard Model and its uncertainty. *JHEP*, 08:042, 2011.

[81] V.N. Gribov and L.N. Lipatov. Deep inelastic e p scattering in perturbation theory. *Sov.J.Nucl.Phys.*, 15:438–450, 1972.

[82] F.D. Aaron et al. Combined Measurement and QCD Analysis of the Inclusive e+- p Scattering Cross Sections at HERA. *JHEP*, 1001:109, 2010.

[83] A. Cooper-Sarkar. Proton Structure from HERA to LHC. 2010.

[84] J. Ahrens et al. Icecube - the next generation neutrino telescope at the south pole. *Nucl.Phys.Proc.Suppl.*, 118:388–395, 2003.

[85] E. Andres et al. The AMANDA neutrino telescope: Principle of operation and first results. *Astropart. Phys.*, 13:1–20, 2000.

[86] V. Aynutdinov et al. Search for a diffuse flux of high-energy extraterrestrial neutrinos with the nt200 neutrino telescope. *Astropart.Phys.*, 25:140–150, 2006.

[87] V. Aynutdinov et al. The Baikal neutrino experiment: From NT200 to NT200+. *Nucl.Instrum.Meth.*, A567:433–437, 2006.

[88] F. Blanc et al. Towards a large scale high-energy cosmic neutrino undersea detector. 1997.

[89] P. Sapienza. Status of the NEMO Project. 2006.

[90] G. Aggouras et al. A measurement of the cosmic-ray muon flux with a module of the NESTOR neutrino telescope. *Astropart.Phys.*, 23:377–392, 2005.

[91] U.F. Katz. The KM3NeT project. *Nucl.Instrum.Meth.*, A626-627:S57–S63, 2011.

[92] G.A. Askaryan. *Soviet Physics JETP*, 14:441–443, 1962.

[93] D. Saltzberg et al. Observation of the Askaryan effect: Coherent microwave Cherenkov emission from charge asymmetry in high energy particle cascades. *Phys. Rev. Lett.*, 86:2802–2805, 2001.

[94] P.W. Gorham, D. Saltzberg, R.C. Field, E. Guillian, R. Milincic, et al. Accelerator measurements of the Askaryan effect in rock salt: A Roadmap toward teraton underground neutrino detectors. *Phys.Rev.*, D72:023002, 2005.

[95] P.W. Gorham et al. Observations of the Askaryan effect in ice. *Phys.Rev.Lett.*, 99:171101, 2007.

[96] I. Kravchenko et al. Performance and simulation of the RICE detector. *Astropart.Phys.*, 19:15–36, 2003.

[97] S.W. Barwick et al. Constraints on cosmic neutrino fluxes from the anita experiment. *Phys.Rev.Lett.*, 96:171101, 2006.

[98] G.S. Varner, L. Murakami, D. Ridley, C. Zhu, and P. Gorham. Evaluation of gigabit ethernet instrumentation for salsa electronics readout (geiser). *Nucl.Instrum.Meth.*, A554:437–443, 2005.

[99] J.D. Bray, R.D. Ekers, C.W. James, P. Roberts, A. Brown, et al. LUNASKA simultaneous neutrino searches with multiple telescopes. 2011.

[100] J. Vandenbroucke, G. Gratta, and N. Lehtinen. Experimental study of acoustic ultrahigh - energy neutrino detection. *Astrophys.J.*, 621:301–312, 2005.

[101] C.L. Naumann, G. Anton, K. Graf, J. Hoessl, A. Kappes, et al. Development of Acoustic Sensors for the ANTARES Experiment. *Int.J.Mod.Phys.*, A21S1:92–96, 2006.

[102] S. Boeser, C. Bohm, S. Hundertmark, A. Hallgren, R. Nahnhauer, et al. SPATS: A south pole acoustic test setup. *Int.J.Mod.Phys.*, A21S1:221–226, 2006.

[103] R. Abbasi et al. Time-Dependent Searches for Point Sources of Neutrinos with the 40-String and 22-String Configurations of IceCube. *Astrophys. J.*, 744:1, 2012.

[104] A. Franckowiak. Search for transient neutrino sources with IceCube. *Proc. 2011 Fermilab Symposium*, 2011.

[105] E. Waxman and J.N. Bahcall. High energy neutrinos from cosmological gamma-ray burst fireballs. *Phys. Rev. Lett.*, 78:2292–2295, 1997.

[106] P. Abreu et al. Search for point-like sources of ultra-high energy neutrinos at the Pierre Auger Observatory and improved limit on the diffuse flux of tau neutrinos. *Astrophys. J. Lett*, 755(1):L4, 2012.

[107] XXV International Conference on Neutrino Physics and Astrophysics, Kyoto, Japan. 2012.

[108] A. Achterberg et al. First year performance of the IceCube neutrino telescope. *Astropart. Phys.*, 26:155–173, 2006.

[109] P. W. Gorham et al. New Limits on the Ultra-high Energy Cosmic Neutrino Flux from the ANITA Experiment. *Phys. Rev. Lett.*, 103:051103, 2009.

[110] W. Heitler. *The quantum theory of radiation.* Dover Pubns, 1954.

[111] J. Matthews. A heitler model of extensive air showers. *Astroparticle Physics*, 22(5):387–397, 2005.

[112] L. Anchordoqui, M.T. Dova, A. Mariazzi, T. McCauley, T. Paul, S. Reucroft, and J. Swain. High energy physics in the atmosphere: Phenomenology of cosmic ray air showers. *Annals of Physics*, 314(1):145–207, 2004.

[113] H. Bethe and W. Heitler. On the stopping of fast particles and on the creation of positive electrons. *Proceedings of the Royal Society of London. Series A*, 146(856):83–112, 1934.

[114] K. Greisen. Progress in cosmic ray physics. *Amsterdam: North Holland p*, 1:189–95, 1956.

[115] K. Kamata and J. Nishimura. The lateral and the angular structure functions of electron showers. *Prog. Theoret. Phys. Suppl*, 6:93, 1958.

[116] W.R. Nelson, H. Hirayama, and D.W.O. Rogers. The EGS4 code system. SLAC-0265, 1985.

[117] D. Heck, G. Schatz, T. Thouw, J. Knapp, and J.N. Capdevielle. CORSIKA: A Monte Carlo code to simulate extensive air showers. Technical report, Forschungszentrum Karlsruhe, 1998.

[118] T. Stanev. *High Energy Cosmic Rays*. Springer Praxis Books, 2010.

[119] J. Alvarez-Muniz, R. Engel, T.K. Gaisser, J.A. Ortiz, and T. Stanev. Hybrid simulations of extensive air showers. *Phys. Rev.*, D66:033011, 2002.

[120] R. Ulrich, J. Blumer, R. Engel, F. Schussler, and M. Unger. On the measurement of the proton-air cross section using air shower data. *New J.Phys.*, 11:065018, 2009.

[121] M.T. Dova, L.N. Epele, and A.G. Mariazzi. The effect of atmospheric attenuation on inclined cosmic ray air showers. *Astroparticle Physics*, 18(4):351–365, 2003.

[122] S.F. Berezhnev, D. Besson, A.V. Korobchenko, N.M. Budnev, A. Chiavassa, et al. The Tunka-133 EAS Cherenkov light array: status of 2011. 2012.

[123] T. Hara, S. Kawaguchi, S. Mikamo, M. Nagano, K. Suga, et al. Observation of air showers of energies above 10-to-the-eighteenth ev. *Conf.Proc.*, C690825:361–367, 1969.

[124] G. Navarra, T. Antoni, W.D. Apel, F. Badea, K. Bekk, A. Bercuci, M. Bertaina, H. Blümer, H. Bozdog, I.M. Brancus, et al. Kascade-grande: a large acceptance, high-resolution cosmic-ray detector up to 1018ev. *Nuclear Instruments and Methods in Physics Research Section A: Accelerators, Spectrometers, Detectors and Associated Equipment*, 518(1):207–209, 2004.

[125] H.O. Klages, W.D. Apel, K. Bekk, E. Bollmann, P. Doll, et al. The KASCADE Experiment. *Nucl.Phys.Proc.Suppl.*, 52B:92–102, 1997.

[126] T. Huege and H. Falcke. Radio Emission from Cosmic Ray Air Showers: Coherent Geosynchrotron Radiation. *Astron. Astrophys.*, 412:19–34, 2003.

[127] J.R. Horandel, W.D. Apel, J.C. Arteaga, T. Asch, F. Badea, et al. Measurement of Radio Emission from Extensive Air Showers with LOPES. *Nucl.Instrum.Meth.*, A630:171–176, 2011.

[128] P. Abreu et al. The Pierre Auger Observatory V: Enhancements. 2011.

[129] A. Bueno, A. Gascon, J.I. Illana, and M. Masip. Propagation of B mesons in the atmosphere. *JCAP*, 1202:028, 2012.

[130] R.M. Baltrusaitis, R. Cady, G.L. Cassiday, R. Cooper, J.W. Elbert, et al. The UTAH Fly's Eye Detector. *Nucl.Instrum.Meth.*, A240:410–428, 1985.

[131] T. Abu-Zayyad, M. Al-Seady, K. Belov, G. Chen, H.Y. Dai, et al. The prototype high-resolution Fly's Eye cosmic ray detector. *Nucl.Instrum.Meth.*, A450:253–269, 2000.

[132] H. Kawai, S. Yoshida, H. Yoshii, K. Tanaka, F. Cohen, et al. Telescope array experiment. *Nucl.Phys.Proc.Suppl.*, 175-176:221–226, 2008.

[133] M. Nagano, K. Kobayakawa, N. Sakaki, and K. Ando. New measurement on photon yields from air and the application to the energy estimation of primary cosmic rays. *Astropart.Phys.*, 22:235–248, 2004.

[134] M. Ave et al. Measurement of the pressure dependence of air fluorescence emission induced by electrons. *Astropart. Phys.*, 28:41–57, 2007.

[135] M. Ave. Temperature and Humidity Dependence of Air Fluorescence Yield measured by AIRFLY. *Nucl. Instrum. Meth.*, A597:50–54, 2008.

[136] J. Abraham et al. A Study of the Effect of Molecular and Aerosol Conditions in the Atmosphere on Air Fluorescence Measurements at the Pierre Auger Observatory. *Astropart.Phys.*, 33:108–129, 2010.

[137] P. Abreu et al. Description of Atmospheric Conditions at the Pierre Auger Observatory using the Global Data Assimilation System (GDAS). *Astropart.Phys.*, 35:591–607, 2012.

[138] J. Abraham et al. The Fluorescence Detector of the Pierre Auger Observatory. *Nucl.Instrum.Meth.*, A620:227–251, 2010.

[139] I. Allekotte et al. The Surface Detector System of the Pierre Auger Observatory. *Nucl. Instrum. Meth.*, A586:409–420, 2008.

[140] X. Bertou et al. Calibration of the surface array of the Pierre Auger Observatory. *Nucl. Instrum. Meth.*, A568:839–846, 2006.

[141] M. Aglietta et al. Calibration of the surface array of the Pierre Auger Observatory. 2005.

[142] J. Linsley and L. Scarsi. Arrival times of air shower particles at large distances from the axis. *Phys. Rev.*, 128:2384–2392, 1962.

[143] A.A. Watson and J.G. Wilson. Fluctuation studies of large air showers - the composition of primary cosmic ray particles of energy e(p) approx. equal 10-to-the-18 ev. *J.Phys.A*, A7:1199–1212, 1974.

[144] P. W. Gorham et al. Observations of Microwave Continuum Emission from Air Shower Plasmas. *Phys. Rev.*, D78:032007, 2008.

[145] S. Argiro et al. The Offline Software Framework of the Pierre Auger Observatory. *Nucl. Instrum. Meth.*, A580:1485–1496, 2007.

[146] G. Corcella et al. HERWIG 6.5 release note. 2002.

[147] G. Corcella, I.G. Knowles, G. Marchesini, S. Moretti, K. Odagiri, et al. HERWIG 6: An Event generator for hadron emission reactions with interfering gluons (including supersymmetric processes). *JHEP*, 0101:010, 2001.

[148] A.D. Martin, R.G. Roberts, W.J. Stirling, and R.S. Thorne. Scheme dependence, leading order and higher twist studies of MRST partons. *Phys.Lett.*, B443:301–307, 1998.

[149] J. Lozano. Production of simulated extensive air showers for the pierre auger collaboration using grid technology. *10th IEEE International Symposium on Parallel and Distributed Processing with Applications*, July 2012.

[150] Information system about auger grid productions (auger key protected). http://cafpe10.ugr.es/ProdStat/stats.php.

[151] T. Sjostrand, S. Mrenna, and P.Z. Skands. PYTHIA 6.4 Physics and Manual. *JHEP*, 0605:026, 2006.

[152] N.N. Kalmykov and S.S. Ostapchenko. The Nucleus-nucleus interaction, nuclear fragmentation, and fluctuations of extensive air showers. *Phys.Atom.Nucl.*, 56:346–353, 1993.

[153] A. Ferrari, P.R. Sala, A. Fasso, and J. Ranft. FLUKA: A multi-particle transport code (Program version 2005). 2005.

[154] D. Heck and J. Knapp. Upgrade of the monte carlo code corsika to simulate extensive air showers with energies $> 10^{20}$ ev. 1998.

[155] A.M. Hillas. Shower simulation: Lessons from MOCCA. *Nucl.Phys.Proc.Suppl.*, 52B:29–42, 1997.

[156] M. Kobal. A thinning method using weight limitation for air-shower simulations. *Astropart.Phys.*, 15:259–273, 2001.

[157] J. Beringer et al. Review of particle physics. *Physical Review*, D86:010001, 2012.

[158] J.L. Navarro, S. Navas, et al. An offline module for surface signal selection through a top down procedure. Technical report, University of Granada, In preparation.

[159] P. Billoir. Fadc trace cleaning in surface detector through a segmentation procedure. Technical Report 074, L.P.N.H.E. Paris VI - VII, 2005.

[160] P. Billoir. Top-down selection of events and stations. Technical Report 072, L.P.N.H.E. Paris VI - VII, 2006.

[161] P. Billoir. Extracting an unbiased sample of random accidental signals from real data in sd tanks. Technical Report 127, L.P.N.H.E. Paris VI - VII, 2010.

[162] C. Bonifazi and A. Letessier-Selvon. De-biasing the station start time. Technical Report 050, The Pierre Auger Collaboration, 2006.

[163] R.A. Fisher. The use of multiple measurements in taxonomic problems. *Annals Eugen.*, 7:179–188, 1936.

[164] A. Hoecker, P. Speckmayer, J. Stelzer, J. Therhaag, E. Von Toerne, and H. Voss. TMVA: Toolkit for multivariate data analysis. *PoS*, ACAT:040, 2007.

[165] P. Billoir, P.N. Dong, P.T. Nhung, and I. Lhenry-Yvon. Long term behaviour of well-behaved sd cherenkov counters. Technical Report 048, The Pierre Auger Collaboration, 2010.

[166] C. Jarne and H. Wahlberg. Long term study of sd monitoring variables from 2004 to 2010. Technical Report 045, The Pierre Auger Collaboration, 2011.

[167] L.D. Landau and I. Pomeranchuk. Limits of applicability of the theory of bremsstrahlung electrons and pair production at high-energies. *Dokl.Akad.Nauk Ser.Fiz.*, 92:535–536, 1953.

[168] A.B. Migdal. Bremsstrahlung and pair production in condensed media at high-energies. *Phys.Rev.*, 103:1811–1820, 1956.

[169] J. Abraham et al. Trigger and aperture of the surface detector array of the Pierre Auger Observatory. *Nucl.Instrum.Meth.*, A613:29–39, 2010.

[170] J. Alvare-Muñiz, P. Billoir, O. Deligny, D. Gora, Y. Guardincerri, J.L. Navarro, S. Navas, M. Roth, and J. Tiffenberg. An extensive review on the down-going neutrino systematic uncertainties from the pierre auger observatory. Technical Report 027, The Pierre Auger Collaboration, 2010.

[171] M. Bahr, S. Gieseke, M.A. Gigg, D. Grellscheid, K. Hamilton, et al. Herwig++ Physics and Manual. *Eur.Phys.J.*, C58:639–707, 2008.

[172] S. Ostapchenko. Monte Carlo treatment of hadronic interactions in enhanced Pomeron scheme: I. QGSJET-II model. *Phys.Rev.*, D83:014018, 2011.

[173] E.J. Ahn, R. Engel, T.K. Gaisser, P. Lipari, and T. Stanev. Cosmic ray interaction event generator SIBYLL 2.1. *Phys.Rev.*, D80:094003, 2009.

[174] S.J. Sciutto. AIRES: A System for air shower simulations. User's guide and reference manual. Version 2.2.0. 1999.

[175] S. Agostinelli et al. GEANT4: A Simulation toolkit. *Nucl.Instrum.Meth.*, A506:250–303, 2003.

[176] O. Blanch. Study of systematic uncertainties for skimming tau neutrinos. Technical Report 054, The Pierre Auger Collaboration, 2006.

[177] J. Conrad, O. Botner, A. Hallgren, and C. Perez de los Heros. Including systematic uncertainties in confidence interval construction for Poisson statistics. *Phys. Rev.*, D67:012002, 2003.

[178] G.J. Feldman and R.D. Cousins. A Unified Approach to the Classical Statistical Analysis of Small Signals. *Phys. Rev.*, D57:3873–3889, 1998.

[179] L. Cazon, R.A. Vazquez, and E. Zas. Depth development of extensive air showers from muon time distributions. *Astropart.Phys.*, 23:393–409, 2005.

[180] R. Brun and F. Rademakers. Root - an object oriented data analysis framework. *Nuclear Instruments and Methods in Physics Research Section A: Accelerators, Spectrometers, Detectors and Associated Equipment*, 389:81–86, 1997.

[181] A. Bevan. class tfeldmancousins.

[182] W.A. Rolke and A.M. Lopez. Confidence intervals and upper bounds for small signals in the presence of background noise. *Nucl. Instrum. Meth.*, A458:745–758, 2001.

[183] W.A. Rolke, A.M. Lopez, and J. Conrad. Limits and confidence intervals in the presence of nuisance parameters. *Nucl.Instrum.Meth.*, A551:493–503, 2005.

[184] J. Conrad. class trolke.

[185] J. Abraham et al. Upper limit on the diffuse flux of UHE tau neutrinos from the Pierre Auger Observatory. *Phys.Rev.Lett.*, 100:211101, 2008.

[186] X. Bertou, P. Billoir, O. Deligny, C. Lachaud, and A. Letessier-Selvon. Tau neutrinos in the Auger observatory: A new window to UHECR sources. *Astropart. Phys.*, 17:183–193, 2002.

[187] T. Hahn. CUBA: A library for multidimensional numerical integration. *Comput. Phys. Commun.*, 168:78–95, 2005.

[188] M. Ackermann et al. Search for Ultra High-Energy Neutrinos with AMANDA-II. *Astrophys.J.*, 675:1014–1024, 2008.

[189] R. Abbasi et al. The first search for extremely-high energy cosmogenic neutrinos with the IceCube Neutrino Observatory. *Phys. Rev.*, D82:072003, 2010.

[190] R. Abbasi et al. Constraints on the Extremely-high Energy Cosmic Neutrino Flux with the IceCube 2008-2009 Data. *Phys. Rev.*, D83:092003, 2011.

[191] P. W. Gorham et al. Erratum: Observational Constraints on the Ultra-high Energy Cosmic Neutrino Flux from the Second Flight of the ANITA Experiment. *Phys. Rev.*, D85:049901, 2012.

[192] I. Kravchenko, C. Cooley, S. Hussain, D. Seckel, P. Wahrlich, et al. Rice limits on the diffuse ultrahigh energy neutrino flux. *Phys.Rev.*, D73:082002, 2006.

[193] K. Martens. HiRes Estimates and Limits for Neutrino Fluxes at the Highest Energies. 2007.

[194] R.U. Abbasi et al. An upper limit on the electron-neutrino flux from the hires detector. *Astrophysical Journal*, 684(2):790, September 2008.

[195] J.K. Becker, P.L. Biermann, and W. Rhode. The diffuse neutrino flux from FR-II radio galaxies and blazars: A source property based estimate. *Astropart. Phys.*, 23:355–368, 2005.

[196] P. Abreu et al. Search for First Harmonic Modulation in the Right Ascension Distribution of Cosmic Rays Detected at the Pierre Auger Observatory. *Astropart.Phys.*, 34:627–639, 2011.

[197] A. Cuoco and S. Hannestad. Ultra-high energy Neutrinos from Centaurus A and the Auger hot spot. *Phys. Rev.*, D78:023007, 2008.

[198] M. Kachelriess, S. Ostapchenko, and R. Tomas. High energy radiation from Centaurus A. *New J. Phys.*, 11:065017, 2009.

[199] R. Abbasi et al. Time-Integrated Searches for Point-like Sources of Neutrinos with the 40-String IceCube Detector. *Astrophys. J.*, 732:18, 2011.

[200] C.W. James, R.J. Protheroe, R.D. Ekers, J. Alvarez-Muñiz, R.A. McFadden, C.J. Phillips, P. Roberts, and J.D. Bray. Lunaska experiment observational limits on uhe neutrinos from centaurus a and the galactic centre. *Monthly Notices of the Royal Astronomical Society*, 410(2):885–889, September 2010.

[201] Files containing analysis tools and results (auger key protected). https://www.auger.unam.mx/AugerWiki/The_Neutrino_analysis_task.

[202] J. Bluemer, D. Gora, M. Haag, M. Roth, and A. Tamburro. On the influence of accidental muons on air shower detection. Technical Report 110, Pierre Auger Observatory, 2008.

[203] P. Billoir, J.L. Navarro, and S. Navas. An offline module for injection of random accidental signals in sd stations. Technical Report 038, The Pierre Auger Collaboration, 2011.

[204] T2 files in different format. (auger key protected). http://ipnweb.in2p3.fr/ auger/AugerProtected/AcceptT2.html.

[205] P. Ghia and I. Lhenry-Yvon. The "communications crisis" in 2009: proposal for handling data between june and november. Technical Report 020, The Pierre Auger Collaboration, 2010.